Utilizing Science and Technology to Enhance a Future Planetary Mission:

Applications to Europa

by

Melissa K. Bunte

A Dissertation Presented in Partial Fulfillment
of the Requirements for the Degree
Doctor of Philosophy

Approved August 2013 by the
Graduate Supervisory Committee:

James F. Bell, III, Chair
David A. Williams
Srikanth Saripalli
Amanda B. Clarke
Stephen J. Reynolds
Philip R. Christensen

ARIZONA STATE UNIVERSITY

December 2013

ABSTRACT

A thorough understanding of Europa's geology through the synergy of science and technology, by combining geologic mapping with autonomous onboard processing methods, enhances the science potential of future outer solar system missions.

Mapping outlines the current state of knowledge of Europa's surface and near sub-surface, indicates the prevalence of distinctive geologic features, and enables a uniform perspective of formation mechanisms responsible for generating those features. I have produced a global geologic map of Europa at 1:15 million scale and appraised formation scenarios with respect to conditions necessary to produce observed morphologies and variability of those conditions over Europa's visible geologic history.

Mapping identifies areas of interest relevant for autonomous study; it serves as an index for change detection and classification and aids pre-encounter targeting. Therefore, determining the detectability of geophysical activity is essential. Activity is evident by the presence of volcanic plumes or outgassing, disrupted surface morphologies, or changes in morphology, color, temperature, or composition; these characteristics reflect important constraints on the interior dynamics and evolutions of planetary bodies.

By adapting machine learning and data mining techniques to signatures of plumes, morphology, and spectra, I have successfully demonstrated autonomous rule-based response and detection, identification, and classification of known events and features on outer planetary bodies using the following methods:

1. **Edge-detection**, which identifies the planetary horizon and highlights features extending beyond the limb;

2. **Spectral matching** using a superpixel endmember detection algorithm that identifies mean spectral signatures; and
3. **Scale invariant feature transforms combined with supervised classification**, which examines brightness gradients throughout an image, highlights extreme gradient regions, and classifies those regions based on a manually selected library of features.

I have demonstrated autonomous: detection of volcanic plumes or jets at Io, Enceladus, and several comets, correlation between spectral signatures and morphological appearances of Europa's individual tectonic features, detection of ≤94% of known transient events on multiple planetary bodies, and classification of similar geologic features. Applying these results to conditions expected for Europa enables a prediction of the potential for detection and recommendations for mission concepts to increase the science return and efficiency of future missions to observe Europa.

DEDICATION

To following dreams

and to never leaving things unfinished -

This work is dedicated,

with love, to my grandmother “Genie”

for her belief that you can do anything if you try hard enough;

with vision, to my advisor and advocate Ron

whose perspective allowed this work to take shape;

with gratitude, to my parents and husband

for their staunch support and sacrifices;

and with dreams, to my sweet Grayson,

as proof that you *can* be anything you want when you grow up.

Shoot for the Moon.

Even if you miss, you’ll land among the stars.

-Les Brown

ACKNOWLEDGMENTS

This research was conducted in partial fulfillment of the requirements for the Degree of Doctor of Philosophy in the School of Earth and Space Exploration at Arizona State University, Tempe, Arizona. Primary financial support was provided by a NASA Earth and Space Science Fellowship. Additional support was provided by a NASA Strategic University Research Partnership with the Jet Propulsion Laboratory and by the Planetary Geology and Geophysics Program. Partial support for related projects was provided by SESE, the NASA Astrobiology Institute, the PGG's Analysis of Lunar and Mercurian Regoliths Grant, the NASA Exploration Systems Mission Directorate Lunar Mapping and Modeling Program, the NASA Lunar Advanced Science and Exploration Research Program, and the NASA Applied Information Systems Research Program.

I thank my advisory committee, Ronald Greeley, James Bell, Srikanth Saripalli, David Williams, Amanda Clarke, Stephen Reynolds, and Philip Christensen for their guidance. Special thanks go to Jim Bell for his expertise as my ending advisory chair. I am supremely grateful for being able to progress with established objectives and methods.

For their collaboration on the Geologic Map of Europa, I thank Ronald Greeley, Thomas Doggett, Patricio Figueredo, Kenneth Tanaka, Trent Hare, and David Senske. I gratefully acknowledge additional contributions, support, and reviews by Jenny Blue, Eric Kolb, Kevin Mullins, Sabine Weiser, Katherine Sever, Brad Dalton, Charles Bradbury, Daniel Ball, and the U.S. Geological Survey.

For their contributions to the Autonomous Detection of Geophysical Activity projects, I graciously acknowledge SESE graduate student Yucong Lin for his efforts to modify

SIFT for use and in assessing classification methods. For initial autonomous studies related to edge detection and hyperspectral endmember matching, I thank lead author and algorithm developer David Thompson, contributors Rebecca Castano, and Steve Chien, and reviewers Kiri Wagstaff , Brian Bue, Richard Doyle, Tara Estlin, Daniel Tran, Trina Ray, David Hayden, Essam Heggy, Mike Foote, Caroline Choinard, and JPL's Artificial Intelligence and Machine Learning groups.

For initial work studying convective models of Europa's ice shell, I thank Allen McNamara. For preliminary exploration of autonomous processing methods, I thank Kiri Wagstaff for leading the study on Dynamic Landmarking of Mars Surface Feature Changes. I also thank Michael Broxton and Mark Robinson for involving me in the study on developing the NASA Ames Stereo Pipeline.

I am also greatly appreciative of the help and support offered by my colleagues, friends, and family. I would like to acknowledge the support of several colleagues who have provided helpful reviews, served as sounding boards for developing thought processes, and provided motivation: Amy Zink, Alicia Rutledge, Kristen Paris, Devin Waller, Christina Leach, Meg Hufford, Mary Pendelton-Hoffer, Leon Manfredi, Rebekah Kienenberger, and Stephanie Holaday. In particular, I thank my parents for supporting my thirst for knowledge and encouraging me to continue with my research. I would especially like to thank my husband, Stephen, who sacrificed so much throughout my graduate pursuits and who has helped to raise our son during these crazy years. Most importantly, I thank my son, Grayson, for so gracefully accepting the long hours of work when Mommy couldn't be there. Stephen and Grayson have made the last few years happy and unforgettable. I look forward to starting a new adventure with them.

TABLE OF CONTENTS

Page

CHAPTER Page

CHAPTER Page

CHAPTER Page

CHAPTER Page

LIST OF TABLES

LIST OF FIGURES

Figure Page

Figure Page

Figure Page

CHAPTER 1

INTRODUCTION: EUROPA AS A TARGET FOR PAST AND FUTURE EXPLORATION

1.1 Exploration History of Europa

Europa was discovered by Galileo Galilei in January of 1610 along with Io, Ganymede, and Callisto. Together, these four large satellites of Jupiter have come to be known as the Galilean satellites. Their discovery, published in *Siderius Nuncius* in March 1610, and a determination that they orbited Jupiter, was the first evidence to support the Copernican theory of a heliocentric solar system. Telescopic observations and mathematical models of Europa were sufficient, in the ensuing three and a half centuries, to derive estimates of the physical and orbital properties of the satellite. It was not until the late 1900's that more detailed information was uncovered by way of the Pioneer, Voyager, and Galileo missions.

As an exercise in determining the safety of a spacecraft mission to the outer solar system with the aim of a "grand tour" of the four large outer planets, the Pioneer missions 10 and 11 were commissioned to assess possible hazards associated with reaching the outer planets and to explore the interstellar environment in that region of the solar system. Pioneer 10 reached the Jupiter system in December 1973 and obtained the first spacecraft view of Europa. The surface was imaged with the photopolarimeter instrument at a resolution of 161 km/px (Figure 1-1; Fimmel et al., 1974, 1980), sufficient to illustrate that the surface was not homogeneous. This led to further investigations with Pioneer 11 in 1974.

Figure 1-1. The first spacecraft image of Europa, taken by Pioneer 10 in 1973. This color composite was made by combining images from the red and blue channels of the Imaging Photopolarimeter. The cross-hatch pattern is an artifact of processing. [NASA/JPL]

Having been deemed a low enough risk, the "grand tour" mission, Voyager, took place within only a few years, with both Voyager 1 and 2 being launched in 1977. Data from the Voyager missions revolutionized understanding of the Galilean satellites. Each satellite was understood to have unique surface features and geologic histories (e.g., Smith et al., 1979a,b). Europa was seen to be almost uniformly bright with a network of extensive linear features (>1000 km) and very few impact craters (Figure 1-2). The bright surface was taken to indicate an icy composition while the linear features suggested a brittle surface subject to tectonic stresses and the low number of impact craters suggested a young surface with possible geologically recent resurfacing (Pieri, 1981; Lucchitta and Soderblom, 1982; Malin and Pieri, 1986). Together, these features suggested a dynamic thermal history. Tidal stresses resulting from the 4:2:1 Laplace resonance between Io, Europa, and Ganymede (Laplace, 1805) lead to diurnal variations in Jupiter's gravitational pull on each satellite. This, in turn, provides a mechanism for internal heating (Peale et al., 1979) that is known to produce volcanism on Io (Morabito et al., 1979) and could control the appearance of surface features such as the cycloidal ridges (Helfenstein and Permentier, 1980, 1983, 1985; McEwen, 1986b). Europa was understood to have thermal properties intermediate between the active uncratered Io and the much more subdued but heavily cratered Ganymede or Callisto.

By the end of Voyager, debates had begun regarding how heat could be transported through the interior (Consolmagno, 1975; Consolmagno and Lewis, 1976, 1977, 1978; Reynolds and Cassen, 1979), the possibility of a current or past liquid water layer and its composition (Cassen et al., 1979, 1982), the thickness of the icy crust and its relationship to the appearance of surface features (Squyers et al., 1983; Helfenstein and Parmentier,

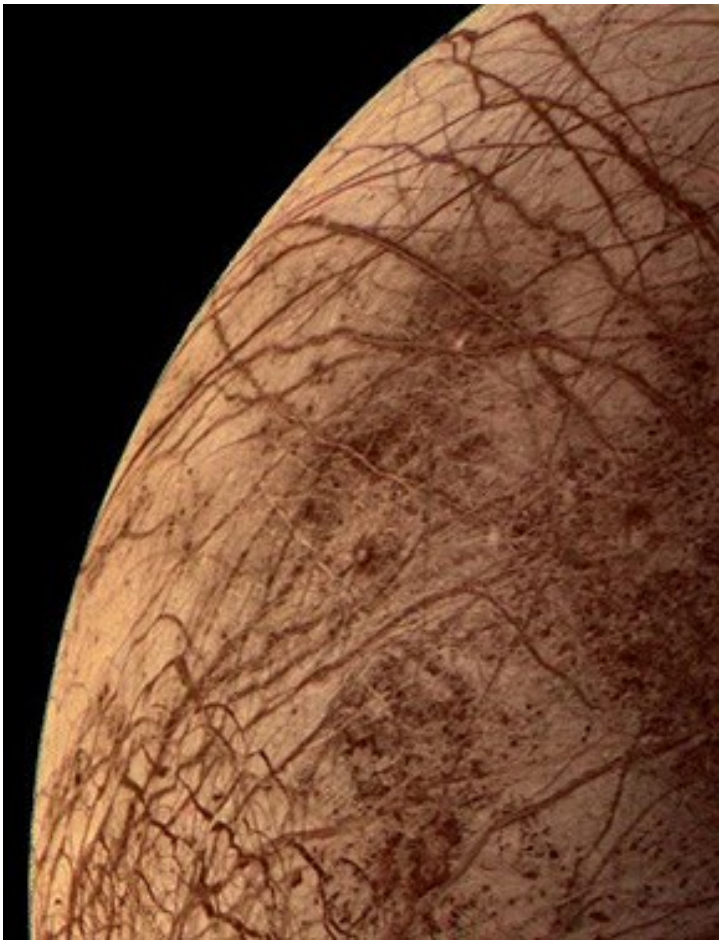

Figure 1-2. The best view of Europa from the Voyager missions, taken by Voyager 2 at closest approach in 1979 at a resolution near 2 km/px. This color composite image shows a portion of the anti-jovian hemisphere and reveals the bright surface crossed by a network of linear features and mottled terrain. [NASA/JPL]

1985), as well as how the formation of Europa could yield a habitable ocean environment (Reynolds et al., 1983; Oro et al., 1992).

Investigations by the Galileo mission, launched in 1989 and reaching the Jupiter system in December 1995, included multiple flybys of each Galilean satellite with 12 encounters with Europa, though considerable data was taken of Europa on orbits primarily targeting other satellites. Imaging at a range of resolutions and viewing geometries with multiple instruments allowed studies of regional terrains, individual features, topography, and composition. Geologic features were revealed to indicate the possibility of sub-ice activity and other internal processes that disrupt the surface (Figure 1-3; e.g., Sullivan et al., 1998; Pappalardo et al., 1998, 1999; Geissler et al., 1998a; see reviews by Carr et al., 1998 and Greeley et al., 1998b). With the return of magnetic data suggesting an electrically conductive internal composition (Khurana et al., 1998; Kivelson et al., 1999, 2000), the idea of a current liquid ocean became an even more alluring explanation for the formation of the diverse surface features, though a concrete determination of the current existence of a liquid ocean remains inconclusive.

Galileo cemented the idea that thermal controls due to tidal forces could result in vastly different surface features on each of the four large satellites. Io, as the satellite closest to Jupiter and orbiting the fastest, experiences the greatest tidal dissipation and the most extensive resurfacing. The amount of tidal forcing to provide heat diminishes with distance from Jupiter and with a decrease in orbital eccentricity resulting from the resonance. Callisto, the most distant of the major satellites and the one not affected by the orbital resonance, shows little evidence of a thermal history and is instead covered with impact craters, having not undergone resurfacing since its formation (Passey and

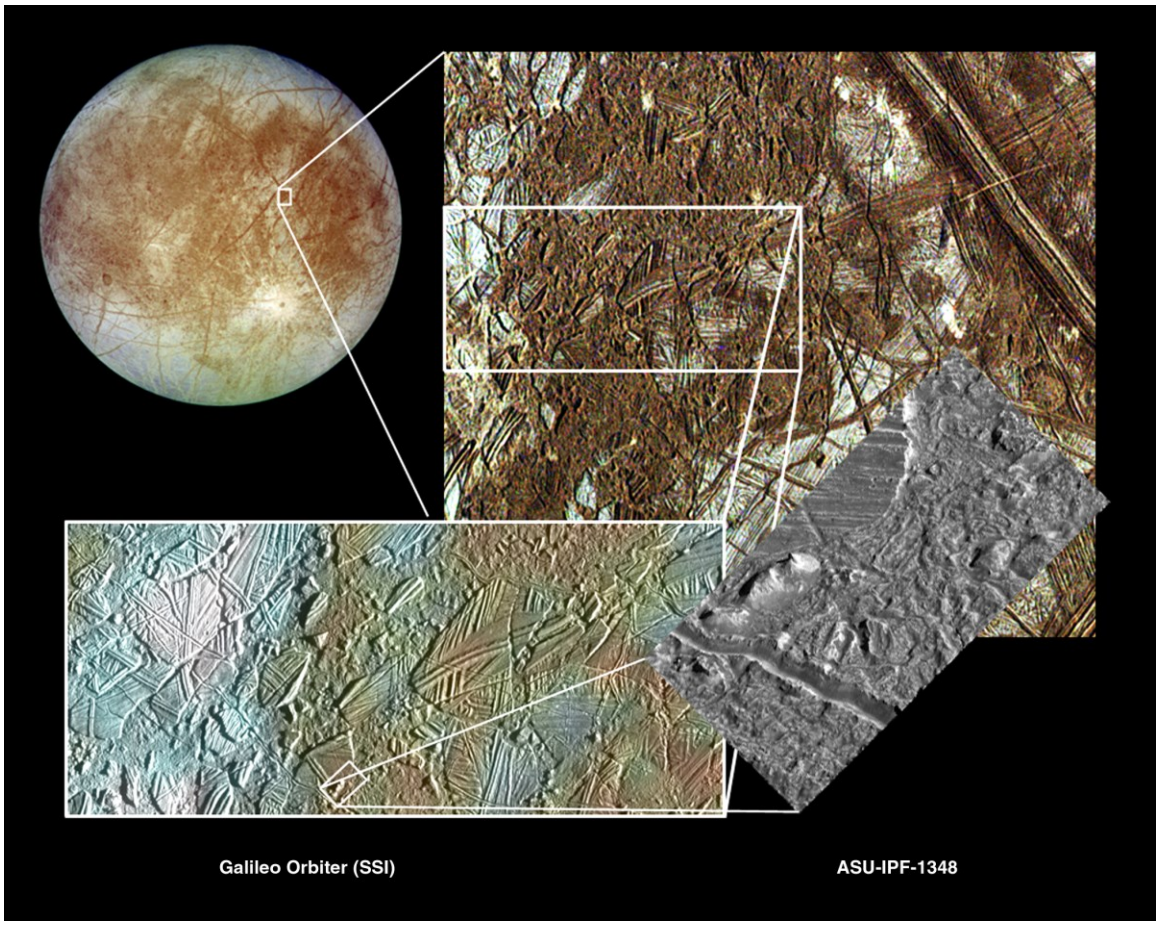

Figure 1-3. Evidence of internal activity at Europa as viewed by Galileo. Features like chaos most likely indicate internal or near sub-surface thermal activity. Conamara Chaos is shown at multiple scales: at regional scale (upper right), the surface is disrupted, though textures are difficult to distinguish. At 54 m/px (lower left), individual rafts and plates, some with preserved ridged plains material, are visible. At 9 m/px (lower right), a plate is rasied compared to the surrounding matrix material. Red-brown areas represent non-ice materials; icy plains are shown in blue. [ASU-SPL, processing by David A. Williams]

Shoemaker, 1982; Schenk, 1995; Greeley et al., 2000a). Europa and Ganymede, the middle satellites, undergo enough tidal forcing to possibly melt Europa's crust to form an interior ocean (Cassen et al., 1979, 1982) with Ganymede experiencing even less resurfacing but remaining warm enough to also maintain a substantial ocean layer. The amazing array of surface features and related interior models are captured in the family portrait of Galilean satellites in Figure 1-4.

Two additional spacecraft observed Europa. Cassini passed by the Jupiter system in 2000 on its way to Saturn. This encounter occurred at the very end of the Galileo mission and allowed the only opportunity for two spacecraft to observe simultaneously. New Horizons also made multiple observations during its 2007 flyby en route to Pluto and the Kuiper Belt. Though these observations provided few new insights, they established that Europa had undergone no major changes. In addition, multiple ground-based telescopes have been used to study Europa, as has the Hubble Space Telescope. These observations have contributed substantially to the understanding of the Galilean satellites.

1.2 Properties of Europa: Major Discoveries

The smallest of the Galilean satellites, Europa is approximately the same size as Earth's Moon, at a radius of 1562 km (Seidelmann et al., 2007). Its mass is also nearly equivalent to that of the Moon and to that of Io as well. At 4.8×10^{22} kg (Anderson et al., 1998), this mass similarity suggested that both Io and Europa might have similar densities and compositions to the Moon. After further studies into density and taking the bright surface albedo into consideration, Pickering (1908) suggested that Europa had a density equivalent to the Moon but that its surface might be covered by a bright material. Jeffreys (1923) was the first to suggest that several of the Galilean satellites might have an icy

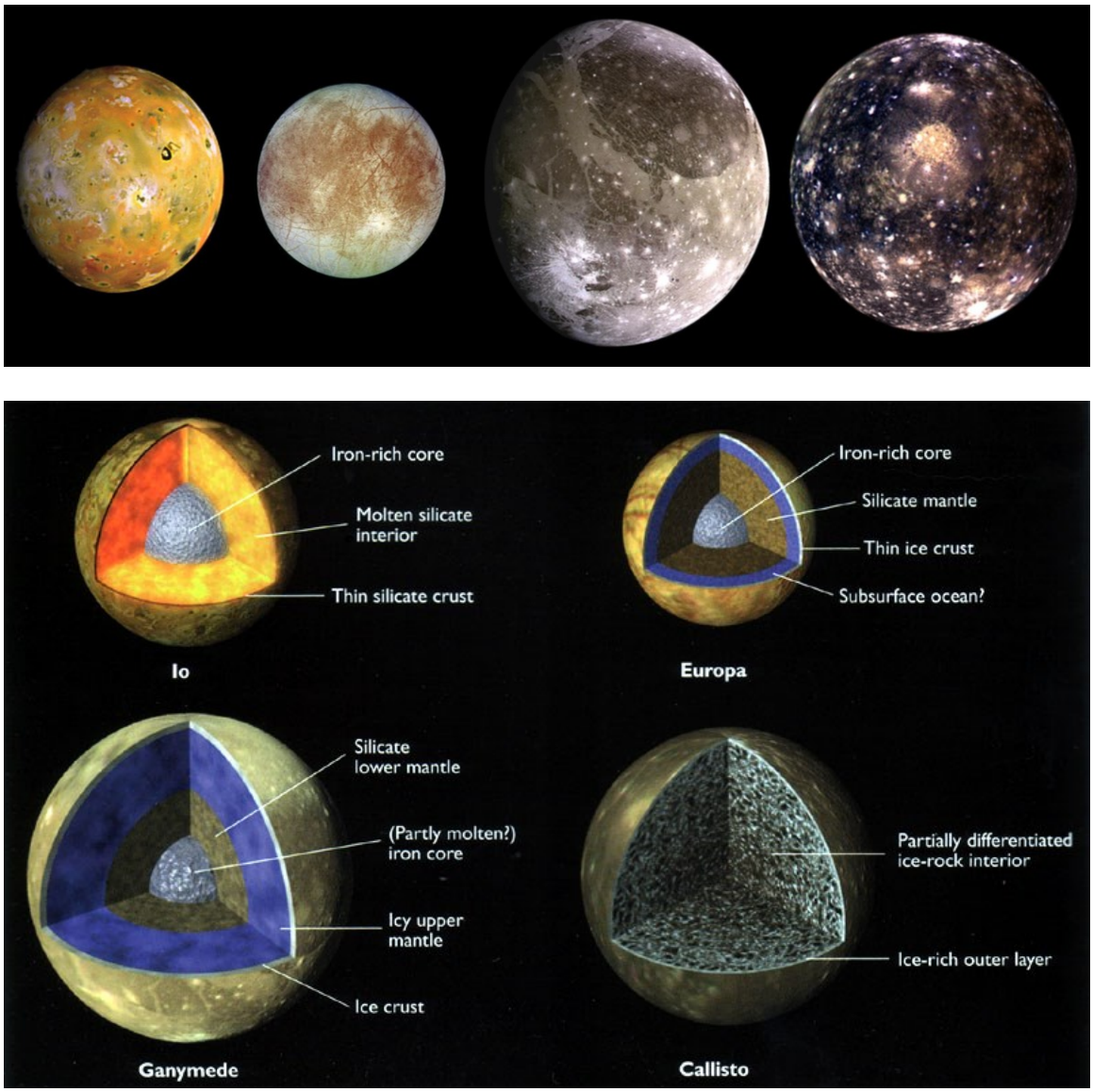

Figure 1-4. The Galilean satellites as viewed by Galileo. Top: The surfaces of the satellites; from right to left: Io, Europa, Ganymede, and Callisto. [NASA/JPL] Bottom: Interior models of the Galilean satellites. Surface mosaics include Voyager images. [NASA/JPL/DLR]

composition. Whipple (1963) further speculated on the high reflectivity of the satellite surfaces and suggested that they were covered in icy materials. It is now understood from gravity data and the modern density value (3.0 g/cm^3) that Europa is a differentiated body with a metallic iron core, a silicate mantle and an outer layer of water of which at least some is a frozen crust (Figure 1-5; Anderson et al., 1998; Kivelson et al., 2000; Kargel et al., 2000).

Magnetic field fluctuations resulting from induced electrical currents within Europa were detected by Galileo (Khurana et al., 1998; Kivelson et al., 1999, 2000; Zimmer et al., 2000). These were determined to be driven by Jupiter's intense magnetic field and an electrically conductive material in Europa's subsurface. The nature of the conductive layer, its thickness, and its depth below the surface have been much debated (Figure 1-5). Gravity data constrain the total water layer thickness to between ~80 and ~170 km (Anderson et al., 1998). Considerations of surface geology constrain the outer ice shell thickness to between ~3 and >30 km (Greeley et al., 2004; Greenberg et al., 2002; Pappalardo et al., 1998; Ojakangas and Stevenson, 1989; Hussmann et al., 2002; Tobie et al., 2003). This implies a liquid ocean layer ~70 km thick. The ice and liquid layer thicknesses could play a large role in determining the method of heat transfer from the interior to the surface (see illustration Figure 1-6). The intensity of conductivity also requires that the conductive portion of the water layer lie within about 200 km of the surface (Zimmer et al., 2000). Spectroscopic data suggest the presence of a non-ice component such as hydrated salts or sulfates such as magnesium sulfate, $MgSO_4$, (McCord et al., 1998b, 1999) or hydrated sulfuric acid (Carlson et al., 1999); a salty ocean is considered the best candidate to explain the electrical conductivity. Models of

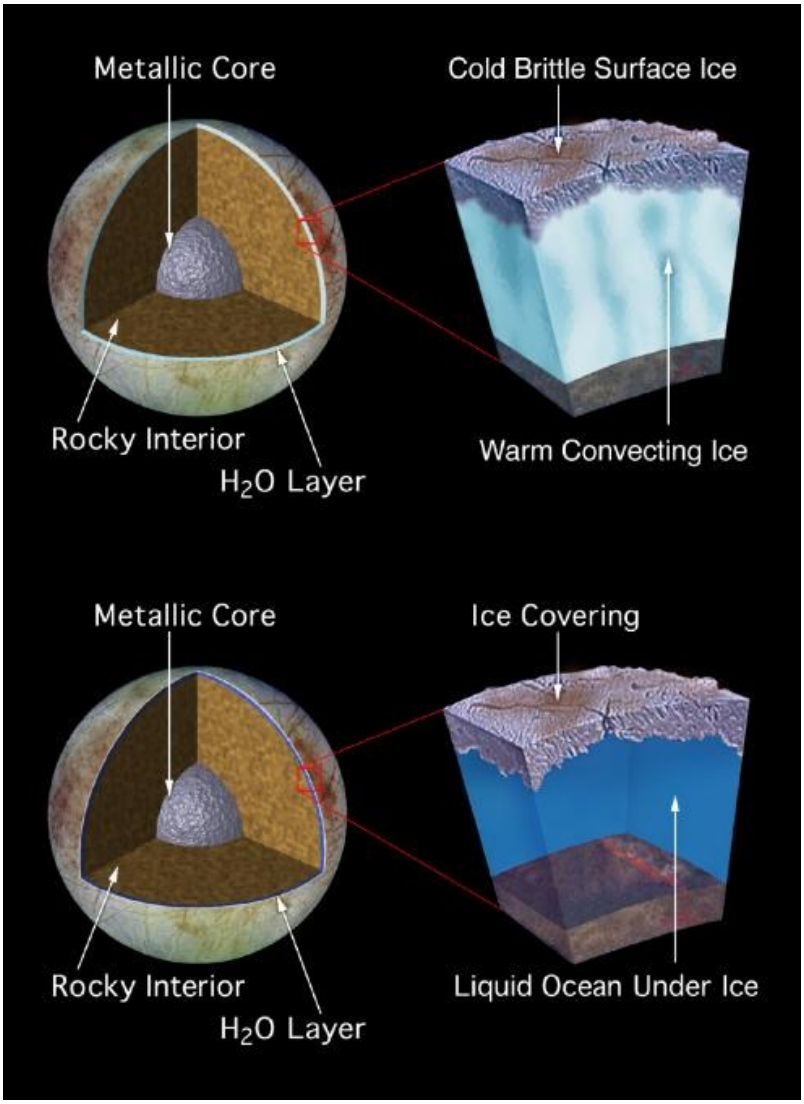

Figure 1-5. The interior of Europa is differentiated and consists of a metallic core, silicate mantle, and a water layer. There is much debate on the thickness of the water layer and whether it consists of warm convecting ice or a liquid layer beneath an ice crust. Galileo data strongly supports the existence of a subsurface ocean. [NASA/JPL]

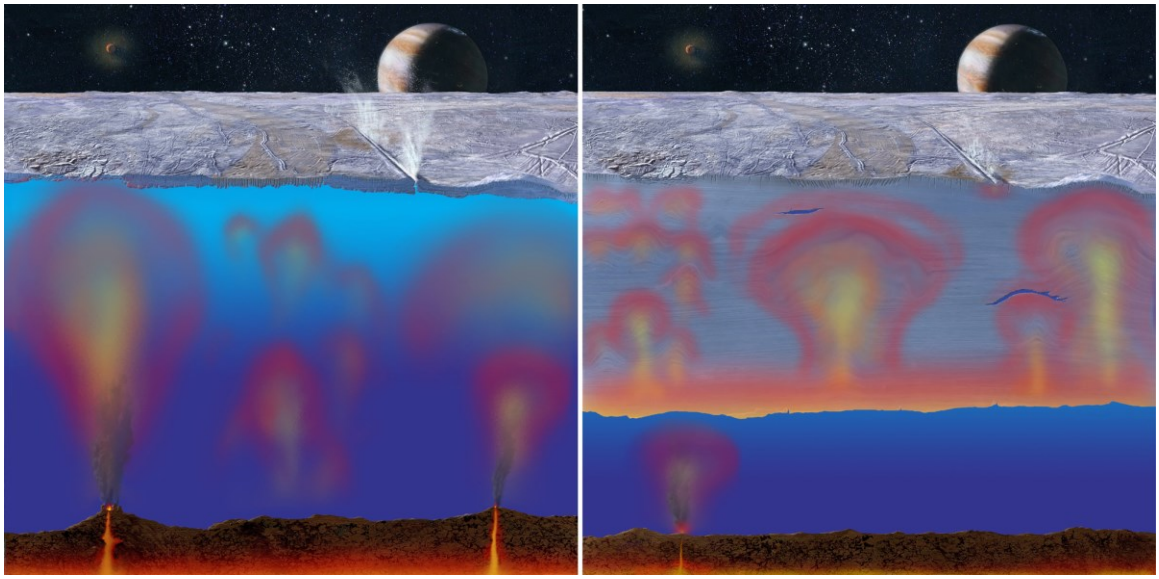

Figure 1-6. Ice and ocean thickness determines the method of heat transfer. If the ice shell is sufficiently thin, direct melting can occur at the surface. If the ice shell is sufficiently thick, the ocean and lower boundary of the ice shell will be warmed slowly and gradual shifting can fracture the brittle surface. [NASA/JPL/Michael Carroll]

salt composition and saturation level relate directly to the level of conductivity and therefore the limits of layer thicknesses. Hand and Chyba (2007) suggest that a relatively freshwater ocean, slightly more salty than terrestrial lakes, is possible but that the ice layer is likely less than 15 km thick and the mostly likely configuration is a very salty ocean beneath an ice shell <4 km thick.

Europa's inclusion in the Laplace resonance with Io and Ganymede forces additional controls on the appearance of the surface and the functionality of Europa's interior. The resonance forces Europa's orbit to be eccentric, further subjecting the satellite to tidal deformation and heating. Tidal heating directly influences the characteristics of the ice shell and ocean as well as how materials within those layers interact with the surface; surface features are expected to show evidence of tidal forces. The presence of the resonance throughout Europa's entire history is speculative, with models suggesting a primordial resonance and a decrease in heating throughout history (Greenberg, 1982, 1987) or an evolving resonance with increased heating throughout history (Yoder, 1979; Yoder and Peale, 1981). Gravity considerations (Anderson et al., 1998) have led others (McKinnon, 1996; Schubert et al., 2004, 2009) to support a complex thermal history with partial melting of the rocky interior that could even drive volcanism at the base of the ocean. The paucity of large impact craters as compared to other satellite surfaces (Smith et al., 1979a,b; Lucchitta and Soderblom, 1982) suggests a young surface age, estimated to be ~40-90 million years (Zahnle et al., 2003; Bierhaus et al., 2009). A young surface certainly indicates recent thermal activity sufficient to erase previous generations of surface features though it does not definitively indicate the thermal evolution of the satellite as related to the tidal dissipation.

The tidal effects on thermal history also affect the tectonic deformation of the surface. Europa is tidally locked to Jupiter with one hemisphere constantly facing the planet as a result of synchronous rotation where the rotation and orbital period are almost equal (Hoppa et al., 1999a). In true synchronous rotation, these values would be exactly equal but measurements have been unable to prove that equality. Several surface feature characteristics have been suggested to form as a result of slight non-synchronous rotation (Greenberg and Weidenschilling, 1984) wherein the satellite librates slightly just as Earth's Moon does; these effects are noted as changes in tidal stress field amplitudes and orientations (Greenberg et al., 1998). The majority of effects contributed to some degree of nonsynchronous rotation are seen in tectonic features (Geissler et al., 1998a; Greenberg et al., 1998; Hoppa et al., 1999b,c; Hurford et al., 2007). To date, no change in position of surface features has been detected due to the absence of time-separated imaging at high resolution (Hoppa et al., 1999a); thus, the determination of deformation of a decoupled ice shell remains unknown. If a decoupled ice shell were conductive and being deformed due to the underlying ocean, lateral variations in the shell thickness could occur (Ojakangas and Stevenson, 1989). This would produce effects of nonsynchronous rotation or true polar wander. Over time, the material distribution within the satellite would change, eventually causing instabilities leading to the change in rotation axis position. This could give rise to observable tectonic patterns (e.g., Leith and McKinnon, 1996; Schenk et al., 2008). Bills et al. (2009) also suggest that features attributed to nonsynchronous rotation are unlikely unless lateral variations in the ice shell thickness are present; they suggest that a small obliquity might instead be responsible for the effects (see also Hurford et al., 2006).

In short, Europa has experienced an enigmatic history due to its physical and orbital characteristics and this has resulted in a dynamic and unique surface. The potential interior ocean is arguably the most interesting discovery related to Europa and it is this characteristic that drives further exploration of Europa. NASA's "Follow the Water" theme extends to Europa with this discovery and marks Europa as a prime target for astrobiological study (Alexander et al., 2009 and references therein).

1.3 Astrobiological Significance

The discovery of extrasolar planets has increased tremendously since the first detection in the late 1980's (Marcy et al., 2005) and the vast majority of them have been determined to be similar to the gas or icy giant planets such as Jupiter or Uranus (Lintott et al., 2013). General expectations are that these planets each have icy satellites analogous to the Galilean satellites of Jupiter, of which three are suspected to harbor internal oceans. If exo-planetary systems are similar, icy satellites, along with their oceans, may be very common (Greeley et al., 2009). Furthering this idea is the understanding that internal oceans may exist at not only Europa, Ganymede, and Callisto, but also at Titan (Lorenz et al., 2008; Tobie, et al., 2005), Enceladus (Spencer et al., 2006; Porco et al., 2006), Triton (Prockter et al., 2005; Stern and McKinnon, 2000), and multiple of Saturn and Uranus's satellites and Kuiper Belt objects. Many of these other potential oceans are more likely to be cold ammonia-rich oceans where sources of energy or heat to support known examples of life are probably lacking (Greeley et al., 2009).

In contrast, Europa (and Enceladus) exhibit compositions and indicators of energy sources that are similar to biological environments that are known to be habitable, sometimes in extreme conditions or in situations like those discovered at hydrothermal

vents (Figure 1-7; e.g., van Dover et al., 2000; Kelley et al., 2001). It is expected that Europa's ocean should be in direct contact with the silicate mantle with pressure and temperature conditions at the silicate-ocean boundary being similar to those on Earth's seafloor. The fact that organisms are known to live in these temperature and pressure conditions without solar energy (e.g., Kelley et al., 2001; review by Hand et al., 2009) raises suspicions that Europa's seafloor environment could also be conducive to the support of life forms.

The discovery of life in the oceans of Europa would be compelling evidence of an independent origin of life (Alexander et al., 2009); likewise the discovery of a habitable environment within the ocean would expand theories on how life could form in such extreme environments and what conditions are necessary for life. Thus, Europa, having been demonstrated as most likely among these satellite candidates to harbor an internal ocean under near- or potentially- habitable conditions and having a surface geology which suggests recent communication between the interior and surface (NASA, 2007), is the highest priority target for exploration (NASA, 2006). Furthermore, the NASA Astrobiology Roadmap (Des Marais et al., 2003) included outer solar system exploration in its objective to search habitable environments, prebiotic chemistry, and signs of life elsewhere in the solar system.

1.4 Future Missions Planned

At the time of this writing, Europa remains a target for future exploration, especially as related to its astrobiological potential, with the main goal being to investigate Europa's habitability or potential to harbor habitable environments.

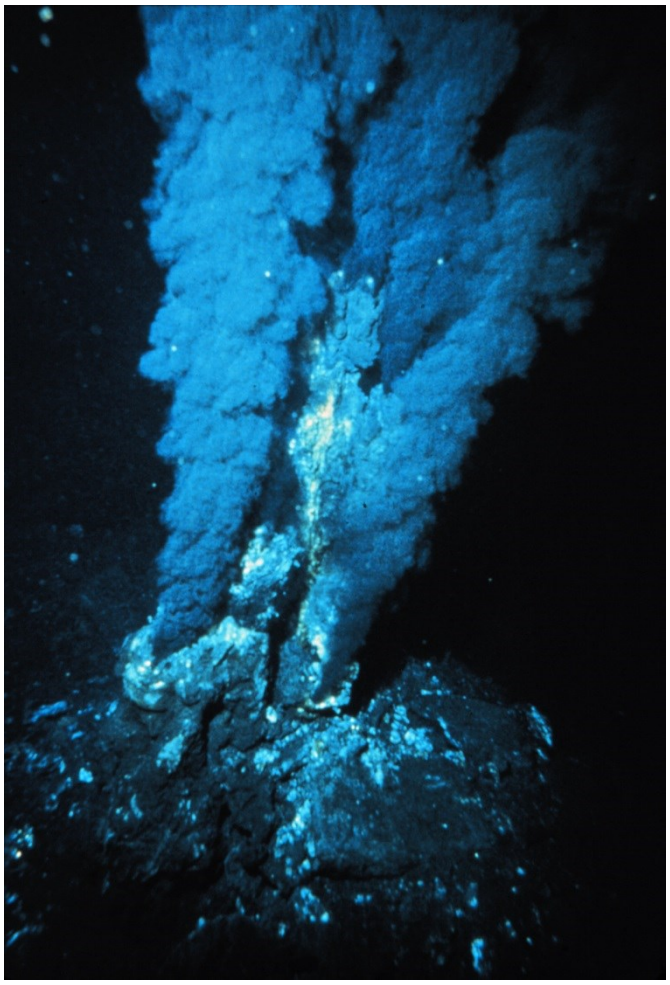

Figure 1-7. Hydrothermal vent ("black smoker") at the Atlantic mid-ocean ridge. [OAR/National Undersea Research Program/NOAA, Photographer: P. Rona]

Over the past two decades, several missions to Europa have been proposed and promoted. Of these, NASA's Jupiter Europa Orbiter (JEO) as part of the Europa Jupiter System Mission (EJSM) joint project with the European Space Agency (ESA), was endorsed by the Nation Research Council's (NRC) first planetary "Decadal Survey", *New Frontiers in the Solar System* (SSB, 2003), as the number one recommended flagship mission to be flown in the decade 2003-2013. Such a Europa Orbiter concept was given high priority by the 2006 Solar System Exploration Roadmap (NASA, 2006), the 2007 NASA Science Plan, and the Outer Planets Assessment Group (OPAG). Despite the high recommendation and science community support, budgetary constraints necessitated a lowering of expectations and the second planetary decadal survey, *Visions and Voyages for Planetary Science in the Decade 2013-2022*, recommended that a Europa mission be carried out only with significant descoping and cost reduction, effectively realizing the impossibility of flying a flagship mission in the cost range of EJSM.

In response to the decadal survey, ESA has proceeded with its plan for the Jupiter Ganymede Orbiter (JGO), the ESA portion of EJSM, and reconfigured the science goals to include objective studies of Ganymede, Callisto, and Europa. That mission is now the Jupiter Icy Moons Explorer (JUICE) and is the first Large-class mission chosen as part of ESA's Cosmic Vision 2015-2025 program. The payload was selected in early 2013 and the mission is slated to launch in 2022 with an arrival at Jupiter in 2030; JUICE will fly by Europa twice and will make measurements of the thickness of Europa's ice crust and identify sites for future in situ exploration.

NASA's response to the descoping of EJSM was a call for mission concept studies that could meet the new cost cap. This yielded the Europa Clipper concept (Europa

Multiple Flyby Mission Study Report). For less than half the cost of EJSM, Europa Clipper (Figure 1-8) can orbit Jupiter for more than 2 years and fly by Europa at least 32 times at closest approaches of within 100km of the surface. This mission could collect information on ice shell thickness, composition, and surface geomorphology. If selected, Europa Clipper could launch as early as 2021 and arrive in the Jupiter system by 2028.

More optimistic plans for future missions include some variety of ice-penetrating probe coupled with a subsurface explorer (e.g., Figure 1-9). While not foreseeable in the near future, such a mission could address many of the questions about Europa that remain unanswered and would be especially rewarding in regards to astrobiological exploration.

1.5 Questions to be Answered

There remain many unanswered questions about Europa. How old is the surface that is visible today and what might the surface have looked like during the past? Exactly what processes are or have been in action to form the current surface and are those processes gradual or short-lived? How deep is the ocean and what is its composition? How thick is the ice shell and is its thickness globally consistent? What is the composition of the non-ice material on the surface and did it originate in the ocean? What is the nature and frequency of the interaction between the ocean, the icy crust, and the surface? Are the physical and chemical conditions in Europa's ice, seafloor, and ocean environment suitable for some form of life? All of these questions require further exploration of the satellite. These are all investigations proposed as part of the future mission concept studies discussed above. They also contribute to answering outstanding questions regarding the formation of planet systems and the evolution of the solar system.

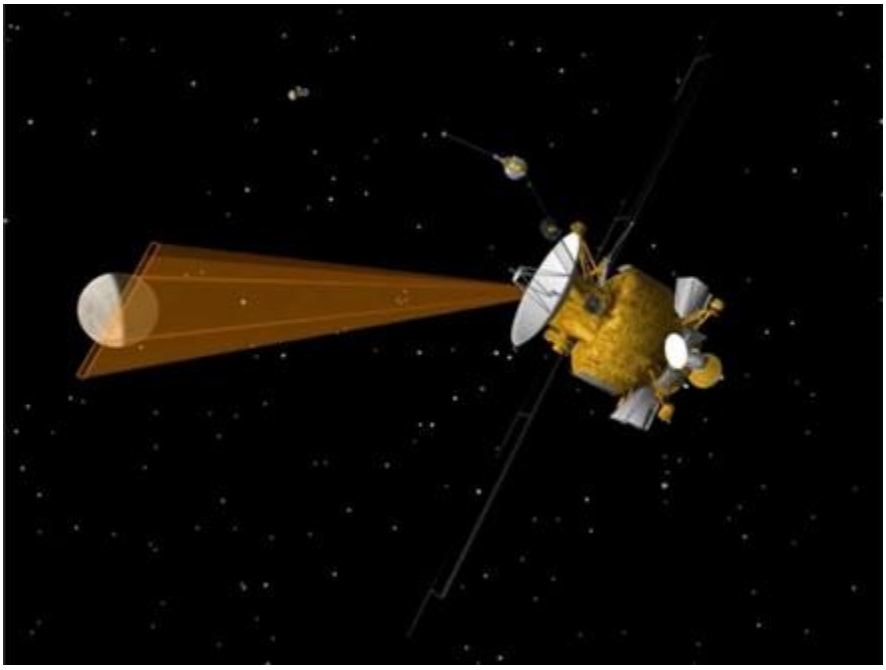

Figure 1-8. Europa Clipper mission concept. [NASA/JPL]

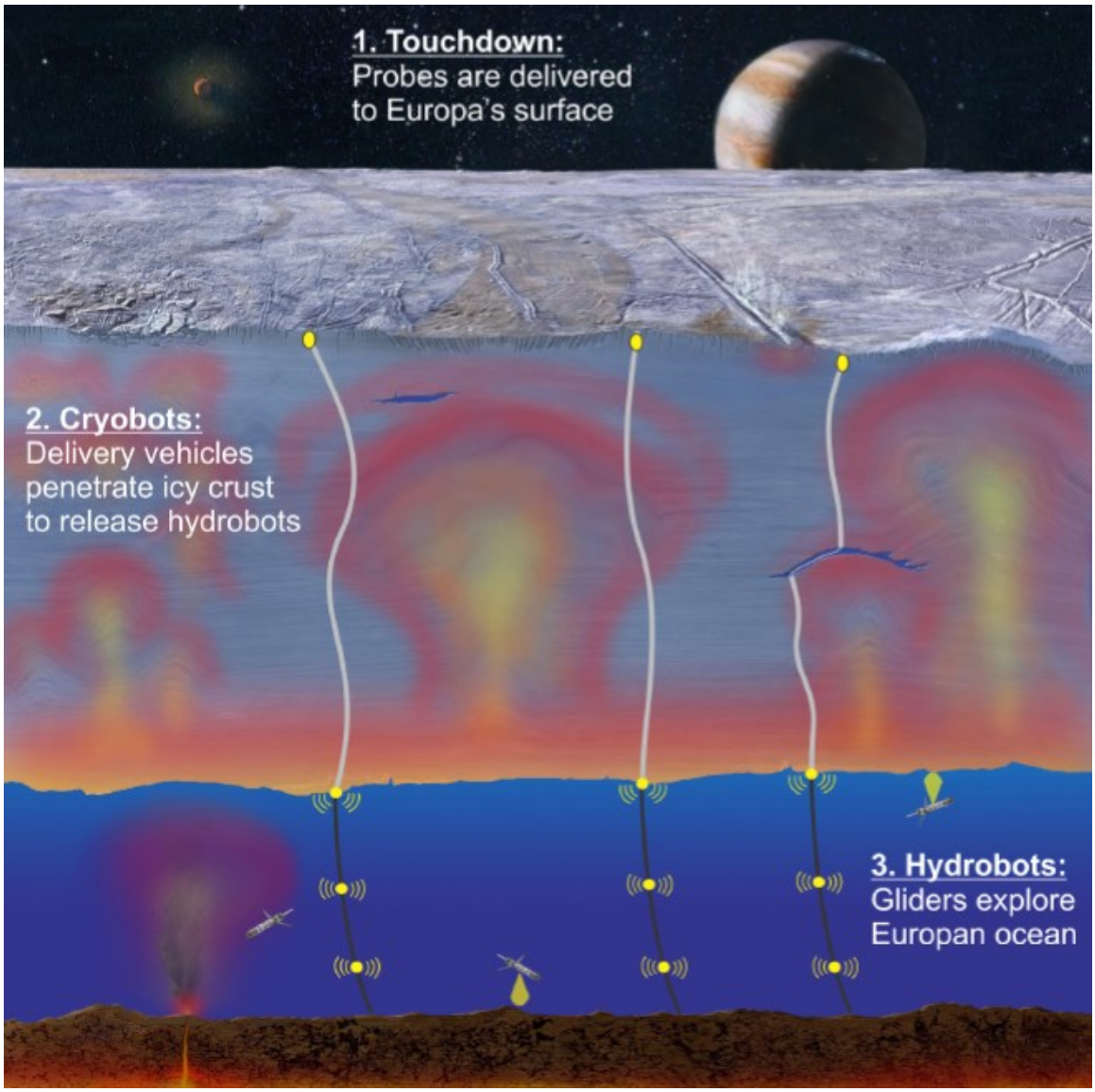

Figure 1-9. A subsurface explorer concept. [NASA NIAC]

This work focuses on building a base of understanding to draw from in answering questions about the surface history and formation processes. It also addresses locating sites of recent or current activity and candidate sites for future exploration.

1.6 Organization of this Dissertation

The purpose of this dissertation is to illustrate how technological advancements and scientific understanding can and should progress simultaneously for optimum exploration potential (Figure 1-10). From previous observations of Europa and other planetary bodies, it is evident that each discovery compels further observation and, often, the development of enhanced technologies- enhanced instruments, better observation techniques, or processing and modeling methods- to promote understanding. Detailed science objectives strengthen future mission plans and new technologies increase the science yield and enrich the missions. In turn, additional missions provide new data for scientific discovery. This work combines the science of geologic mapping to understand the geologic processes currently or previously in action at Europa with the technology of autonomous onboard processing methods to identify areas of interest relevant for future study of Europa.

This work first focuses on Europa's surface, with mapping and an analysis of the varied types of surface features and the possible processes responsible for their formation. A better understanding of the stratigraphic relationships between geologic units leads to a description of Europa's recent geologic history. A more in-depth look at formation processes, the conditions necessary for those processes to occur, and the expected appearance of surface features constitutes an exploration of Europa's near sub-surface geophysical dynamics.

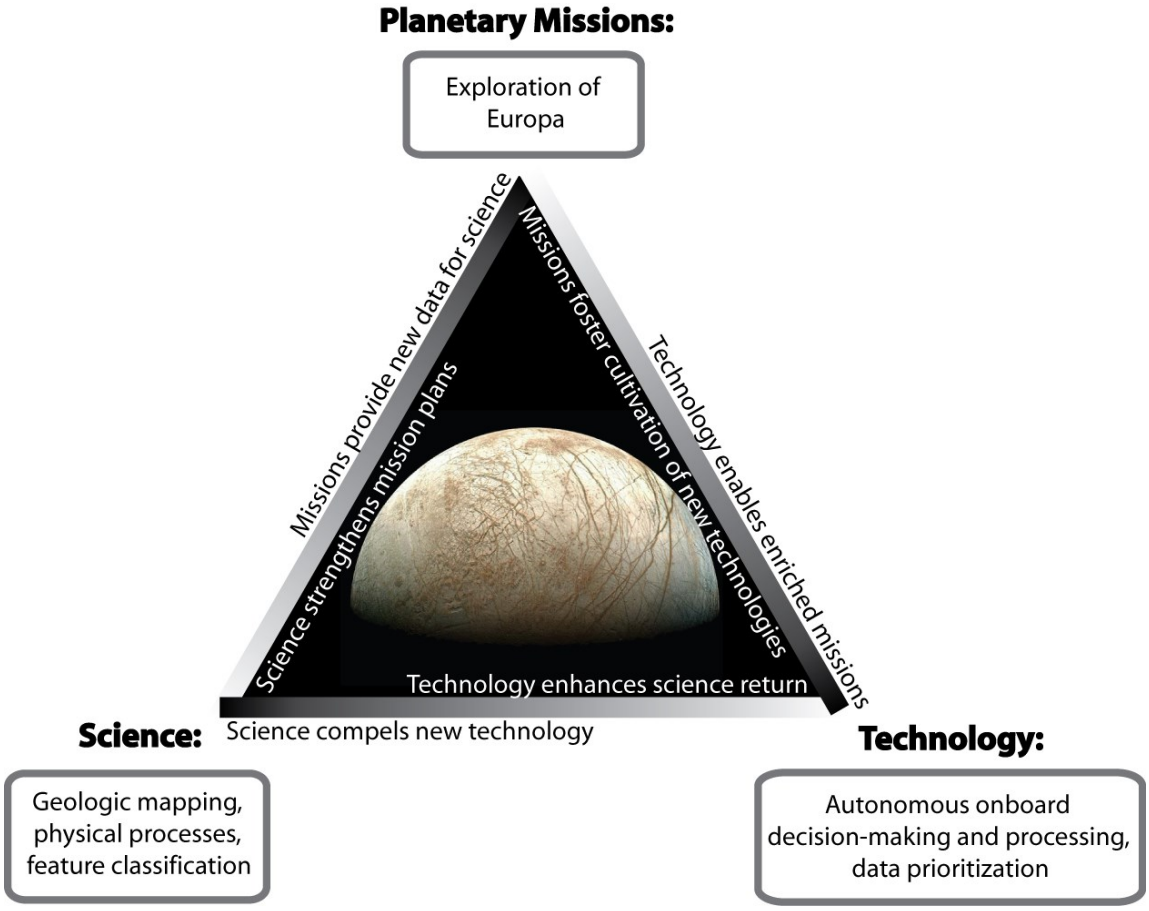

Figure 1-10. Synergy of Science and Technology to enhance the potential of future exploration of Europa. [Background image: NASA/JPL]

A look at the examples of geophysical activity at other planetary bodies in the outer solar system sets the stage for a better understanding of how future missions to Europa can be objectified. This section focuses on methods by which a robotic spacecraft mission can autonomously detect and identify surface expressions of geophysical activity, such as volcanic plumes on Io or comet outgassing. In particular, a method of onboard image processing is tested using images of a range of activity at multiple targets; this testing is meant to establish the range of instrumentation, measurement, processing, and feature characteristics that can accurately be detected. These criteria are then applied to types of activity that are expected or proposed for Europa to assess the benefit of using autonomous processing methods in a future mission to Europa. Finally, a discussion of how similar methods could benefit other missions throughout the solar system promotes continued exploration.

1.7 Synopsis of Results

Major results of this dissertation include the first complete post-Galileo global map of geologic and structural features on Europa, an assessment of the types of autonomous processing methods that can be used onboard a spacecraft to detect geophysical activity and the examples of such activity that must be included in a comparison database for supervision classification methods to be successful without limiting a mission's capability to perform synergistic or opportunistic science investigations, and constraints on the types of features and geophysical events that could be detected on Europa, if present, during a future spacecraft mission.

The material comprising the individual chapters of this dissertation is included in research papers published or in preparation for publication in international research

journals as well as a USGS investigations series geologic map. As such, each represents the efforts and contributions of collaborators who are given due recognition in the acknowledgements section and Appendices C and D.

CHAPTER 2

UNDERSTANDING THE GEOLOGIC HISTORY OF EUROPA THROUGH GLOBAL GEOLOGIC MAPPING

2.1 Introduction

Europa, with its indications of a sub-ice ocean (Cassen et al., 1979, 1982; Anderson et al., 1998; Kivelson et al., 2000; Kargel et al., 2000; Schubert et al., 2009; Nimmo and Manga, 2009; Zolotov and Kargel, 2009; Vance and Goodman, 2009), is of keen interest to astrobiology and planetary geology. Knowledge of the global distribution and timing of Europan geologic units is a key step for the synthesis of data from the *Galileo* mission, and for the planning of future missions to the satellite. This chapter reviews surface material units of Europa as presented in a 1:15 Million scale global geologic map based on the highest quality imaging to date. Discussions address the scale of units and features that are relevant for interpreting formation processes, the geologic history derived from stratigraphic relationships, and the features that are most important for future study.

The surface of Europa is dominated by albedo features which indicate level of surface disruption and are somewhat geographically isolated and by extensive linear features which transcend the graded boundaries of the albedo features. The International Astronomical Union (IAU) has designated eight types of features seen on Europa: regiones, chaos, linea, flexūs, maculae, lenticulae, craters, and large ringed features (described in Doggett et al., 2009). Geographic regions are characterized in terms of the five main surface units summarized by Greeley et al. (2000) and Figueredo and Greeley (2004): plains, chaos, band, ridge, and crater materials, with the addition of lenticulae as a type of chaos (Pappalardo et al., 1998a). Nomenclature for individual features is

assigned based on the Greek myth of Europa and Celtic mythology. Regiones (singular: regio) are large areas defined by color or albedo differences. Low albedo regio are generally associated with chaos materials (Doggett et al., 2009; Collins and Nimmo, 2009) though the texture is only discernible in high resolution images. Lucchitta and Soderblom (1982) noted the mottled appearance of the low albedo regiones which is also typical of lenticulated plains. High albedo regio are associated with plains materials and show the most evidence of ridge formation (Lucchitta and Soderblom, 1982; Doggett et al., 2009). Chaos, broken or disrupted terrain (Collins and Nimmo, 2009), is typified by rafts or blocks of ridged plains materials when viewed at high resolution; these rotated, translated, and sometimes uplifted rafts are surrounded by a hummocky matrix (Carr et al., 1998; Spaun et al., 1998a). Linea are defined as any elongated structures of positive or negative relief (see Kattenhorn and Hurford, 2009; Prockter and Patterson, 2009). Current interpretations group ridges, bands, and flexūs (singular: flexus), along with ridge complexes and ridged bands as linea units (see review in Doggett et al., 2009). Maculae (singular: macula) are low albedo spots; these are generally included as small exposures of chaos materials (Fagents, 2003). Lenticulae (singular: lenticula) are also small dark spots, though these are smaller than maculae and are expressed as domes, depressions ("pits"; Pappalardo et al., 1998a), or spots (when no relief is evident; may be low albedo, i.e., Spaun et al., 1998a). These are included as a gradation of chaos material. Craters exhibit a range of morphologies from simple bowl shapes to complex structures: flat floors, central peaks, and terraces (Moore et al., 1998, 2001; Schenk, 2002; Schenk and Turtle, 2009). Large ringed features are interpreted to be impact relics (Moore et al.,

1998; Schenk, 2002). All craters and large ringed features, along with their ejecta deposits, are identified as crater materials.

2.2 Previous Mapping

The first geologic map of Europa (Lucchitta and Soderblom, 1982) was produced at a hemisphere scale with low resolution *Voyager* data. Following the acquisition of higher resolution data by the *Galileo* mission, researchers have identified surface units and determined sequences of events in relatively small areas of Europa through geologic mapping (Head et al., 1998; Senske et al., 1998; Spaun et al., 1998a,b; Klemaszewski et al., 1999; Prockter et al., 1999; Sullivan et al., 1999b; Williams et al., 1999; Kadel et al., 2000; Figueredo et al., 2002; Prockter and Schenk, 2002; Kattenhorn, 2002) of images at various resolutions acquired by *Galileo*'s Solid State Imaging (SSI) camera (Belton et al., 1992). These works provided a local to sub-regional perspective and employed different criteria for the determination and naming of units. Unified guidelines for the identification, mapping and naming of Europan geologic units were put forth by Greeley et al. (2000) and employed in regional-to-hemispheric scale mapping (Figueredo and Greeley, 2000, 2004) which was expanded into a preliminary global geologic map (Doggett et al., 2009) that serves as a basis for this first complete post-Galileo perspective on global mapping.

2.3 Data

The Voyager spacecraft imaged Europa during flybys in March and July 1979. Voyager 1's global images ranged in resolution from 30 to 100 km/line pair (lp). Voyager 2 provided multispectral coverage of ~20% of the surface with resolutions as high as 2-4.5 km/lp between ~130°and ~210° longitude. Galileo imaged Europa during 21 orbits

between June 1996 and January 2002; of these, 12 were targeted flybys of Europa. Regional views were obtained at medium resolutions of several hundred meters per pixel. Resolutions up to 450 m/px were obtained on several distant viewings. High resolution imaging was possible during the targeted flybys with resolutions as high as several tens of meters per pixel. Approximately 36% of the surface was imaged at 1 km/px or better in Galileo data. Roughly 5% of the surface was imaged stereoscopically but an additional 20% has been assessed through photoclinometry ("shape from shading") techniques (Schenk, 2004, 2006). Figure 2-1 illustrates the resolution coverage of the Voyager and Galileo missions combined. The drastic variation in viewing geometry (Figure 2-1) during Galileo imaging is atypical for spacecraft observations. While this range of illumination allowed characterization of morphology and photometric properties, it must be carefully considered when determining surface geology. The mapping techniques section of this work will expound on procedures used in maintaining consistency of unit definition throughout images.

The cartographic base for this geologic map is a controlled photomosaic of Europa (Figure 2-2; USGS Map I-2757, 2002) which combined the highest quality images of moderate resolution coverage supplied by the Galileo Solid State Imager (SSI) and the Voyager 1 and 2 cameras (Batson, 1987; Becker et al., 1998, 1999, 2001). Due to the failure of Galileo's high-gain antenna, high-resolution imaging was concentrated on a few characteristic terrain and feature types. As Galileo high-resolution coverage is limited in area, Voyager data remain the highest-resolution coverage of some areas, particularly the strip centered near 150°. The digital map was produced using Integrated Software for Imagers and Spectrometers (ISIS; Eliason, 1997; Gaddis et al., 1997; Torson

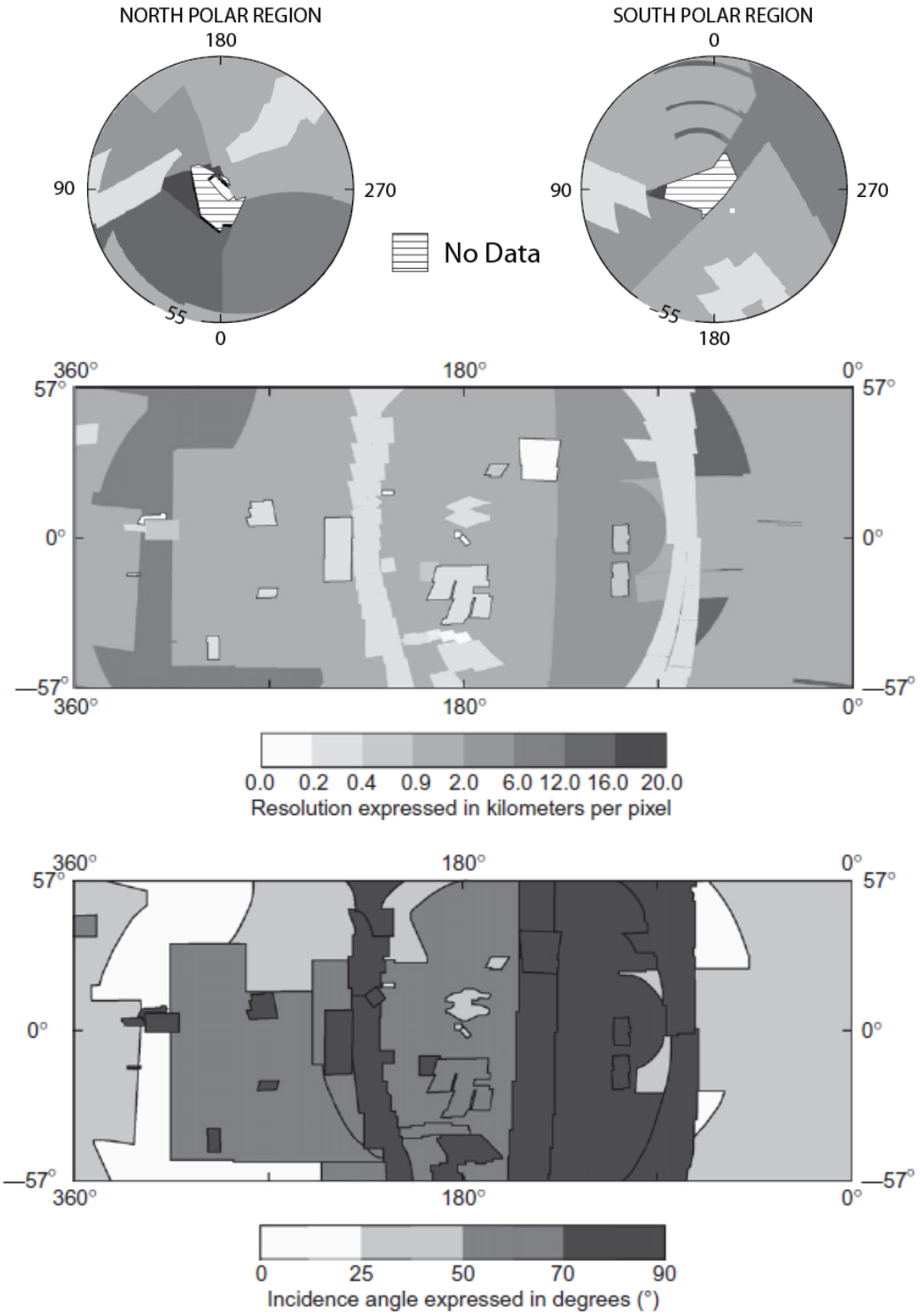

Figure 2-1. Index of resolution and incidence of all images used in the Europa photomosaic. [USGS]

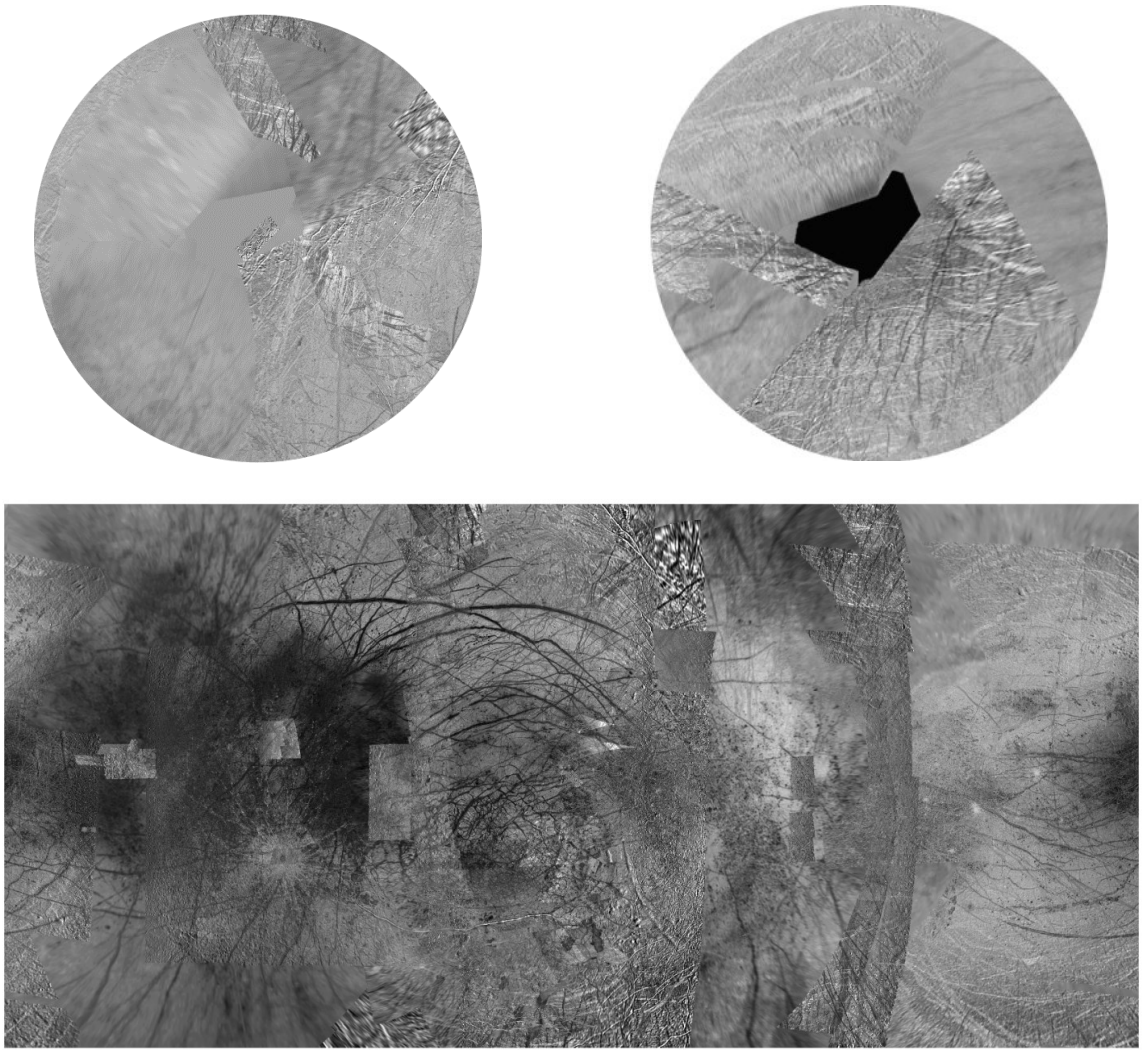

Figure 2-2. Controlled photomosaic of Europa, including polar coverage (USGS, 2002). Top left: North polar region; uniform light gray at the pole indicates no data. Top right: South polar region; black indicates no data. Bottom: Mercator projection of the equatorial region. This image has been enhanced for clarity to illustrate albedo and texture differences. North is up; image is centered on the anti-jovian point at 180°. [USGS]

and Becker, 1997). Individual images were radiometrically calibrated and photometrically normalized using a Lunar-lambert function with empirically derived values (McEwen, 1991; Kirk et al., 2000). A linear correction based on the statistics of all overlapping areas was then applied to minimize image brightness variations. Although consistency was achieved where possible, different filters were included for global image coverage as necessary: clear/blue for Voyager 1 and 2 (Danielson et al., 1981); clear, near-IR (757 nm), and green (559 nm) for Galileo SSI (Belton et al., 1992). The process of creating a geometric control network began with selecting control points on the individual images, making pixel measurements of their locations, using reseau locations to correct for geometric distortions, and converting the measurements to millimeters in the focal plane. These data were combined with the camera focal lengths and navigation solutions as input to a photogrammetric triangulation solution (Davies et al., 1996, 1998; Davies and Katayama, 1981). The final constructed Sinusoidal projection mosaic was then reprojected to the Mercator and Polar Stereographic projections, for latitudes below and above 57°, respectively.

During the creation of the USGS global mosaic, many of the higher resolution images were down-sampled to 500 m/px, resulting in the consistent but degraded portrayal of observable features. Moreover, only images of moderate emission/incidence angles were used in order to reduce contrast differences between the images. Prior to mapping, all of the individual, full-resolution images used in the photomosaic (USGS, 2002) were imported into a Geographic Information System (GIS) application used for mapping. In addition, other high-resolution images not used in the mosaic were manually registered to the base mosaic for use in the GIS application. An updated 200 m/px mosaic using the

entire collection or originally controlled and calibrated images as well as the high-resolution non-calibrated images was generated for digital release with the geologic files. Overall, adequate resolution imaging for generalized global-scale geologic mapping is available for all but two areas at the poles.

Color imaging of Europa does not cover the entire surface, thus a color photomosaic for mapping purposes was not made. However, full disk color views of the leading and trailing hemispheres were taken by Galileo (Figure 2-3). These were used to address context and indications for composition when defining geologic units.

2.4 Mapping Technique

Geologic mapping generally follows the presumption that units are three-dimensional and can be mapped by their stratigraphic relationship to other units in order to determine the procession of events leading to surface exposures. Units are volumes of rock or ice, generally of an identifiable origin, and are defined by distinctive or dominant facies. Structures represent alteration of geologic units in response to tectonic, volcanic, or other processes. Planetary mapping conventions (i.e., Wilhelms, 1990; Skinner and Tanaka, 2003; Tanaka et al., 2005) describe units and structures using objective characteristics such as texture, color, and albedo (see also Shoemaker and Hackman, 1962; Wilhelms, 1972; Head et al., 1978; Batson et al., 1990). Due caution was exercised given that the mosaic has a resolution varying from 12.6 to 0.23 km per pixel, as well as variations in illumination and viewing geometry, to avoid making distinctions between units that are artifacts of these variations. Units are also defined by allostratigraphic relationships in which unconformities are inferred between overlying and adjacent units by differences in morphology (North American Commission on Stratigraphic Nomenclature; Salvatore,

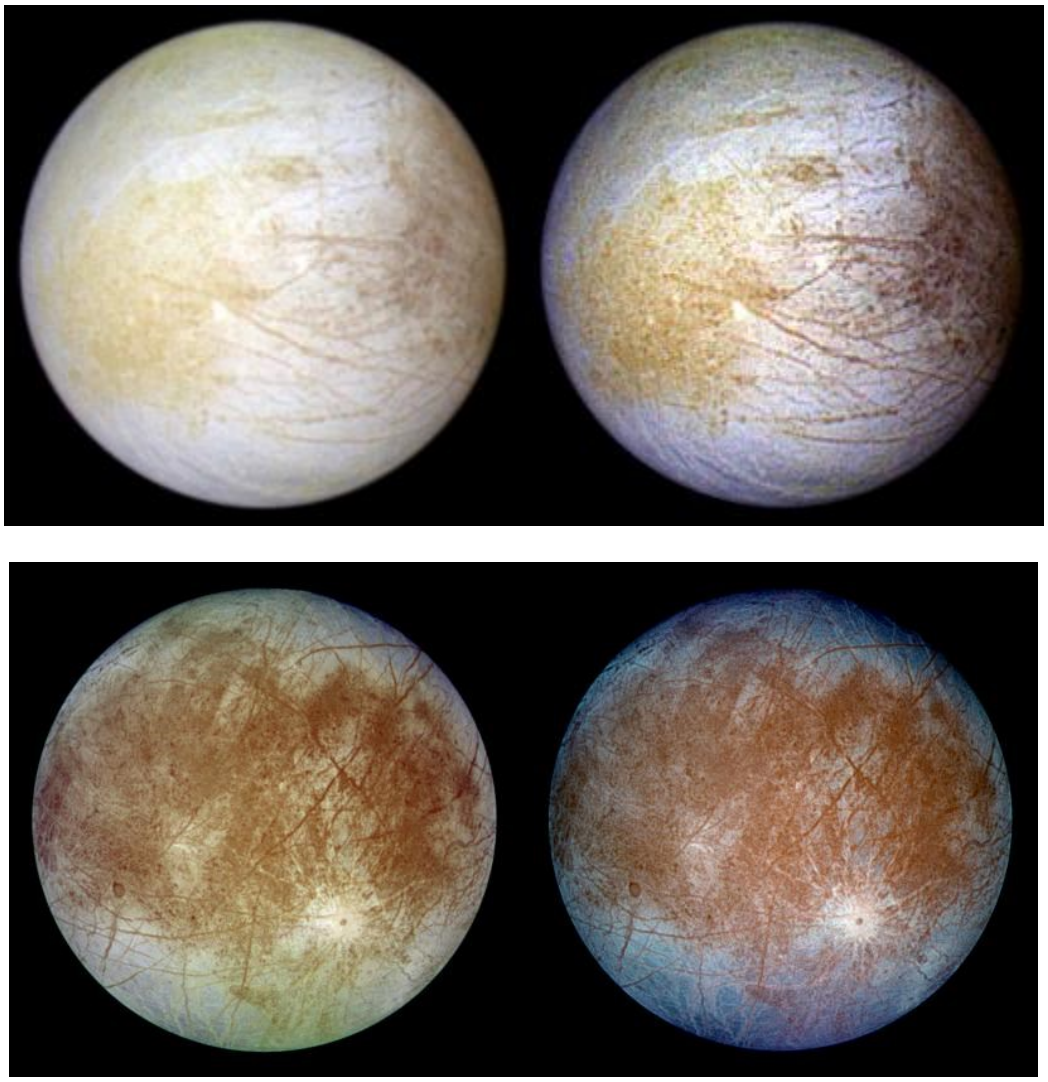

Figure 2-3. Color views of Europa's leading and trailing hemispheres, as imaged by Galileo's Solid State Imaging camera. Images on the left are natural color; images on the right are enhanced to show structural detail. The two hemispheres exhibit noted color differences. Bright white or bluish regions (light blue = fine-grained ice; dark blue = coarse-grained ice) are composed mostly of water ice with few non-ice materials. Brownish mottled regions represent rocky material covered by hydrated salts and other red materials. Top: Leading hemisphere at 12.7 km/px. [NASA/JPL/U. of Arizona] Bottom: Trailing hemisphere at 6.9 km/px. [NASA/JPL/DLR]

1994). In some cases, structures are so distinctive and characteristic of certain units that they are used as part of a unit's defining characteristics. In the case of Europa, structures such as ridges and lenticulae are so prevalent and are representative of specific formation processes that they both contribute to the definition of units and are units themselves. This practice is not often used but has been established in cases where structure is inferred to be a strong control on unit formation, especially with regard to Venus (Tanaka et al., 1994), Europa (Greeley et al., 2000), and Ganymede (Patterson et al., 2010). This approach limits extraneous symbology to convey information. Map units and structures require sufficient areal extent and geologic significance to be effectively portrayed at the scale of the map. Small exposures of potentially unique materials are not mapped due to limitations in size but are included within more extensive units. Similarly, lineaments, which exhibit differing facies that would normally identify them as separate material units but which are too small in extent are mapped as structural line symbols; though they are often too small in width to be included as structures, their importance to defining the geologic history of the surface dictate that they be included and their extensive lengths yield identifiable structural symbols; this is also true of lenticulae that would normally not be plotted as their average dimensions are less than 20 km in any direction.

As is the case with most planetary maps, due to their reliance on remote sensing to determine units, origins of units are not always clear. Planetary mapping standards (USGS, Wilhelms, 1972, 1990; Tanaka et al., 2004) have developed the need to separate observations of characteristics and interpretations so that objective descriptions are valid for any dataset but that interpretations are subject to change (Greeley et al., 2000). This is

especially valid for Europa, as similar textures are juxtaposed with a variety of other units, possibly indicating a variety of origins for the same unit.

Units are grouped by their morphologic type (e.g., 'chaos materials') and named by the same token to reflect their morphology. Previous maps (e.g., Doggett et al., 2009) also employed geographic typing and naming. Geographic associations are avoided here in an attempt to acknowledge general processes that occur globally. Unit symbols indicate the unit group (e.g., 'p' for 'plains'); subscripts indicate the specific unit designation (e.g., '$_r$' for 'ridged'). Specific units within each unit group are listed in approximate chronostratigraphic age, where that age is understood or inferred. Unit groups are also listed in approximate chronostratigraphic order, though individual units are discussed relative to each other in cases where one unit is a gradation of another unit. This is consistent with the need to apply interpretations of modification or resurfacing. As in Wilhelms (1990), when a region is so modified that it no longer has its original properties, it is designated as a separate unit (see also examples from Ganymede; Head et al., 1997). Unit colors reflect groups: cool colors represent plains and chaos materials with plains shown in shades of blue and chaos materials shown in shades of green; warm colors represent structures with lineaments shown in shades of red and crater materials shown in shades of yellow. Mantling materials are shown in a stippled pattern, as is the case of secondary crater materials. Variations in the color spectrum are intended to loosely indicate relative ages, i.e., darker greens indicate younger chaos materials while lighter shades indicate older chaos materials. Shades intermediate between blue and green identify units which are temporally and morphologically intermediate between plains and chaos, reflecting the progressive disruption of plains into chaos. Plains and linea

materials are slight variations on this age spectrum. For plains materials, dark blue represents the ubiquitous ridged plains while light blue indicates lenticulated plains; the reverse hue is intended to more readily indicate the difference in density of lenticulae. The purple shade representing the banded plains is intended to indicate the ties between plains and the identifying lineaments otherwise shown in shades of red. The shading of lineament units loosely indicates order of progression in formation; however, such a progression is not ubiquitous, thus symbol colors are assigned to aid in establishing distribution.

In regard to contact types, at the scale of the map (1:15M), very few contacts are visibly sharp. 'Certain' contacts indicate sharp margins where known; otherwise, they indicate a strong confidence of boundary location based on texture and albedo. These are easiest to establish in high resolution coverage areas. 'Approximate' contacts are applied in all cases where sharp margins cannot be established at the scale of the map or at better scales (1:10M or 1:5M). Often, an 'approximate' contact is necessitated by the inability to confidently identify texture in lower resolution coverage areas. It should be noted that most unit boundaries are also gradational in nature (Figure 2-4). This gradation was best explained by Doggett et al.'s (2009) description of *lenticulated terrain*. At the boundaries of most chaos units, rafts of plains material can be identified in high resolution views. Additionally, rafts of chaos material, identified by Doggett et al. as *microchaos*, can be seen in the plains unit. At the scale of the map, these rafts are not mappable as individual units. The size of the rafts decreases with distance from the overall boundary such that the smallest 'chaotic' features extending into the plains unit are single lenticula structures. The near-boundary, intermediate-sized rafts indicate a defining characteristic

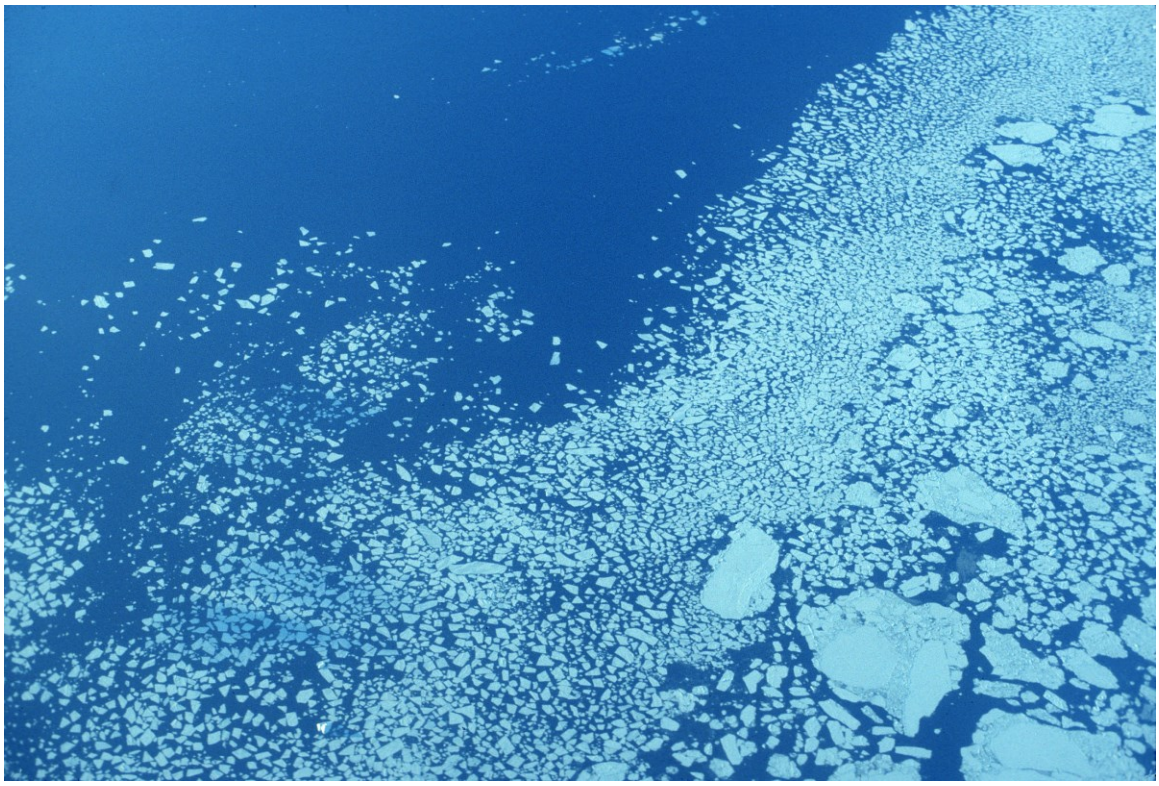

Figure 2-4. Gradational boundaries. Exemplified by rafts of two different materials in a gradation of sizes, as in this image of ice rafts at the edge of an Antarctic ice sheet (off right), unit boundaries are often difficult to define due to the interconnected relationship between units. Rafts of plains material are found within the chaos units and rafts of chaos material extend into the plains units. [Image courtesy of Edmund Stump]

of the lenticulated terrain where plains and chaos materials are represented in approximately equal area. While this terrain is easily distinguished in high resolution images and plottable on larger scale maps, it is generally too narrow to plot at 1:15M scale and is not identifiable, though presumed to exist, at all chaos boundaries. This terrain gradation is seen at most unit boundaries and is seen as an identifying characteristic in establishing formation processes. The inability to determine similar gradation at all boundaries due to the variations in resolution and illumination necessitate that all boundaries be marked as approximate, where the area of gradation is smaller than the uncertainty in approximate boundary location (i.e., all approximate contacts are assumed to also be gradational, and vice versa).

The small dimensions and close spacing of structural features such as lineaments, combined with their high density, would necessitate that structural symbols be plotted on a separate map view from the units if all such structures of mappable dimension were to be included at 1:15M scale. The problem is amplified when attempting to trace the path of individual lineaments through multiple intricate cross-cuttings, buried sections, undulations, and braided or anastomosing patterns or to distinguish individual lenticulae. Thus, only those lineaments crucial to establishing stratigraphic relationships or to accurately portraying a representative number of each lineament type are plotted. Of the ~1500 identifiable lineaments, approximately 150 are plotted. These were chosen based on three overall criteria:

1. prominence, including visibility and length (>100 km);
2. usefulness in constraining stratigraphy;
3. representation of density and distribution of each type of lineament.

To further simplify the map, linea less than 20 km in width are mapped using line symbology. Variations in viewing geometries and resolution, along with the small variation in topography as seen at low resolution and the prevalence of topographic patterns internal to many lineaments, prevent identification of traditional structural identifiers such as strike and dip, fault offset direction, or fault block downthrown direction for every lineament. Thus, these identifying symbols are dispensed with in favor of colored symbols to identify general patterns for each feature type; patterns are described for type examples. Linea greater than 20 km in width are mapped as material units; all of these are identified as band material. Very long or highly visible lineaments tend to be young and most are identified as a class of ridges, the double ridge. Due to their prominence, the number of these young double ridges plotted is disproportionately high compared to other types and ages of lineaments; however, including them is useful in determining the frequency of formation of these features in recent history.

Lineaments which serve as stratigraphic markers were established by Figueredo et al. (unpublished manuscript circa 2006) following pioneering lineament-by-lineament stratigraphy (Stempel and Pappalardo, 2002; Figueredo et al., 2004b; Sarid et al., 2004, 2005). Defining characteristics of stratigraphic markers include one or more of the following criteria:

1. regional extent, especially if the lineament provides a “bridge” across low-resolution areas;
2. clear relative stratigraphy compared to other features or geologic units, especially if the lineament can be dated relative to multiple other features or units;
3. formation time constraints.

Lineaments chosen as "framework" stratigraphic markers are assumed, with few exceptions, to form in rapid events and so serve as allostratigraphic or unconformity boundaries (cf. Skinner and Tanaka, 2003) and bracket the temporal occurrence of geologic units or other feature formation events. The 100 framework linea chosen by Figueredo et al. (unpublished) are used here without change.

The remaining ~50 lineaments include those of prominence and were chosen to supplement the framework lineaments in representing the number, length, and orientation of all types of lineaments. Unfortunately, viewing geometries and resolution differences often prevent the identification of lineament type, the tracing of full lineament length, or the visibility of certain lineament orientations. The distribution chosen cannot account for all of these variations, thus further imaging is necessary to fully understand the global lineament distribution.

2.5 Material Units and Structures

The following section describes the four primary material unit types defined for this map (Figures 2-5 and 2-6): crater, linea, chaos, and plains materials (cf. Greeley et al., 1998, 2000a; Senske et al., 1998; Head et al., 1999a; Prockter et al., 1999; Figueredo and Greeley, 2000, 2004; Doggett et al., 2009). The linea materials, of which ridges and bands were defined in these previous studies as separate unit types, are described as one group of structures represented as distinct facies and are shown overlaid on the unit map. The following descriptions include the respective characteristics of individual units and structures (listed in the legend, Figure 2-7), relative relationships to other units, and, where appropriate, their relationship to previously defined units (e.g., Lucchitta and Soderblom, 1982; Greeley et al., 2000; Doggett et al., 2009). Interpretations of formation

or evolutionary processes are outlined here and addressed further in Chapter 3. A summary of unit and structure descriptions and interpretations can be found in Appendix A. Images of type localities are shown in Figure 2-8.

2.5.1. Plains Materials

Globally extensive plains appear smooth at regional or global resolution and were mapped as smooth materials from examination of Voyager images (i.e., Figure 2-9; Lucchitta and Soderblom, 1982) but are intensely ridged at higher resolution (Head et al., 1998, 1999a; Spaun et al., 1998b; Sullivan et al., 1999b; Kattenhorn, 2002). Three distinct units of plains materials are recognized and are identified by varying degrees of texture and disruption by structures such as lenticulae or bands.

Ridged Plains

Characterization: Ridged plains are characterized by interwoven cross-cutting ridges and troughs at multiple scales (Figure 2-10) with a range of dimensions and various geometries including arcuate, sinuous, and anastomosing and exhibit evidence of degradation in various states (Head et al., 1998, 1999a; Spaun et al., 1998b, 2003; Sullivan et al., 1999a,b; Kattenhorn, 2002). Sets of parallel and sub-parallel ridges are common, as are short ridge segments that are oriented randomly (Greeley et al., 1998b; Patel et al., 1999). Varying degrees of texture, deformation, albedo, lenticulae density, and topographic relief, along with embayment and linea cross-cutting are prevalent. The ridged plains are cross-cut by wide ridge complexes and bands and are sparsely cratered.

The ridged plains correspond to the brightest areas of Europa, notably the Falga (Figure 2-9) and Balgatan Regiones in the northern antijovian and southern subjovian hemispheres, respectively, where prominent and lengthy linea are prevalent. The northern

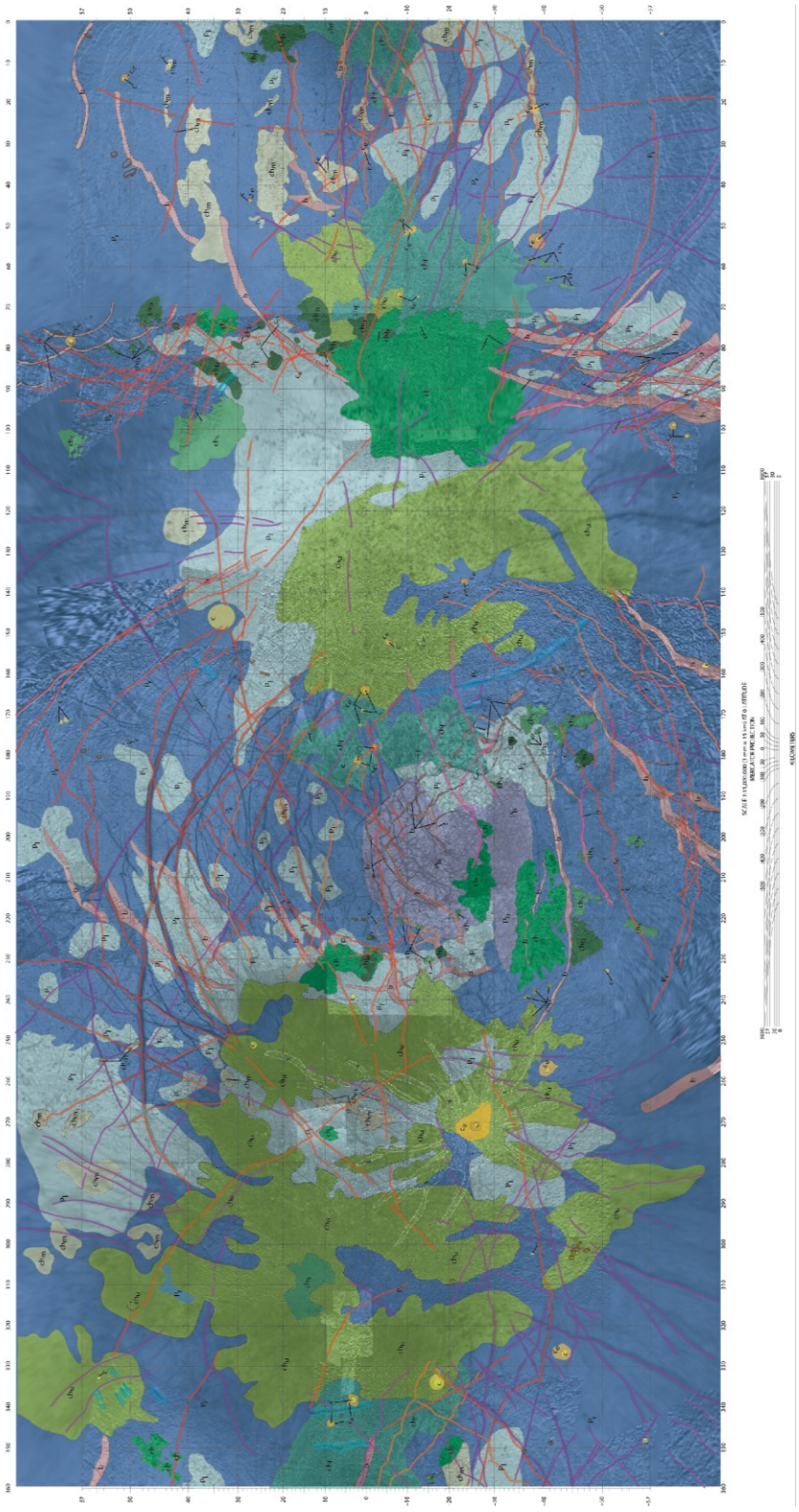

Figure 2-5. Geologic map of Europa at 1:15M scale. North is to the left. Unit descriptions follow in the text.

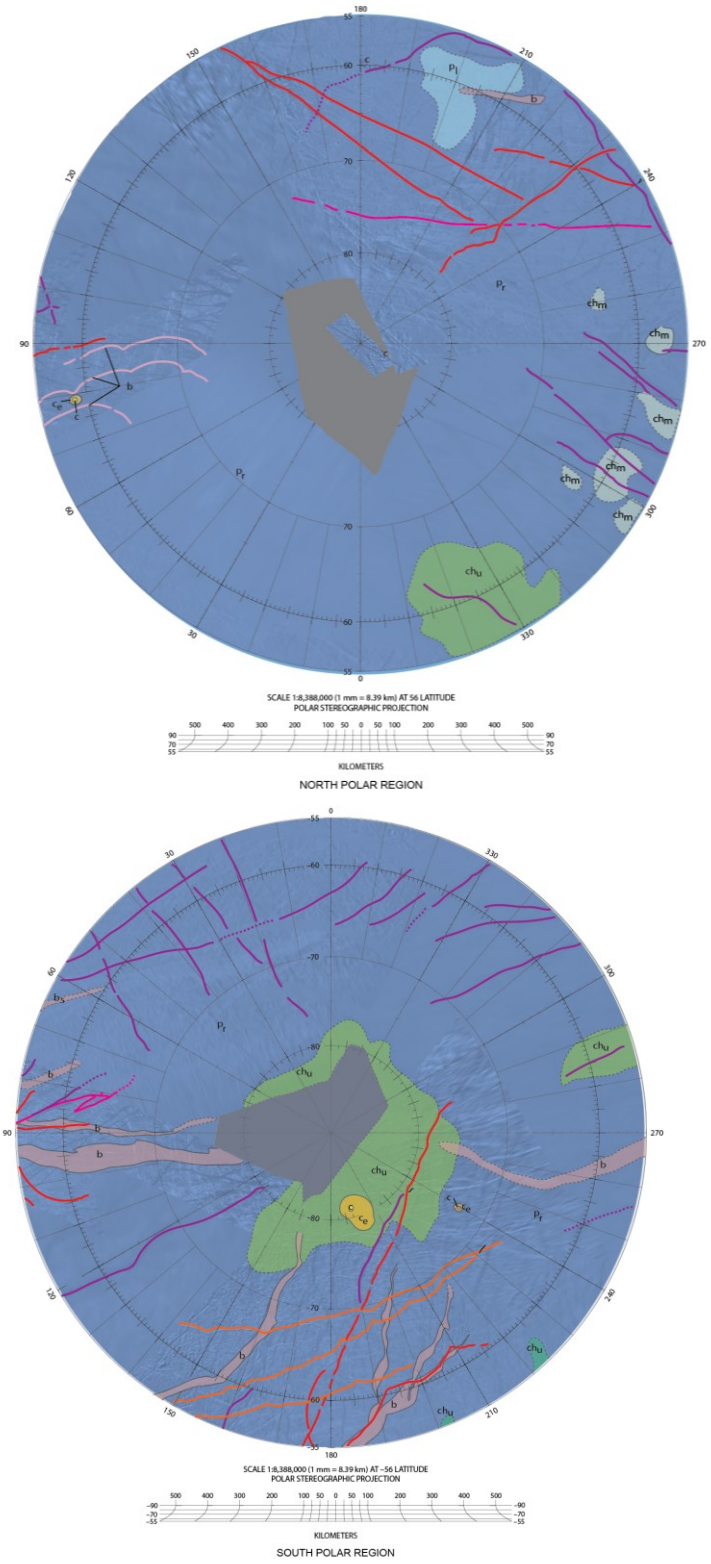

Figure 2-6. Geologic map of the North (top) and South (bottom) poles of Europa at 1:15M scale.

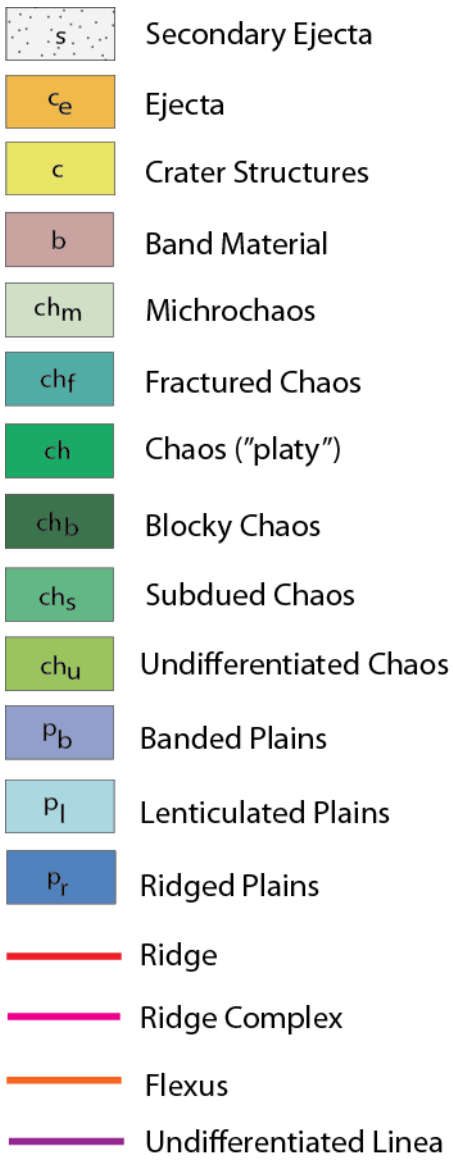

Figure 2-7. Legend for geologic units and structures. The full version of the map, legend, and unit descriptions can be viewed in the USGS series map publication.

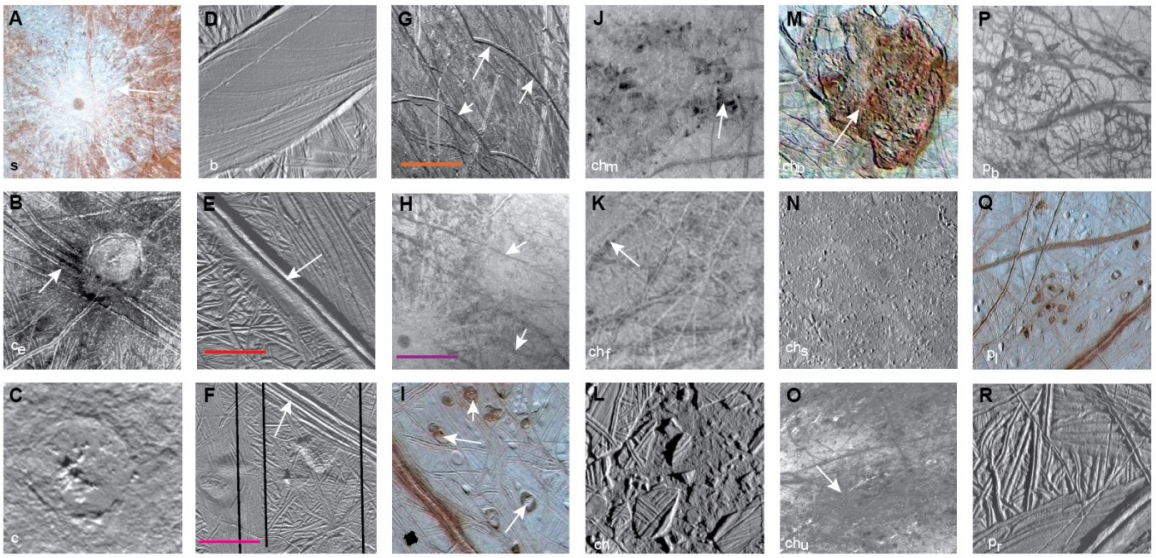

Figure 2-8. Material unit and structure type examples. A) secondary crater materials, s; B) crater ejecta, c_e; C) crater material, c; D) band material, b; E) ridge material, [red line]; F) ridged band material, [pink line]; G) flexus [orange line]; H) undifferentiated linea, [purple line]; I) lenticulae, [dot]; J) microchaos, ch_m; K) fractured chaos, ch_f; L) general chaos material, ch; M) blocky chaos, ch_b; N) subdued chaos, ch_s; O) undifferentiated chaos, ch_u; P) banded plains, p_b; Q) lenticulated plains, p_l; and R) ridged plains, p_r. [Base images: NASA/JPL]

pole is also typified by ridged plains, though this area lacks the younger distinctive linea. The ridged plains serve as the background for the linea-dense regiones and are extensive beyond the defined regiones. The overall topography of the ridged plains is relatively flat with only slight variations in elevation from one ridge structure to the next. Local areas of the ridged plains exhibit brighter than average terrain and more limited topography (Greeley et al., 2000). Differences in albedo, surface texture, and, to some extent, topographic relief cause contacts between the ridged plains and other material units. Stereographic studies reveal topographic relief to be no more than ~2 km (Schenk, 2004, 2006).

The ridged plains material is the oldest mappable terrain visible on the surface of Europa (Chapman et al., 1998; Greeley et al., 1998b, 2000, 2004; Senske et al., 1998; Head et al., 1999b). It has been referred to as *undifferentiated plains material* (Greeley et al., 2000) due to prolific overprinting by younger and younger ridges to distinguish the ridges within the background plains material from the youngest ridges that are so apparent and which are discussed as a separate material unit. Within the matrix of ridged plains material, several distinct morphological characteristics have been identified (Patel et al., 1999); these include: “parallel-linear”, “sinuous”, “convex”, “hummocky”, “lineated”, “en echelon”, and “mélange”. These adjective terms describe the individual features recognizable within the ridged plains; however, at the scale of the global geologic map, these features are not distinguishable one from the other and as such, the material is mapped as a single unit.

Some localities are disrupted by pits and domes or appear to be smoothed with embaying darker albedo material; local areas within ridged regions where linear features

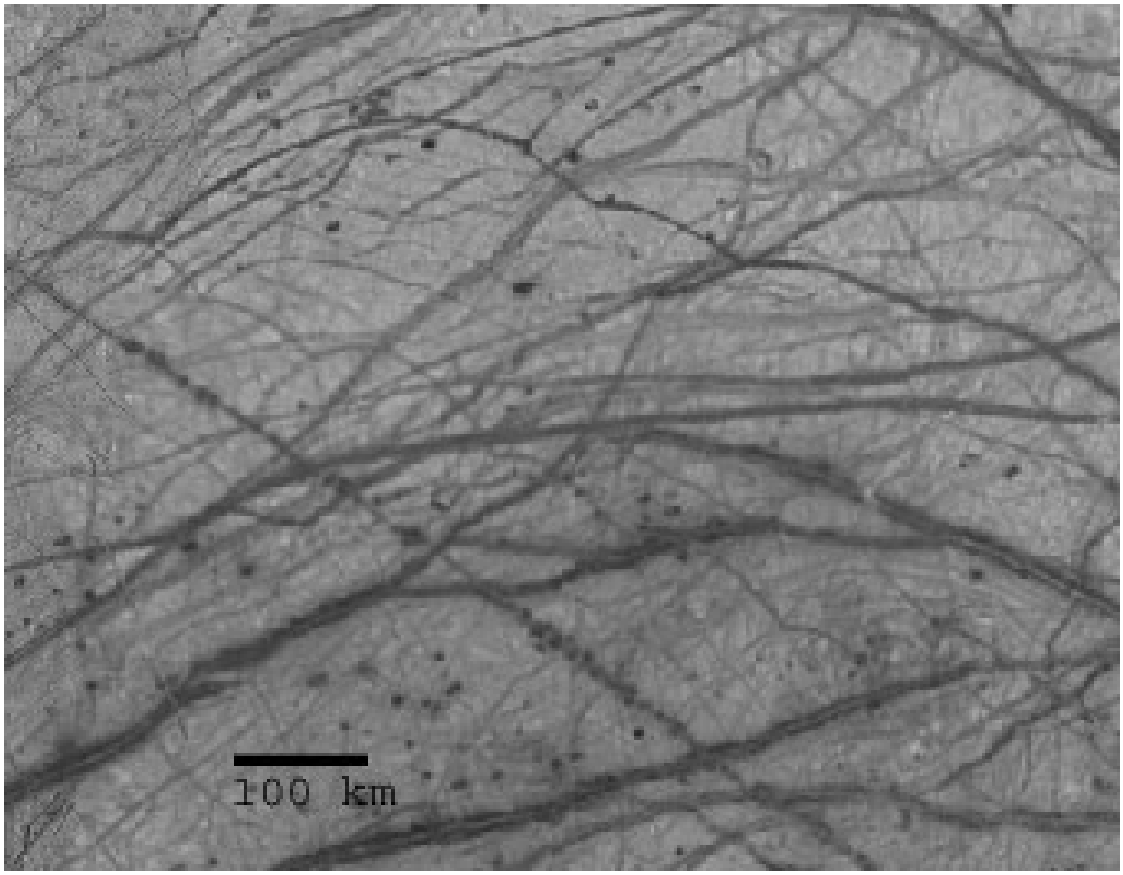

Figure 2-9: The *ridged plains* of Falga Regio in the northern hemisphere shown at 1.57 km/pixel. The prominent dark lineaments here are individual ridges, discussed as a separate unit type. These ridges demonstrate the prevalence of ridge formation within the ridged plains; however, the ridged plains unit is best represented by the bright background surface material. Note that at this regional scale, the texture of the ridged plains is not evident. [NASA/JPL]

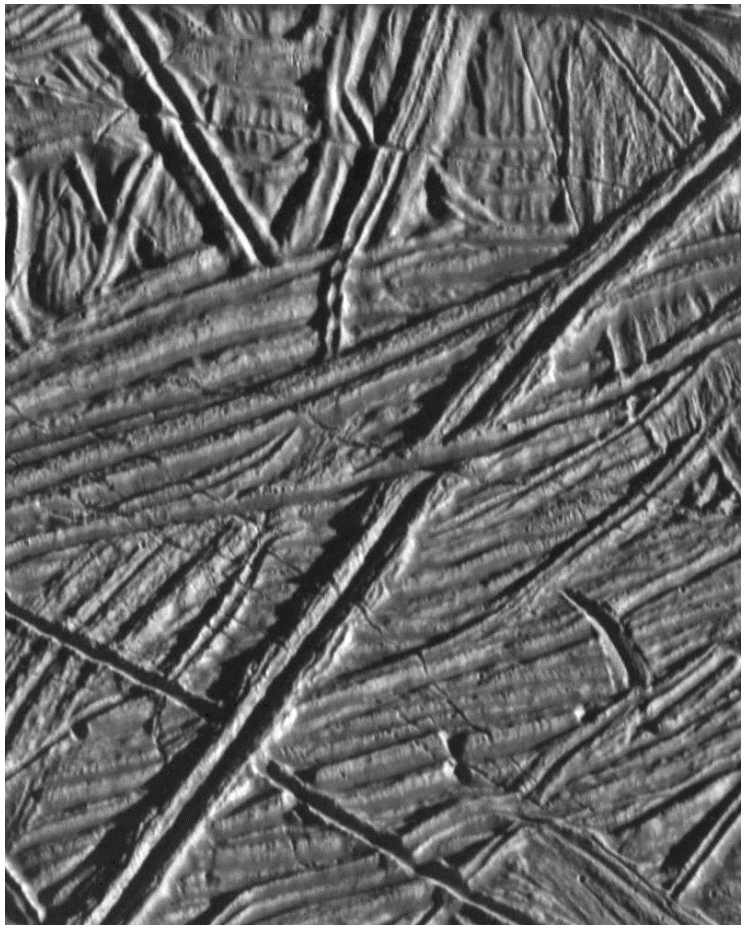

Figure 2-10: The *ridged plains* shown at high resolution, illustrating the texture of multiple overprintings of ridges. Image is 12 x 15 km. [NASA/JPL]

are not recognizable that exhibit these terrain characteristics (cf. *subdued pitted plains* and *subdued plains* of Figueredo and Greeley, 2004) are not separated from the *ridged* unit as they are too small to be visible at map scale. The most prominent examples are located in the leading hemisphere near Murias Chaos. These locales share characteristics with knobby or hummocky chaos units which have relaxed or been embayed. No remnants of the ridged plains are visible in these areas; thus, these are termed subdued chaos.

The truly *smooth* plains unit identified by Greeley et al. (2000) is not mapped as a separate unit as it encompasses only small areas (<5 km) which are not visible at map scale (Figure 2-11). Greeley et al. (2000) also define a global *undifferentiated* plains material that consists of both *ridged* and *smooth* plains material as well as other materials not visible at map scale. The designation of *undifferentiated* results from the inability to distinguish small ridges and ridge sets at lower resolutions. However, recent mapping (Doggett et al., 2009) does not map the *ridged* and *undifferentiated* units separately. The realization that the *ridged* material appears drastically different under different viewing geometries (i.e., the *fractured* plains described by Lucchitta and Soderblom, 1982) and at different resolutions along with the acknowledgement that such areas are crosscut by dark and bright curvilinear zones (Smith et al., 1979a,b; Lucchitta and Soderblom, 1982; Greeley et al., 1998) and continuous lineaments hundreds of kilometers long (Smith et al., 1979a,b; Belton et al., 1996; Geissler et al., 1998a) establish that these areas are likely to be similar in appearance to Falga Regio and Balgatan Regio. Close examination of textural and albedo differences between these regiones at resolution boundaries dictates that the *ridged* plains designation be extended into the lower resolution coverage areas.

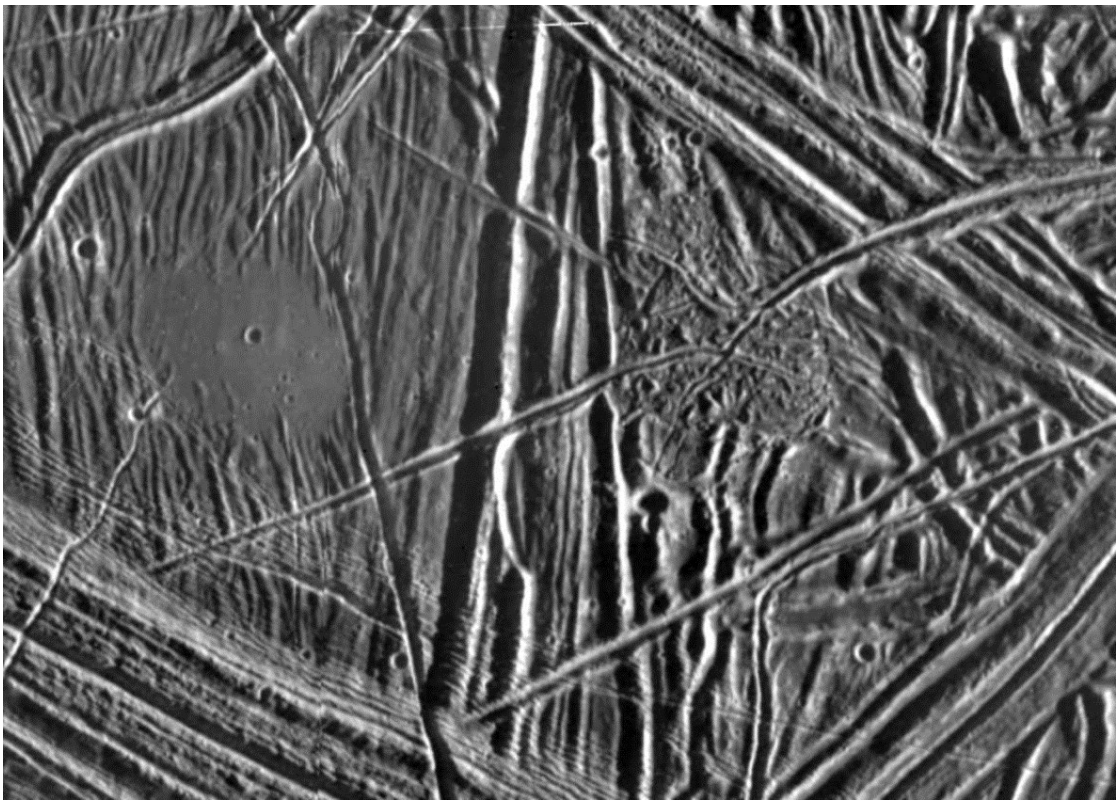

Figure 2-11. The “smooth” plains texture is exemplified in the circular area to the left where no ridge structure is evident. Superposition indicates that this smooth texture resulting from a fluid material flooding the surface and embaying pre-existing ridge structures. The smooth area is 3.2 km across. [NASA/JPL]

Thereafter, there is little to no discernible evidence of gradational changes that necessitate an undifferentiated unit distinction. This presumes that changes in viewing geometries prevent the low topography features from being distinguished. For the purposes of a global view of material units, all background materials are presumed to have similar morphology to the *ridged plains*, following the precedent of Doggett et al. (2009).

Interpretation: The multiple orientations of individual ridge segments within the *ridged plains* considered with the density of ridges and the abundance of intersecting and cross-cutting relationships suggests that the *ridged plains* formed as a result of multiple episodes of ridge building with repeated overprinting (Geissler et al., 1998b, Patel et al., 1999; Sullivan et al., 199b; Figueredo and Greeley, 2004). Alternatively, a single continuous process of ridge building (Greenberg et al., 1998) could be responsible provided that diurnal stresses and nonsynchronous rotation play a part in establishing orientation. The overall formation process is indicative of tectonic resurfacing (Head et al., 1997) in that the original properties of the material and its surface are so extensively modified that the material no longer resembles its original condition (Wilhelms, 1990).

The *ridged plains* are interpreted from cross-cutting relationships to be the oldest materials on Europa (Greeley et al., 1998; Head et al., 1998a; Senske et al., 1998). A presumption that the large young *ridges* form in a similar manner to the *ridged plains* leads to the interpretation that the processes of ridge building and tectonic resurfacing could be contemporaneous throughout Europa's recent geologic history. The formation of other units could have been coincident with these processes (Greenberg et al., 1998). Alternatively, the majority of ridge building and tectonic resurfacing could have been

largely restricted to the earliest of Europa's visible history, transitioning over time to styles of resurfacing that did not generate additional overprinting of the ridged matrix (Head et al., 1999b; Pappalardo et al., 1999; Kadel et al., 2000; Spaun et al., 1999a). The latter is supported by the morphological differences between individual ridges or linear features and the small-dimension ridges in the plains. The characteristics of and processes that form the individual ridges that make up the *ridged plains* unit are discussed below.

Lenticulated Plains

Characterization: It has been noted that varying degrees of ridge density and other textural or albedo differences are evident throughout the ridged plains units (Doggett et al., 2009). Among these graded differences is the density of lenticulae. Single lenticulae are discussed as a separate material unit marked by structural symbols. Evidence of multiple merged lenticulae or those whose darker material appears to embay the surrounding terrain is also discussed as a unit of *microchaos* (Spaun et al., 1999a,b; Doggett et al., 2009; Prockter et al., 1999). The appearance of dense clusters of lenticulae, where each lenticula is distinguished as a separate structure, within the ridged plains units mark a distinction from the ubiquity of ridged plains that must also be noted. Ridged plains material is easily discernible but is disrupted, superposed, and embayed by pits, domes, or low albedo material. All types of lenticulae, i.e., pits, domes, and spots, seem to be represented and distributed fairly evenly. In some cases, individual ridges or narrow bands appear to superpose the lenticulae. Elongated areas of lenticulated plains are common bounding young lineaments or bands. Throughout the ridged plains, particularly in the equatorial region and higher latitudes of the trailing hemisphere, the concentration of lenticulae gives the plains a "speckled" appearance (Figure 2-12). The

density of lenticulae gives the surface a darker than average albedo as compared to ridged plains. Lenticulated plains are most commonly found at the contact boundaries of chaos material and appear to represent a gradation from chaos to ridged plains materials. Doggett et al. (2009) attempted to describe this gradation as *lenticulated terrain*, an intermediate unit between chaos and ridged plains, though their map did not indicate locales consistent with this designation. In low-resolution coverage areas, the dark albedo of the "spots" is the most evident indicator of lenticulation; pits and domes that do not differ in albedo from the background plains are indistinguishable. These areas are also marked as *lenticulated plains* even though the structures are not resolved.

Interpretation: From high resolution, low phase angle observations, it is apparent that these concentrations of lenticulae have not formed throughout the ridged plains; therefore, they are assumed to be recent evidence of activity. The morphological similarities between lenticulae and larger chaos areas suggest related formational processes, thus lenticulated plains should be considered a morphological evolution from ridged plains to microchaos and other chaos unit types; as processes that produce new lenticulae progress, individual lenticulae merge to form microchaos and/or low albedo melt material upwells to generate the mottled appearance of other chaos types. Proposed models for lenticulae formation include diapirism, possibly in conjunction with partial melting of a salt-rich icy lithosphere (Pappalardo et al., 1998; Rathbun et al., 1998), ice-shell melt-through (Carr et al., 1998; Greenberg et al., 1999; O'Brien et al., 2002; Greenberg et al., 2003), and ice volcanism (Fagents et al., 1998).

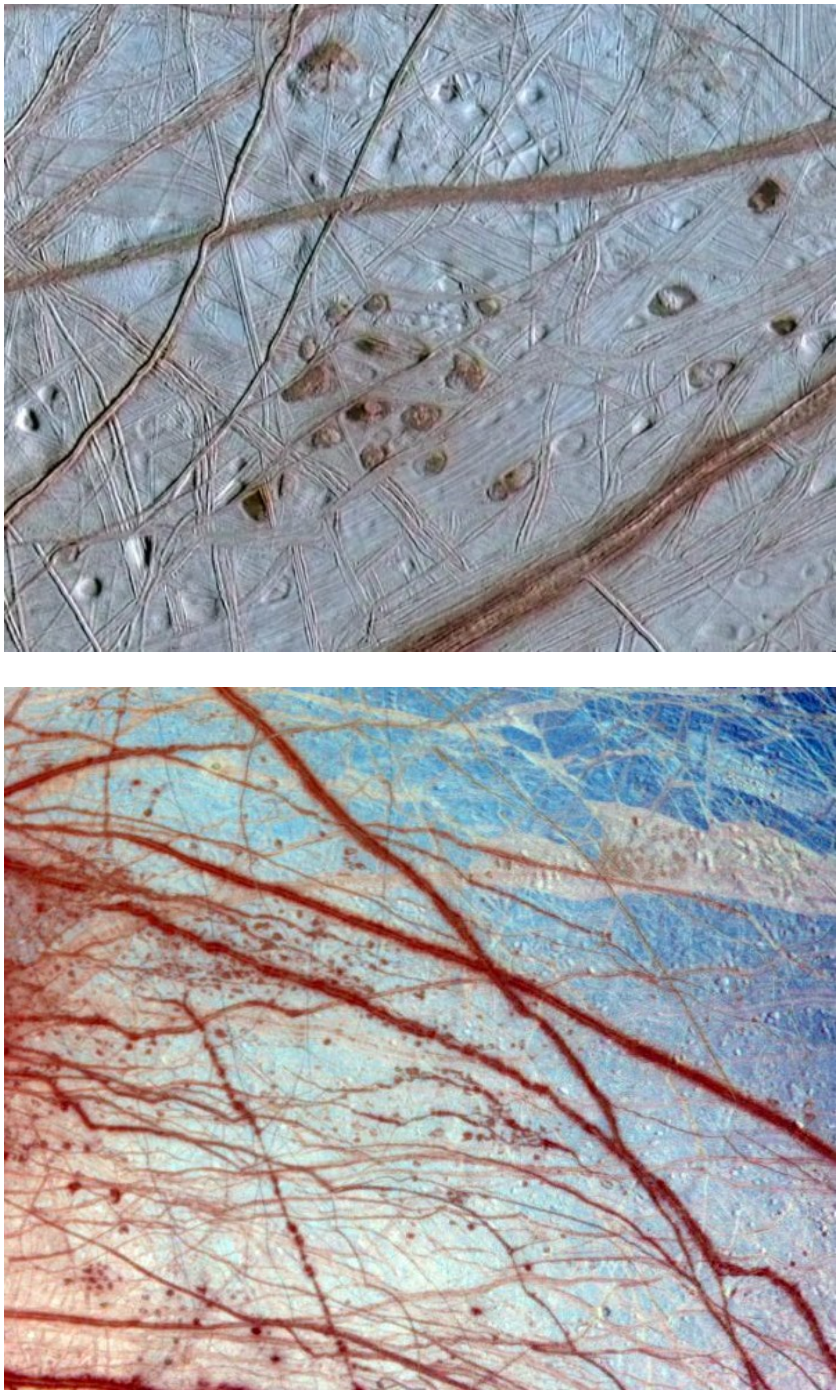

Figure 2-12. *Lenticulated plains* are represented by the high density of individual lenticulae structures. Top: Single structures are identifiable but are closely spaced. Bottom: At lower resolution, the overwhelming density of lenticulae (red spots) becomes apparent as an identifying characteristic of the plains. [NASA/JPL]

Banded Plains

Characterization: Argadnel Regio, southwest of the anti-jovian point, is noted for its short and wide dark smooth bands (Figure 2-13). Typically termed the "wedges" region, this equatorial area exhibits the common ridged plains as a background surface and is superposed by the dark bands. The ridged plains here seem to be typical of other ridged plains, though perhaps a bit more disrupted. The presence of the bands, which are themselves a variation on typical bands, indicates some geologic process at work in this area that is not present elsewhere. This area is therefore termed the *banded plains*. Young ridges cross-cutting this region are also slightly different that other ridges elsewhere. Both the wedges and ridges are more arcuate. In the northern portion of Argadnel Regio, short, curved bands are common. The southern region is dominated by an increasingly disrupted set of fractures, all of which appear to be short and narrow compared to the background ridged plains structures. The change from curved bands to short fractures is gradational. The banded portion of the region to the east is also populated by lenticulae, particularly dark spots, and small areas of microchaos. This area is distinguished as lenticulated plains due to the dense population of lenticulae, though the presence of bands indicates that both features were forming at the same time. Central and southern areas are disrupted by chaos and overprinted by ridges and flexūs.

Interpretation: Pull-apart bands are inferred to be brittle ice dilation zones that open along fractures and separate the crust into plates; the zones are infilled with darker material derived from the interior and may translate over the lower-viscosity subsurface (Schenk and McKinnon, 1989; Belton et al., 1996; Sullivan et al., 1998; Greeley et al., 1998b; Prockter et al., 1999; Tufts et al., 2000; Doggett et al., 2009). With time, dark

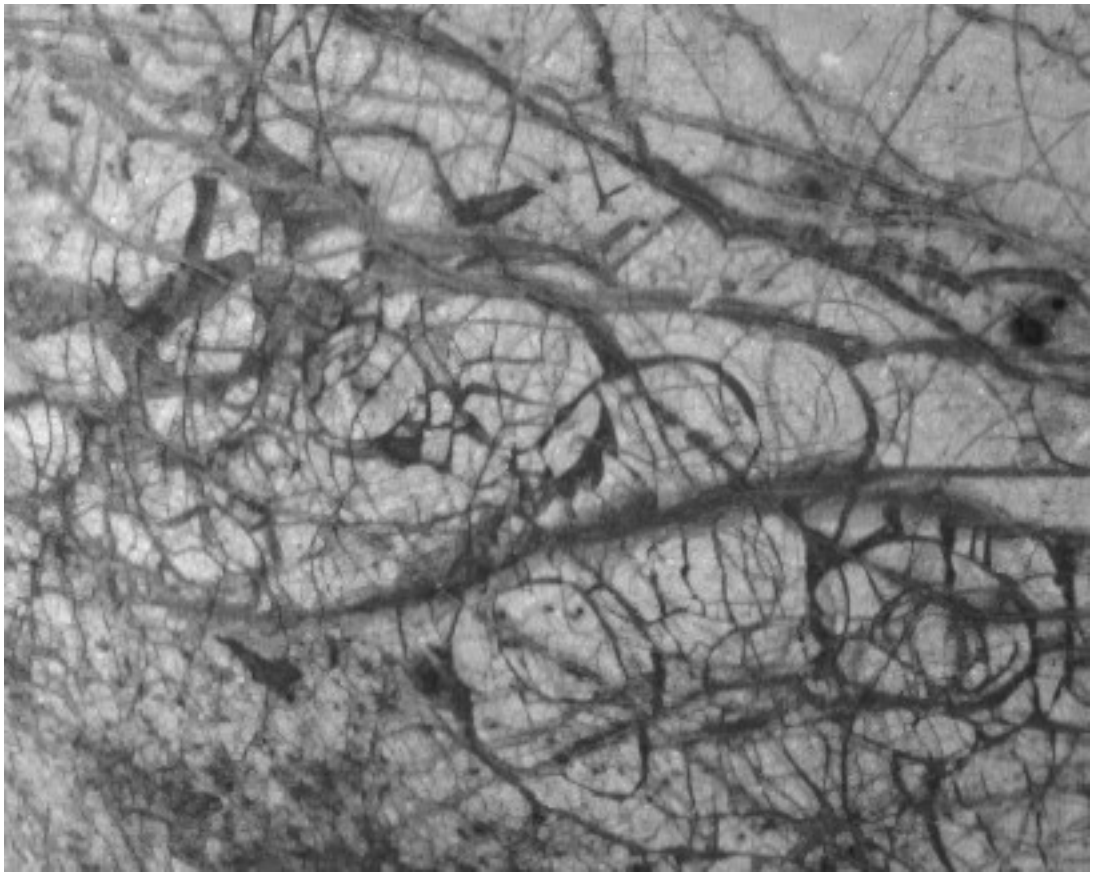

Figure 2-13. *Banded plains* of Argadnel Regio, at 0.23 km/px. Note the highly arcuate short dark bands. The boundaries of this unit are approximate and defined by the termination of this curvature, regardless of the background material. [NASA/JPL]

materials brighten (Pappalardo and Sulllivan, 1996; Greeley et al., 1998a,b; Geissler et al., 1998). Banded plains are interpreted to be the result of intense tectonic disruption, probably by tidal stress forces, of the older plains unit (Doggett et al., 2009). The occurrence of this disruption at the anti-Jovian point is potentially driven by convection in a region of locally high heat flow (Prockter et al., 2002).

2.5.2. Chaos Materials

Disrupted or "chaotic" terrain is expressed in a variety of textures on Europa. Distinctions based on texture, general age, and with respect to inconsistent resolution and illumination constrain the global understanding of chaos but do allow the identification of several varieties of chaos texture and gradational relationships. Other classifications have been discussed (see reviews by Collins and Nimmo, 2009; Doggett et al., 2009); this map attempts to combine the heritage of these classifications with an allowance for interpretation where high resolution images of consistent lightning conditions are available.

Features generally associated with chaos materials include low albedo in global or regional resolution and sharp embaying contacts with brighter, smoother plains units. At low resolution, regions of chaos can also have transitional areas of dark albedo spots in a high albedo matrix but this could also be equivalent to what has been mapped as lenticulated plains in high resolution. At higher resolution, the chaos is seen to be hummocky plains with plates of younger plains units in a matrix of dark, knobby material. Variations in elevation, degree of disruption, and density of lenticulae have led to discussion on the level of disruption that establishes the differences between chaos, lenticulae, and plains (Figueredo et al., unpublished).

Several separated occurrences globally, with different appearances related to differences in photometry and resolution within the base mosaic. Chaos is younger than all surrounding material units, with some cross-cutting lineaments. A sub-type is blocky (elevated or knobby) chaos that is younger than other chaos units (Figueredo and Greeley, 2000, 2004). They are interpreted to be where pre-existing plains units have been disrupted by endogenic process that fractures the ice into plates and rafts them in a matrix of material brought to the surface from the interior, overturned plates, or both.

Lenticulae

Characterization: The feature class of lenticulae includes small isolated depressions ("pits"), domes, and low albedo "spots", each approximately 10 km in diameter (Pappalardo et al., 1998a). Some retain vestiges of pre-existing terrain (Figure 2-14). This may include positive relief with discernible scarps, ridge, or chaos textures on exposed high relief surfaces or within low-lying pits. Lenticulae typically occur as widely spaced individual structures, though some exist in dense clusters within plains regions. Where individual structures are identifiable, they are marked by a structural symbol (dot). Approximately 5,000 of these are marked in the geologic map; they are not marked on the print version of the map but are included in a digital layer in the GIS file. There is no symbol difference to indicate their type; however, the GIS data table feature indicates the class (i.e., pit, dome, spot, or undifferentiated). Where dense clusters of lenticulae occur within a confined area, they are mapped as *lenticulated plains*; these clusters are only visible within plains regions. In some cases, the plains texture appears to superpose or embay the lenticulae structures; the reverse is also true. Where multiple lenticulae appear to have merged together with two or more individual structures superposed, embaying, or

disrupting each other, they are mapped as *microchaos* following the description of Spaun et al. (1999a,b).

Interpretation: Proposed models for lenticulae formation include diapirism, possibly in conjunction with partial melting of a salt-rich icy lithosphere (Pappalardo et al., 1998; Rathbun et al., 1998; Head and Pappalardo, 1999), ice-shell melt-through (Carr et al., 1998; Greenberg et al., 1999; O'Brien et al., 2002; Greenberg et al., 2003), and ice volcanism (Fagents et al., 1998). All types of lenticulae are considered as a group here, following the genetic relationship proposed by Pappalardo et al. (1998a; see also Carr et al., 1998; Greeley et al., 1998b; Spaun et al., 1998a). As the disrupted texture and low albedo are common to other types of chaos, the lenticulae are interpreted to be a form of chaos (Spaun et al., 1999a,b; Riley et al., 2000) or a morphological gradation from lenticulae to increasingly more chaotic materials (i.e., Greenberg et al., 1999). The low albedo material is presumed to upwell and flood small areas of the surface, eventually spreading to larger areas and resulting in the dark material that signifies more mottled or chaotic terrains.

Microchaos

Characterization: Microchaos units are typified by patches of low albedo material where multiple lenticulae structures appear to be merged (Figure 2-15) such that each individual structure is not differentiated (Prockter et al., 1999a). As with lenticulated plains, microchaos regions occur only within the ridged plains units. They commonly occur adjacent to young lineaments, suggesting a genetic relationship between the formation of lenticulae and lineaments.

Figure 2-14. Lenticulae, including pits, spots, and domes. Many individual structures are evident, as are a variety of morphologies (arrows). Note that some lenticulae exhibit preserved ridge structures or appear to be a combination of morphologies, as in the feature to the far right. [NASA/JPL]

Interpretation: Though the low albedo is typical of chaos materials, microchaos regions do not share all of the features associated with chaos; thus, they are identified as a transitional unit where lenticulae or lenticulated plains becomes more disrupted toward developing into chaotic terrain (cf. Spaun et al., 1999a; Riley et al., 2000; Sotin et al., 2002).

Fractured Chaos

Characterization: Low albedo regions where narrow ridges and fractures are prominent but the low albedo material masks the overall appearance of background plains are termed fractured chaos; the narrow fractures that are visible superpose any pre-existing ridged plains and the low albedo material. Lineaments are high albedo and viewing geometries tend to make east-went trending lineaments most visible (Figure 2-16). The low albedo material appears to embay adjacent plains units but the lineaments often continue across unit boundaries. Low albedo material surrounding and embaying the lineaments is consistent with lenticulae, though no individual structures are evident. No elevated material or block structures are evident. The fractured chaos unit includes a disproportionate number of impact craters, including Cilix, when compared to other chaos or plains units. In these cases, the craters are most evident due to the contrast between bright ejecta and dark plains. The three occurrences of fractured plains are grouped at or near the sub- and anti-jovian points.

Interpretation: Fractured plains are interpreted as the modification of pre-existing plains by some form of endogenic activity which floods inter-ridge topographic lows with dark, viscous material that erupted from lenticulae within the unit, perhaps in a partial melting mode, and is thus somewhat of an intermediate between ridged plains and typical

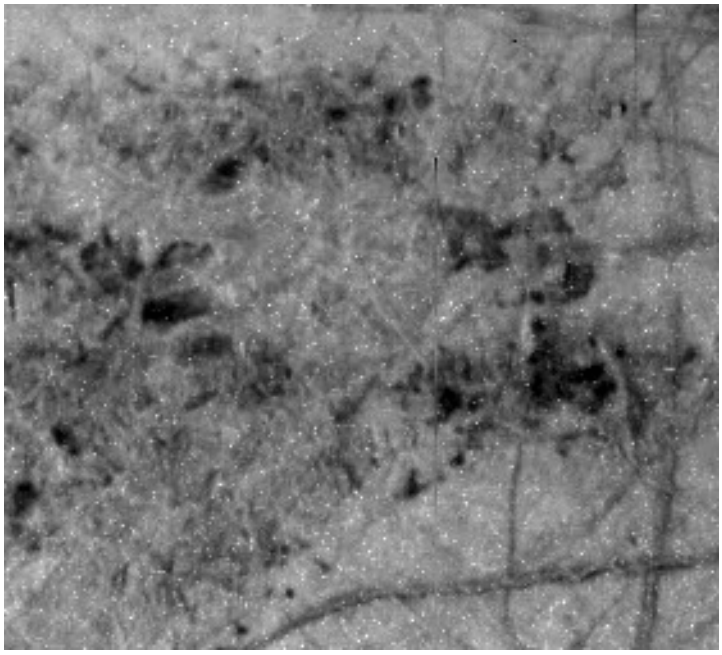

Figure 2-15. Microchaos at medium resolution. Note the large dark patches that appear similar to lenticulae where individual structures are not evident. [NASA/JPL]

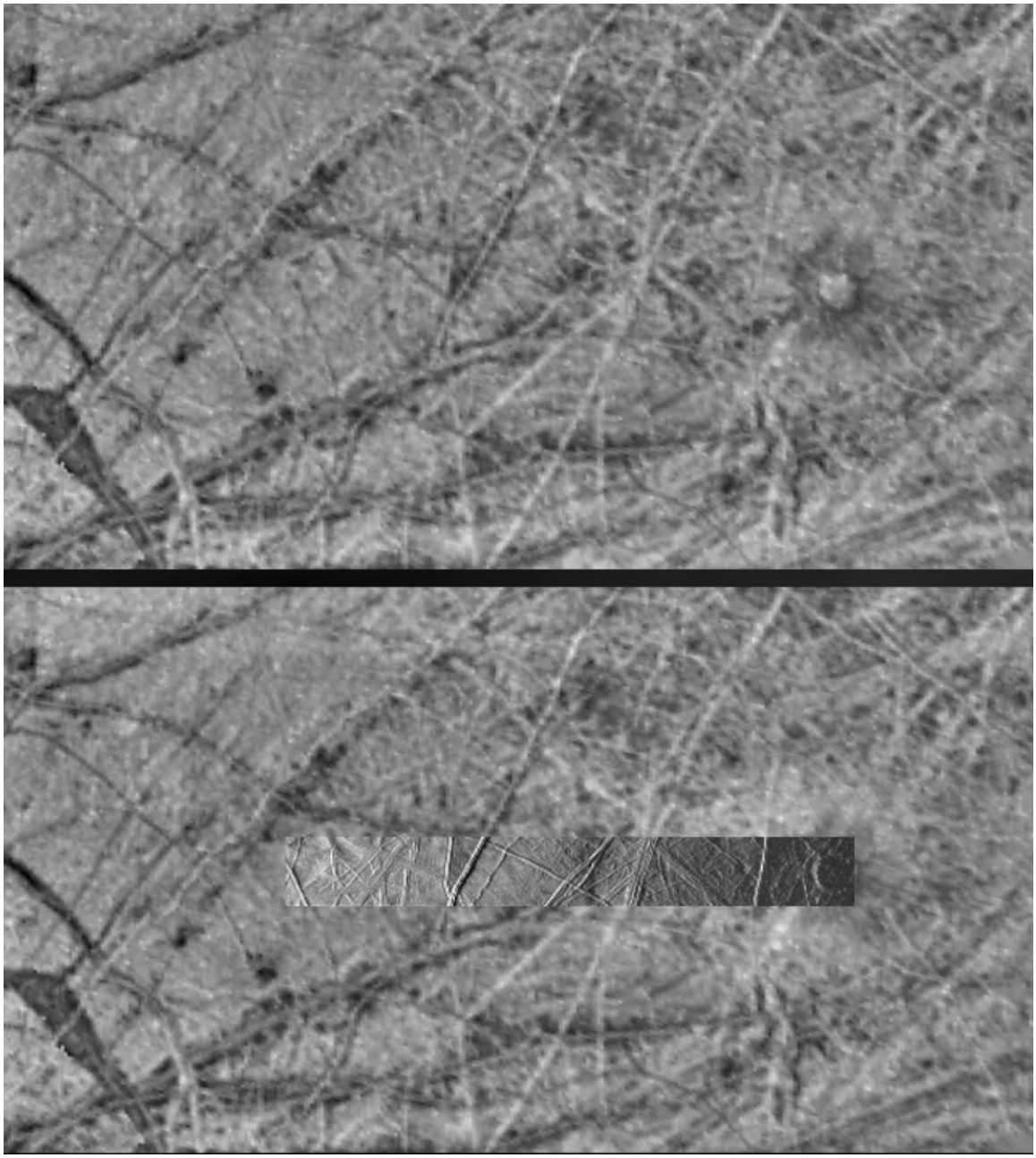

Figure 2-16. Fractured chaos under different lighting conditions. Top: High-Sun images, where illumination is from overhead, emphasize albedo differences. Bottom: Low-Sun images, where illumination is from the side, emphasize topography. Note the high-resolution inset in the bottom image shows evidence of relief. The crater on the right is Cilix, 25 km in diameter. [NASA/JPL/ASU]

chaos. The geographic association with the sub-Jovian and anti-Jovian points is intriguing, suggesting the possibility of the global stress field controlling the occurrence of this unit, or the particle field environment having an effect on the coloring of the unit, but it could also be coincidental. The occurrence of this unit centered on the 180° longitude line is equivalent to the gray mottled terrain unit in the Voyager map (Lucchitta and Soderblom, 1982).

Chaos

Characterization: Low resolution images exhibit a low-albedo mottled appearance which has become associated with chaotic materials (Figure 1-2, brown areas in Figure 2-3; Lucchitta and Soderblom, 1982). As in the type example of Conamara Chaos (Figure 2-17), high resolution images reveal isolated blocks, plates, and massifs where ridged material is preserved (i.e., the *platy chaos* defined by Greeley et al., 2000). Blocks, plates, and ridged massifs are juxtaposed with each other such that each material cannot be separated into individual units at the scale of the map. Plates can be visualized in their original positions by rotation or translation within the matrix material (Figure 2-18). Plates with preserved ridge structures are often elevated relative to the surrounding blocky material or plains (Williams and Greeley, 1998; Schenk and Pappalardo, 2002). On this map, general chaos material refers to areas that exhibit some evidence of this "platy" texture; as such, it is mainly confined to regions that were imaged at high resolution. By degrading the resolution of these images, the "speckled" appearance noted by Prockter et al. (1999) becomes apparent. It is strongly suspected that other areas of chaos that exhibit this "speckled" chaos are similar in nature; however, this map represents those areas imaged at lower resolutions or less favorable illuminations as

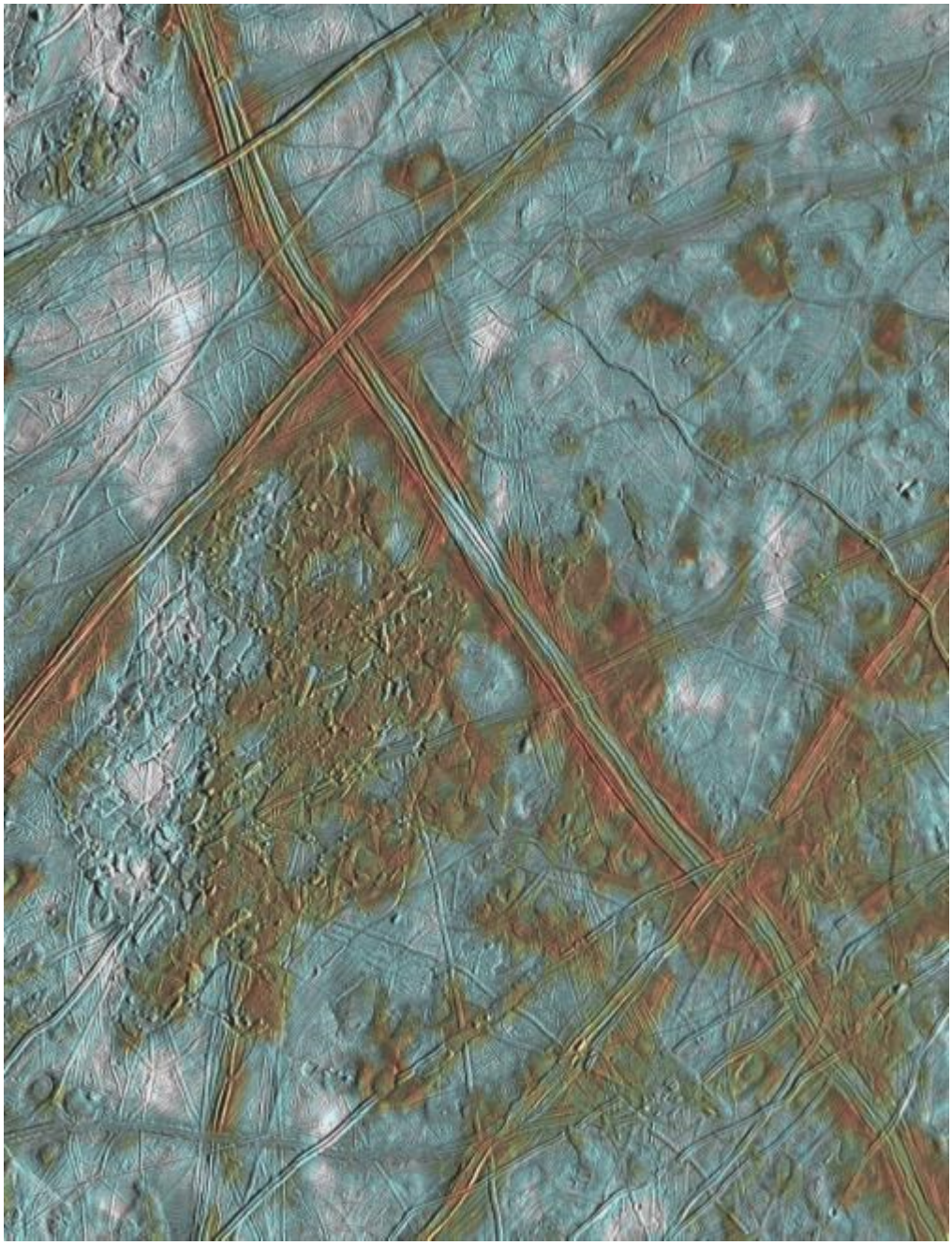

Figure 2-17. Conamara Chaos at medium resolution. Conamara is located directly south of the "X" formed by the intersection of Agave Linea and Asterius Linea. The margin between the chaos region and the surrounding lenticulated plains is sharp. [NASA/JPL]

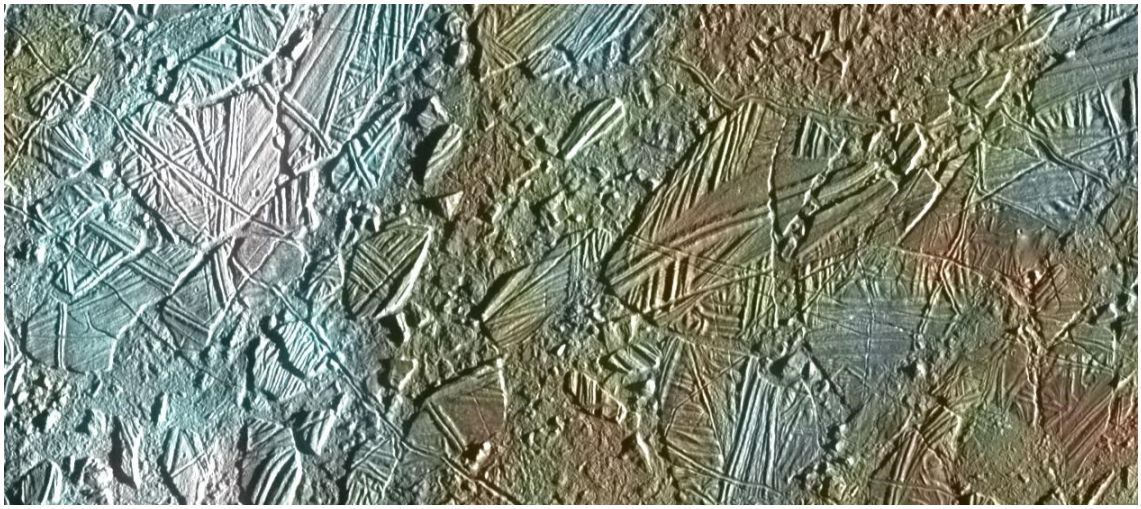

Figure 2-18. Conamara Chaos at 54m/px. Individual plates with preserved ridge material can be rotated and translated as in a jigsaw puzzle to fit into their original configuration. The blocky matrix exhibits small tilted blocks. Reddish-brown areas represent non-ice material resulting from geologic activity. White areas are rays of material ejected from the nearby Pwyll impact crater. Blue tones distinguish between coarse- (dark blue) and fine-grained (light blue) ice. [NASA/ASU/U. of Arizona]

undifferentiated chaos, as no definitive evidence of the platy structure is discernible. This general platy chaos is expected to degrade into a more mottled texture which would also have the speckled appearance at lower resolutions. However, any materials in a lower resolution coverage area which are immediately adjacent to the platy material where image boundaries allow tracing of albedo signatures across the boundary are also included in this designation (i.e., Figure 2-19). Each exposure is constrained to a small area with the exception of the equatorial area in the leading hemisphere that was imaged at high resolution; changing viewing geometries across that swath illustrate a gradation from a platy texture with dense fracturing in the east to a slightly smoother surface with fewer and more widely spaced plates in the west. Further west beyond the high resolution swatch, albedo features can be traced along the image boundary and the immediately adjacent material exhibits the speckled appearance with evident fractures. The unit boundary is defined where the number of plates becomes lower than the number of identifiable lenticulae.

Interpretation: Chaos regions are interpreted as areas of focused heat flow perhaps with local melting (Collins et al., 2000, Collins and Nimmo, 2009). In a melting model, blocks are analogous to buoyant icebergs (e.g., Greenberg et al., 1999). Solid-state ice rising diapirically to the surface is possible in situations of partial melting (Collins et al., 2000). These thermal gradients disrupt the cold, rigid lithosphere, causing fragmented slabs of colder material to rotate and translate within the framework of the original ridged plains matrix material (Pappalardo et al., 1998; Spaun et al., 1998). Other interpretations for chaos formation include: brine mobilization (Head and Pappalardo, 1999; Collins et al., 2000; Pappalardo and Barr, 2004; Kargel et al., 2007), sill-injection (Crawford and

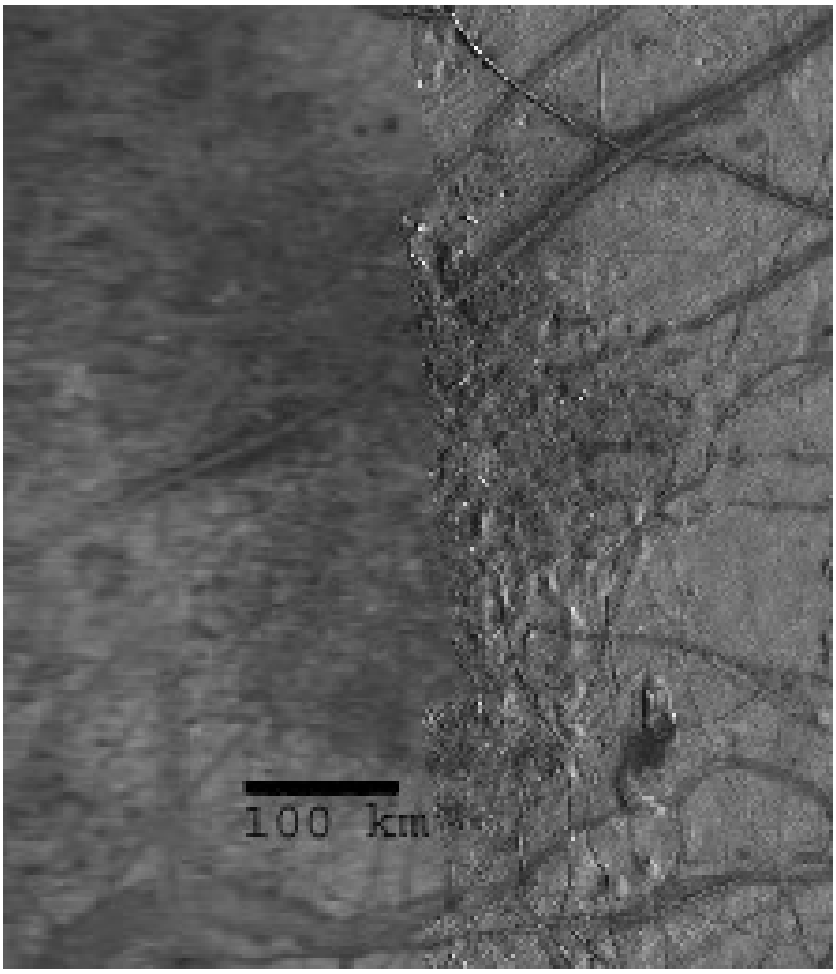

Figure 2-19. Example of apparent textural difference in a chaos unit across a resolution boundary. This segment, extracted from the global photomosaic, shows chaos material on the right, which is bounded to the east by lenticulated plains. Albedo features can be traced to the west across the resolution boundary. The crater Manannán is to the far west of the image. Higher resolution coverage substantiates the designation of chaos for this region. [NASA/JPL, USGS]

Stevenson, 1998, Collins et al., 2000; Manga and Wang, 2007), and impact modification (Billings and Kattenhorn, 2003; Cox et al., 2005). One or more of these processes may be in action to form the general chaotic texture.

Blocky Chaos

Characterization: Small areas of mottled appearance, often with low albedo exhibit (at high resolution) multiple titled blocks which has been termed "knobby", "blocky", or "hummocky". Boundaries are often embaying the surrounding terrain with low albedo material. In some cases, ridged plains textures extend partially into the blocky terrain and then are embayed by the dark albedo material. Thera Macula and Murias Chaos (Figure 2-20; Figueredo et al., 2002) are typical examples of blocky chaos. In some cases, blocky material is elevated and bounded by scarps.

Interpretation: Blocky chaos regions are interpreted to be further disruption of the general platy chaos regions which have been disrupted to the point that no evidence of the ridged matrix remains, except at boundaries where noted.

Subdued Chaos

Characterization: Regions that exhibit some blocky texture but are dominated by smoother surfaces are defined as a separate unit as they are no longer dominated by a single texture (Figure 2-21). Ridges are not preserved in these small areas. Blocks appear to be less tilted and elevated than in blocky chaos.

Interpretation: The subdued classification is intended to indicate a relaxation of blocky or general chaos. These areas may have been embayed by medium-to-low albedo materials such that blocks, plates, or ridges are no longer evident. Thrace Macula is classified as subdued; though it is strikingly similar to Thera Macula, the two regions

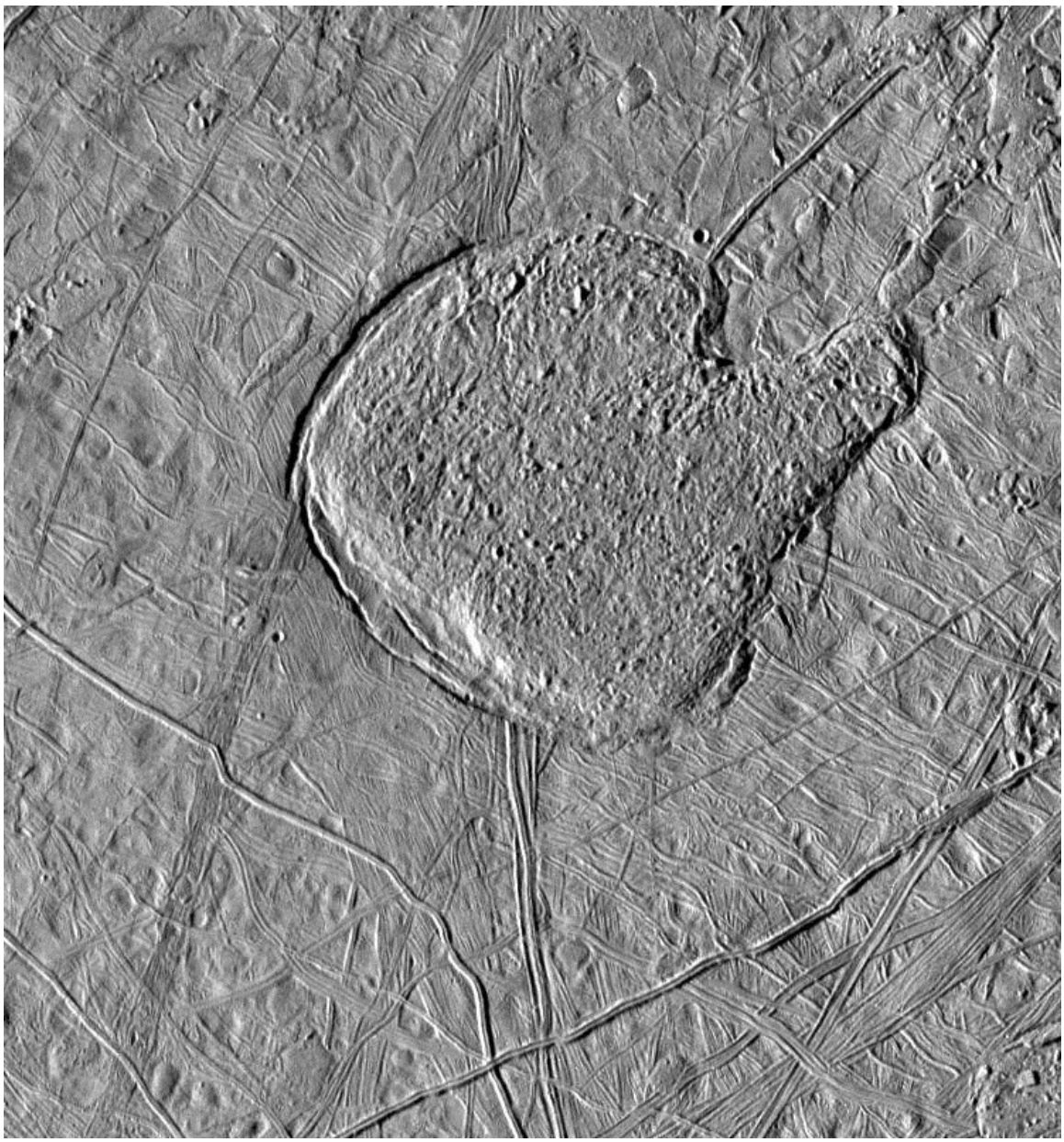

Figure 2-20. Murais Choas, the “mitten” feature, is comprised of blocky chaos similar to the matric material withing “platy” chaos regions. The entire feature is elevated and the surrounding area, especially the southwest margin, has been bent downward and cracked. Resolution is 235 m/px. [NASA/JPL/U. of Arizona]

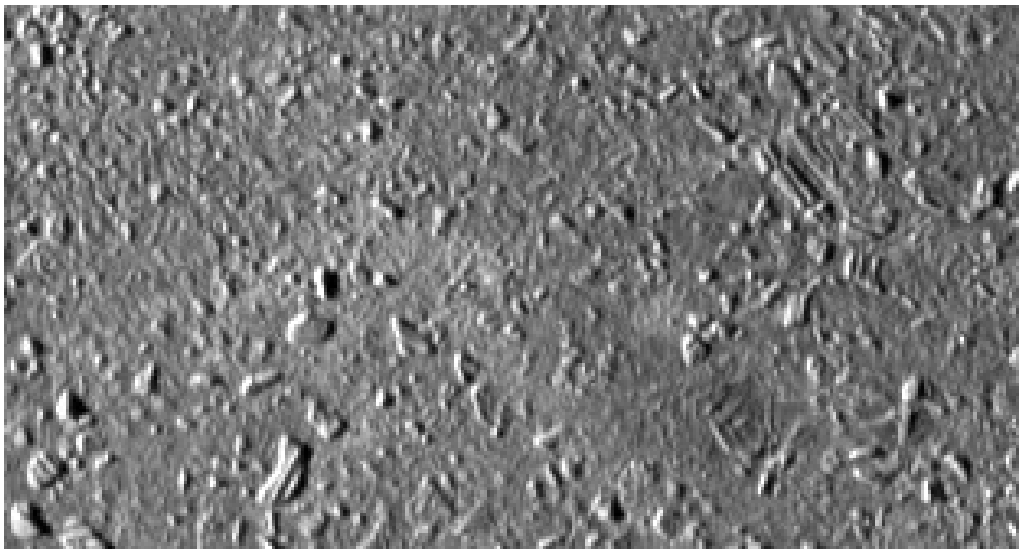

Figure 2-21. Subdued chaos material, where blocky or "knobby" texture is apparent but is dominated by smoother terrain. [NASA/JPL]

appear to be different ages (i.e., Schmidt et al., 2011, 2012). The two regions both exhibit blocky texture, but within Thrace Macula, the blocks comprise a far lower surface area and the region is dominated by smoother material (Figure 2-22). The margins are typified by low albedo material embaying the surrounding terrain and obscuring the ridges that extend into the region.

Undifferentiated Chaos

Characterization: Regions of chaos that are consistent with previous definitions of mottled terrain (i.e., Lucchitta and Soderblom, 1982) and are not imaged at high enough resolution to distinguish or negate the presence of plates, blocks, or elevated massifs are termed undifferentiated chaos. These areas share characteristics of lenticulated plains or microchaos in low-resolution images such that they appear "speckled" (Figure 2-23). At resolution boundaries, it is possible to trace albedo features into lower resolution coverage areas; these appear disrupted with no ridged matrix visible at high resolution. The absence of ridged texture is a defining characteristic that distinguishes these areas from plains material. The high density of low albedo "speckles" also distinguishes undifferentiated chaos from lenticulated plains and microchaos. Superposing ridges are visible, though these are less prominent in undifferentiated chaos materials than in lenticulated plain units; the ridges are more subdued in undifferentiated units.

Interpretation: Large regions of chaotic materials that cannot be distinguished due to low resolution and viewing geometries are termed undifferentiated. These areas show some evidence of disruption as in other chaos materials. Other chaos materials may degrade to the appearance of undifferentiated chaos over time; however, the inconsistent resolution and illumination coverage prevents a determination.

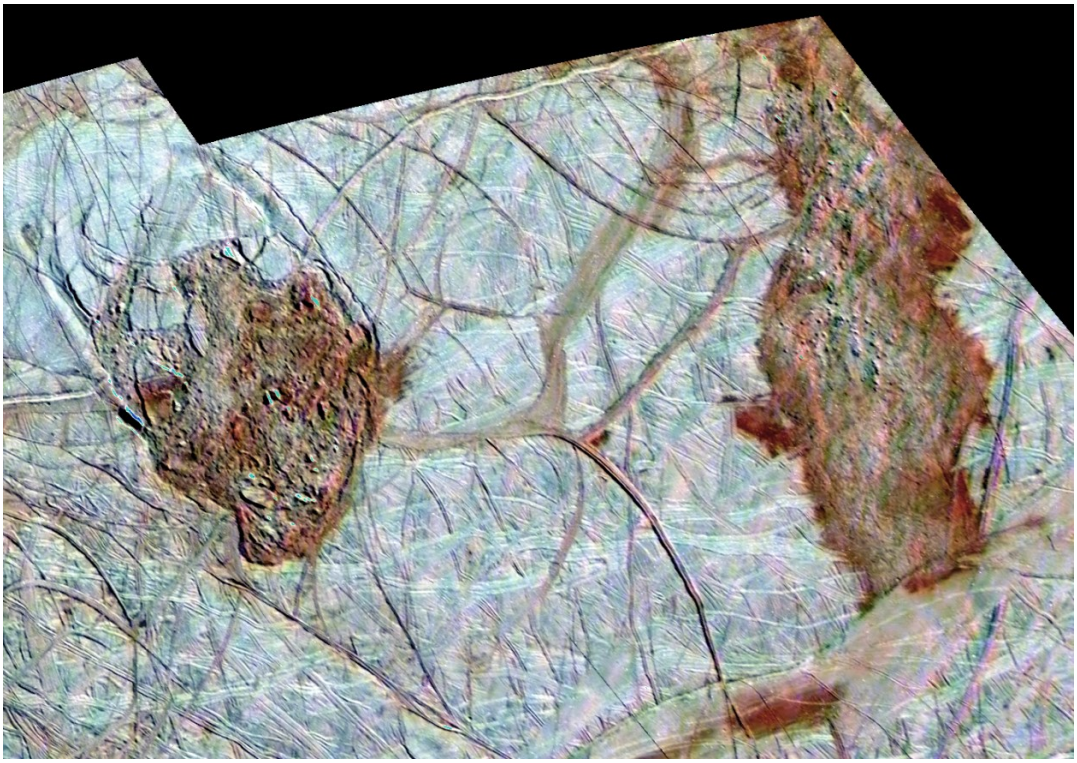

Figure 2-22. Thera (left) and Thrace (right) Macula represent the gradation from blocky to subdued chaos. [NASA/JPL/U. of Arizona]

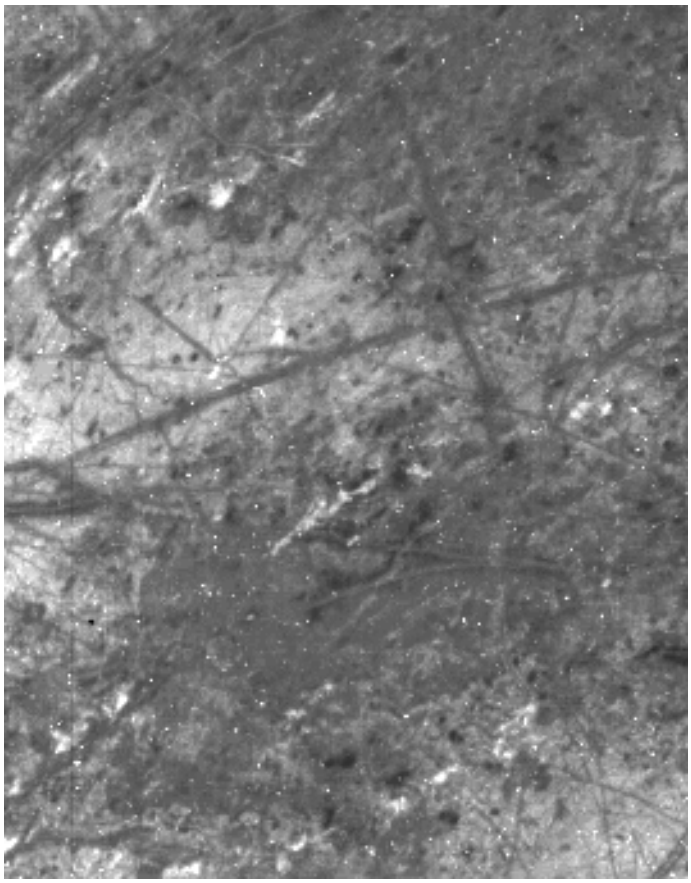

Figure 2-23. Undifferentiated Chaos. At global resolutions, chaos material is exemplified by low albedo and a mottled texture. [NASA/JPL]

2.5.3 Linea Units

Distinct from the densely spaced ridges in the background plains are the widely spaced lineaments that consistently cross-cut younger plains units. These lineaments appear to represent a middle period of the geologic time represented by Europa's current surface, with some lineaments being overprinted by younger chaos or plains units and all but two craters (the exceptions being Tyre and Callanish, which have some superimposed lineaments; Figure 2-24). Lineament types include fractures or troughs, double ridges, ridge complexes or ridged bands, and several types of bands, including smooth, dark, lineated, or pull-apart (Figure 2-25). With the exception of bands wider than 20 km, lineaments are too narrow to plot at map scale. Their ubiquity and importance to the overall surface history of Europa dictate that they be included in the map; thus, they are plotted by structural line symbols with color coding to indicate unit type differences. As discussed above, the density of lineaments dictates that only a selection of lineaments, prioritized by the criteria described above, be included in the map. This ~10% of traceable linea are shown isolated on Figure 2-26.

Band Material

Characterization: Bands are linear, curvilinear, or cycloidal zones distinguished by albedo and/or texture contrast to the surrounding terrain (Greeley et al., 2000; Figueredo and Greeley, 2004; Prockter and Patterson, 2009). Typical bands exhibit sharp margins and may have bounding ridges (Doggett et al., 2009). The interior structure of bands typically exhibits a series of subdued subparallel ridges and troughs or material that is structurally smooth (Figures 2-27, 2-28). When ridges and troughs are present, they are topographically subdued, ~300-400 m wide with regular spacing and are triangular in

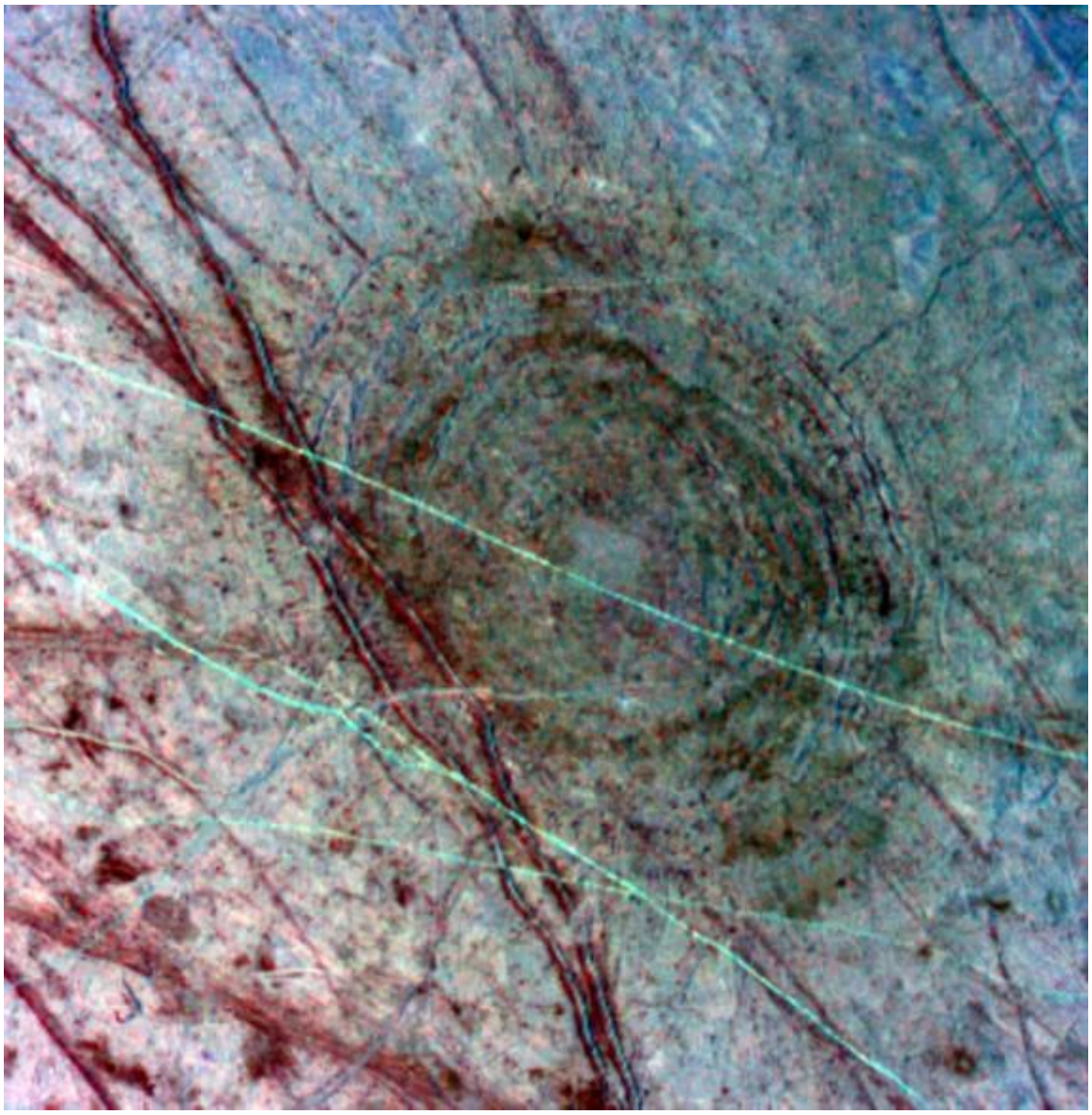

Figure 2-24. The 140 km diameter Tyre multi-ring impact basin is cross-cut by several younger lineaments. Red colors indicate water with other components, probably hydrated salts or sulfates. [NASA/JPL]

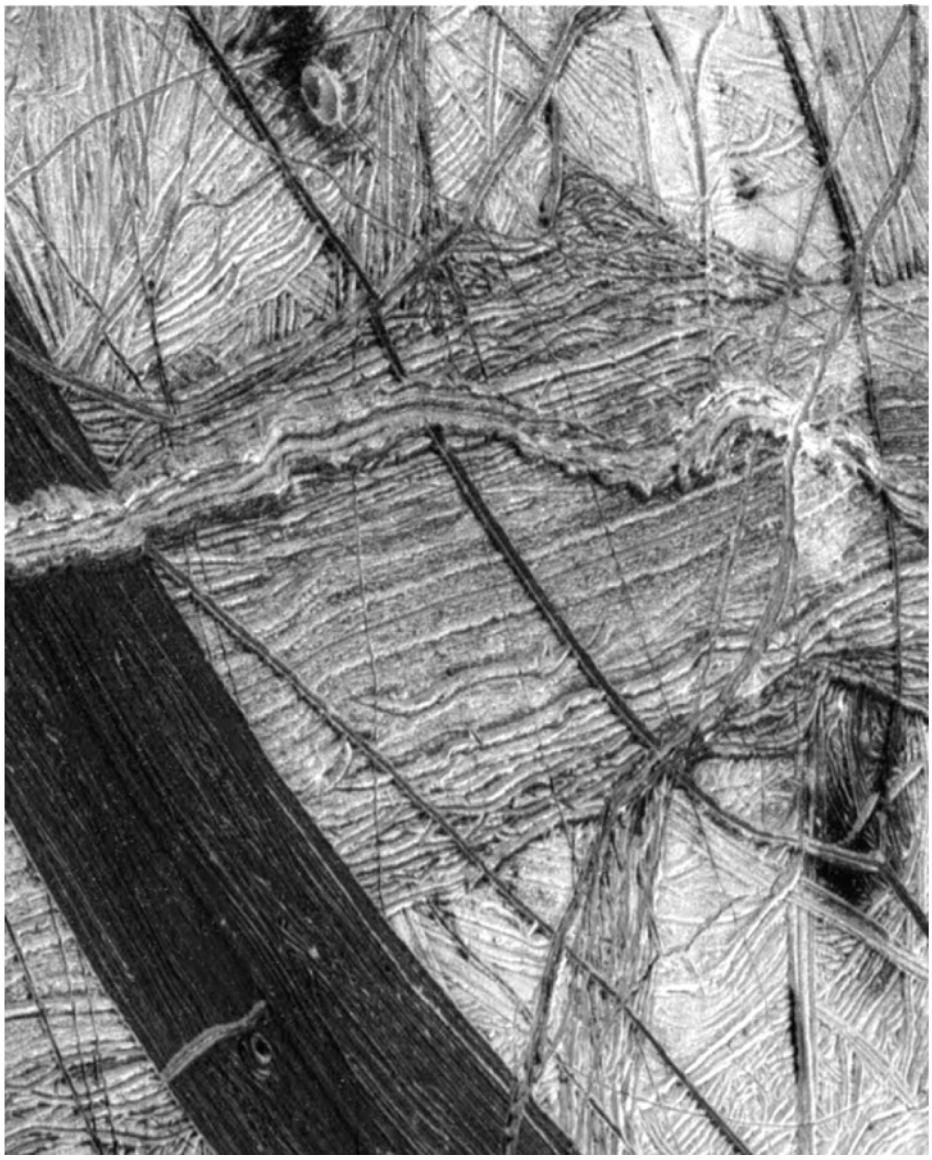

Figure 2-25. A variety of lineaments. A double ridge (center) with evident slope material crosscuts a dark smooth band with subdued lineation (left) which in turn crosscuts a wider, more hummocky, bright band. Ridged plains are visible in the background and narrow double ridges are common. [NASA/JPL]

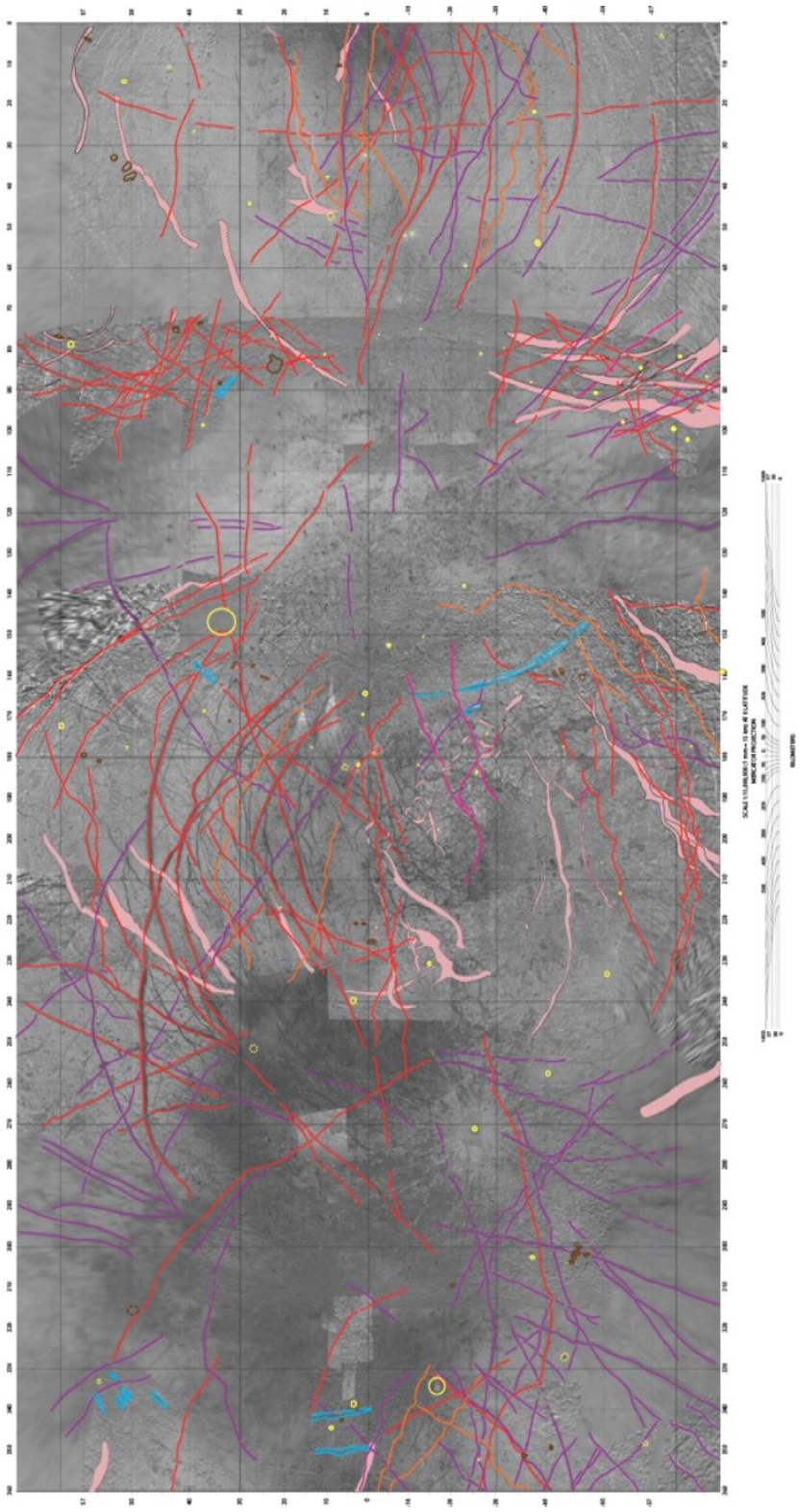

Figure 2-26. Structural map of Europa at 1:15M scale. Structure descriptions are given in the text. See Figure 2-5 for symbol identification.

cross-section (Doggett et al., 2009). In some cases, there exists a single narrow trough, near or offset from center, that is surrounded by a hummocky textured zone. At low resolution, these bands appear to have a smooth texture.

Though previous reviews have grouped bands into several sub-classes, including smooth or lineated (e.g., Greeley et al., 2000, 2004; Prockter et al., 2002); bright or dark (Tufts et al., 2000); or ridged (Figueredo and Greeley, 2000; Stempel et al., 2005). Here, all previously defined types of bands are grouped together with the exception of ridged bands which are treated as a separate unit and are analogous to ridge complexes (i.e., Greenberg et al., 1998). Grouping of all band types is necessary to represent global distribution of all bands. Imaging conditions prevent the identification of all types of bands in a global perspective.

The most common bands are dilational, or "pull-apart" bands (Figure 2-29; Tufts et al., 2000). These are typically low albedo bands with reconstructable margins and interior morphologies that include subdued lineation in the form of faults or ridges (lineated bands) or smoother hummocks (smooth bands). Bright bands (see review by Prockter and Patterson, 2009) are high albedo with interior morphologies similar to dilational bands but without reconstructable margins.

Interpretation: Dark bands appear to be dilational and margins can be reconstructed to close the band (Schenk and McKinnon, 1989; Pappalardo and Sullivan, 1996; Sullivan et al., 1998); interiors are presumed to consist of subsurface material that has been emplaced by upwelling. Bright bands disrupt pre-existing terrain but cannot be reconstructed (Schenk and McKinnon, 1989; Greenberg, 2004; Prockter et al., 2002). Dark bands have been interpreted to form from the following mechanisms: (1) fracturing

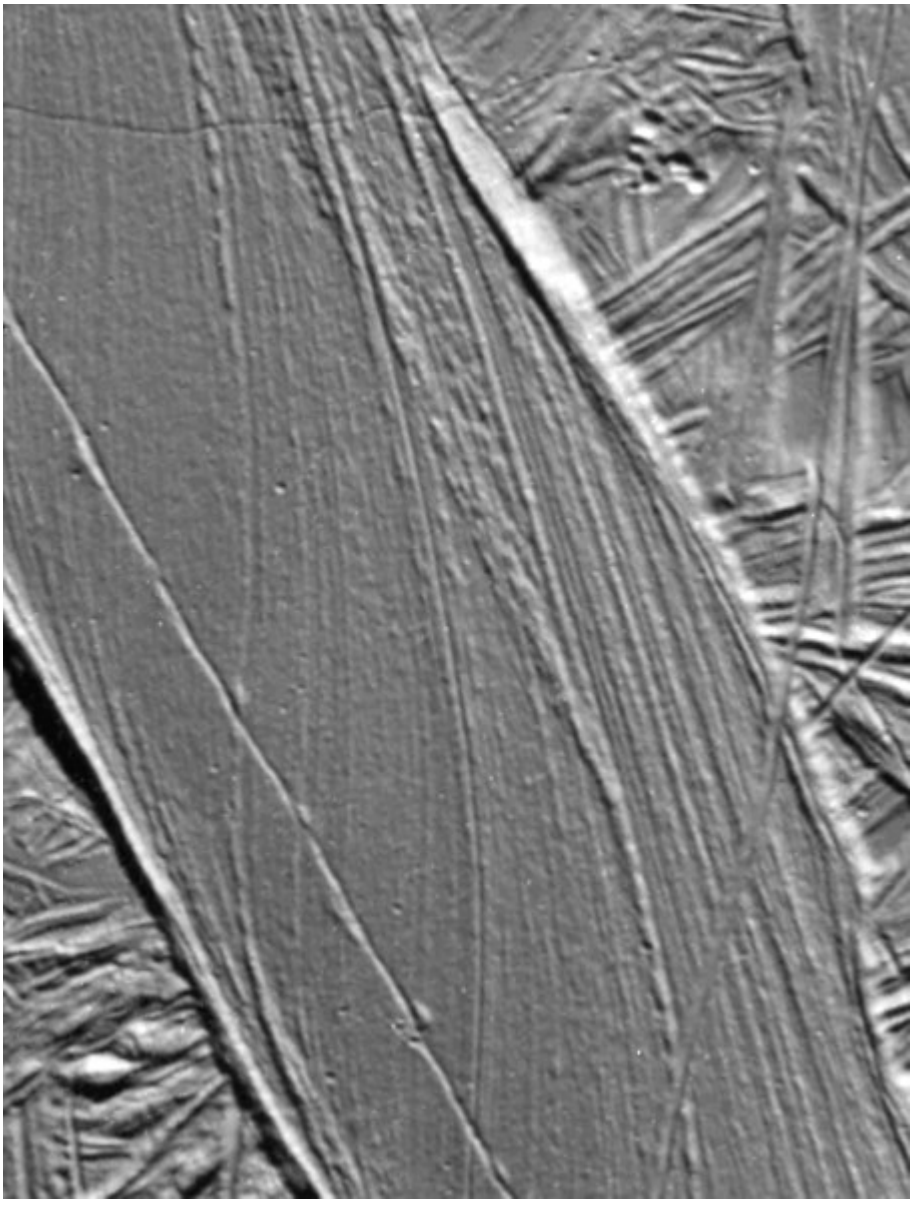

Figure 2-27. This portion of Astypalaea Linea exhibits sharp margins and subparallel lineations. Resolution is 39 m/px. [NASA/JPL]

Figure 2-28. A perspective view of Agenor Linea illustrates the hummocky nature of band interiors. [Base image: NASA/JPL; Processing by Paul Schenk, LPI]

Figure 2-29. “Pull-apart” or dilational bands, also known as “wedges”. These dark bands are largely confined to Argadnel Regio and superpose older, brighter bands and ridged plains. They are also cut by younger double ridges. [NASA/JPL]

of a brittle surface layer overlying a ductile subsurface with subsequent rifting and infilling (Pappalardo and Sullivan, 1996 and others), (2) tidal pumping due to cyclically varying tidal stresses (Tufts et al., 2000 and others), and (3) mid-ocean ridge spreading with buoyancy (Sullivan et al., 1998 and others). Bright bands are interpreted to result from (1) dike intrusion (Lucchitta et al., 1981), (2) contraction (Schenk and McKinnon, 1989 and others), or (3) dextral shear with extension (Prockter et al., 2002 and others). Bands may represent a transitional mechanism which exploits pre-existing fractures or develops in a progression along with ridged bands, ridge complexes, and ridges.

Ridges

Characterization: Linear features with two or fewer crests and their accompanying slope material are identified as ridges. Ridge material most commonly occurs in the form of double ridges (Figure 2-30), or ridge pairs separated by a medial trough. Double ridges are typically 0.2-4 km wide; maximum positive relief is no more than 1 km (Figure 2-31). They range in length from a few kilometers to >1000 km with widths up to several km and are convex to trapezoidal in cross-section (i.e., Doggett et al., 2009). Ridges may exhibit tapering, flank slopes (Head et al., 1999a), and mass wasting (Sullivan et al., 1999a; Moore et al., 2009). Dilation, sinuous margins, anastomosing and discontinuous sets, and bifurcation are common. Some ridges are cycloidal (see flexūs). Material associated with individual ridges is too small to plot on the map print at map scale; thus, general ridge material is plotted as structural line symbols though they correspond to a specific formation process and time. Only 150 of the most prominent or stratigraphically significant ridges are plotted as *framework lineaments* (Figure 2-26).

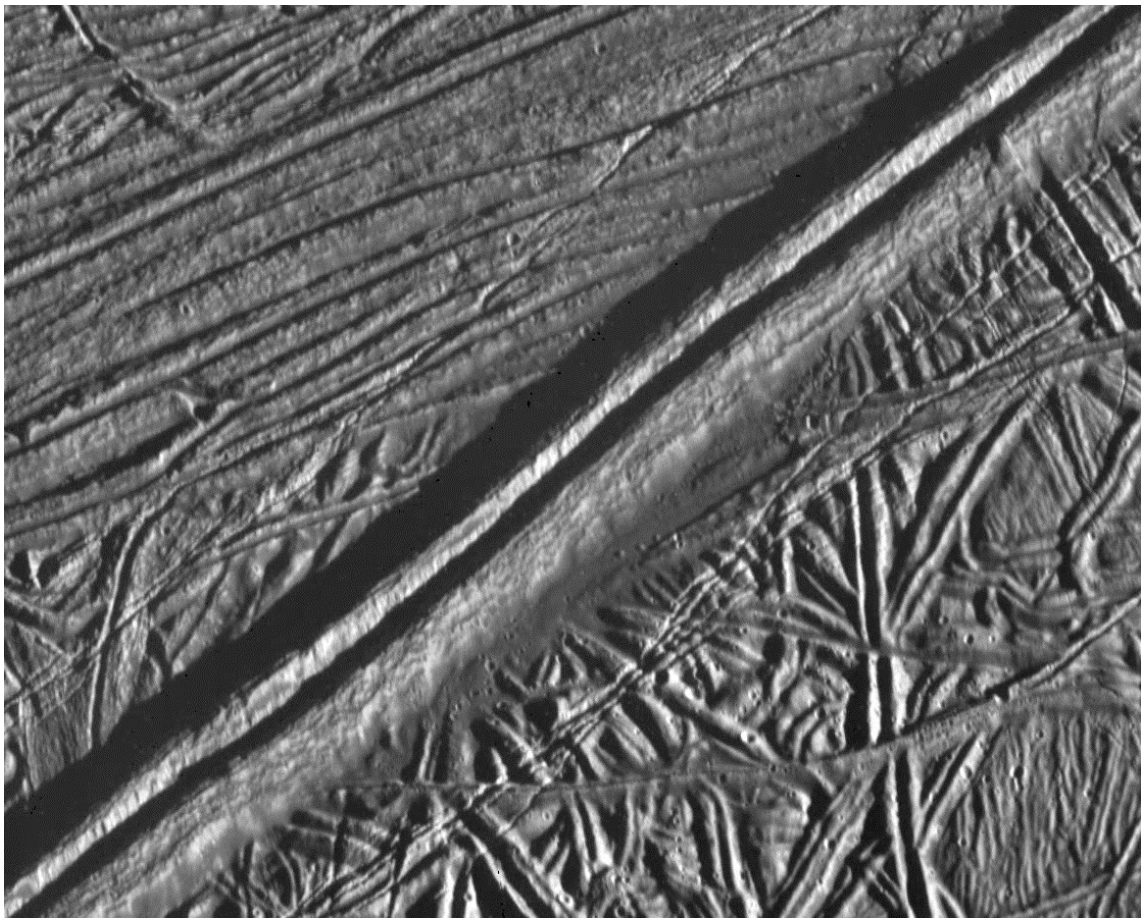

Figure 2-30. A double ridge cross-cuts older ridged plains and a lineated band. The ridge crests bound a central trough and form a triangular to trapezoidal cross-section. Mass wasted deposits are visible on the flanks of the double ridge. Smaller troughs and raised flank troughs are visible in the background matrix. [NASA/JPL]

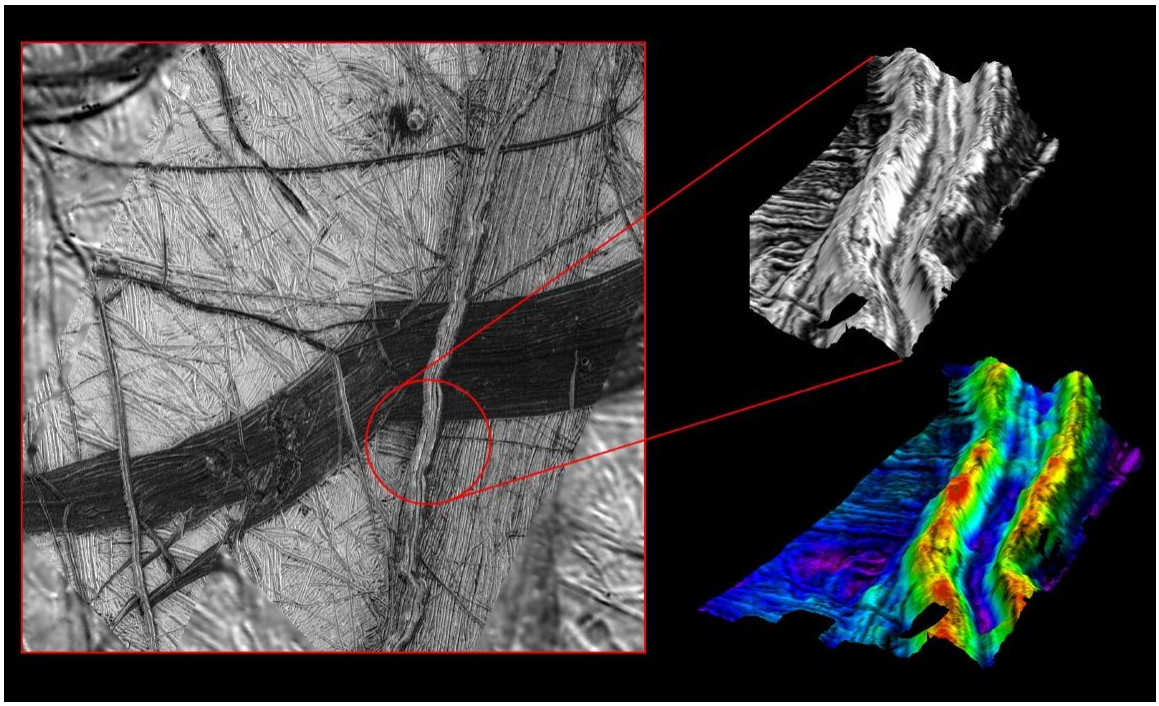

Figure 2-31. Topographic relief is a maximum of 1 km. East-west trending double ridge (circled) cuts across older background plains, a dark band, and a ridge complex. Three dimensional perspective (top right) shows the ridge topography and V-shaped trough. Bright material, pure water ice, prevails at the ridge crests and slopes; dark material, ice mixed with silicates or hydrated salts, is confined to valley floors. The ridge crest reaches a height of 300 meters (red, in lower right) above the surrounding terrain. The valley is 1.5 km wide. Surrounding ridged plains are shown in blue. [NASA/JPL/ASU]

Interpretation: Double ridges may form by (1) cryovolcanism (Kadel et al., 1998; Fagents et al., 2000), (2) incremental buildup or wedging (Turtle et al., 1998), (3) upwarping through linear diapirism (Head et al., 1998a, 1999), or (4) compression along fractures (Sullivan et al., 1998). More likely scenarios include (1) tidal pumping by repeated opening and closing of fractures (Pappalardo and Coon, 1996, Greenberg et al., 1998, and others) or (2) shear heating (Gaidos and Nimmo, 2000; Nimmo and Gaidos, 2002).

Ridged Bands/Ridge Complexes

Characterization: Ridged bands or ridge complexes consist of a collection of subparallel anastomosing single or double ridges (i.e., Prockter and Patterson, 2009). Trends are linear or curvilinear with no obvious bilateral symmetry. Margins are sinuous or undulating. Individual ridges may deviate from the overall trend and become incorporated in other throughgoing complexes (Figure 2-32); these deviations are a defining characteristic of ridge complexes that differentiate them from "lineated" bands where lineations remain largely parallel and/or are very subdued and relaxed.

Interpretation: Ridge complexes or ridged bands likely undergo a similar mechanism to double ridges. They may form by successive buildup of individual double ridges within a confined region (Geissler et al., 1998; Greenberg et al., 1998; Figueredo and Greeley, 2000). Active ridges may transition into ridge complexes (Belton et al., 1996).

Flexūs

Characterization: Cycloidal ridges consist of connected arcuate segments of similar length and show planforms that are convex in the same direction, forming congruent curved segments joined at sharp cusps (Figure 2-33). Several examples, particularly those

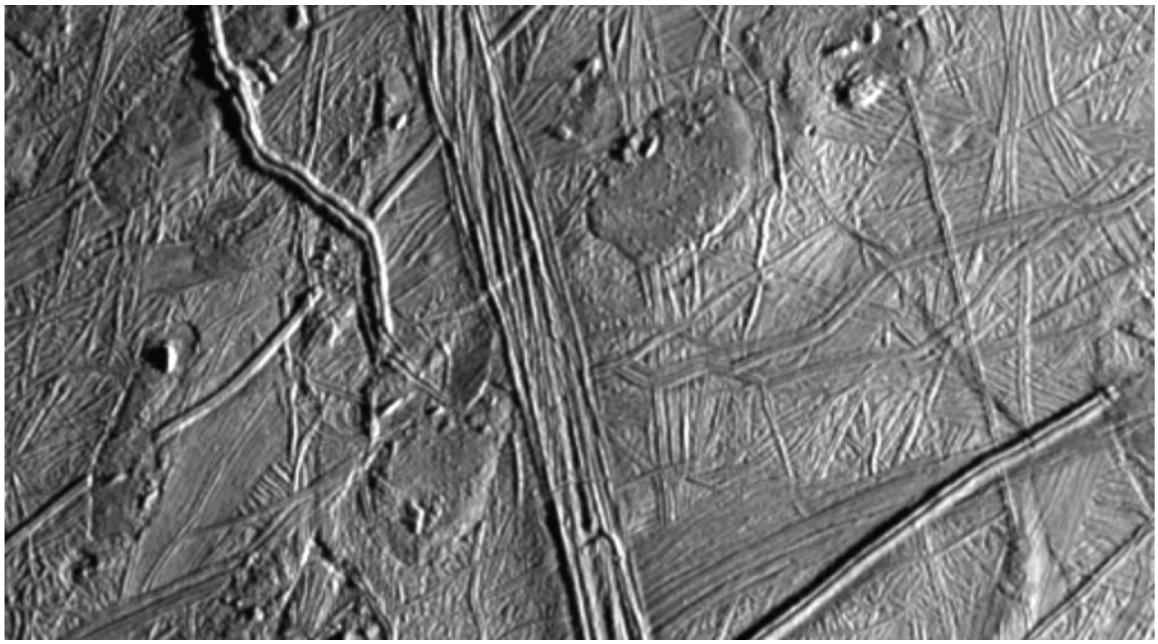

Figure 2-32. Ridge complex where individual ridge structures in the interior of the complex deviate from the overall trend. [NASA/JPL]

in the northern leading hemisphere, exhibit internal morphologies similar to smooth band material though most are more similar to double ridges. The flexūs designation indicates the dominant formation process that controls the overall planform of features.

Interpretation: The cycloidal shape is suggested to be controlled by a changing direction of crack propagation under the control of Europa's diurnally rotating stress field. Propagation speeds are interpreted to be slower than Europa's orbit around Jupiter (Hoppa et al., 1999b).

Undifferentiated Lineae

Characterization: Ridge types without differentiable characteristics at the scale of the map are plotted as undifferentiated linea (Figure 2-34). These include cracks, raised-flank troughs, or more complex ridge structures with albedo too low to distinguish topography.

Interpretation: These linea are most likely examples of small fractures, ridges, or subdued/brightened ridge complexes that are unclassifiable due to resolution and viewing geometry constraints.

2.5.4 Crater Units

All material comprising a crater's floor, central peak (when present), wall, raised rim, and ejecta deposits is mapped as crater material. Multi-ring structures (i.e., Tyre and Callanish) are included as general crater materials and are not mapped as a separate unit; this grouping is in keeping with the effort to represent the density and spacing of all features. In contrast to other structures where, for example, only a portion of lineaments of each type are shown in order to illustrate a proportionate number of features with attention to density, orientation, and geographic location, the small density of craters (Chapman et al., 1998; Moore et al., 2001) on Europa necessitates attention to every

Figure 2-33. Flexus in the northern leading hemisphere. The cycloidal features here show both double ridge and smooth band morphologies. [NASA/JPL]

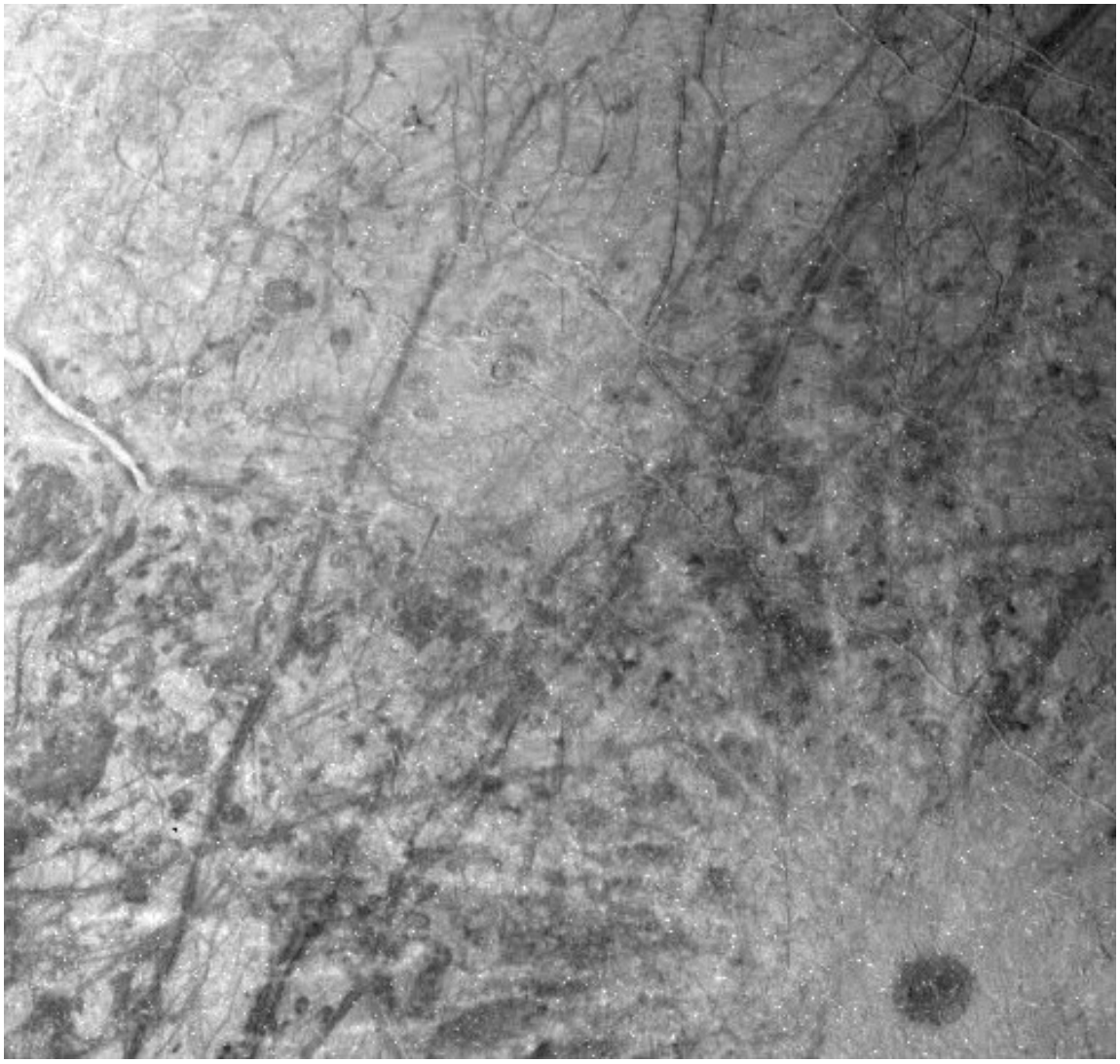

Figure 2-34. Undifferentiated linea do not have distinguishable morphologies at the scale of imaging. The north-south trending dark linea in this image may be double ridges, though resolution and viewing geometry is not sufficient to distinguish characteristics. [NASA/JPL]

crater. These are essential in estimating overall surface age and play some importance in determining relative unit age. Though there are only several dozen craters of a size large enough to represent on the map, every known crater assumed to be a primary crater is included as a structural symbol.

Secondary Crater Material

Characterization: The bright rays emanating from the Pwyll structure are mapped as a separate unit as this is the only rayed ejecta material (Figure 2-35). Many small circular depressions are evident within the high albedo material that mantles nearby chaos.

Interpretation: Most small craters appear to be secondary impact craters, particularly from the Pwyll impact, as indicated by size-frequency distribution (Bierhaus et al., 2001, 2009; Moore et al., 2001; Schenk et al., 2004). Rayed ejecta from the Pwyll impact is the only preserved rayed material of mappable extent (Moore et al., 2001). Tyre and Callanish both appear to have produced secondary impact craters (Bierhaus et al., 2005), but they are not grouped closely together sufficiently to garner a mappable expanse.

Crater Ejecta

Characterization: Ejecta deposits formed by impact events include hummocky material distributed radially away from crater rims and low albedo material adjacent to impact structures (Figure 2-36). Some materials are raised as in a pedestal or rampart structure. In low resolution coverage areas, craters are often identified by the presence of their bright ejecta, even when the crater structure is not evident.

Interpretation: Dark ejecta is thought to include non-ice materials excavated from the subsurface and/or brought by the impactor (Greeley et al., 1982; Ong, 2004). The

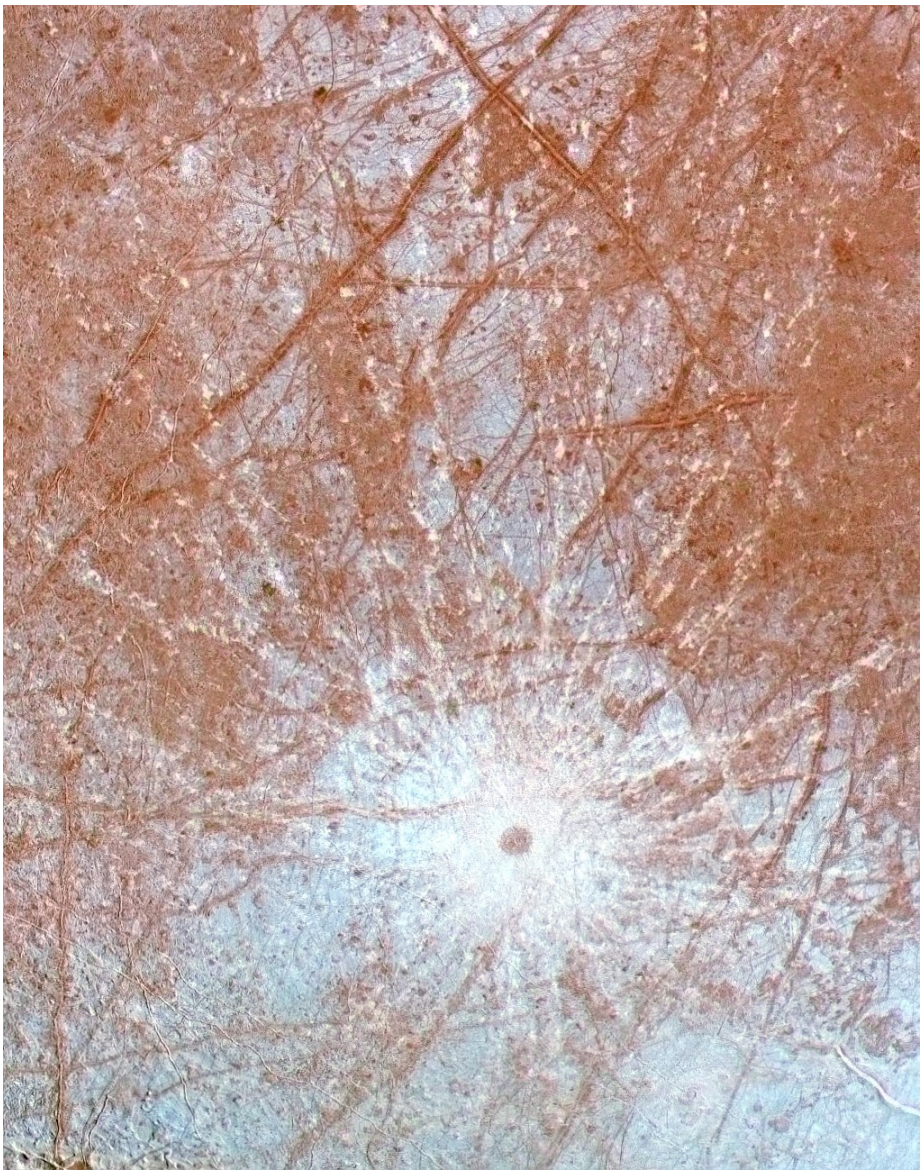

Figure 2-35. The Pwyll impact structure is surrounded by a bright continuous ejecta blanket. Lengthy rays extend radially around the impact structure and mantle surrounding chaos (brown areas). [NASA/JPL]

pedestal is due to a convex upward scarp, possibly formed by outward creep of warm, plastically deforming ice (Moore et al., 1998).

Crater Material

Characterization: Crater materials consist of the floor and rim of circular depressions as well as the materials associated with multi-ring structures. Impact structures range from small simple bow-shaped craters to complex craters with central peak materials and terraces to relaxed multi-ring structures. Of the ~25 craters larger than 10 km, the dominant morphology is a complex crater with a central peak (see Figure 2-36; Schenk and Turtle, 2009).

Interpretation: The minimum diameter for the transition from simple to complex morphology is 5-6 km, as compared to 10-20 km on terrestrial bodies. Transient crater depths lead to an assessment that craters 10-18 km in diameter and 3-6 km deep did not penetrate to a liquid layer; thus ice must have been several kilometers thick at the time of crater formation (Moore et al., 2001). Structures with multiple concentric rings are interpreted to be relic impacts that penetrated into liquid water or warm ice (Moore et al., 1998; Schenk, 2002). Compared to the cratered terrains of other solar system bodies, the paucity of impact craters on Europa's surface serves as a stark indicator of geologically recent global resurfacing. The paucity of primary impact craters suggests a relatively young global surface age of ~40-90 M.y. (Bierhaus et al., 2009) though the basin-forming impacts have been attributed to the period of Late Heavy Bombardment, resulting in an older inferred age of 1-3 G.y. (Neukum, 1997).

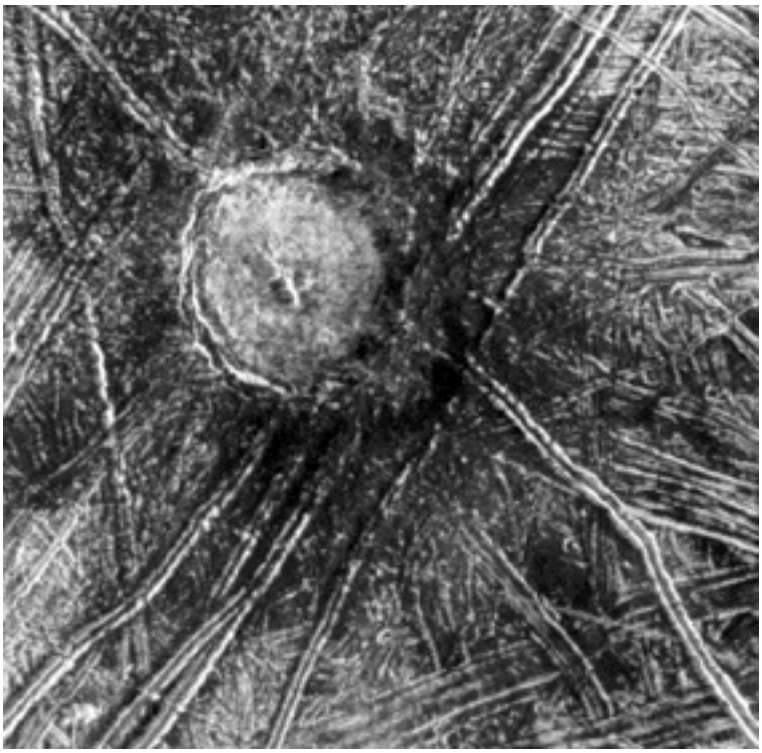

Figure 2-36. The Cilix impact structure is surrounded by dark ejecta. The complex crater exhibits a flat floor, terraced walled, and a central peak. [NASA/JPL]

2.5.5 Other Structures

In addition to the lineaments described above as material units, other structures plotted on the global structure map include extensive arcuate troughs, bounding scarps for elevated blocks or larger-than-average depressions or domes, and crater rims. With the exception of impact crater rims, each of these structures has been associated with an endogenic formation process directly related to the formation of other material units such as chaos. Depressions and domes are a variety of, or similar to, lenticulae. Elevated blocks are most commonly associated with blocky chaos uplift and subsequent fracture from loading (i.e., Figueredo et al., 2002). Finally, the arcuate troughs have been suggested to form portions of antipodal great circles as a result of impact basin formation; their positions are suggested to be indicators of a combination of non-synchronous rotation and true polar wander (Schenk et al., 2008). These troughs either post-date ridges and chaos without having disrupted them or they pre-date other features and the ridges and chaos form unaffected by the presence of the arcuate troughs (Schenk et al., 2008). Other structural features are certainly evident in abundance. Faulting, especially strike-skip faulting, is common in lineament formation (see reviews by Kattenhorn and Hurford, 2009 and references therein); however, these are not readily evident at the scale of the map and so are not included. Similarly, structural symbols for scarps unrelated to uplifted chaos material and ridge crest or trough down-slope symbols are also not included, as most of these features appear as general lineaments at map scale.

2.6 Geologic History

All of the currently visible features on Europa's surface were emplaced within a timeframe consistent with Earth's Cenozoic period (Doggett et al., 2009) and are much

younger than most features formed on Mars during the Late Amazonian, on the Moon during the Copernican period, or on Mercury during the Kuiperian period (see Doggett et al., 2009, Figure 21). The resurfacing history is also much different from that of the other Galilean satellites, Ganymede and Callisto, which both have a more extensive cratering history. Io, with its apparent complete lack of impact craters and obvious current resurfacing, is also not of an equivalent surface age. Bierhaus et al. (2009) discusses a comparison of surface age between Europa and Venus which has a similar lack of craters, with a globally random distribution which indicates global resurfacing within the last 500 M.y. (Phillips et al., 1992). However, Hauck et al. (1998) note that venusian plains could represent a spread of ages; the same is understood for Europa (e.g., Head et al., 1999b; Pappalardo et al., 1999; Kadel et al., 2000; Spaun et al., 1999a). This inability to rely on crater counts to establish age defines a major problem in understanding the geologic history of Europa.

In determining relative age relationships between material units on most maps of planetary bodies, crater densities are used as a proxy for estimating age: higher crater densities overall or higher densities of large craters indicate an older surface. On Europa, where there is a paucity of impact craters, crater densities are ineffective in determining relative age relationships in most cases. The surface of Europa only reflects a small fraction of the age of the body's existence; the low number of craters indicates a young surface with strong evidence of recent global resurfacing (Zahnle et al., 2003). Crater densities, especially of the ridged plains, yield a surface age estimate of ~40-90 M.y. (Bierhaus et al., 2009). Embayment and cross-cutting relationships can be used to establish relative age of adjacent units, but determining a global history requires further

methods. A manuscript in preparation for submission (Figueredo et al., unpublished) details the global mapping and sequencing of all major lineaments (>100 km in length) into seven sparsely connected regional networks that are broken up by intervening areas of chaos and/or low image resolution (see Figueredo et al., 2004). These networks define regional stratigraphic frameworks that allow temporal correlation of features on a hemispheric scale. Even using this unique method of determining relative age, a global history based on lineament sequencing is not reliable as the formation of chaos resurfaces or prevents the further formation of lineaments. However, a great deal is understood about the resurfacing in Europa's recent history.

Pole-to-pole (Figueredo and Greeley, 2004) and initial global (Doggett et al., 2009) mapping group the chronology of formation periods into four episodes after the stages of emplacement established by Lucchitta and Soderblom (1982). Current understanding of the formation periods are outlined in a Correlation of Map Units (Figure 2-37). The four periods are defined below according to the major processes active within each period and are bounded by the lineament stratigraphy defined by Figueredo et al. (unpublished). Overall, there is a notable transition from the formation of ridged plains to linea formation to chaos formation over the first three periods (Figueredo and Greeley, 2004).

2.6.1 Balgatanian Period

The earliest period involved the development of ridged plains through repeated overprinting of closely-spaced lineaments and narrow bands. This tectonic resurfacing (Head et al., 1997) is considered to be the longest period of the four (Figueredo and Greeley, 2004). All subsequently forming units appear to have developed through disruption of the ridged plains (Lucchitta and Soderblom, 1982); this is especially true of

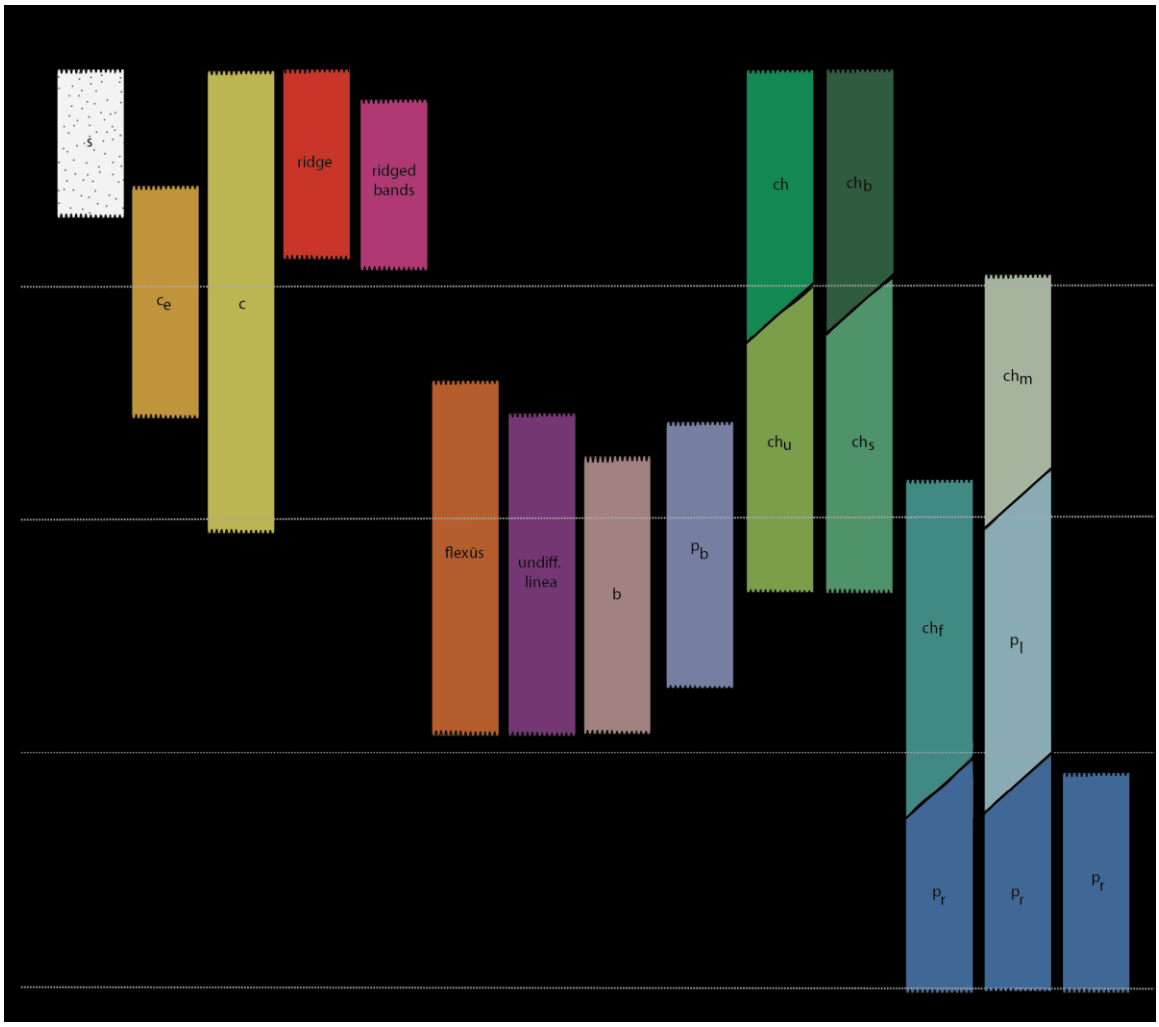

Figure 2-37. Correlation of Map Units. Unit descriptions are given in the text and in Appendix A.

chaos units where the ridged plains texture is preserved in small plates that have been broken and displaced from their original location. Any surface features that formed prior to this period of development are presumed to have been entirely resurfaced by the ridged plains development (Doggett et al., 2009) or to have been incorporated into current units (e.g., Greenberg et al., 1999). Balgatan and Falga Regio (see http://astrogeology.usgs.gov/maps/planetary-maps-and-globes for locations of named features) are dominated by ridged plains as well as younger plains-crossing ridges. Falga Regio exhibits far more lenticulation than is evident within Balgatan Regio; thus Balgatan is considered the type locality of ridged plains and for period naming. The highest resolution images of ridged plains most often used to describe texture was actually taken within Argadel Regio, where ridged plains serve as a background for dark bands; medium resolution images that illustrate the ubiquity of ridged plains cover most of Falga and Balgatan Regio.

2.6.2 Argadnelian Period

The second period of formation is characterized by the disruption of ridged plains by the formation of lenticulae and the emplacement of dark material to form the lenticulated and banded plains. The formation of prominent, widely spaced lineaments not interwoven into the ridged plains background is the dominant process of the period. These lineaments include ridges in all regions and the dark bands of Argadnel Regio. In the most recent portion of this period, initial chaos regions began to form and the Tyre and Callanish impact events occurred. As Argadnel Regio is the location for both the dark bands and several prominent ridges that formed during this period, it is considered the type locality for naming the period.

2.6.3 Annwnian Period

The third period is dominated by the formation of chaos. The large provinces of chaos that formed within Annwn, Dyfed, Powys, and Tara Regio are all representative of this time period. Further disruption of the ridged plains with the continued formation of lenticulae and microchaos as the process controlling chaos formation acts on the plains is also prevalent, especially at the boundaries of chaos regions. There is evidence of earlier lineaments being reactivated during this period (Klemaszewski et al., 1999) and for continued lineament formation. Of the major chaos regions, Annwn Regio best represents a proportionate distribution of chaos, lenticulation, and lineament formation that occurred during this period.

2.6.4 Pwyllian Period

The fourth, and most recent, period is marked by continued formation of chaos, especially the small areas of knobby chaos such as Murias Chaos, and the continued degradation of older chaos. Development of ridges also continued, with the youngest and most prominent double ridges seen today having preserved crest and flank structures. Most notably, the formation of young impact craters occurred during this period. The most prominent of these is Pwyll Crater with its extensive ray system.

2.7 Summary

Data obtained by the Voyager and Galileo missions has revolutionized understanding of the Galilean satellite system and the differing geologic histories of the large satellites. With the unfortunate failing of Galileo's high-gain antenna, the planned volume of images of Europa was severely diminished, making a future mission to observe the satellite necessary to better understand the surface features and formation history.

Coverage from Voyager and Galileo is sufficient to clarify the relationships between material units and to pose many questions for future observation. The question of how chaos and lineaments form may not be settled without further high-resolution imaging and topographic and interior studies.

On the basis of this mapping effort, four main material unit types are recognized: plains materials, linea materials, chaos materials, and crater materials. Plains material is subdivided into ridged, lenticulated, and banded units. Linea material is subdivided into bands, ridges, ridge complexes, flexūs, and undifferentiated lineaments. Chaos material is subdivided into lenticulae, microchaos, fractured chaos, general chaos (often called "platy"), blocky or "knobby" chaos, subdued chaos, and undifferentiated chaos. Crater materials are subdivided into groups encompassing secondary materials, ejecta, and materials associated with crater morphology. While the definition of these material units is aimed at understanding their formation processes in relation to the exotic composition of Europa's crust and the possibility of a past or present global ocean beneath the surface ice layer, definitive associations with processes cannot be determined without further study. Discussion of these processes and the implications for global resurfacing history are discussed further in Chapter 3.

Mapping techniques used for Europa differ somewhat from other planetary maps. Wide variations in resolution and viewing geometries prevent the mapping of small expanse units or subtle variations in unit textures. Ensuring a globally consistent representation of units requires grouping features with a range of morphologies into single units. In addition, the nature of chaos materials prompts the definition of unit boundaries as gradational and approximate in most cases. The prevalence of lineaments

over the entire surface requires that only a representative portion of lineaments be presented on the map sheet to ensure visibility; due caution has been practiced to show proportional relationships between these units and features, as they each influence the formation and evolution of the other. Perhaps most different from other mapping efforts is the attempt to establish relative ages on the basis of linea cross-cutting relationships without the benefit of crater density dating, as is common elsewhere. This unique technique constrains four periods of formation where each period is dominated by the formation of one or more unit types.

The post-Galileo view of Europa's young surface provides a range of likely scenarios of formation. Though none of these can be confirmed without further observations with globally consistent coverage, they do lead to questions that will shape future exploration. This global geologic map provides a synthesis of the overall history of this unique icy satellite and will be a useful frame of reference for future exploration of the jovian system and other potentially active outer solar system bodies, as discussed in the remaining chapters of this dissertation.

CHAPTER 3

EXPLORING THE UNDETERMINED NATURE OF EUROPA'S GEOPHYSICAL ACTIVITY

3.1 Introduction

Understanding the modes of formation for Europa's surface features is pivotal in interpreting the overall geologic history. From Chapter 2, it is evident that the features exhibited at Europa's surface can be grouped into four main classifications based on similar morphology. Determining whether all units of a single type (i.e., all types of chaos) form by the same mechanism is an outstanding question that cannot be better constrained without further observation. Many models have been presented to explain the range of conditions necessary for a mechanism to produce the observed features. Likewise, variable conditions have been assessed to explain differences in appearance between units of the same type. The following is a discussion of the processes that have been proposed to form the main feature types, including a comparison of all proposed models with respect to multiple constraints. With reference to relationships established by the global map, this work presents the most likely formation mechanisms responsible for forming the features identified in the map. Special attention is paid to outline evidence that links mechanisms to a global process.

Most authors that have attempted to explain the formation mechanisms of Europa's surface features follow the principle of parsimony, which would suggest that all features in a feature class could or should be formed by the same mechanism, perhaps in evolutionary stages. While the global occurrence of features suggests that a formation mechanism can be in control globally and the indications of gradations from one unit to

another could suggest an evolutionary step in an overall process, the variety of features grouped into a single class increases the likelihood of multiple processes to explain formation. The same is true on Earth; mountains with similar morphology can form by either volcanic or tectonic processes, for example. This discussion explores a range of formation processes and presents potential Earth analog examples for each feature.

3.2 Chaos

Disrupted or "chaotic" terrain is expressed in a variety of textures on Europa including lenticulae, microchaos, fractured chaos, general ("platy") chaos, blocky (or "knobby") chaos, subdued chaos, and undifferentiated chaos. Collins and Nimmo (2009) presented a detailed assessment of formation mechanism that have been proposed for various types of chaos (see Figure 16 of Collins and Nimmo, 2009) and established a set of observational constraints that any model must be able to explain, including morphology, tectonic setting, and size. Collins and Nimmo explored the justification for lumping all features with evidence of a disrupted matrix material together with lenticulae features as types of chaos. This is consistent with mapping results which show examples of transition between multiple of these features.

Chaos regions are interpreted as areas of focused heat flow and perhaps local melting (Collins et al., 2000, Collins and Nimmo, 2009). One or more of the following processes may be in action to form the general chaotic texture:

1. In a melting model, blocks of chaos (assumed to be the "platy" variety) are analogous to buoyant icebergs (e.g., Greenberg et al., 1999) and the matrix is sea ice that formed as the top of the ocean froze (Carr et al., 1998; Greeley et al., 1998). Solid-state ice rising diapirically to the surface is possible in situations of

partial melting (Collins et al., 2000). A heat source at the base of the ice shell may melt the overlying ice, creating a hole which exposes the ocean and allows free floating icebergs and blocks ~2 km thick (Greenberg et al., 1999; Thomson and Delaney, 2001). This scenario is similar to Earth's pack ice (Figure 3-1). Thermal gradients disrupt the cold, rigid lithosphere, causing fragmented slabs of colder material to rotate and translate within the original ridged plains matrix framework (Pappalardo et al., 1998; Spaun et al., 1998). Tilted matrix morphologies could be caused by block interactions as in Figure 3-2. This model requires extreme energy and thin ice to maintain exposed liquid at the surface (Pappalardo et al., 1999; Collins et al., 2000). Under certain thermal, pressure, and compositional regimes, melt-through can explain the formation of the matrix and plates as well as plate motion but does not easily explain lenticulae formation. Melting, combined with block movement analogous to compression and extension, could also explain the inter-plate morphologies within chaos regions. As in Figure 3-3, repeated freeze-melt cycles, combined with plate motion and collision, causes the plate edges to be broken off and refrozen into slush between plates. Given the longevity of features currently seen on Europa, the ice shell is not expected to be thin enough to allow complete melting to any extent over long time periods. However, localized melting or other targeted density or thermal variations could account for the variety of morphologies that are seen. Perhaps the ice shell is layered with density variations between layers too small to be recognized in gravity measurements. This type of layering would open a range of possibilities for ocean-ice-surface interchange as thermal

conditions would be much different than those expected for a single, nearly homogeneous ice layer. Melosh et al. (2004) speculated that multiple stacked convecting layers would increase density with depth, possibly preventing mixing between layers but only on the short timescales that such layering could persist; episodic catastrophic thermal energy release could lead to surface disruptions. Melosh et al. (2004) also speculated that the timescale necessary to melt through an ice shell of 10 km thickness is on the order of 10 M.y., approximately the age of the surface indicated by crater counts. They suggest that complete melt-through of the ice shell could occur episodically, given vigorous convection in the liquid layer and resulting in a complete resurfacing followed by a period of cooling and ice thickening, similar to what has been suggested for Venus (Turcotte, 1993).

2. Diapirism is recognized as the most likely explanation for the formation of lenticulae, possibly in conjunction with partial melting of a salt-rich icy lithosphere (Pappalardo et al., 1998a; Rathbun et al., 1998; Head and Pappalardo, 1999). This mechanism would be similar to salt diapirs on Earth (Figure 3-4). Convective diapirs rise due to thermal or compositional buoyancy, possibly enhanced by tidal heating and the generation of melt (Barr and Showman, 2009). While the size of diapirs is controlled by the thickness of the thermal boundary layer and therefore expected to be consistent so that it easily explains the consistent size of lenticulae, special mechanisms, such as merging diapirs, must be considered to explain larger chaos formations such as microchaos (Spaun et

Figure 3-1. Antarctic pack ice with polygonal blocks that are free to move as liquid remains exposed at the surface. [Photographer: James Stringer]

Figure 3-2. Potential analog for the tilted blocks within the chaos matrix. This texture is most easily seen when tilted blocks are substantially thicker than the positive-relief plates. [Photographers: Barbara and Jack Donachy]

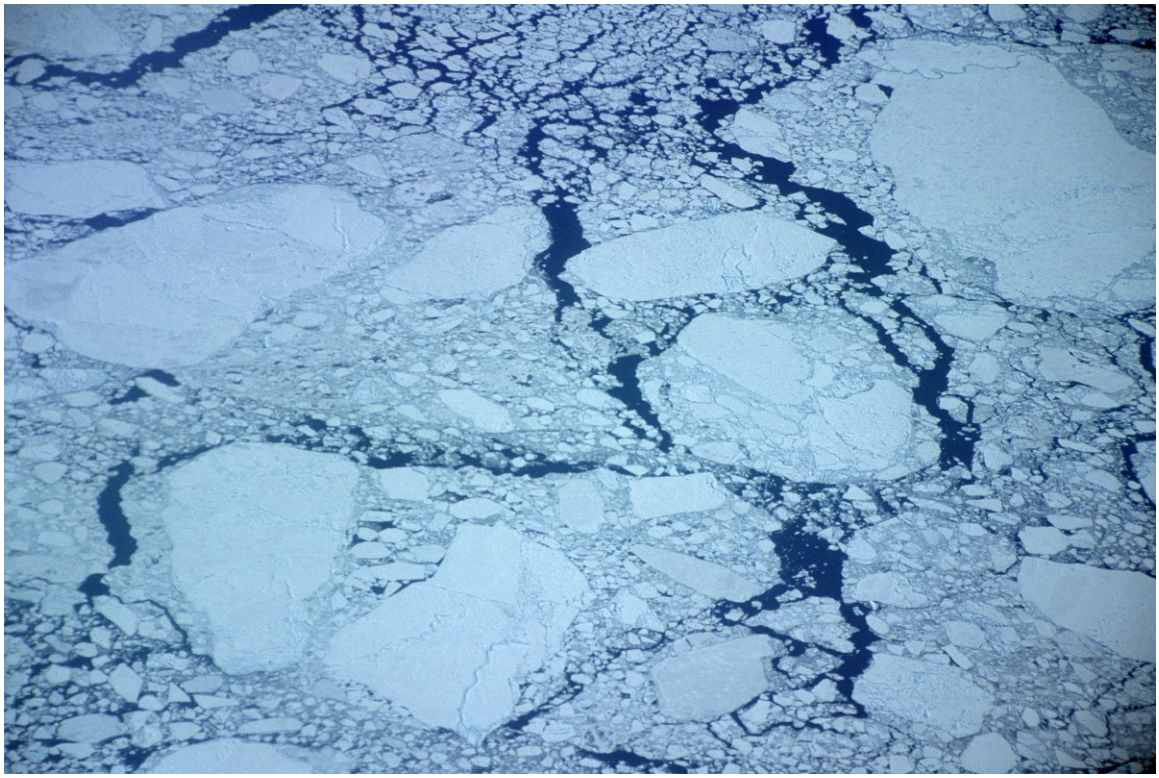

Figure 3-3. Potential analog for inter-plate morphologies within the chaos matrix. Repeated freeze-melt cycles, combined with plate motion similar to what could be expected with compression-extension cycles, causes the plate edges to be broken off and refrozen into a slush. [Image courtesy of Edmund Stump.]

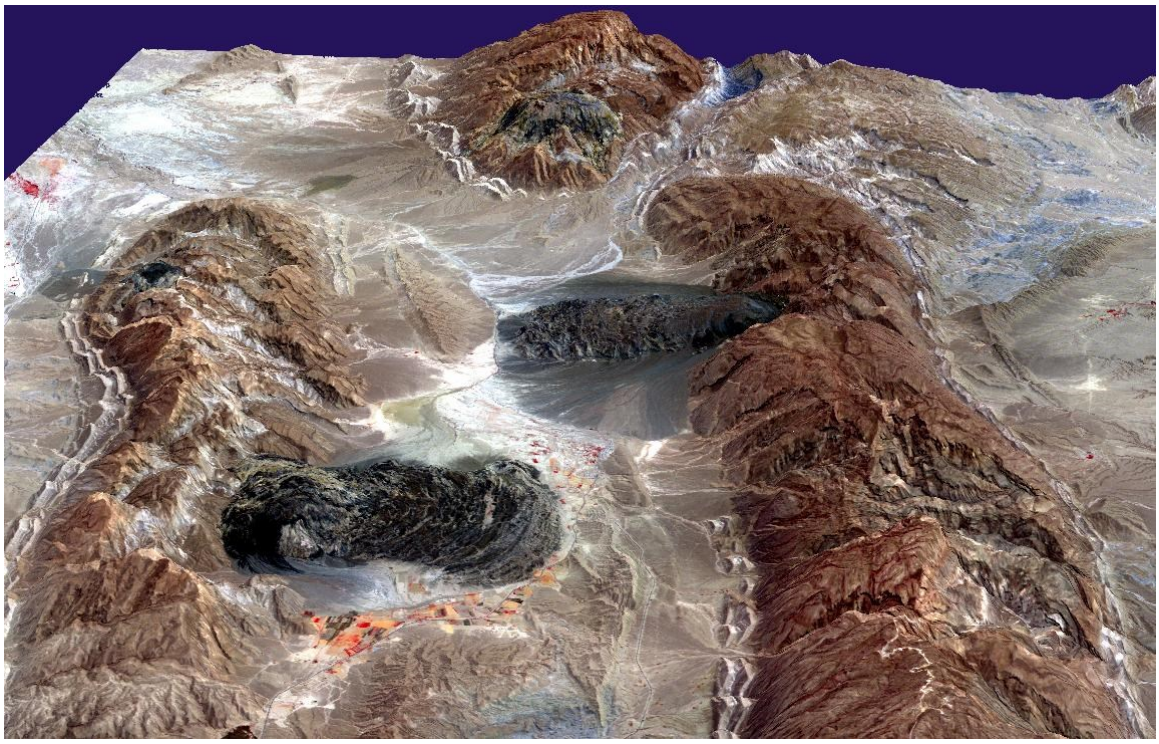

Figure 3-4. Salt diapirs in Iran. Diapirs uplift salts to create dark deposits at the surface. Gravity causes the exposed salt to flow downslope to form the lobate morphology. [NASA/GSFC/MITI/ERSDAC/JAROS, and U.S./Japan ASTER]

al., 1999; Figueredo and Greeley, 2004; Schenk and Pappalardo, 2004) but cannot adequately explain expansive chaos units. Conversely, large scale upwellings would be required to explain large areas of chaos. As discussed for Venus, differences in diapiric rise could vary the appearance of all features, regardless of size: instabilities due to partial melting, diapirs that results from a chemical rather than thermal boundary, or flow induced by diapirs would all vary the resulting surface features size (Manga, 1997).

3. Brine mobilization (Head and Pappalardo, 1999; Collins et al., 2000; Pappalardo and Barr, 2004; Kargel et al., 2007) is explained by rapidly freezing sea ice trapping salts within the ice structure. Slower-freezing ice rejects brines from the crystal structure (Head and Pappalardo, 1999). As seen under Antarctic ice, when sea water freezes into sea ice, the slow process releases the salt into the surrounding water, creating super-salty brine. The brine percolates through cracks in the ice into the sea water below the ice. Being denser and much colder than the surrounding water, the brine sinks and causes the sea water to freeze on contact. This rapid freeze traps the brines in an ice stalactite, or "brinicle" (BBC Nature video available at http://www.bbc.co.uk/nature/15835017). The uncertain variations in composition within Europa's icy shell may allow this type of brine mobilization which could contribute to buoyancy variations between plates and the matrix (e.g., Pappalardo and Barr, 2004). Proposed heat sources to cause melt include diapirism or sub-surface heating at the base of the ice shell. Collins and Nimmo (2009) suggest a hybrid method of heating involving a basal heat source

enhanced by tidal heating. Large scale or localized pockets of mobilized brine could explain most forms of chaos through thermal and buoyancy variations.

4. Injection of liquid from the ocean directly into the ice shell (Crawford and Stevenson, 1998, Collins et al., 2000; Manga and Wang, 2007) with the assistance of exsolved gases to force widening of cracks (Crawford and Stevenson, 1998) or pressurized injection (Collins et al., 2000; Manga and Wang, 2007) would form sills of melt of 10m thickness and 10m of surface expression with the potential to drive small effusions of cryovolcanic materials, especially in cases where dikes extend from the shell to a pressurized ocean (Collins and Nimmo, 2009). While this model is not capable of explaining the observed morphologies of chaos without special circumstances, there are examples of similar, though smaller scale, occurrences on Earth which could be relevant for study. Figure 3-5 shows gases escaping from the base of Abraham Lake, Alberta, Canada. The rising bubbles are trapped as the ice thickens from the bottom; under pressure, the bubbles flatten into sill-like structures. Melting or cracking that exposes the bubbles releases the gas explosively; this could be an analog for cryovolcanic activity at Europa similar to the cryovolcanism described to form lenticulae (Fagents et al., 1998).
5. Impact modification could also explain some ice disruption. Exogenic heat sources such as impactors can affect the morphology of ice locally. Billings and Kattenhorn (2003) and Cox et al., (2005) suggest similarities between terrestrial explosion craters on floating ice (Figure 3-6) where small plates of the original surface are preserved in a slushy matrix that fills a hole left by impact. Collins

Figure 3-5. Methane bubbles trapped as ice freezes in Abraham Lake, Canada. The instability of the ice also results in crack propagation. [Photographer: Darwin Wiggett]

Figure 3-6. Terrestrial explosion crater in ice resulting from the Chelyabinsk meteor airburst and subsequent meteorite falls, Russia, 2013. [Environmental Protection Agency]

and Nimmo (2009) point out several large impact structures that penetrated the ice shell; the crater morphologies are preserved without noted chaos textures that differ from their surroundings. This lack of chaos suggests that impact may not always lead to matric disruption. Also the variation in crater size and preservation indicates that the thickness of the ice shell may vary over the entire surface. No correlation between crater depth and disruption level (i.e., amount of melt) is possible due to the low density of craters.

Given the geographical associations between chaos units and their gradational boundaries, there is reason to suspect that heat regimes across those boundaries could be similar. In fact, Collins and Nimmo (2009) suggested that brine mobilization should be capable of explaining all types of chaos formation. However, the textures and morphologies of chaos units are varied enough to acknowledge that heat regimes in different geographic locations should be different enough to produce those varied morphologies. There is sufficient evidence to suggest that lenticulae form by diapirism. Merging of diapirs could easily result in the gradation of lenticulae to microchaos (cf. Greenberg, 1999; Prockter et al., 1999a). Low albedo material upwells and floods small areas of the surface, eventually spreading to larger areas and resulting in the dark material that signifies more mottled or chaotic terrains. The appearance of fractured chaos suggests a mechanism more in line with partial melting, perhaps initiated by diapirism, where low albedo material floods inter-ridge topographic lows. As Collins and Nimmo (2009) suggest, brine mobilization seems the most likely scenario for the formation of platy and blocky chaos and, by extension, subdued chaos as these three units are evolutionary gradations. This relaxation may be due to continued infill and embayment of

the matrix material. It is important to note that each of these proposed mechanisms depends on a heat source and most acknowledge similar heat sources. If turbulent convection is expected in the liquid layer, all of these mechanisms may be operable simultaneously. If the ice sheet is thin and fracturing is concentrated where the ice is most brittle due to tidal flexure, crack propagation downward through the ice would alter the thermal regime, focusing small diapirs or partial melting near the fractures. The concentration and distribution of salts within the ice and liquid layers then controls the density of the ice and leads to elevation differences.

3.3 Ridges

The formation of ridges is addressed by collectively considering all ridge types: single or double ridges, ridge complexes, and the ridged plains. The morphological similarities suggest similar mechanisms controlling their formation such that other authors have considered processes that could explain all types of ridges (see review by Prockter and Patterson, 2009). In this case, mapping results support the notion that similar processes may control all types of ridges; however, mapping does not preclude that multiple processes are at work. Methods of ridge formation include the following models:

1. Cryovolcanism could produce materials which would accumulate over time to build levees of extruded material (Figure 3-7; Kadel et al., 1998; Fagents et al., 2000). Kadel et al. (2000) revisited their cryovolcanic theory and determined that highly symmetric and continuous deposits over the long distances typical of ridges were unlikely. However, if a relatively homogenous volume of gasses and salts are dissolved in the upper few kilometer of the ice shell, fracturing, along with any process that results in heating at the trough, would allow the exsolution

Figure 3-7. Lava levee. A fissure in the Mauna Loa volcanic field allows the buildup of levees on both boundaries due to the quick cooling of ejected lava. The symmetry of Europan ridges is similar to these levees though the extreme lengths of the ridges requires special formation conditions. [USGS/HVO]

of those gases and salts. This would most easily explain spectral differences between the trough and ridges or ejecta on the outer edges of the fractures. Levees to build the ridges are best explained by contraction and extension to provide pressure for uplifting material.

2. Incremental buildup or wedging (Turtle et al., 1998), in which cracks propagate upward from the ocean into the ice, opens a conduit for liquid to be injected into the cracks from beneath. This model adequately describes the morphology of simple ridge forms but is not as successful in describing ridge complexes (Prockter and Patterson, 2009). Related processes have been described on Earth. A simple example is that of ice needle formation, where subterranean liquid is forced to the surface through capillary action at which time it freezes and builds a column or levee of ice needles. Alternatively, frazil ice may form in the liquid layer due to supercooling or rapid pressure loss at the base of the ice layer; turbulence then mixes the liquid and ice, allowing the ice crystals to adhere to the faces of the fractures (Figure 3-8).
3. Upwarping could result from linear diapirism (Head et al., 1998a, 1999) in a similar fashion to lenticulae formation but with elongated diapir expressions. However, ridge complexes with multiple ridge sets cannot be explained by a single linear diapir and the consistent spacing of ridges in complexes is unlikely to be explained by evenly spaced linear diapirs.
4. Compression along fractures (Sullivan et al., 1998; Patterson et al., 2006; Tufts et al., 1999; Kattenhorn and Hurford, 2009) could explain buckling of material to produce a washboard pattern of nonoverlapping subdued ridges (as in Figure 3-

Figure 3-8. Frazil ice forms beneath the water surface, then adheres to solid surfaces or moves along with turbulent flow in Yosemite Creek. [National Park Service]

9). This model requires a thin brittle lithosphere and is more suited to describing the ridged plains than individual ridges.

5. The tidal pumping model (Pappalardo and Coon, 1996, Greenberg et al., 1998; Tufts et al., 2000) advocates repeated opening and closing of fractures controlled by diurnally varying stress fields. A trough would be opened during tension, allowing liquid to flow upward. As the liquid is exposed, it freezes into slurry. During compression, the trough would be forced closed, pushing the slurry out of the trough and into a pile at the margin of the trough similar to pressure ridges in arctic sea ice (Figure 3-10). Through repeated operation, this process could build double or multiple ridge sets and possibly even some bands (Tufts et al., 2000). This model presents similar problems to the melting model for chaos: it requires maintained exposure of liquid water at the surface and the narrow opening expected with the current understanding of stress fields may not be sufficiently wide to provide enough force to push the material upward. Prockter and Patterson (2009) provide an assessment of these conditions and suggest that additional processes could be combined with tidal pumping to meet the requirements for extruding material in this manner.
6. Shear heating could provide thermal buoyancy during strike-slip motion in the way of frictional heating (Gaidos and Nimmo, 2000; Nimmo and Gaidos, 2002). Warm ice melted from fracture walls by the friction would rise to form ridge crests. This model explains the uniformity of ridge morphology; in addition, repeated episodes could build more complex structures (Prockter and Patterson,

Figure 3-9. Ice ridges on the Antarctic ice sheet. These ridges are generally non-overlapping and subdued compared to other ridge types. [Photographer: Stephen Hudson.]

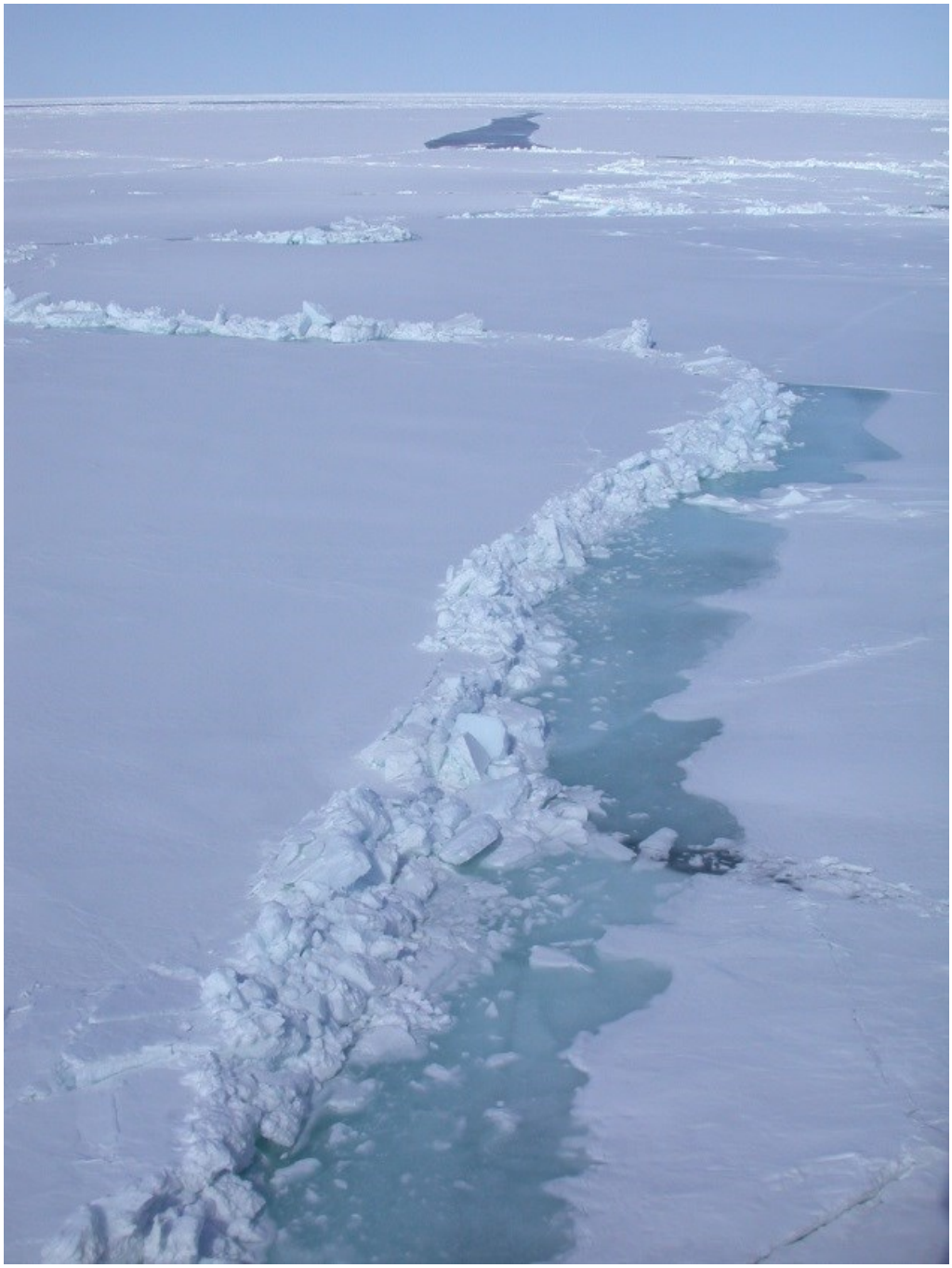

Figure 3-10. Pressure ridge in the Arctic. [NOAA; Photographer: Hajo Eicken]

2009). An advantage of this model is that it does not require fractures to penetrate the entire thickness of the ice shell to provide a conduit from the ocean.

Ridge complexes or ridged bands likely undergo a similar mechanism to double ridges. They may form by successive buildup of individual double ridges within a confined region (Geissler et al., 1998; Greenberg et al., 1998; Figueredo and Greeley, 2000). Mapping results support the theory that active ridges may transition into ridge complexes (Belton et al., 1996; Manga and Sinton, 2004). This interpretation can be supported by the tidal pumping and shear heating models. Aydin (2006) questions whether all ridges would eventually develop into ridge complexes and suggests that zonal conditions lead to the formation of complexes. Though this idea is presented as a rebuttal to the transitional relationship between ridges and complexes, it does not definitively preclude the relationship.

Multiple authors have discussed the possible transition of tectonic deformation over Europa's history (see reviews by Prockter and Patterson, 2009 and Kattenhorn and Hurford, 2009 and references therein). They propose that Europa's shell has thickened over time therefore changing the style and intensity of deformation from one of multiple overprinting episodes (i.e., ridged plains formation) to one where single features are preserved and other styles of resurfacing (i.e., chaos formation) become more common. Mapping results support this interpretation and stresses that ridge formation, in any style, continues through most of Europa's visible history. Further analysis of ridge relationships to other materials is needed to more confidently relate formation processes to particular formation times. For example, it may be found that linear diapirism may be a potential explanation for ridges that are confined to regions with high densities of lenticulae, which

likely form by a similar process. This type of relationship would correlate formation processes across multiple unit types.

3.4 Bands

A high number of bands appear to be dilational as indicated by the evident margin reconstruction to close the band (Schenk and McKinnon, 1989; Pappalardo and Sullivan, 1996; Sullivan et al., 1998). These dark bands have been interpreted to form by one of the following mechanisms:

1. Fracturing of a brittle surface layer overlying a ductile subsurface allows subsequent rifting and infilling (Pappalardo and Sullivan, 1996; Tufts, et al., 1999, 2000; Prockter et al., 2002),
2. Tidal pumping due to cyclically varying tidal stresses results in cracks dilating and closing while liquid water freezes and is pushed onto the surface (Pappalardo and Coon, 1996, Greenberg et al., 1998; Tufts et al., 2000). Just as in the discussion of ridge formation, this model can be applied to band formation; repeated opening and freezing cycles form additional sets of ridges. With relaxation, the band's internal morphology of ridges becomes subdued. Prockter and Patterson (2009) reviewed the potential for the tidal pumping model to produce bands, especially as their formation is constrained in time while the formation of ridges by a similar process is not constrained in time. They summarize findings that ice thickness, porosity, and compositional variation would need to be taken into account to confidently assess this method of formation.
3. Mid-ocean ridge spreading on Earth forms morphologies similar to the internal morphologies of bands with a central trough, bounding parallel lineations, and

hummocks (Figure 3-11). This similarity led to the proposal that a similar mechanism occurs on Europa (Sullivan et al., 1998; Prockter et al., 2002; Stempel et al., 2005). These proposals consider differences in morphology between bright and dark bands to potentially represent the velocity of spreading; faster spreading creates morphologies similar to smooth bands.

Bright bands, which disrupt pre-existing terrain, are interpreted to result from

1. dike intrusion of uncontaminated icy material (Lucchitta et al., 1981),
2. contraction and rapid relaxation of the thin surface (Schenk and McKinnon, 1989; Greenberg, 2004), or
3. dextral shear with extension due to strike-slip offsetting which must be controlled by nonsynchronous rotation and diurnal stress (Prockter et al., 2002; Kattenhorn, 2004; Geissler et al., 1998a).

Bands may represent a transitional mechanism which exploits pre-existing fractures or develops in a progression along with ridged bands, ridge complexes, and ridges. Each proposed mechanism correlates with the observed features of one or few examples, so determining a single formation model that could be responsible for all band formation is impossible without further observation. However, the idea of a spreading and buoyancy model with a brittle surface layer applies to almost all dark bands. The understanding that diurnal stresses and tidal flexure resulting from Europa's slightly eccentric orbit around Jupiter provide the opportunity for both contraction and extension effects supports a transitional regime.

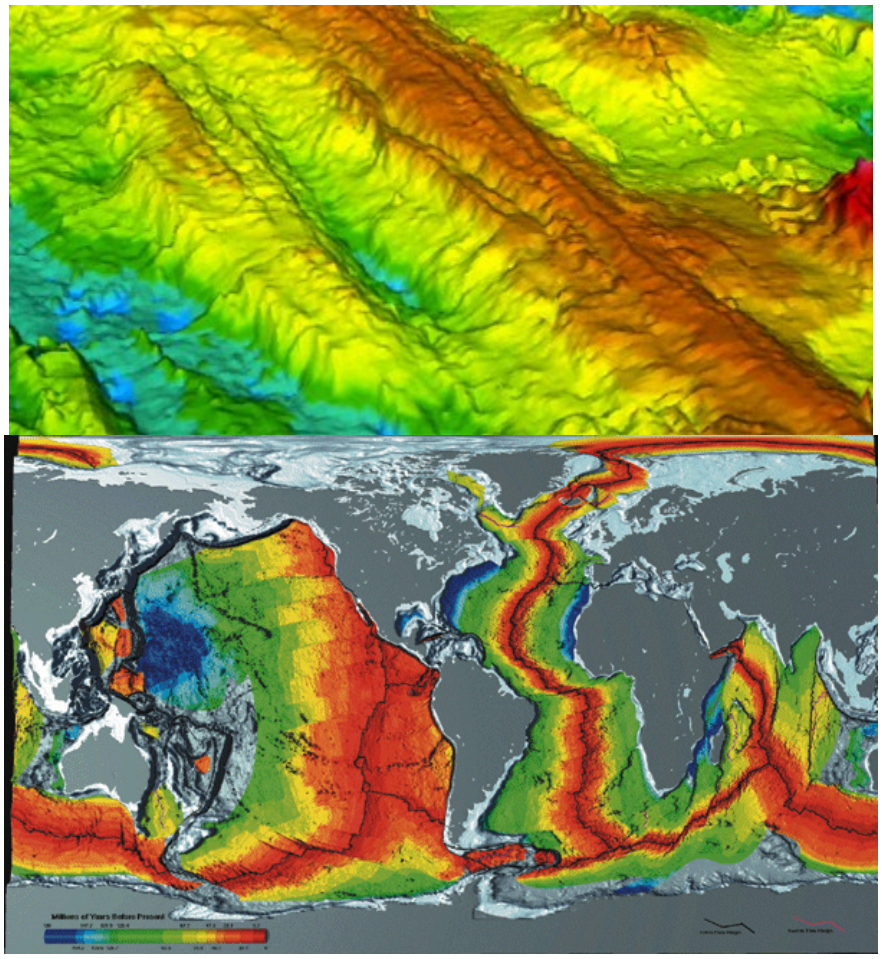

Figure 3-11. Top: Bathymetric image of the East Pacific Rise. Highest elevations are indicated in red; low elevations are in blue. Note the double ridge structure. [Image courtesy of Haymon et al., NOAA-OE, WHOI] Bottom: Seafloor spreading is evident at crustal plate boundaries; young, higher elevation spreading centers (red) are bounded by older materials. [NOAA]

3.5 Implications for the Ice Shell

Given the morphologies and stratigraphic or evolutionary relationships between geologic units outlined in Chapter 2 and the associated origins debated here, it is possible to speculate on the current condition or resurfacing history of Europa's ice shell.

The prevalence of lineaments indicates that the majority of the ice shell is brittle; tidal flexing may be all that is required to fracture the surface as this would induce episodic expansion and contraction, i.e., tidal pumping, to produce pressure features. This type of cyclic action would also induce shear heating that would, in turn, melt material along fracture walls; shear heating does not require that fractures penetrate the entire thickness of the ice shell.

Distribution of salts within the ice layer may play an important role in regulating the heat flow required for certain morphologies to form. Most likely, the salts are trapped in brine pockets or between layers of ice. Given that the depths of lineaments are globally consistent and that all appear to exhibit the same composition within their troughs, it may be possible that multiple individual layers of ice bounded by layers of brine, make up the total ice layer. This would be consistent with all fractures penetrating to the outermost, most brittle ice layer and brine layer but not downward through the entire ice sheet.

Mapping results support the interpretation that the ice shell has thickened over time, allowing the formation of fewer lineaments at present than during the early Balgatanian and Argadnellian Periods. Thickening, in turn, results in a less brittle shell, thus any lineament formation would require higher stresses. A thicker shell over time also forces a change in heating regime. The stratigraphically young chaos regions indicate a change in heating regime from frictional heat within lineaments to convective heat exchange across

the ocean-ice boundary. Lateral variations in the shell thickness would account for the apparent geographic association between chaos regions. Partial melting to allow brine mobilization and diapirism best explains the formation of chaos regions; the intensity and extent of diapirism is controlled by the intensity of convection within the liquid layer. Over time, more intense localized heating could allow complete melt-through, eventually resurfacing the entire satellite.

3.6 Discussion

By illustrating that features on Earth similar to those described for Europa can be formed by multiple processes, this work serves to outline that no single process is necessarily solely responsible for the formation of all related features. The reader should keep in mind that the structure and thickness of the ice shell, ocean, and interior layers is not well constrained. Some of the processes described above require a uniform thickness or method of heating. Neither of these conditions is known for Europa; as with Earth, there may be significant variations in heat source and propagation, ice thickness, ocean depth or composition, and convective regimes. These differences would result in variations in the processes that form individual features. Continued observation and exploration of Europa is necessary for constraining formation mechanisms further.

CHAPTER 4

CAPABILITIES OF AUTONOMOUS FEATURE AND EVENT DETECTION

4.1 Autonomous Science

Recent exploration of autonomous operations and data processing has led to the development of a wide range of algorithms aimed at conducting specific tasks: facial recognition, vehicle tracking, and urban heating monitoring are terrestrial examples familiar to the reader. Monitoring campaigns for water usage, vegetation growth or recession, ice sheet expansion or recession, atmospheric weather pattern tracking, or surface mapping are other terrestrial examples of how autonomous algorithms can be applied. In general, these objective studies require repeated observations over short time scales and some method of comparing stored and new data. For these terrestrial examples, communication relay times are minimal such that data storage can take place on the ground while an Earth orbiting satellite takes and relays new data for comparison. Fast processing times allowed by non-limiting computing resources enable real-time analysis and determinations of change.

Similar methods of observation for other planetary bodies and phenomena have been attempted in limited measure due to the severely constrained computing resources onboard spacecraft. Therefore, most analysis for feature or change detection occurs on the ground over long time periods long after the data has been acquired. The ability to conduct this processing in real- or near-real time onboard the spacecraft, given appropriate resources, would enable additional science observations. New science questions that could be addressed with a form of autonomous processing are: How quickly is material in the plumes of Io ejected? Do Io's plumes change over short time

scales? What is the time scale of thermal changes or crack expansion at Enceladus' south pole? Can individual surface features be monitored for change over the period of a single mission? Can new plumes be detected in real time? What are the detailed characteristics of targeted features? Each of these questions requires a long sequence of observations that demands a high volume of spacecraft resources that would otherwise be directed away from other observations. Can a single observation be a trigger for recording data from other instruments or for retargeting future observations to reobserve?

The necessity of repeated observations limits the science goals that can be accomplished in any mission. A method of processing those observations onboard and relaying only pertinent information that results from the processing, rather than relaying all data obtained, frees resources to accomplish other goals. The methods of autonomy discussed below all require the integration of large datasets. Particularly in the case of requiring a comparative database to be stored onboard for reference during processing, the issue of memory usage constrains other activities onboard, making it essential that processing use limited resources.

4.2 Detectable Events and Their Significance

Spacecraft missions to the outer solar system have identified active yet transient geophysical events on multiple bodies including explosive and effusive eruptions on Io (Morabito et al., 1979), geyserlike ejections on Enceladus (Hansen et al., 2005, Johnson et al., 2005, Saur et al., 2005, Spencer et al., 2005, Spencer et al., 2006) and Triton (Smith et al., 1989, Soderblom et al., 1990), and outgassing of comet nuclei (e.g., A'Hearn et al., 2011). These discoveries have been largely serendipitous; the very nature of the activity limits the ability to predict its presence, location, timing, and duration. The

uncertain nature of the activity necessitates an understanding of the limitations of its physical characteristics (e.g., size, diffusivity, vertical extent, and shape) that are detectable in future observations.

These phenomena provide constraints for subsurface processes, interior dynamics, surface-interior interactions, and models of composition for each respective satellite (Smith et al., 1979; Lopes-Gautier et al., 1999; Porco et al., 2006; A'Hearn et al., 2011). Characterizing the events requires sustained or repetitive observations that are both memory and bandwidth depletive (i.e., Clark, 2007). With few exceptions (i.e., Smith et al., 1979), such long observation sequences and sequences taken under repeated viewing conditions have proven to yield a large portion of images which, while scientifically valuable, contribute little to no significant additional information when compared to other similar images.

4.2.1 Plumes: Characteristics, Mechanics

Two types of volcanic plumes have been identified (Figure 4-1; McEwen and Soderblom, 1983; Lopes and Spencer, 2007) on Io where they were first predicted and discovered. One class is smaller plumes reaching heights less than 100km. These are optically dense and eject sulfur dioxide rich gas and dust. These plumes are fountain to umbrella shaped and the area near the source region is the most optically dense (Lopes and Spencer, 2007). The Prometheus plume is the archetype of this smaller dust plume class; its source is known to migrate. Kieffer et al. (2000) suggest that the plume results from hot silicate lavas interacting with the icy sulfur dioxide substrate. The plume source is also associated with an advancing lava flow (McEwen et al., 1998) and smaller plume-like jets at the flow margin (Milazzo et al., 2001). Larger plumes reach heights up to

400km, are faint and diffuse, and form shield-shaped dust streams. The archetype of this class is the Pele plume; Pele's source appears to be an overturning lava lake that exposes hot lava and releases sulfur gases. Tvashtar is the largest plume of this class. A third class, called stealth plumes (Johnson et al., 1995), lack high quantities of dust and are only visible during eclipse as auroral emissions (Figure 4-1). These plumes are understood to occur explosively either ballistically, where erupting gases decompress to a pressure near the ambient or by shock, where the vent gas pressure is significantly higher than the ambient (Cook et al., 1979; Strom et al., 1981; Kieffer, 1982; Strom and Schneider, 1982).

Plumes on Enceladus are jets or geysers of water vapor and ice originating from long narrow fissures at the southern pole (Figure 4-2; Porco et al., 2006; Waite et al., 2006; Hansen et al., 2006). Just as tidal stresses from Jupiter keep Io warm enough to produce high temperature volcanism, it now appears that tidal stresses from Saturn may control the volume of material produced in Enceladus' geysers. While Enceladus is at its apocenter in its slightly eccentric orbit and therefore under tension, the plume source is brighter, indicating an increased production of plume material (Hedman et al., 2013).

Other types of plumes are visible at Triton and multiple comet nuclei (Figure 4-3). Triton exhibits approximately 50 plumes, visible as 'wind streaks'. These streaks provide a characteristic morphology and albedo that could be distinguished with a feature recognition method. Comet outgassing to form a coma has been imaged at high enough resolution to reveal individual jets supplying that material to the coma. These jets are similar in appearance to Enceladus' jets, though at a smaller scale.

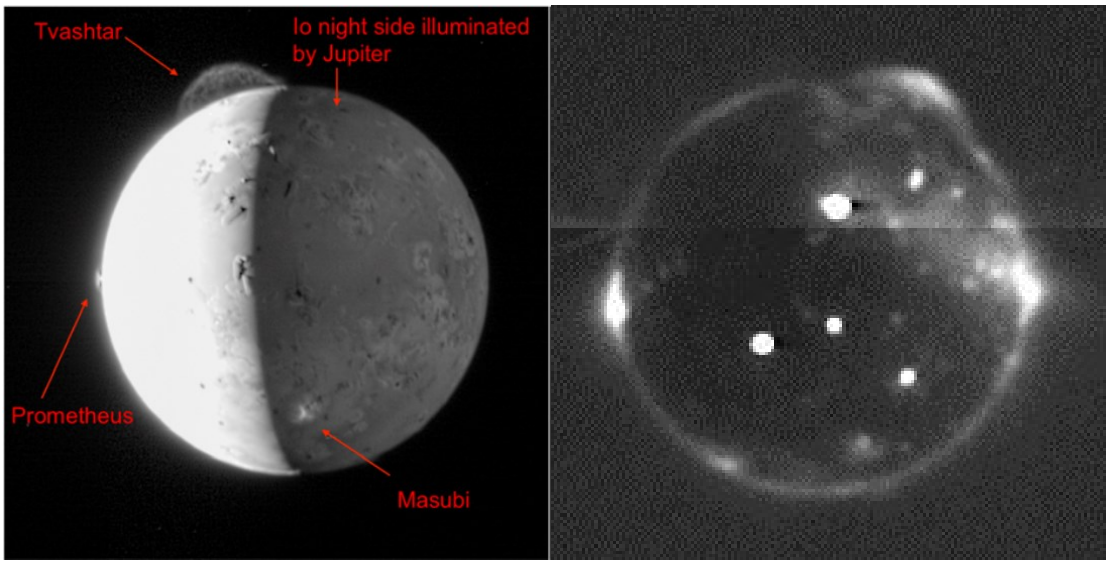

Figure 4-1. Left: Volcanic plumes on Io are grouped into two main classes: small, optically dense, umbrella shaped plumes like Prometheus and larger, diffuse, shield shaped plumes like Tvashtar. Right: Io in eclipse reveals many smaller plumes that lack a significant portion of dust. The brightest points are the glow of incandescent lava (Pele is at left center); the edge of the disk shows the auroral glow and is denser over active volcanoes (Tvashtar's plume is at top and the equatorial bright edges are magnetospheric effects); the smaller plumes are diffuse glows. [NASA/JHUAPL/SwRI]

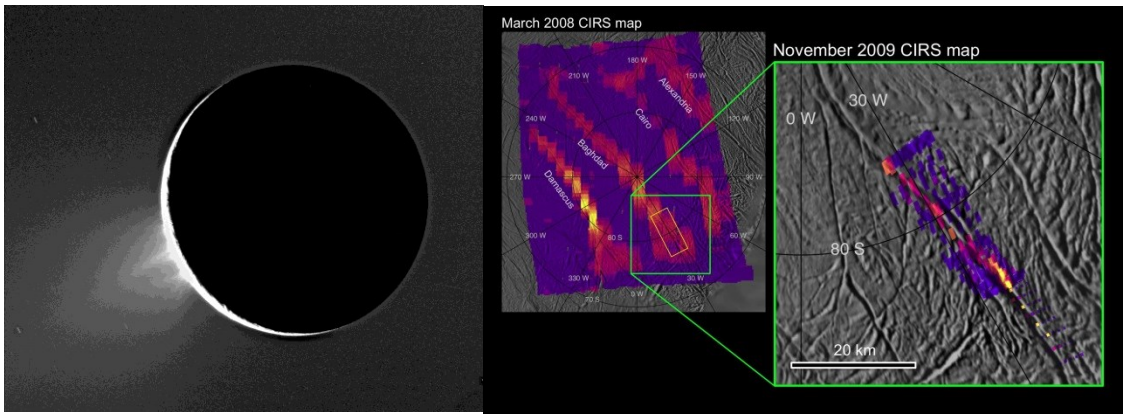

Figure 4-2. Left: Southern polar geysers on Enceladus are best viewed in reflected light; Right: Cassini Infrared Spectral Mapping reveals temperature differences aligned with fractures which have been determined to be the source points of the geysers. [NASA/JPL/GSFC/SwRI/SSI]

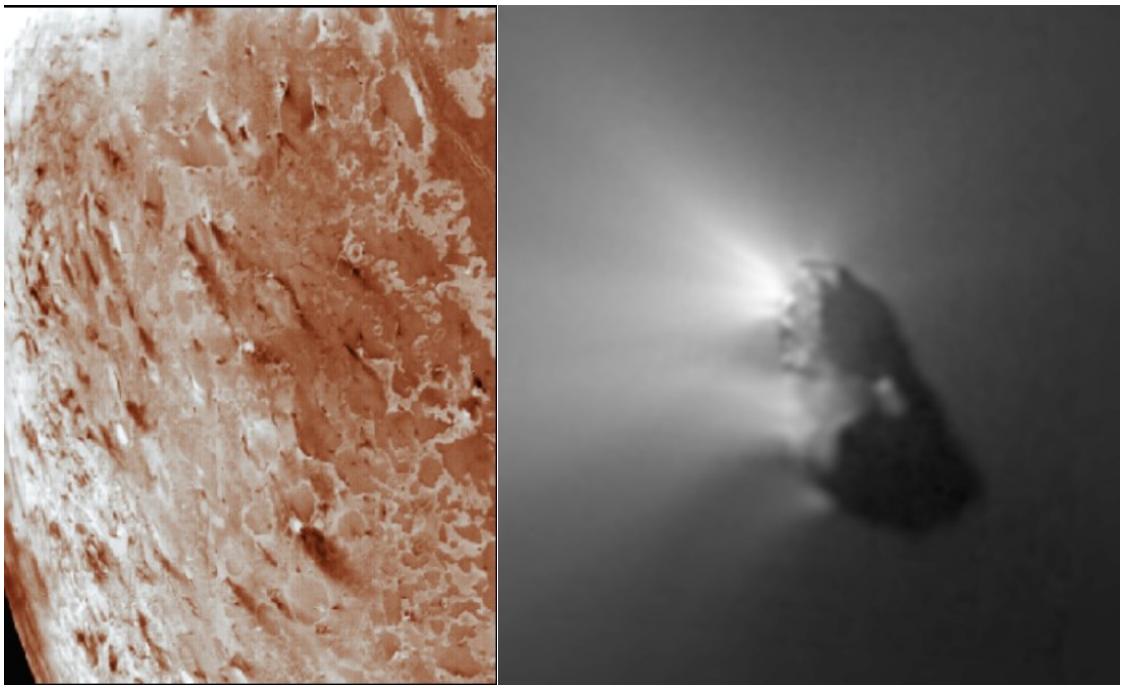

Figure 4-3. Plumes and wind streaks on Triton and jetting to supply the coma of Comet Halley. [NASA/JPL]

4.2.2 Surface Change

Surface deposits emplaced by plume fallout are defining characteristics of plumes on Io. Activity can be inferred by changes in color (i.e., Figure 4-4), intensity, and shape of these deposits, as well as by the changes attributed to frost deposits. The plumes and their fallout contribute to the resurfacing of Io's entire surface; the explosive eruptions indicate composition of the interior. Similar, though much smaller scale color changes are observed elsewhere. Triton's plumes deposit dark material in streak patterns (Figure 4-3); no repeat observations are available to determine changes. Europa's bands are interpreted to brighten over time and chaos regions are interpreted to darken over time; additionally, ridge flanks may be brightened due to frost deposits or darkened due to the emplacement of low albedo material. These changes, however, are not associated with highly contrasting colored materials.

4.2.3 Features Classes

Observation of the outer solar system bodies reveals stark contrasts between features as they exhibit such varied morphologies. Particularly for Europa, the appearance of lineaments is extremely different from the appearance of chaos materials; these in turn are different from the ridged plains background. The ability to autonomously distinguish each of these feature types from one another could allow onboard mapping of the surface at low to medium resolution. Comparison with a database map could reveal surface changes by the formation or motion of large features such as the expansion of chaos regions.

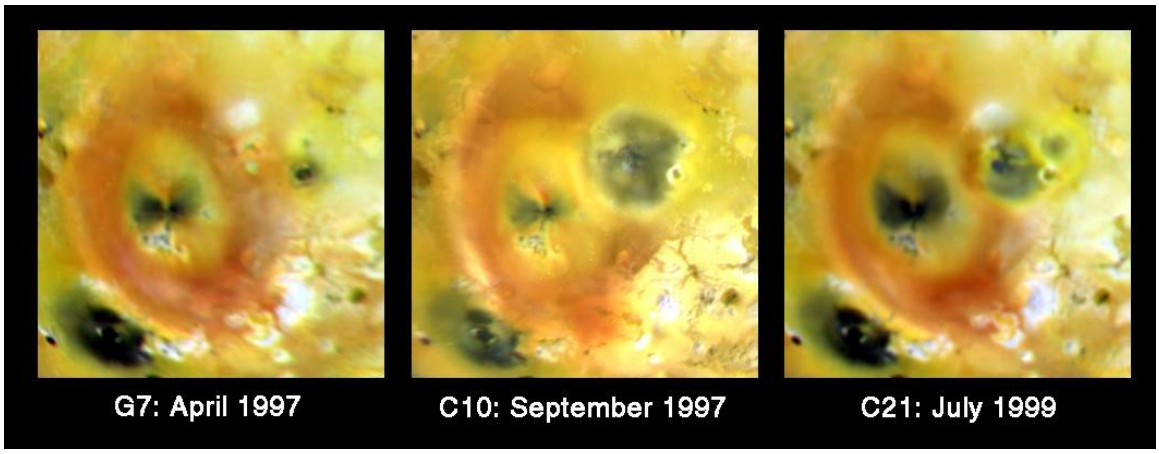

Figure 4-4. Changes to the Pele and Pillan plume rings over time. Eruption of the Pillan center develops a dark ring that obscures Pele's red ringed deposit; then additional deposition of Pele's ring superposes the Pillan deposit. [NASA/JPL]

4.3 Necessity for Autonomy

The ability to process observations onboard could facilitate monitoring campaigns and optimize the science value of returned data by preserving severely limited spacecraft memory and bandwidth for high priority observations. Images could be obtained at a high rate, ensuring the highest probability of capturing events. These images could then be processed onboard for the detection of events with certain characteristics. Only the relevant images with successful detections would be saved for downlink, thereby overcoming the critical memory and downlink limitations suffered by many spacecraft. In addition to preserving downlink bandwidth, a motivating benefit to onboard analysis is the opportunity for reactive operations. Given the highly unpredictable nature of geophysical events and the long reaction time demanded by ground processing and subsequent retasking of future observation sequences, any action to track or reobserve a dynamic event is only possible with onboard detection and the ability of the spacecraft to autonomously retask. Algorithms for automated response to events or feature detections such as enhanced Virtual Machine Learning (VML; Rabideau and Chien, 2009) would allow the acquisition of the most relevant data and possibly the use of complementary instruments. This type of prioritization can be applied to tour phase imaging and single rendezvous observations to enhance science, operations, responsiveness, and other aspects of mission productivity.

Overall, autonomous processing of data onboard a spacecraft using the methods discussed herein addresses one or more of three main issues:

1. Science Prioritization,
2. Resource Conservation, and

3. Reaction and Resilience.

Each of these issues must be addressed in future missions to explore unknown or uncertain environments with limited resources. The autonomous methods described herein illustrate the variety of uses for which autonomy has already proven useful and how these methods could be applied to detecting activity at Europa. Specifically, a selection of methods suitable for detecting plume activity, distinguishing feature characteristics and differentiating multiple types of features is explored. In addition, these methods are addressed in terms of how they might be useful in detecting changes between the time of previous observations and any future exploration.

4.4 Autonomous Methods in Use

Recent developments in similar onboard algorithms have been successfully applied to planetary and terrestrial missions. Algorithms in use aboard the Mars Exploration Rovers (MER) were able to detect dust devil activity using a method of background subtraction and identify clouds using a method of sky segmentation (A. Castano et al., 2008). Detections were flagged for priority downlink and manual examination. Algorithms currently in use onboard the Earth Observing One satellite (EO-1) use a variety of methods to detect explosive and effusive volcanic activity (Davies et al., 2007), to differentiate between surface materials (e.g., sulfur and ice; R. Castano et al., 2008), and to detect cryospheric changes (Doggett et al., 2006). As examples of how autonomous detections can trigger onboard decision-making and reactive maneuvers, positive detections for change or activity in all three of these cases trigger repeat imagery during subsequent overflights of EO-1.

The types of decision-making algorithms used onboard MER and EO-1 have also been tested with outer solar system data on the ground with excellent results. A superpixel endmember algorithm (Thompson et al., 2010), in which the mean spectra for segmented groups of spatially contiguous pixels are compared, can successfully expose Europa's spectrally salient features (Bunte et al., 2011). Edge detection algorithms can identify the planetary horizon and detect any ejected material that is reflective and extends beyond the sunlit limb (Bue et al., 2007; Thompson et al., 2011a,b). This method is able to distinguish the size of the protruding portion of volcanic plumes relative to spatial resolution of the image. A modification to the edge detection algorithm is sufficient to detect outgassing on non-ellipsoid targets such as comets (Thompson et al., 2011a,b).

Other applications of autonomous processing are also being utilized during ground processing of data. These could potentially be modified for use onboard in real time. A particular example is the use of a new automated stereo image processing software package (Broxton et al., 2009) designed by the Intelligent Robotics Group at NASA Ames Research Center which was intended primarily for use with the recently digitized Apollo Metric Camera Image dataset. Stereoimage pairs and digital elevation models (DEMs) were generated from Apollo 15 Orbit 33 Metric images which were not taken with the intent of use in stereo (Figure 4-5). These products were used to conduct a hypsometric analysis of slope distribution between lunar highlands and mare. This type of technology could be used in flight as a substitute for power intense altimetry experiments.

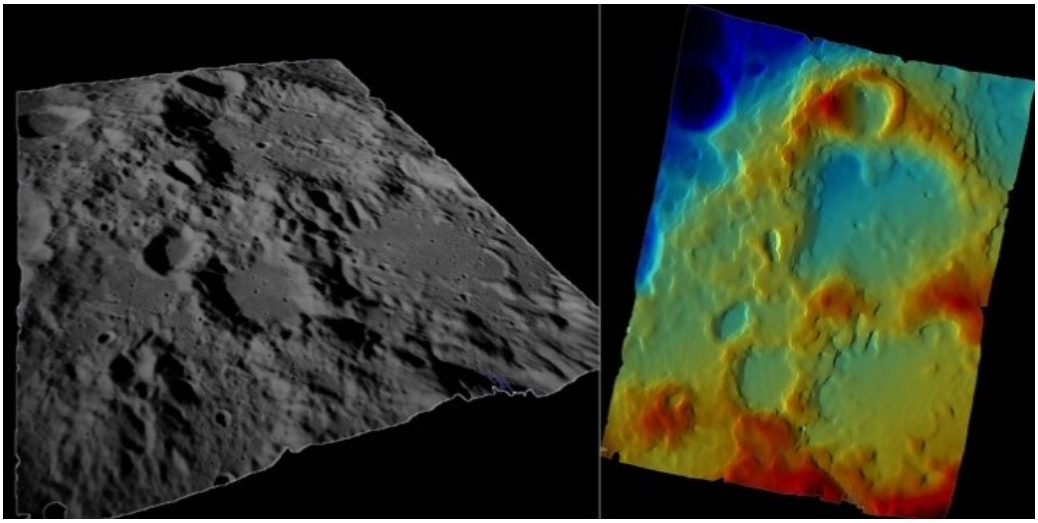

Figure 4-5: Stereopair (left) and DEM (right) created from Apollo Metric frames AS15-M-0081 and AS15-M-0082 using new stereo image processing software. [Images courtesy of M. Broxton, NASA-ARC]

4.5 Plume Detection Methods

Several algorithms were explored for their potential to detect geophysical activity by the specific expressions of volcanic plumes or outgassing. First, an edge detection method, which masks the planetary disk and searches for bright features at the planetary horizon, was tested for its ability to identify large plumes at the limb. Then, a supervised classification method was tested using a manually classified database of known plume characteristics as a comparison for the algorithm to identify plumes regardless of positioning. This method was developed further to apply to multiple types of feature detection.

4.5.1 Edge Detection

Bue et al. (2007) demonstrated the first algorithm for plume detection using a histogram analysis technique and edge threshold method and were able to detect 78% of plumes in the images they analyzed. The histogram segmentation depended on morphological analysis of connected high-intensity pixels used to define the edge of the satellite by fitting a least-squares circle to the limb points. Radial profiles of distances from the center of the ellipse to the most distant high-intensity pixel indicated the presence of a plume in the image; if the distance to the pixel was greater than the mean radius of the ellipse, a plume was present. Their false detection rate was 22%, though they noted the flexibility of the algorithm to set a threshold based on the desire for a certain percentage of positive or false detections.

This method was expanded upon by Thompson et al. (2012a,b). Using the Canny edge detection algorithm (Canny, 1987), the planetary horizon can be identified in an image. An ellipse is then fit to the horizon using the RANSAC method (Fischler and Bolles,

1981) which randomly samples points along the horizon which have high spatial derivatives to define the ellipse. Bright pixels that lie outside the ellipse are identified as plumes (Figure 4-6). Threshold values for locating plumes include a range of up to 10% of the planetary diameter and intensities greater than a threshold standard deviation above the mean background (of space). Thompson et al. (2012a,b) found that a threshold standard deviation of 0.5 was optimal for balancing detection and false detection rates; more lenient thresholds result in higher detection rates at the expense of increased false detections. This method was found to be useful in both processed and uncalibrated images; threshold settings allows for excluding imaging artifacts (Figure 4-7). The method was found to perform best when a majority of the planetary disk (>30%) was included for the RANSAC ellipse selection; lower percentages of visible disk resulted in incorrect disk fit due to an insufficient number of pixels to define the ellipse. Other failures (Figure 4-8) typically involved cases of planetary glare or low signal to noise ratio and resulted in improper ellipse fits, precluding positive plume detection. In a selection of ~70 images which included sequences of single-band images of Io and Enceladus, 76.9% of images containing plumes generated a positive detection. 11 of 17 known plumes were detected; of these, plumes 2-3 pixels in height represented the minimum size limit for positive detection. There were no false detections. These tests suggest that image quality is a primary constraint on this algorithm's detection performance in addition to the disk visibility constraint.

Though the edge detection method is highly successful at detecting plumes that extend beyond the planetary limb with no false detections, this method alone is not sufficient for

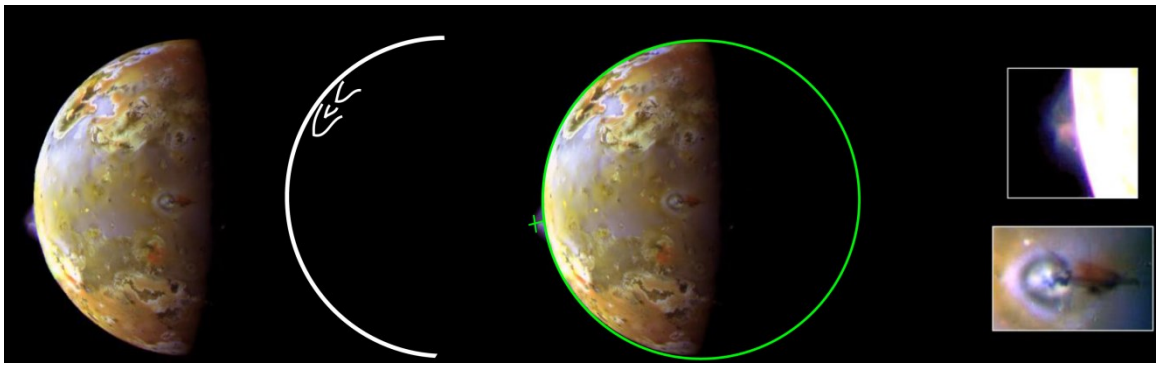

Figure 4-6. The edge detection method, *after* Thompson et al., 2012a. From left: Galileo image of Io; horizon defined by the Canny and RANSAC methods also identifies sharp edges of high contrast in the disk image; best fit ellipse and positive detection; zoomed views of the Pele and Prometheus plumes visible in this image. The Pele plume on the limb is easily detected while the Prometheus plume viewed at nadir against the background surface is not. [Background Galileo images: NASA/JPL/Univ. of Arizona]

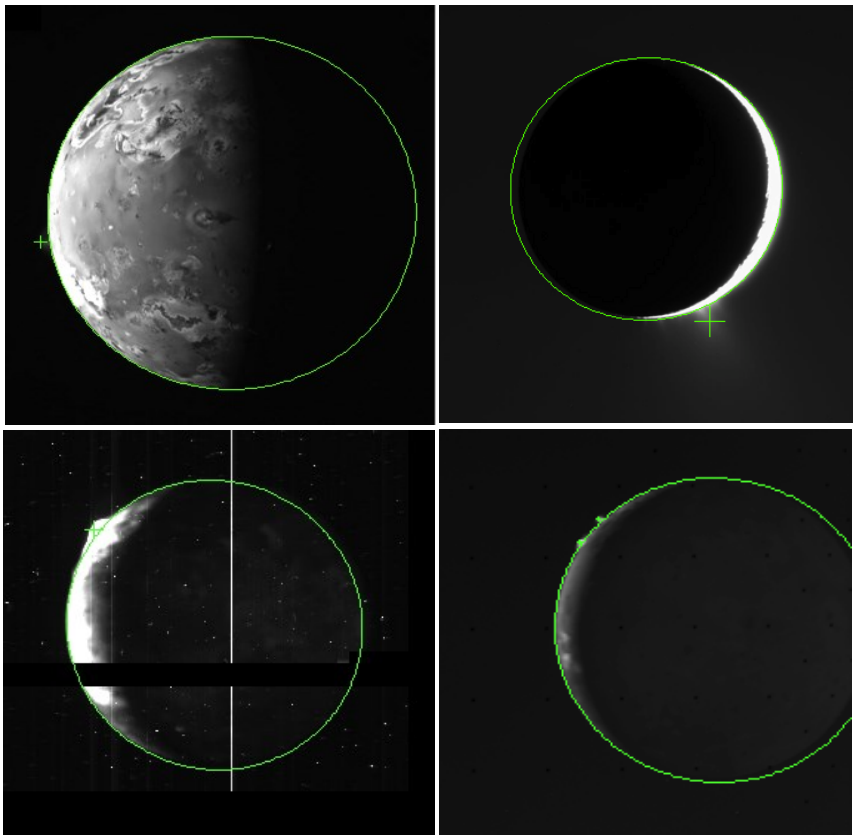

Figure 4-7. Typical detections with the edge detection method, *from* Thompson et al., 2012a. Green ellipses signify the best fitting ellipse; plus signs show the locations and sizes of positive detections. Clockwise from upper left: Io's Pele plume is detected; Enceladus' plume is distinguished from the planet glare in this processed Cassini image; multiple Ionian plumes are detected in this Voyager image with the smallest being less than 3 pixels in height; a positive detection in this Galileo image overcomes high noise and imaging artifacts. [Background images: NASA/JPL/Univ. of Arizona (Galileo); NASA/JPL (Voyager); NASA/JPL/Space Science Institute (Cassini)]

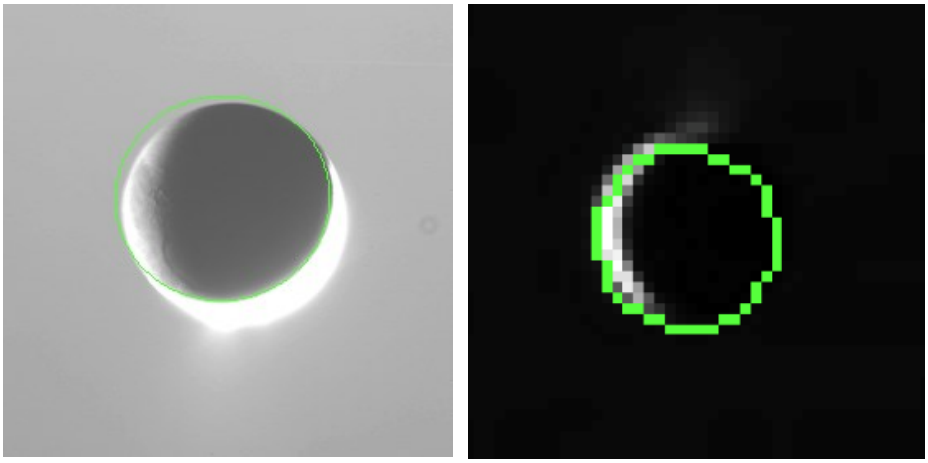

Figure 4-8. Typical failures of the edge detection method *from* Thompson et al., 2012a. Failures occur when the ellipse cannot be defined due to glare or an insufficient number of pixels. [Background images: NASA/JPL/Space Science]

detecting all plume activity. As Figures 4-6 and 4-7 show, plumes that are viewed at nadir against the background surface are not identified as they are masked during the horizon selection. Also, the lack of false detections can be viewed as a disadvantage if the target of observation exhibits an unknown level of activity. Allowing some threshold of false detections increased the likelihood of serendipitous detections in unknown conditions. To address the opportunistic detections and those of plumes not visible at the limb, other methods such as supervised classification are explored.

4.5.2 Supervised Classification

Combining feature extraction methods with supervised classification techniques overcomes limitations of other methods which require a single strong edge, limb-views, sequential observations, or similar views from multiple instruments. The following onboard processing technique analyzes images for the presence of any event that ejects material above the surface, does not require a limb view, and is capable of distinguishing characteristics of multiple features.

The method of detecting geophysical features outlined here are based on supervised learning computer vision methods in which an algorithm is trained to recognize specific characteristics that are first manually identified and classified. Supervised classification employs *a priori* knowledge of a site (i.e., R. Castano et al., 2008) and a set of images exemplifying that knowledge that can be used as development or training tools for the algorithm. In this application of the supervised classification technique known as Scale Invariant Feature Transform (Lowe, 1999), the identity of outer planet satellite surface cover materials and material ejected above the surface should be recognized based on a variety of previously observed characteristics. The focus is on the detection of transient

geophysical phenomena such as volcanic plumes, geysers, or outgassing. Object recognition in cluttered scenes requires that local image features be unaffected by clutter or partial occlusion and at least partially invariant to image transformations and viewing conditions. They must also be sufficiently distinctive to identify them among many alternatives. This approach transforms an image into a large collection of local feature vectors, each of which is invariant to image translations, projective distortions, and illumination changes (Lowe, 2004). A selection of images from the Voyager, Galileo, Cassini, New Horizons, and EPOXI missions is used to illustrate the approach and evaluate performance. Effectiveness, limitations, and applications of supervised classification detectors are also discussed.

Scale Invariant Feature Transform

The Scale Invariant Feature Transform (SIFT) is a computer vision algorithm which transforms image data into scale-invariant coordinates relative to local image attributes (Lowe, 1999). Following the method of Lowe (1999), manually identified features of interest must first be extracted from a set of reference images and stored in a database. The local image attributes of a new image are matched by individual comparison to the feature database. Candidate matches are selected based on the Euclidean distance between descriptive vectors for each attribute. False matches are common if there is no similar feature in the database. Correct matches are culled from the full set of matches by identifying subsets of keypoints that agree on several characteristics. A nearest neighbor approach to indexing is used to identify candidate feature models. When at least 3 keypoint descriptors agree on model parameters, there is strong evidence for the presence of a feature of interest.

Keypoints

Features are identified using a staged filtering approach. Each image is convolved using a Gaussian function similar to a low pass filter at different scales to generate a scale-space (Witkin, 1983). Motivation for generating a scale-space representation of data is that physical objects are composed of different structures when viewed at different scales. There is no way to know *a priori* what scale is ideal to qualitatively or mathematically describe the structure of any previously unobserved plume, so the most reasonable approach is to consider the description of a plume at multiple scales. A linear scale-space is most suitable to not introduce new structures at coarse scales that do not correspond to simplified versions of structures at fine scales (Lindeberg, 2008). Slight changes in the physical appearance of an overall plume are negligible compared to the difference in appearance of the entire plume with respect to the background image (Figure 4-9). The differences between successive Gaussian-blurred images are calculated. Locations that represent the extrema of the difference-of-Gaussian function (Lowe, 2004) are selected as candidate keypoints so that keypoints are stable at all scales in the image. This scale-space extreme detection can produce several thousand keypoints, thus creating a descriptor for each keypoint is necessary to assess the probability of a positive match and reduce the number of keypoints of interest.

Keypoint Descriptors

Each keypoint is used to generate a vector that describes the local image region relative to its scale-space coordinate frame. The magnitude and orientation of the change in gradient is calculated for every pixel surrounding a keypoint. As in Lowe (2004), a typical surrounding region comprises a 16 x 16 grid of pixels where a vector describing

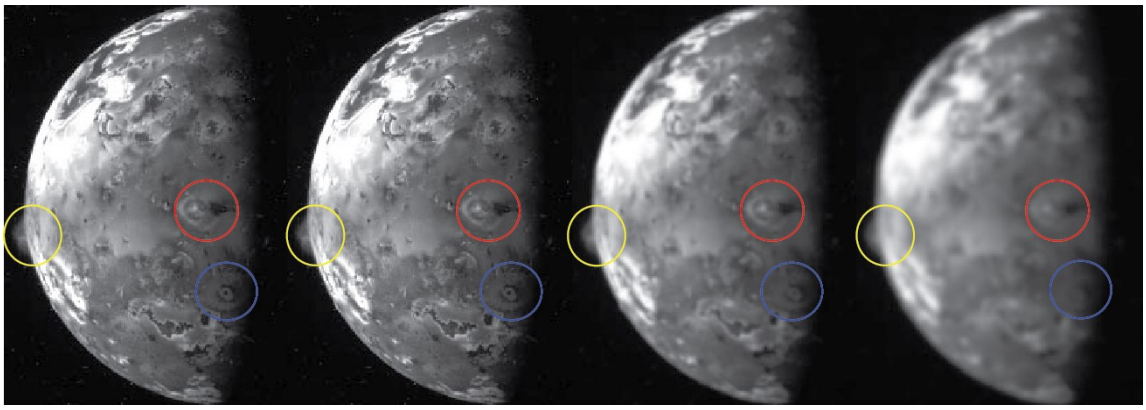

Figure 4-9. Gaussian scale-space for a typical image. The original Galileo image (left) is progressively convolved by multiples of a scale factor. Pixel values for the difference between each successive convolution are calculated; features which correlate to extreme values are selected as keypoints. Three geologic features are identified here. *Yellow*: The Pillan plume extends beyond the limb; its vent source is visible on the surface. *Red*: The Prometheus plume itself is not visible because it points directly toward the spacecraft; the material it deposited is a bright ring around the source and its shadow is visible to the right of the ring. Note that the shadow shares a similar appearance with dark flow features. *Blue*: The Culann ring deposit is also visible while the plume itself is not. Note that the ring is so much less distinct that in the final convolution it is almost indistinguishable. [Background Io image: NASA/JPL]

the magnitude and orientation of the gradient change is generated for each of the 256 pixels. An 8-bin histogram for each 4 x 4 sub-region is weighted by a Gaussian function dependent on the size of the region such that the overall keypoint descriptor is a vector of all values of the histograms (Figure 4-10). This results in a 128 element descriptor for each keypoint that is invariant to scaling, rotation, image location, illumination, and viewing geometry. Changing the array size can alter the detection accuracy. A larger array stores more information and may result in increased accuracy overall but may not be a significant improvement over smaller arrays relative to computing time needed for larger vector dimensions.

Classification with k-Nearest Neighbor

Using the *k*-Nearest Neighbor (*k*NN) classifier, a feature vector descriptor is classified based on the majority class of other features within a neighborhood defined by Euclidean distance (Cover and Hart, 1967). The best candidate match for each keypoint is found by identifying some set of its nearest neighbors in the database of manually classified features in training images where the variable *k* indicates the distance to the single nearest neighbor (k=1), the second nearest neighbor (k=2), or successively more distant neighbors. Figure 4-11 illustrates the method of majority class determination. *k*NN does not require a particular spatial distribution of feature vectors and is thus adaptive to unpredictable plume characteristics.

Analysis

The images examined with this method include spacecraft images of planetary bodies where plumes are known to exist. Specifically, this includes images of Io, Enceladus, and Comet 103/P Hartley 2 from the Voyager, Galileo, New Horizons, Cassini (released as of

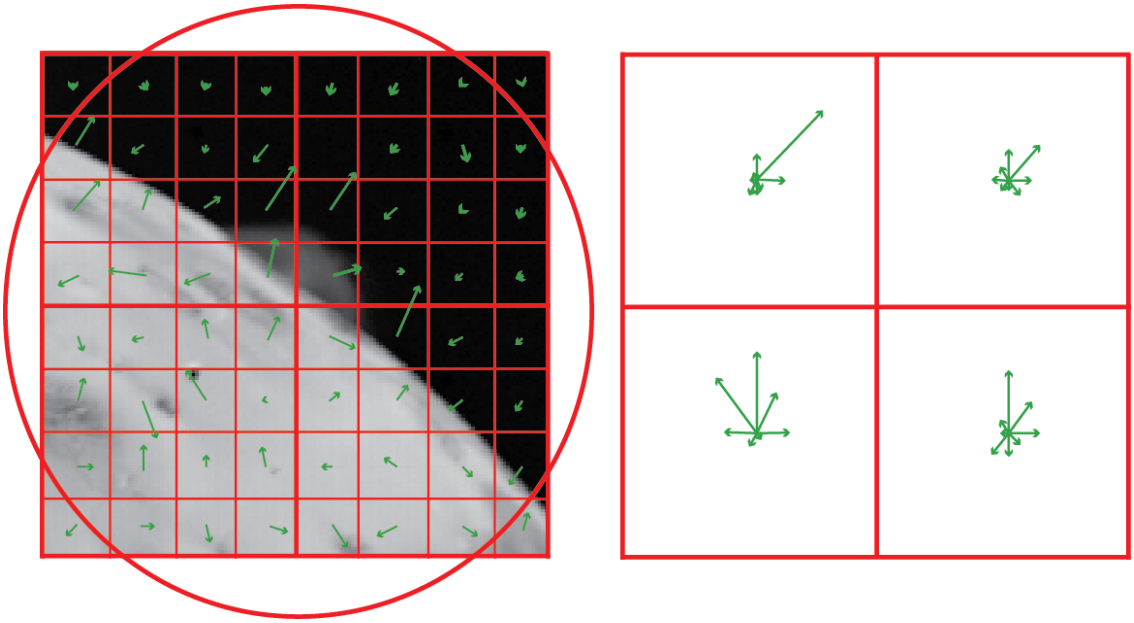

Figure 4-10. Stylized representation of keypoint descriptors (not to scale). A keypoint at the center of the circle is compared to other sample points within an 8x8 grid. *Left:* The gradient magnitude and orientation at each sample point near the keypoint are binned by subregion (here, a 4x4 grid) to generate orientation histograms *Right:* Arrow length corresponds to the sum of the gradient magnitudes near that direction within the region. Voyager image overlaid with keypoint descriptors *after Lowe, 2004.* The keypoint at the center of the grid would have an overall vector descriptor indicating that the Prometheus plume has a greater contrast to space than to the surface. [Background image: NASA/JPL]

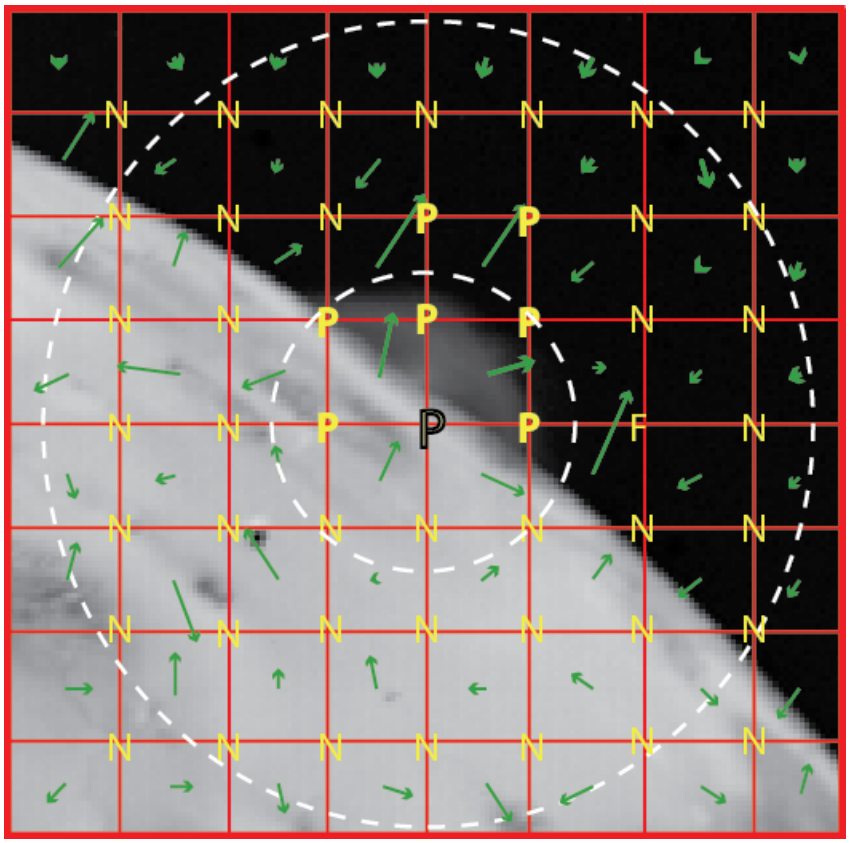

Figure 4-11. *k*NN Classification: In this example, each grid intersection should be treated as a single keypoint. The sample at the center of the grid is classified according to the most common class within the threshold distance, *k*. Within a 1 unit threshold (inner circle), the center keypoint would be classified as a positive feature, P. Within *k*=3 (outer circle), the most common class would be negative, N, and the point would be classified as N. Thus, a smaller *k* is most efficient for classification. An example of potential misclassification is shown: the point marked F (center right) shows an overall gradient similar to that defined for a plume; the true feature does not extend to this keypoint, thus this point may be classified as P when it should be N if *k* is too large. [Background image: NASA/JPL]

early 2013), and Deep Impact EPOXI missions in which plumes or outgassing have been manually identified. Uncalibrated images were used to simulate a range of onboard data conditions and feature characteristics prior to post-downlink processing that could enhance the appearance of features.

Images were subjected to the SIFT algorithm to generate keypoints and keypoint descriptors. Note that in examples presented here, the final image with positive SIFT features is produced using the image convolution where all features are most stable, thus the final image may not be at an aesthetically ideal resolution. The low number of images containing the desired characteristics compared to the overall number of images in all datasets examined necessarily limits the training set. To ensure that the training database included a statistically sufficient sample size to accurately represent the population of plumes, a random selection of 1/3 of the images were manually classified. Every keypoint descriptor was manually assigned a classification according to the presence or absence of the feature of interest. Positive features correlate to a visually identified plume; all other features are assigned a negative classification. The random selection is intended to ensure that the widest range of plume characteristics can be identified positively to build the most robust training database.

Descriptors for the remaining images were matched to the database descriptors using the *k*NN classification algorithm. A large majority of descriptors correspond to negative features such as surface material gradients and background noise, resulting in a high ratio of negative to positive features. This ratio dictates that a plume will be surrounded mainly by negative features, therefore the smallest k is most appropriate to classify a feature; k=1 best discriminates classes. Figure 4-12 illustrates the classification process.

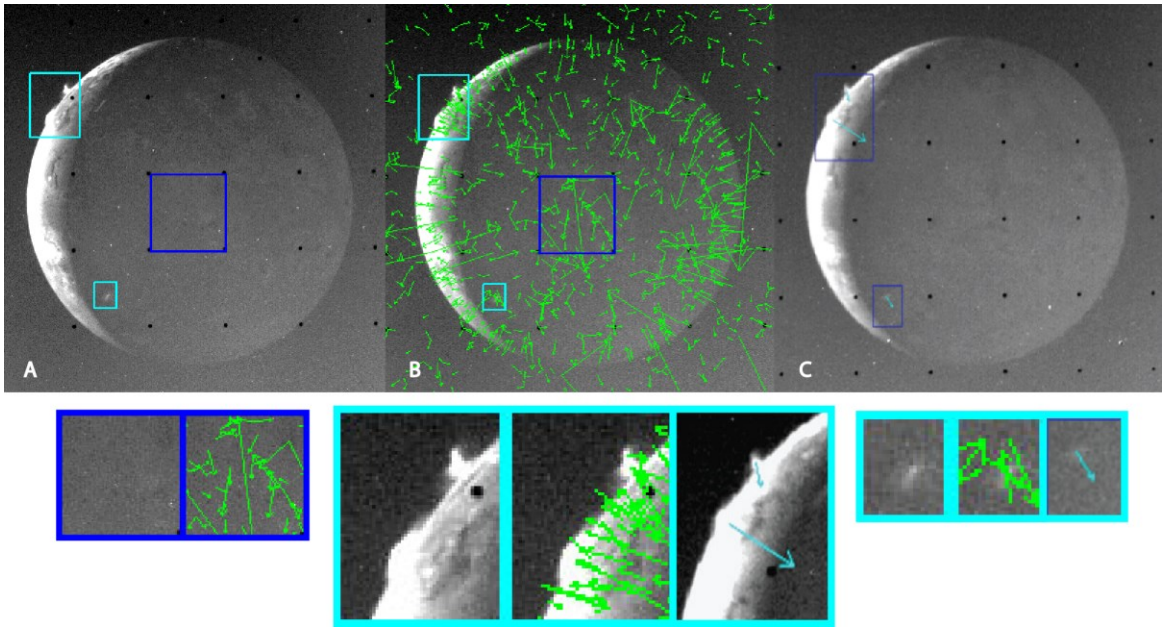

Figure 4-12. SIFT + *k*NN process. *A*: Original Voyager image of Io. Light blue boxes outline known plumes; dark blue box selects a random region of the image. *B*: Same image with SIFT keypoints (green arrows) prior to *k*NN. Refer to the insets with dark blue outlines to illustrate the diversity of keypoint vectors. *C*: Features detected by SIFT + *k*NN (blue arrows): Amirani (top) and Maui (bottom) plumes on the limb; Masubi plume at terminator in shadow. The zoomed insets show the progressive analysis for plume identification. [Background image: NASA/JPL]

4.6 Plume Detection Results

SIFT+*k*NN was applied to images of Io, Enceladus, and Comet Hartley 2 where plumes or jets can be manually detected (Table 4-1). This encompasses single-band images taken with the Galileo SSI instrument, Voyager and Cassini narrow- and wide-angle cameras, and the New Horizons LORRI instrument. Observations include sequential and non-sequential images; sequential images offer extremely similar views which serves to increase detection rates due to the nature of the SIFT algorithm. The selection of images used to test this approach is not limited by the amount of the planetary disk or limb that is visible or by the number or placement of strong edges that appear in the scene. The greatest limitation on the image appearance is the phase angle or degree of overexposure that may be present; a distinct albedo gradient is necessary to produce any keypoints. A unique training database was generated for each mission dataset.

SIFT features mainly resulted from surface material gradients and background noise, resulting in a high ratio of negative features to positive features in training. However, SIFT+*k*NN detected plumes of different shapes, sizes, and orientations. The most notable improvement over previous methods is the ability to detect features that do not extend beyond the planetary limb (Figure 4-13). Detections were successful regardless of noise and image artifacts but failed where plumes were lost in glare or classification failed. In all cases, false negatives occurred when plumes were less than 9 pixels in size regardless of position or orientation. Of all images containing plumes, ~73% generated at least one detection and 73-94% of overall plumes or jets were detected in each image set, making this algorithm comparable to edge detection methods. Detection rates for the

Table 4-1. Statistics of plume detection for each image set. These results were obtained using SIFT + *k*NN (*from* Lin et al., 2012).

Mission		**1st trial**		**2nd trial**	
	Test Images	**Detection Rate**	**False Detections**	**Detection Rate**	**False Detections**
Cassini	23	93.30%	27	88.20%	23
New Horizons	44	70.00%	55	74.29%	63
Galileo	11	67.67%	19	72.73%	18
Voyager	81	95.14%	160	92.47%	157
EPOXI	23	94.15%	Undistinguished	94.37%	Undistinguished

Voyager and Cassini datasets were significantly higher than for the other datasets; this is attributed to a smaller variety of plume characteristics in these images. In EPOXI images of Comet Hartley 2, more individual jets were detected than with previous methods.

4.6.1 Io

The distinct appearance of volcanic plumes (Geissler and Goldstein, 2007; Lopes-Gautier et al., 1999) allows for ideal positive detection when visible on the limb of Io. Plumes populate a large portion of the satellite and many are visible against the background surface rather than on the limb. Telltale characteristics indicate their difference from the highly varied background surface (Geissler and Goldstein, 2007). Viewing geometries are not typically as favorable as Figure 4-13A of the Tvashtar plume, the largest of all of Io's plumes. More nadir views make the dimensional filamentary nature of each plume more difficult to discern. Viewing plumes on the limb, as in Figure 4-13 B and C, are generally more revealing even when the plumes are very faint. The Prometheus plume seen in nadir view in Figure 4-13B is not detected, nor is its shadow, suggesting that an additional feature class based on the characteristics of a plume deposit is needed to successfully detect all active volcanic plumes.

Of the 20 volcanic centers on Io known to produce explosive eruptions and emplace pyroclastic deposits (Geissler and Goldstein, 2007; Spencer et al., 2007), at least 11 of the known plume columns were successfully detected (Table 4-2). Additional plumes were unresolved in gradient distributions. Dust columns were more likely to be detected than the gas due to the higher optical density of the dust columns. For Io images, plumes 65% brighter than the background were easily detected (Figure 4-14) even when they did not exhibit a dense dust column.

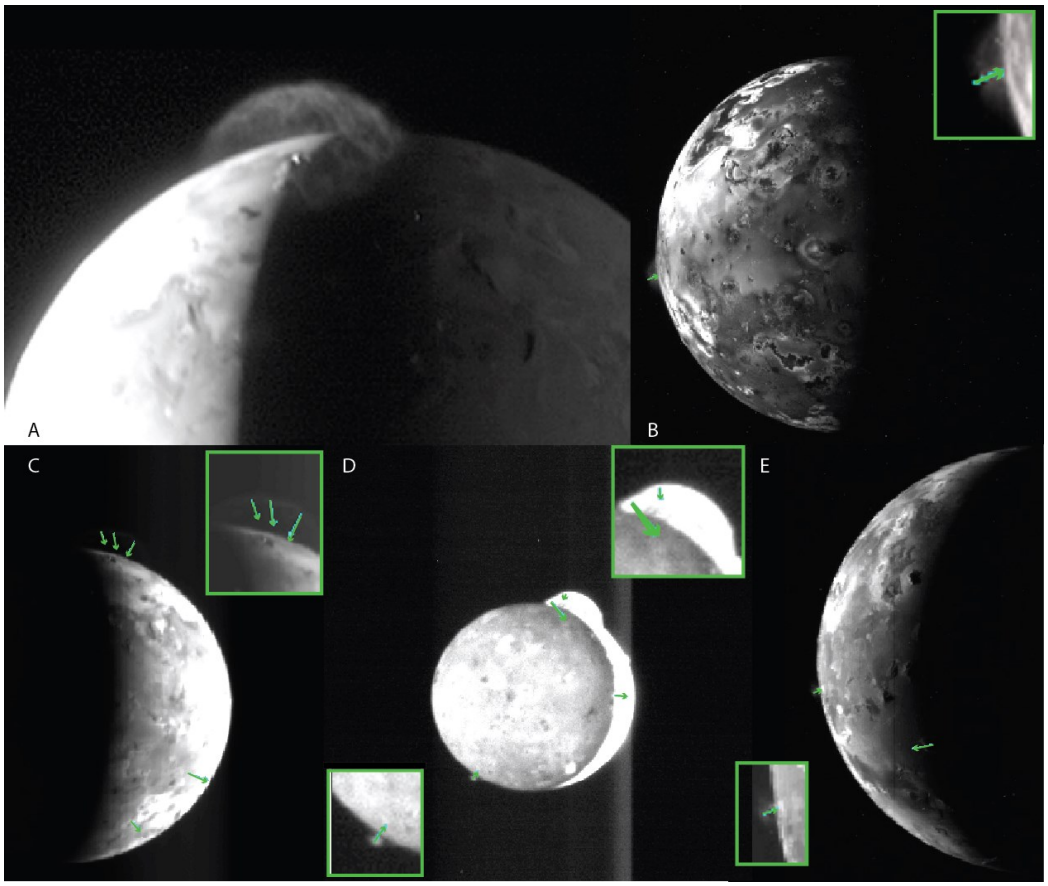

Figure 4-13. A. Tvashtar plume viewed at the terminator by New Horizons. B [Galileo]. Positive detection of the Pillan plume in limb view; Prometheus plume and shadow not detected. C [New Horizons]. Tvashtar plume detected on the limb, multiple keypoints are necessary for large objects; false positives near the limb result from non-uniform brightness due to overexposure. D [New Horizons]. Positive detections of the Tvashtar (top) and Lerna (bottom) plumes; the Masubi plume at the terminator does not have a sufficient gradient compared to the overexposed limb. E [Galileo]. Positive detection of the Culann plume; an additional feature is detected at the terminator. [Background images: NASA/JPL/Univ. of Arizona (Galileo); NASA/JHUAPL/SwRI (New Horizons)]

Table 4-2. Detection of Io's plumes.

Plume	**Detection**	**Location**	**Height (km)**
Acala	Possible	in eclipse	
Amirani	Y	limb	60-87
Culann	Y	limb	
Kanehekili	N	limb	75-101
Kurdalagon	Possible		100
Lerna	Y	limb	150
Loki	Possible	terminator	16-382
Marduk	Y	faint, limb	52-92
Masubi N	Y	terminator	70
Masubi S	N	unresolved	80
Maui	Y	limb	57-148
Pele	Possible	limb	426
Pillan	Y	limb	109-118
Prometheus	Y	limb	67-90
Ra	Y	limb	104
Thor	Y	limb	107
Tvashtar	Y	limb	350
Volund	Possible	limb	96-98
Zal	Possible	terminator	80
Zamama	Y	limb	62-80, 100

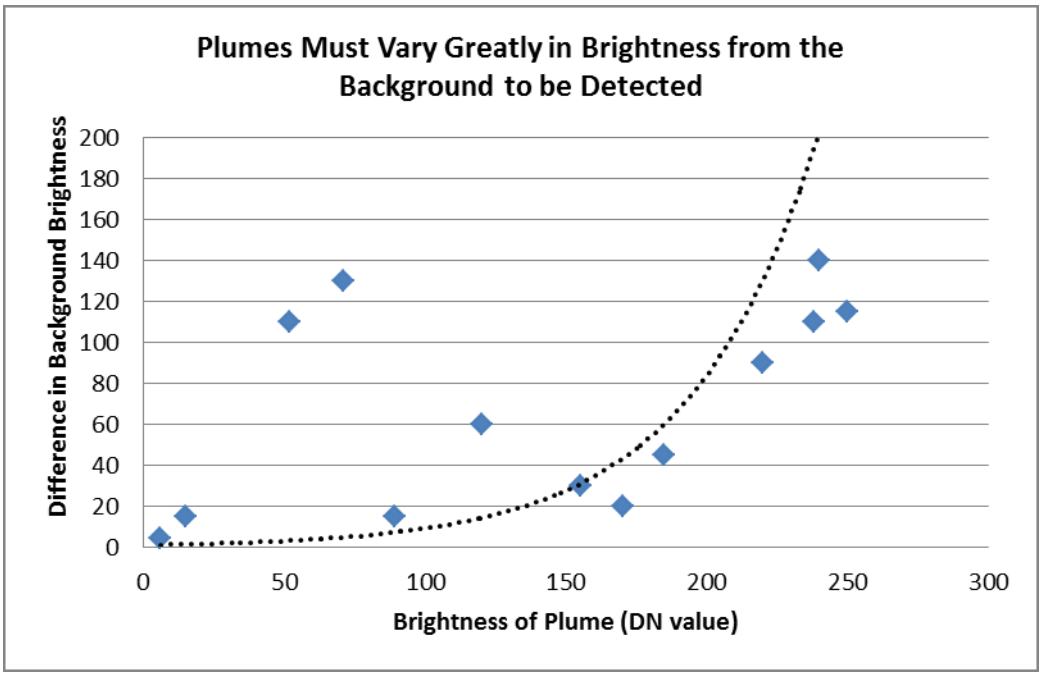

Figure 4-14. Brightness gradient is the most constraining quality of a plume in regard to producing a positive detection. The plume's brightness must vary by ~65% from the background in order to be detected. Plumes are generally brighter (higher albedo) than the surface because the dust particles are highly reflective. The points inside and above the curve are cases where the plume is faint compared to an extremely bright adjacent surface feature. In two of these cases, the plume is at the lower limits of pixel size for detection (in low resolution images); in the third case, the plume is fairly faint but is detectable due to its height and the fact that the image is of higher resolution.

4.6.2 Enceladus

More than 30 individual jets have been identified emanating from the south polar region of Enceladus. These jets bear a stark contrast to the prominent volcanic plumes of Io. While volcanic plumes and deposits on Io are dramatic and globally distributed, the jets of Enceladus are faint and originate only at the south pole, so that they can only be visually detected in limb views. They are optically dense enough to exhibit a significant albedo gradient for SIFT detection though their small size and proximity limit the number of individual detections that can be made (Figures 4-15 and 4-16). In views where the limb of the satellite is illuminated, the highest gradient in brightness is against the background surface rather than against space (Figure 4-15); this image shows that it is possible to detect the source points of plumes. The brightness gradient of the plume itself is low as the plume is spread out rather than a narrow jet. In images where the limb is not illuminated or there are multiple edges (Figure 4-16), positive detections show that detections do not depend on contrasting edges as in the edge detection method. In images of Enceladus, 5 main sources of the 30 identified jets are detectable using SIFT+*k*NN. Note that the visibility of the 30 sources (Figure 4-15, top) depends on post-processing while the SIFT method is utilizing unprocessed images to replicate the condition of images onboard.

4.6.3 Comet 103/P Hartley 2

The SIFT algorithm does not require a smooth elliptical edge, so it is appropriate to detect outgassing events on non-ellipsoidal targets like comet nuclei. The limited number of images of Comet Hartley 2 taken at closest approach with sufficient resolution to detect jets from outgassing severely limits the training set of vector descriptors that can

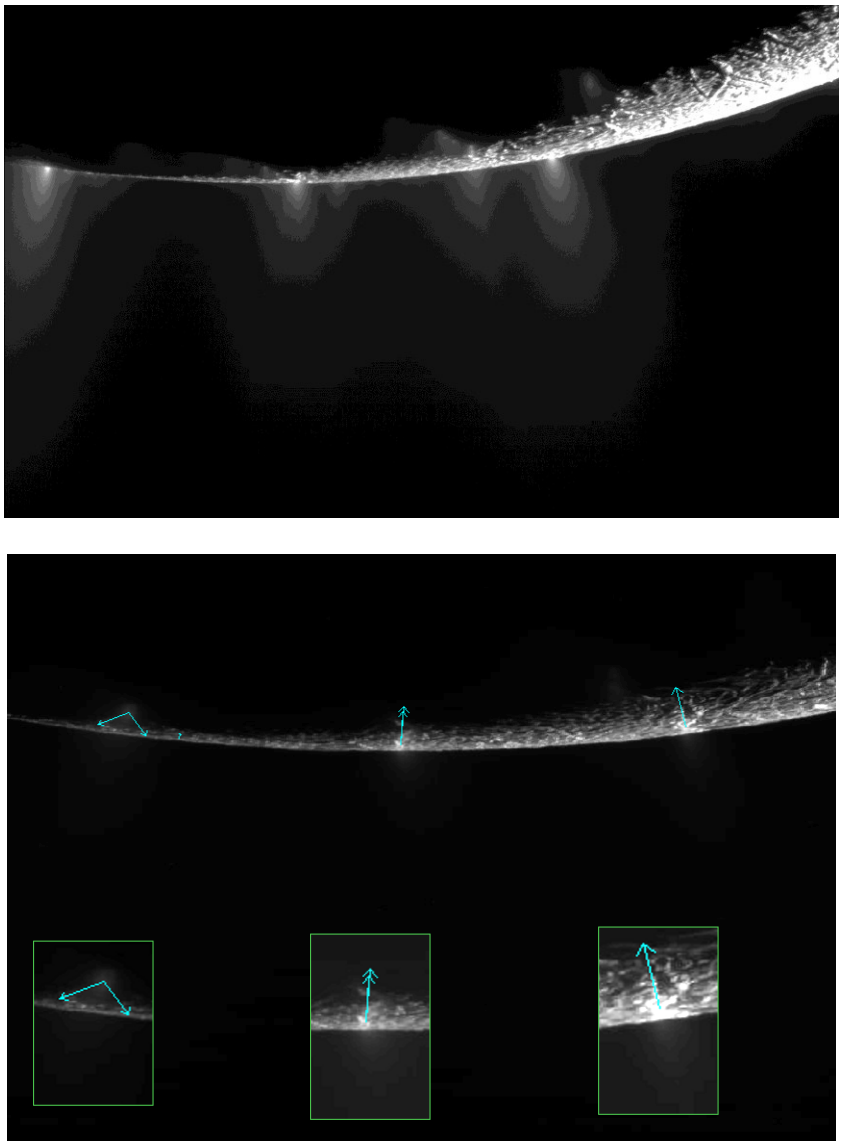

Figure 4-15. Top: A fully processed image of Enceladus's jets reveals many individual jets that are visible extending beyond the limb and against the background surface in eclipse. Bottom: In a similar unprocessed view, fewer individual jets are visible though the ultimate detections are of the plume sources rather than the portion of the jets that extend beyond the limb. [Background images: NASA/JPL/Space Science Institute]

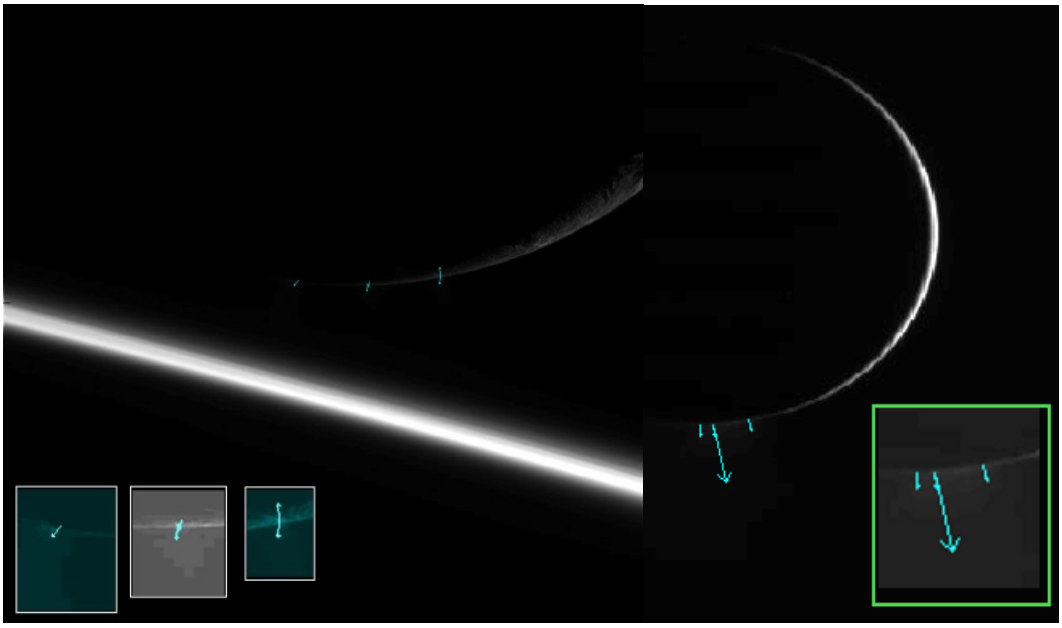

Figure 4-16. Jet detection on Enceladus. The jets are only visible in limb view. The number of individual jets detected depends on viewing geometry. Left: Three groups of jets are identified; the bright stripe from center left to bottom right is sunlight in the atmosphere over the night side of Saturn. Right: Even at a greater distance and lower resolution, three groups of jets are still detectable. [Background images: NASA/JPL/Space Science Institute]

be used to classify the remaining images. Nevertheless, SIFT has the capacity to detect many small individual jets without an overwhelming number of false positives or false negatives (Figure 4-17). Note that there is more than one keypoint descriptor associated with each jet; this is attributed to some degree of diffusivity or brightness change being detected outward from the surface of the nucleus. Further extant, there is a lack of additional keypoint descriptors which may indicate the lack of stark delineation between jets as the cloud of ejected material becomes uniform (see also A'Hearn et al., 2011) so that there is not a dominant gradient or orientation of brightness change for SIFT to recognize. The SIFT plus *k*NN classification method detects more individual jets than preliminary edge detection methods (Thompson et al., 2011).

4.7 Other Applications of Autonomous Processing

To begin exploring other methods and capabilities of autonomous processing that could be applied for similar objectives, alterations to the *k*NN classification system were tested to address the issue of recognizing multiple types of features and a spectral filtering method was applied to Galileo Near Infrared Mapping Spectrometer (NIMS) data of Europa to determine the potential for identifying features based on their spectral signatures rather than their morphologies.

4.7.1 Feature Classification by Expanding KNN Classifiers

In addition to positive plume detections, the *k*NN classification technique allows the classification of other features with the addition of another class in the training database. This is demonstrated by the successful identification of mountain slopes (Figure 4-18). Mountains often appear similar to plumes as bright surface features against the background surface; more favorable viewing conditions reveal their texture and

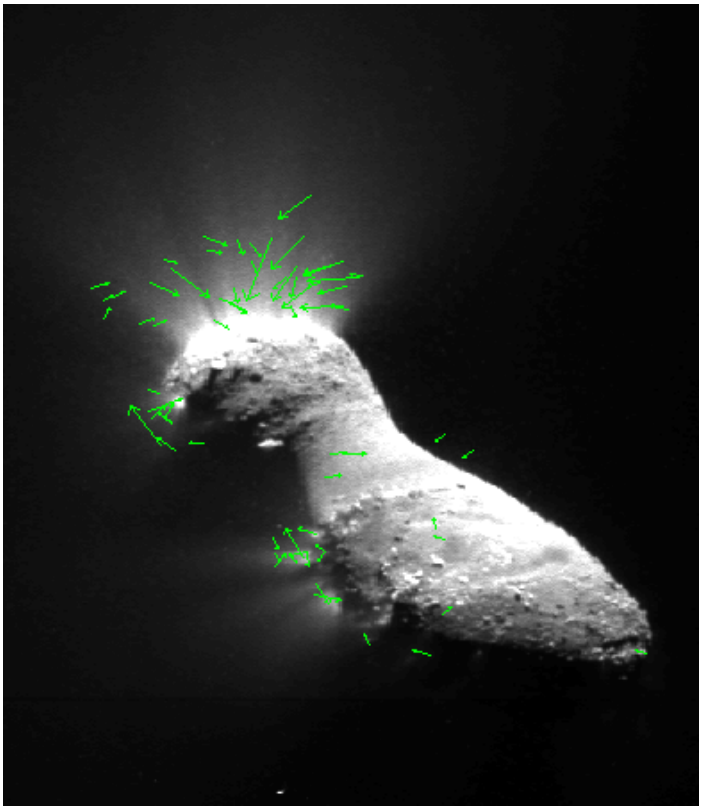

Figure 4-17. Outgassing on Comet 103/P Hartley 2. Many small jets are ejected from this hyperactive comet nucleus. [Background EPOXI image: NASA/JPL-Caltech/UMD]

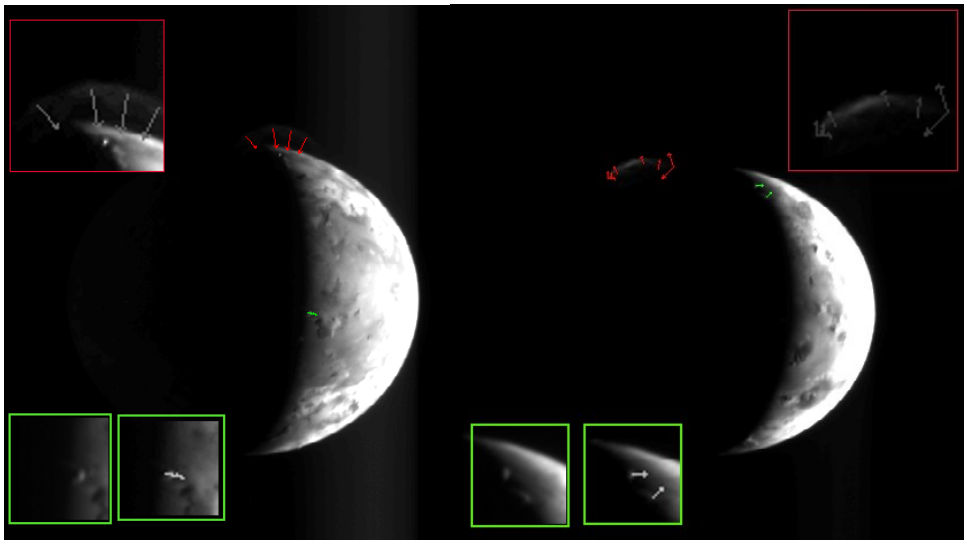

Figure 4-18. Classification of mountain slopes. When a third object class is defined, *k*NN successfully distinguishes between bright plumes and bright mountain slopes. Note that the slopes shown here (insets with green keypoint vectors) are not on the limb though they are all at or near the terminator where illumination effects highlight their topography. The bright plume Tvashtar is also identified in red. [Background New Horizons images: NASA/Johns Hopkins-APL/SWRI]

topography (Turtle et al., 2007). Many of the isolated mountain peaks are tall enough to extend beyond the planetary limb and so would be detected by edge detection methods. Adding a new feature classifier to a small subset of the training set resulted in the accurate detection and classification of several mountain slopes not situated on the limb.

4.7.2 Spectral Correlation

Future outer planets missions are limited in downlink bandwidth; under these circumstances, hyperspectral image data volumes limit their achievable coverage and science return over the mission lifespan. This is of particular concern for a future mission to Europa. Hyperspectral images might reveal novel spectra associated with fresh upwellings, surface material from eruptions, or other transient phenomena such as plumes or thermal anomalies. However, such features might be missed during standard mapping campaigns that accumulate coverage slowly and rarely target the same location twice. Automated processing allows many images to be acquired and analyzed onboard, thus increasing the opportunity to capture transient events and identify features associated with endmember materials. These key spectra could be downlinked *in lieu* of the image to characterize full spectral diversity at minimal additional bandwidth cost. In case of a significant anomaly, ground operators can downlink the entire image or schedule follow-up observations.

The harsh Jupiter radiation environment complicates automated analysis by constraining available computing power and limiting algorithm options. Additionally, it causes high levels of instrument noise that human analysts typically address by averaging spectra over surface features. This work favored a spatial averaging method that mimics such an approach and is computationally feasible for onboard use (Bunte et al., 2011). A

superpixel endmember detection algorithm (Thompson et al., 2011) was used to identify salient surface features. Superpixel segmentation over-segmented the images into homogeneous connected regions where all pixels have a similar value (i.e., color, grayscale). Thereafter, the images were represented using the mean spectra of their superpixels. Spatial averaging alleviated mitigated noise and reduced the number of spectra by one or more orders of magnitude, easing computational burdens for subsequent processing.

The superpixel endmember detection method was applied to the catalog of Galileo NIMS images of Europa. All images greater than 30 sample lines with a spatial resolution better than one degree of planetary latitude or longitude per pixel were included. This study was limited to the visible near-infrared region and only considered the spectral window between 0.7 and 2.5 microns. Detector saturation was addressed by extrapolating with a constant value from left to right across gap regions. Images were preprocessed with a median filter of one-pixel diameter which also helped to reduce pervasive shot noise. After this initial processing, the superpixel endmember detection algorithm was employed to produce a rank-ordered list of the most salient regions as in Thompson et al. (2011). Performance was evaluated by identifying key spectral features in previously published studies of NIMS data for comparison with salient spectra and by assessing the correlation between endmembers and surface morphology (Bunte et al., 2011).

A total of 30 images were analyzed by the endmember detection method; 17 produced viable spectral results. The average number of endmembers detected for each image was 8.5; the number ranged from 3 to 30 and was correlated with the quality and resolution of the original images. From the 17 viable images, 120 regions of interest were determined.

Comparison with SSI images revealed a strong correlation between autonomously detected regions of interest and surface morphology (Figure 4-19).

Each image and its endmember regions of interest were examined by hand to assess the correlation with surface morphology and to evaluate the endmember priority ranking with respect to surface feature. 35% of the regions of interest are preferentially associated with dark linear features (i.e., fractures, ridges, or flexūs) while 65% correspond to the surrounding icy plains or chaos. Evaluating only the top 3- or top 10-ranked endmembers reveals a consistent distribution; this suggests that linea are overrepresented relative to their fractional coverage of the surface. The distribution may be influenced by the selection of NIMS targets but reflects attention to both large-scale and outlier features. Comparison of the salient spectra to previously published studies (Dalton et al., 2003) confirmed that the autonomously retrieved spectra showed similar features such as the water of hydration absorption features at 1.5 and 1.9μm. Several of the salient spectra included the absorption feature at 2.05μm that was attributed by (Dalton et al., 2003) to amide peptides (Figure 4-20). Figure 4-20 illustrates the similarities between the autonomous and manually extracted spectra. The diversity in the near 2.0μm absorption feature as explored by (McCord et al., 1998, 1999, 2010) showed a correlation with surface features; spectra from dark linea have a narrower absorption feature than the spectra from icy plains regions (Figure 4-21).

This method (Bunte et al., 2011) demonstrates a possible onboard autonomous process that could be used to select regions of interest and to return averaged data rather than complete imaging data. This work confirms the ability to detect and distinguish between different groups of geologic features by their average spectral signatures. In addition, this

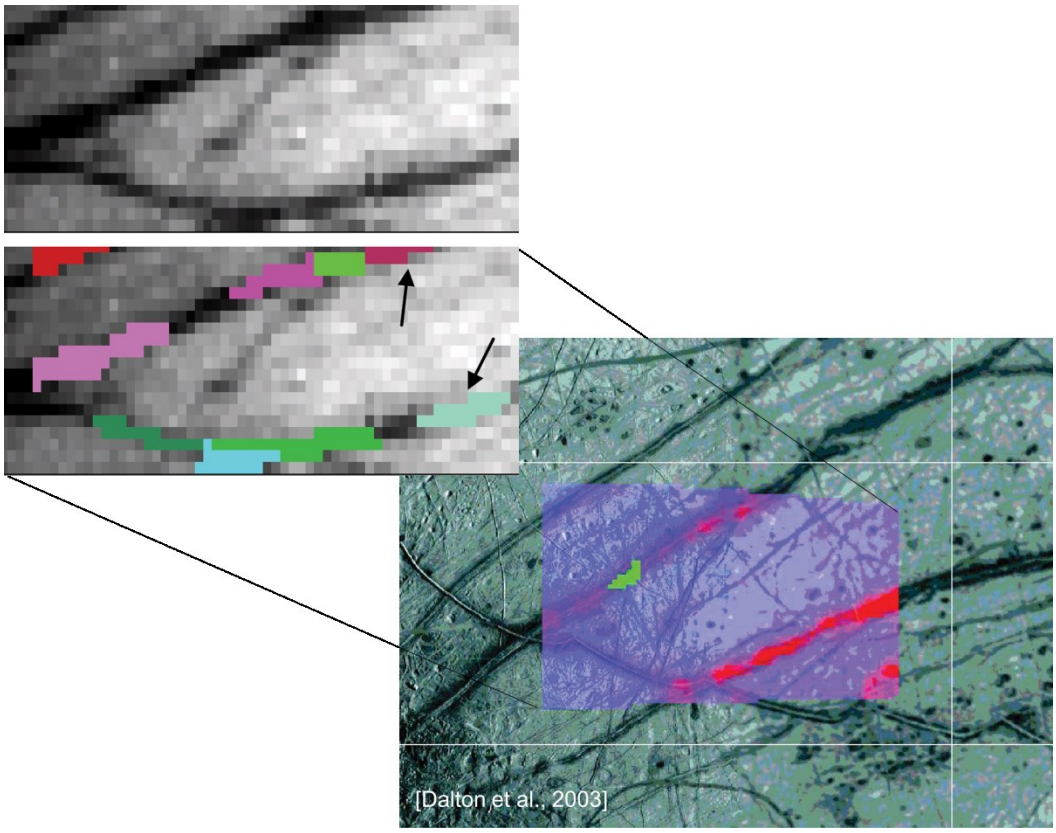

Figure 4-19. Galileo NIMS 11ENCYCLOD01A. Top left image pair shows the original spectral image and the same images marked with regions of interest. Each color represents a region of interest selected autonomously according to homogeneity. These 9 regions coincide with dark linear features and are ranked in the top 20 of the 30 regions for this image. Spectra for two regions (arrows) in Figure 4-11. Bottom image is a composite of the NIMS image overlain on an SSI image to illustrate the alignment of spectral signatures with geologic features (*from* Dalton et al., 2003). Note the similarity of the autonomously selected regions at top with the manually selected regions selected in the bottom image.

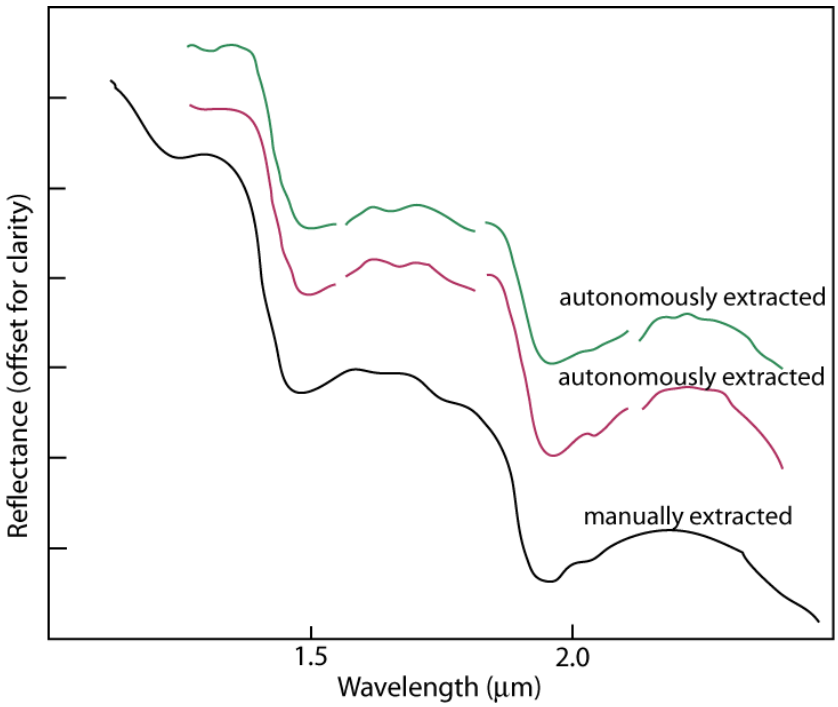

Figure 4-20. Spectra for regions of interest selected autonomously (top pair) compared to manually extracted spectra of Europa (bottom, *after* Dalton et al., 2010). Autonomously extracted spectra from regions selected by endmember detection method (colors match Figure 4-19). Both exhibit absorption features at 2.05µm (see Dalton et al., 2003). Breaks in spectral lines are due to removal of overlapping data. Black line: manually extracted average spectrum of Europa's dark terrain.

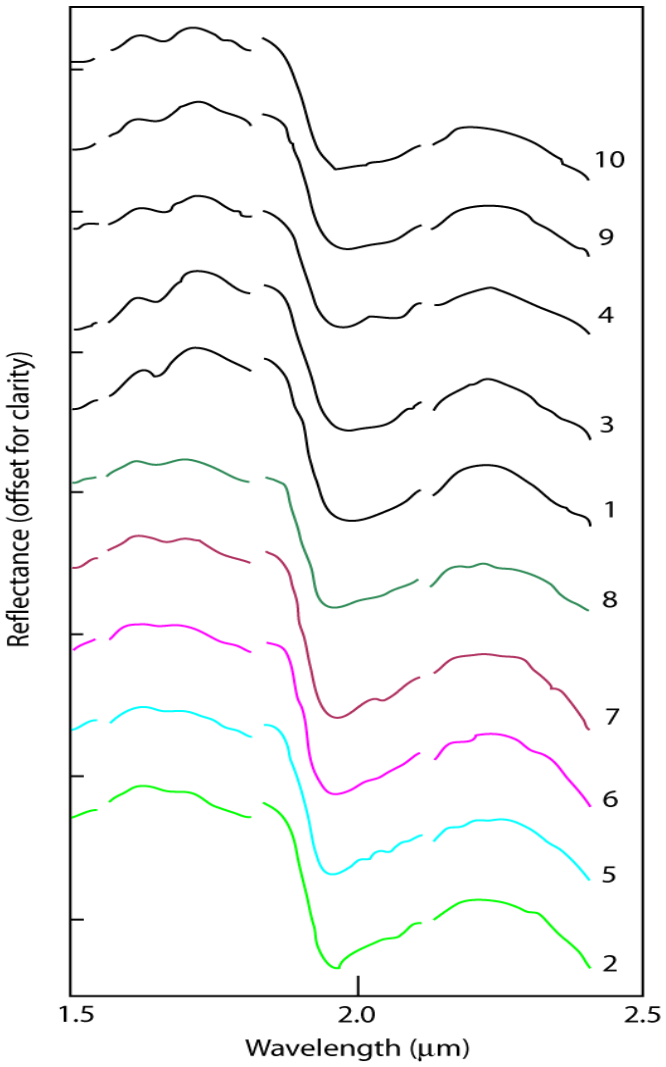

Figure 4-21. Spectra for the top 10 endmembers selected autonomously; full spectral diversity is captured in these endmembers. The variation in the absorption feature at 2µm illustrates that autonomous extraction captures the key water absorption distortion in dark linea noted by (McCord et al., 1998, 1999, 2010). Colors match regions of interest shown in Figure 4-19 for dark linea; black are icy plains. Spectra from dark linea have a narrower absorption feature than the spectra from icy plains regions.

algorithm can accurately retrieve spectra for features and anomalies that were not anticipated in advance of spacecraft observation. Numerical endmember detection does not require prior input from a spectral library or assumptions of surface composition and automatically identifies most spectral features reported in published analyses of the NIMS Europa data.

4.8 Detectability

The range of image sets studied using SIFT+*k*NN reveals a series of results regarding detectability that apply to each individual data set. In an analysis of all Galileo images of Io, no less than 65% of plumes extending beyond the limb can be detected regardless of interfering conditions. In addition, 7% of plumes visible in nadir views against a varied background can be detected; this is a major improvement over other methods as they cannot distinguish features from the background. Overall, plumes must be 65% brighter than their background surface and this brightness requirement is independent of plume height in pixels. However, effective resolution, viewing conditions, and exposure times greatly influence detectability and must be considered when planning future observation sequences. Size limitations on detection, when considered independently of brightness gradients, are directly related to the array sizes used by SIFT; the optimum array size limits detections to a minimum of 6 pixels in height which is slightly larger than plumes that can be detected by the edge detection method alone. Exploration of the database needed for comparison to yield optimum results indicates that with only partial characterization of activity, the supervised classification technique can detect up to 90% of large scale events. Targeting and detecting a higher percentage of these events in

future observations will required more detailed characterization or a more advanced intelligent algorithm capable of recognizing features.

4.9 Discussion

Applying a supervised classification approach to the problem of autonomously detecting and classifying volcanic plumes in spacecraft data successfully allows detection under a variety of conditions. This approach could enable sustained monitoring campaigns or rapid responsive execution for reobservation of active events. The SIFT algorithm identifies gradient changes in an image and, when combined with *k*NN, can detect and identify multiple classes of features based on characteristics which have previously been manually identified. Just as plumes are most easily viewed in high phase angle images or when the planetary body is eclipsed as in the edge detection examples, SIFT and *k*NN are most successful under those conditions but are also applicable to detecting features of unknown characteristics.

This method is capable of detecting most known plumes or jets with a reasonable number of false detections given the added ability to distinguish other types of structural features. One goal of this autonomous processing is to detect and classify unknown features in future mission observations; detection of the greatest variety of events is desired even at the expense of not detecting prominent features. The supervised classification approach allows all known plume characteristics to be positively identified; the false detection rate that persists throughout all datasets tested is necessary so as not to limit the degree of unknown characteristics that a classifier positively identifies or to preclude new and geophysically important detections. The rate of misclassification can be reduced by enlarging the training database at the expense of autonomy as it necessitates

further manual interaction. The detection rate can be improved by reiterating the classification process at the expense of increased false detections.

A goal of autonomous processing is to both identify multiple types of features and to confidently distinguish between them. In showing that this method can distinguish between at least three classes of features (plumes, non-plumes, mountains), a basis for extending the classification abilities to other surface features such as plume deposits on Io, fractures on Europa and Enceladus, plume trails on Triton, and chaos and lenticulae on Europa is established. The ability to distinguish between reflective plumes and illuminated mountain slopes strengthens the argument that this method is capable of distinguishing surface features which exhibit a definite gradient pattern. For example, the ringed deposits that result from plume fallout share a similar geometric and albedo pattern that could be used to define a feature class for recognition by *k*NN. This ability would make the many ringed deposits viewed at nadir (i.e. Prometheus or Culann, Figure 4-1) detectable as active or recently active plumes. This type of pattern recognition in cluttered scenes is ideal for identification and tracking of geologic features and changes during the tour phase of a spacecraft operation.

The SIFT+*k*NN method has proven to be useful in detecting and identifying features. The edge detection method is also capable of identifying those features on the limb with a lower rate of false detections. While it is demonstrated here that the higher false detection rate with SIFT+*k*NN is actually more suitable for future observations to allow serendipitous discovery, there is an argument to combine the two algorithms, especially for tracking known activity at expected locations. Combining techniques for repeated comparison can increase detection rate at the expense of increased false detection. This

implies that combining multiple autonomous techniques where processing constraints allow can increase science return. If the qualities of a plume or other feature are known and remain consistent relative to parent planet or resolution, a minimal database can be established even with increased positive detections (Lin et al., submitted). With advances in processing and memory resources, the computational requirements of multiple processing steps should prove to be non-depletive, particularly if such an effort allows additional science imagery to be downlinked. Refining these algorithms for onboard use with no manual interaction during processing would certainly require flexibility in the system intelligence but could be beneficial in terms of returning data variety.

When identifying features by comparison with other features or previous images, the use of a large comparison data set is essential. Building a database which represents the full range of observed, expected, and unknown feature characteristics is essential to yield the most effective data from future missions, where mission lifetime and data-limiting conditions will preclude real- or near real-time human interaction for identifying sites of geophysical activity on the planetary targets to be observed. However, the unknown nature of potential features will require a flexible database to avoid missed detection of valuable data. Altering the selection of images used to build the comparison database, increasing the database size, and varying or combining multiple methods of classification produce a range of results. Tailoring the combination of these methods to the observational needs of a particular planet or feature type will be an important exercise for future missions.

The development of these algorithms and their application to the remainder of the outer solar system mission datasets should be a priority prior to future missions.

Establishing a complete analysis of how geologically distinct features can be distinguished from one another, especially where plume deposit materials are distinctly identifiable against the background surface, is essential for detecting any potential plume activity on Europa. Most importantly, further statistical analysis of the data is necessary to constrain the instrumentation, observation, and geological conditions under which a successful feature or event detection and identification can be made. This will allow recommendations for future observations with the goal of discovering or monitoring geologic transient events on Europa and other bodies.

CHAPTER 5

ASSESSING EUROPA'S POTENTIAL FOR ACTIVITY

5.1 Introduction

Young surfaces on outer solar system bodies are typically associated with active resurfacing processes. Io, with an overall surface age of approximately 60 M.y. (Schenk et al., 2004) and predicted age boundaries between 0.3 and 2.3 M.y. (Zahnle et al., 2003; Schenk et al., 2004), harbors over 150 active volcanic centers, some of which produce explosive eruptions with gas and dust columns, commonly referred to as plumes. Enceladus' south polar fractures are the source of plumes; this area of the surface may be an average of 0.5 M.y. old while the remaining surface where activity is not detected may be ~4 G.y. old (Porco et al., 2006). In both the cases of Io and Enceladus, plumes are understood to be derived from endogenic processes. Plumes seen at Triton may also be endogenic (Kirk et al., 1995) but are more likely to be driven by sublimation (Smith et al., 1989; Kirk et al., 1995) as is the case for comet outgassing (A'Hearn et al., 2011). The surface properties and internal dynamics expected for Europa would most likely indicate endogenic processes for any plume or other surface activity.

5.2 Projected Activity

The young surface of Europa implies an active method of resurfacing. The examples of plumes elsewhere are known to provide a very effective method of resurfacing, so plumes would be the expected activity at Europa as well, particularly in light of the tectonic activity that could lead to venting.

From mapping results in Chapter 2 and discussions of formation processes in Chapter 3, it is apparent that the geologic units most likely to indicate any surface activity are

chaos and linea units with the chaos margins and linea central troughs having the highest potential to exhibit any type of venting or outgassing. Crater and plains materials indicate much older surfaces which, at present, do not indicate any substantial level of activity with the caveat that lenticulae in the lenticulated plains be considered chaotic features as in the lenticulae unit/structures.

Lenticulae, microchaos, fractured chaos, platy chaos, blocky chaos, and subdued chaos could all exhibit indications of current activity. Likewise, ridges, ridge complexes, and bands could show evidence of change over time. In most cases, subtle changes since the time of Voyager and Galileo would be the most likely indicators of activity and detecting those changes will depend heavily on repeated high resolution imaging. Larger scale changes, such as some variety of plumes or color change, are also expected based on similarities between Europa and other satellites like Enceladus and Triton as well as smaller satellites where activity in the form of cryovolcanism is expected but as yet unobserved.

The most likely example of potential plume activity was addressed by Fagents et al. (2000). If a thin ice shell overlying a liquid water ocean or water pocket is cracked open by tidal or other stresses, any liquid water exposed will immediately boil and create a vapor cloud. Dissolved volatiles could exsolve and drive a larger gas-rich spray. This creates a deposit near the vent. Evidence of this type of activity is seen at linea boundaries as in Figure 5-1, which compares a prominent double ridge with a fissure vent on Earth's Kilauea volcano.

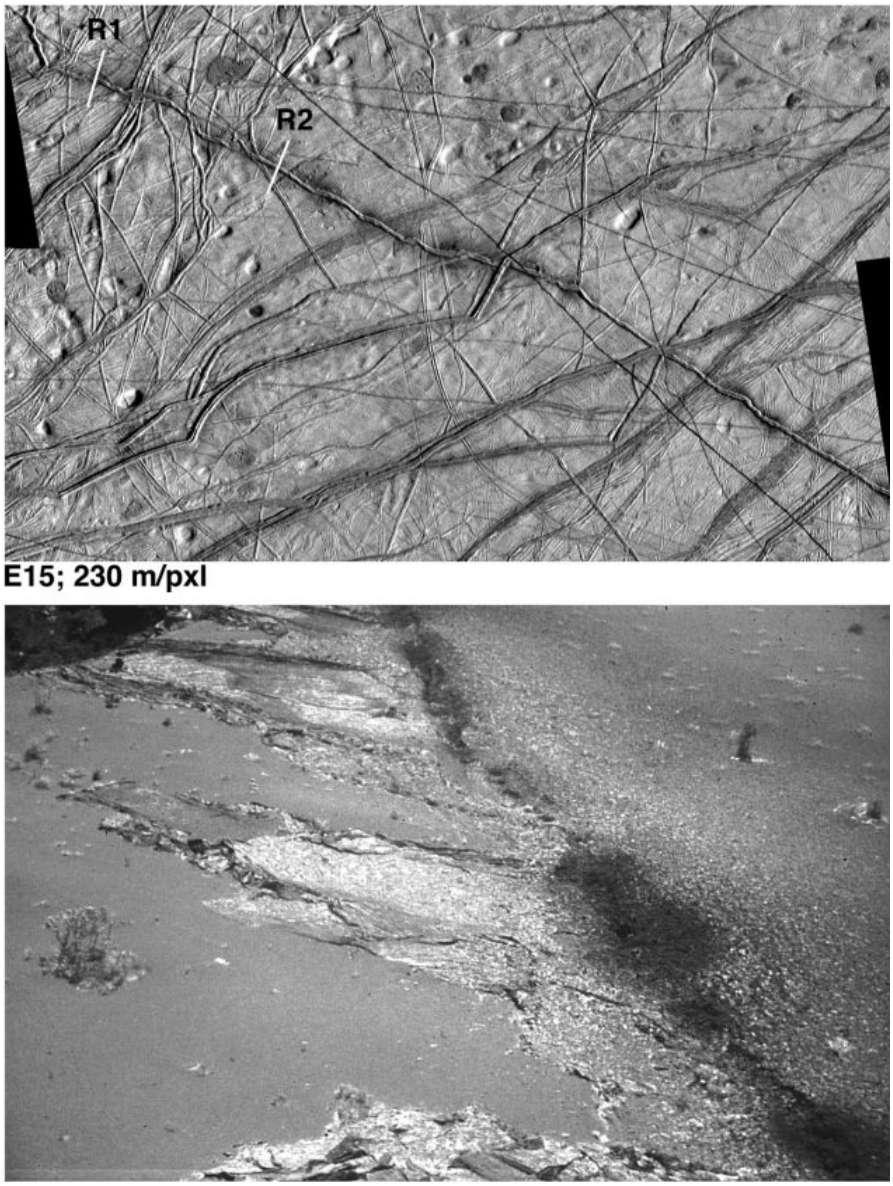

Figure 5-1. Near-fissure deposits at Rhadamanthys Linea and a Kilauea fissure, *from* Fagents et al. (2000). Top image shows the dark margins of a europan double ridge with a central trough. Bottom image shows the dark deposits caused by venting from a fissure at Kilauea volcano, Hawai'i. [Used with permission.]

5.3 Detectability

Examination of all images from the Voyager and Galileo observations of Europa revealed no definite change over that period of observation (Phillips et al., 2000). That study primarily searched for plume activity similar to that discussed in Chapter 4 using a method of single image division to reveal change. The lack of circular plume deposits or observed brightness differences on the planet limb led Phillips et al. (2000) to conclude that Europa has experienced no large scale activity in the few thousand years and that any activity potentially present would be small scale and sporadic.

If activity is present at Europa, it is assumed that plume or venting activity will likely be a prominent type. Several authors have addressed the conditions necessary to produce plume-like activity at Europa (Crawford and Stevenson, 1988; Fagents et al., 2000; Quick et al., 2013). Their results are compared with the detection limits discussed in Chapter 4 to determine whether the characteristics of plume activity match proven detectable levels.

5.3.1 Detectability of Plumes

Fagents et al. (2000) propose two mechanisms by which plume-like materials or dark deposits could be emplaced on Europa: explosive volcanism or conductive heating through sublimation. Explosive volcanism can occur by either a ballistic or shock model.

The ballistic model involves the decompression of erupting gases to the pressure of the ambient environment. This decompression results in particles and condensed gases following ballistic paths of ejection to form umbrella-shaped plumes as in the case of large Pele-type plumes on Io (Strom and Schneider, 1982; McEwen et al., 1998). The low gravity and low pressure on Europa would most likely cause gas-rich eruptions to behave ballistically with allowance for plume size to vary as a function of gas composition (i.e.,

Figure 5-2; Fagents et al., 2000). Volatiles with entrained brines are known to erupt at lower velocities (Kargel et al., 1991, 1995), resulting in smaller deposits or lower gas to dust ratios (Fagents et al., 2000).

The shock model involves the pressure of erupting gas greatly exceeding the ambient pressure such that the density and velocity distribution of particles in the plume are inhibited, causing shorter, more diffuse plumes (Cook et al., 1979; Strom et al., 1981; Kieffer, 1982; Strom and Schneider, 1982). This scenario is most likely to be observed at the tips of cracks that propagate upward from a liquid layer to the icy crust (i.e., Figure 5-3; Crawford and Stevenson, 1988), in locations where volatile-bearing water is exposed to zero pressure (Greenberg et al., 1998) or near pressurized magma reservoirs (Fagents et al., 2000). As confining pressure is released, gases exsolve and bubble nucleation leads to gas streams with entrained water. As gases depressurize, the water materials would be ejected to form wide deposits.

Under the ballistic model, Fagents et al. (2000) find that, under a range of compositional values, ejection velocities, and ejection angles, plumes may reach ~25 km in height with an average of ~12 km. Quick et al. (2013) expounded upon these estimates and found plume heights of <30-45 km with widths of <200 km. These estimates are consistent with smaller Promethean type plumes on Io. However, both authors find that large-scale eruptions are a less likely method of cryovolcanic expression than crack venting by the shock model. Both authors also express concern that the dark margins at lenticulae are so thin that they must have been emplaced quickly in contrast with the constant activity needed to maintain a plume. They suggest that enhanced local heating or

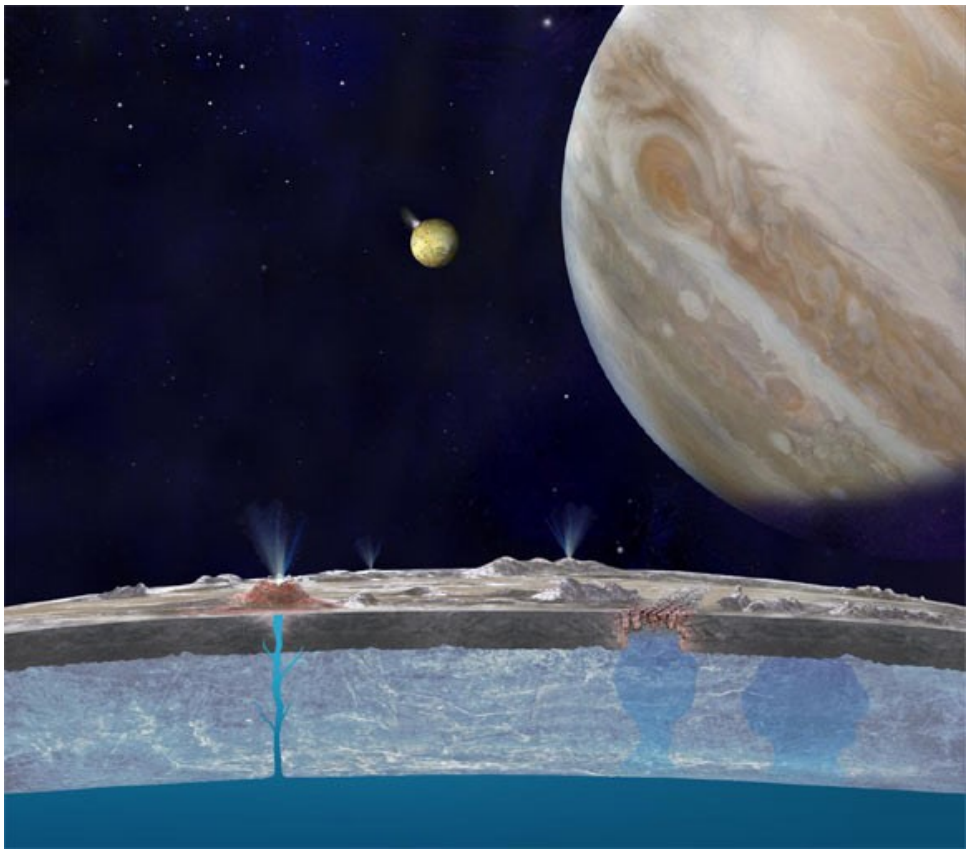

Figure 5-2: Explosive eruptions could produce plume-like features. [NASA/JPL]

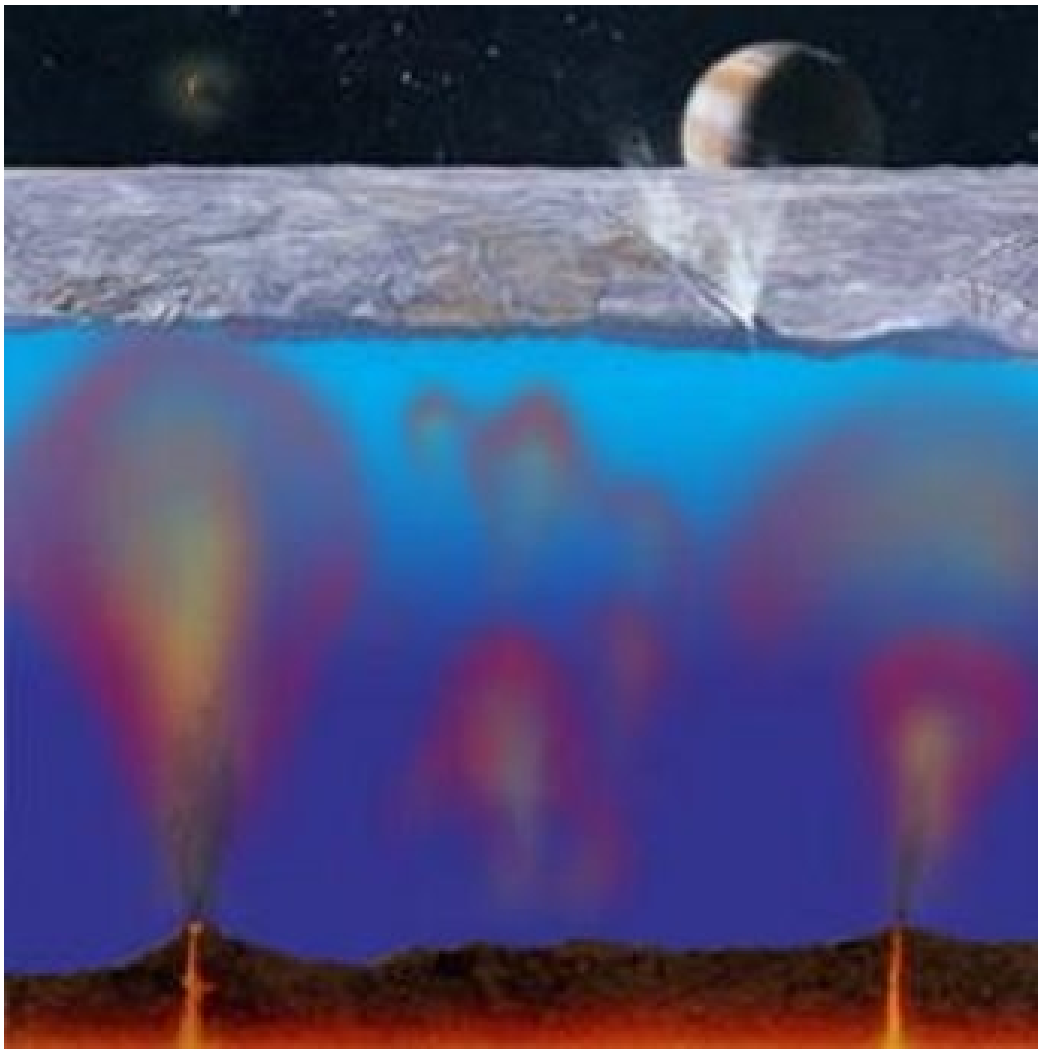

Figure 5-3. Assuming an appropriate ice shell thickness (see Figure 1-6 caption), crack venting could produce jets like those at Enceladus. [NASA/JPL/Michael Carroll]

large tidal stresses, like those inferred at chaos margins and ridge central troughs may be more conducive to producing short lived venting.

Given the detection limits established for known plumes and venting in Chapter 4, the activity that Fagents et al. (2000) and Quick et al. (2013) describe should be detectable. A 7 pixel minimum size for the array sizes used in SIFT translates to the need to view plumes of 12-25 km in height 1.7-4.3 km/px resolution consistent with Voyager and Galileo imagers. When viewed at the limb at the appropriate resolution, these plumes would be detectable. These models consider plume optical depths, or the amount of light that is not scattered or absorbed, as a proxy for plume reflectivity and find them to be similar to those of Ionian plumes (Quick et al., 2013). Under those conditions, model plumes would certainly be at or greater than 65% brighter than the background, thus making them easily detectable. This takes into account volatile compositions that may be common on Europa: CO_2, CO, SO_2, and H_2O (Fagents et al., 2000). NH_3, CH_4 are not considered as spectral data indicates minimum concentrations of those materials.

It should be noted, however, that these models assume continuous eruption, which has already been determined to be unlikely. Both models considered here note that small, low-albedo features are more likely than reflective plumes. These would be similar to the dark linea bounding deposits in Figure 5-1. The shock model or sublimation could more easily explain those features; resulting deposit widths would be on the order of 1-50 km (Fagents et al., 2000). The feature classification adaptation of the supervised classification method would not be able to detect such small features regardless of their brightness gradient compared to the surrounding surface.

5.3.2 Detectability of Other Types of Activity

With the understanding of lenticulae formation by Pappalardo et al. (1998), some new formation of lenticulae should be expected and likely detectable, especially by darkening of "spots" but also by new upwelled domes; in addition, the spreading, widening, or merging of lenticulae should be expected given the interpretation that lenticulae can merge to form microchaos and progressively develop into other types of chaos. Changes to lenticulae (i.e., size, darkening, or the embayment of previously preserved matrix material) or the emergence of new lenticulae may be on a scale that is possible to observe with the spectral averaging method presented in Chapter 4; they are certainly too small to be recognized with the supervised classification technique presented to search for plumes. The addition of new lenticulae is manually detectable but a new detection method will have to be explored to recognize their presence autonomously.

In the typical regions of chaos, individual blocks of preserved ridged plains are expected to exhibit translation or rotation, though this could only be confirmed in areas that have previously been imaged at high resolution such as Conamara Chaos. Extreme tilting of chaos blocks could potentially be detectable in the manner of mountain slope faces (section 4.7.1); however, the size of the blocks and image resolution may be too low for this method to be viable. Chaos block movement or the relaxation and smoothing of chaos matrix material are expected over time, as is the darkening of chaos units due to new upwelling or melting. These types of changes will require more detailed characterization for a supervised classification technique to be utilized for feature identification, though spectral averaging could be used to detected albedo changes or for comparison of blocky to relaxed materials.

Other types of activity that are generally expected at Europa include alterations to or formation of new tectonic features such as fractures or ridges, albedo or color changes along lineaments, or topographic and morphologic changes to ridge crests and flanks. Greenberg et al. (1998) estimate that a measurable amount of material may be added to ridge crests or flanks when processes are active. Tidal stresses may result in the formation of new cracks or fractures, the propagation of existing fractures, or the strike slip offset of pre-existing features (Hoppa et al., 1999). With the development of feature recognition algorithms, significant lengthening of linea or widening of bands could be autonomously detected. Brightness changes have been identified in the development of bands over time (Greenberg et al., 1998); likewise, albedo changes are expected over time due to frost deposits (Kadel et al., 1998; Geissler et al., 1998). These brightness gradient changes could be detectable with a variation on the supervised classification method as long as they are of sufficient area and gradient difference from the background; spectral methods may be more successful at detecting these smaller changes.

5.4 Future Sites for Exploration

As noted above, the most likely areas to observe for potential activity are the margins of chaos regions and active lineaments (i.e., those with dark margins, relaxed flank slopes, or bright deposits nearby) as these are the locations most likely to undergo sufficient local heating to produce gas exsolution. Given the need to detect change to indicate ongoing activity, the sites chosen for observation (Figure 5-4) should be those that have been imaged at high resolution during previous missions. Conamara Chaos (Figure 2-17) or Murias Chaos (Figure 2-19) would be excellent choices for locations to detect chaos matrix relaxation, plate motion, block tilting, or albedo changes. Thera and

Thrace Maculae also provide locations with considerable thermally controlled morphologies that would yield information about chaos relaxation and the method by which low-albedo material embays the ridged plains (Schmidt et al., 2012). Controlled landings targeting these small sites would require highly constrained landing ellipses and landers capable of adjusting to the undulating topography. As a site of notable brightness, Agenor Linea (Figure 2-26) would provide an excellent site to determine a formation mechanism for bands; it also provides access to the ridges plains and chaos in close proximity. In a case where comparative studies are not necessary, a landing site in the northern plains would provide an opportunity to acquire higher resolution of the polar region and to determine if stress regimes and thermal conductivity are higher at the poles than at the equator, as suggested by models of non-synchronous rotation (Greenberg et al., 1998).

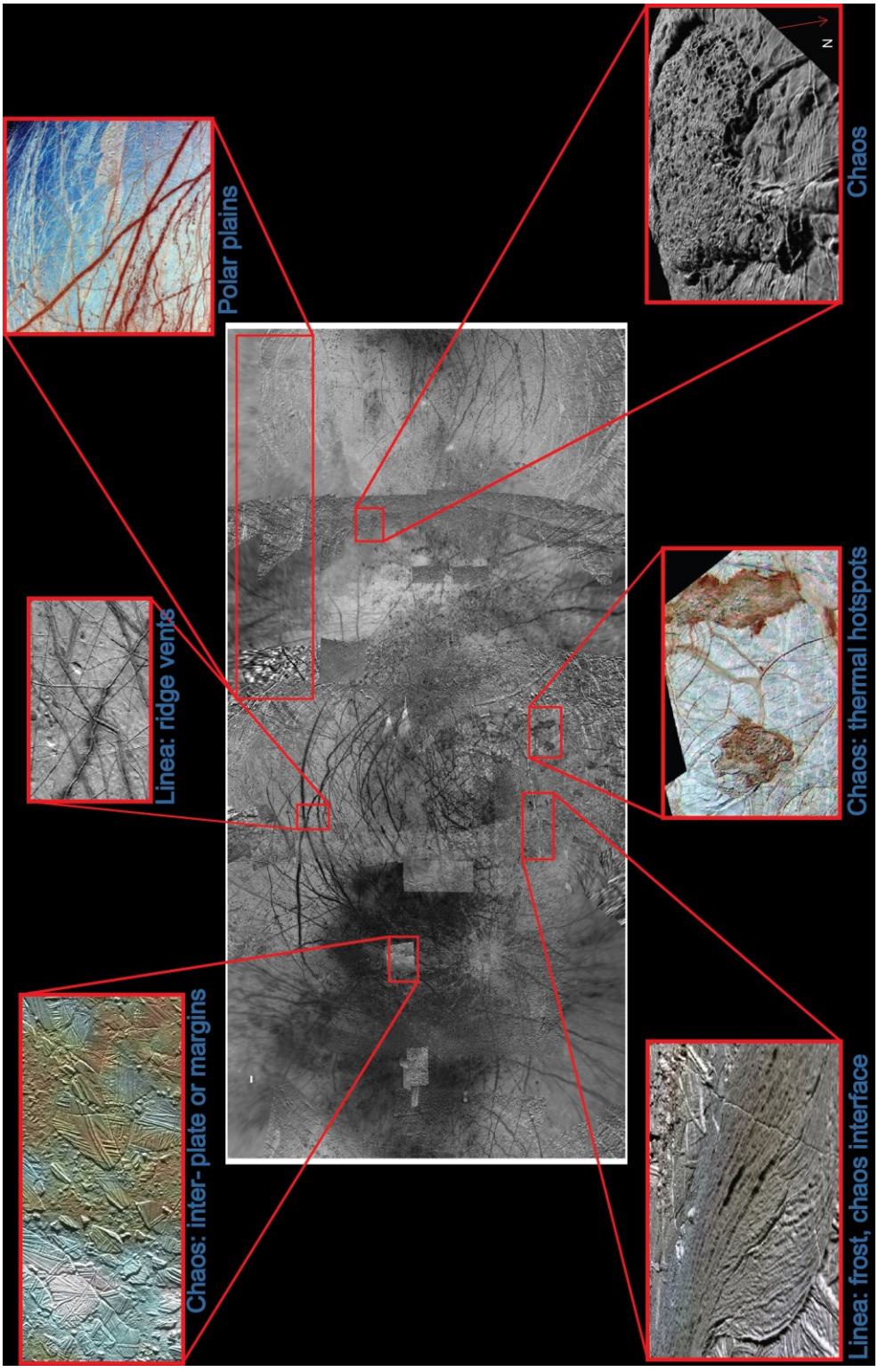

Figure 5-4. Potential landing sites for future exploration of Europa.

CHAPTER 6

APPLICATIONS FOR FUTURE MISSIONS TO OTHER OUTER SOLAR SYSTEM BODIES

6.1 Introduction

Spacecraft missions to the outer solar system have identified active yet transient geophysical events on multiple planetary bodies; these phenomena provide constraints for formation, composition, dynamics, and subsurface processes. The uncertain nature of the activity and the unknown environmental conditions near each body necessitate an understanding of the limitations of the physical characteristics of activity that are detectable in future observations and the hazards that may be encountered in detecting them. Characterizing the activity requires sustained or repetitive observations that demand an inordinate fraction of a spacecraft's limited resources, so efficient observation strategies are crucial. Hazardous environments require that a spacecraft making the observations be resilient to myriad unknown conditions. Detection of activity driven by model-based experiments utilizing automated onboard data processing will enhance the resilience of future planetary missions. Prior to the development of new missions to the outer solar system, modeling potential geophysical conditions of primitive planetary bodies can limit uncertainty in the occurrence and appearance of geophysical activity, leading to the selection of techniques for onboard instrument data processing that will enable us to explore the detectability of those parameters. A more thorough understanding of activity and its detectability enable the establishment of system functions and effectual spacecraft system architecture that will ensure rigorous detection, maximum spacecraft resilience, and increased science return.

How can the information presented for potential observation of activity at Europa based on an assessment of surface features, their potential modes of formation, the potential range of activity for each feature, and the range of similar features at various scales on other bodies be applied to establish the limits of detectability to future missions? Questions like this must be addressed to increase discovery and science return of future explorations. Once those limits are understood, what instrumentation and computing concerns must be addressed for functionality?

Future space missions demand an extraordinary level of flexibility and resilience to counterbalance the wide-ranging performance requirements and un-modeled environmental conditions likely to be encountered when exploring dynamic environments, particularly in deep space. Anticipated challenges include:

1. **Long duration investigations**, such as the New Horizons (Guo and Farquhar, 2005) mission and Kuiper Belt exploration, where human problem-solving interaction is restricted but radiation exposure and distance increase function failures;
2. **Hazardous conditions that limit mission lifetime**, such as high radiation at Europa which affects electronics lifetime or the toxic atmosphere and extreme heat of Venus (Hoofs et al., 2009) which permit few communications relays to Earth; and
3. **Uncertain environments**, where encounters occur without *a priori* knowledge of efficient data collection methods for optimum science return. Active bodies precipitate unpredictable appearance and levels of activity which may dictate

specific measurement sequences; however, illumination conditions and trajectory are also unpredictable.

An important aspect of the desired resilience to these problems is rapid, reliable autonomous onboard response to unpredictable science data and measurement conditions such as feature dimensions, albedo, and diffusivity, thermal anomalies, and compositional variance.

6.2 Evidence of Activity and Limitations on Observability

Geophysical activity is often evidenced by the presence of volcanic plumes or outgassing in the form of jets, geysers, or exospheres, disrupted surface morphologies inconsistent with surrounding terrain such as faults, flooding, or local melting, or changes over time to morphology, color, temperature, or composition. These characteristics reflect important constraints on the interior or near-surface dynamics of a planetary body and control surface evolution. On bodies with significant atmospheres, atmospheric effects also control the appearance or evolution of the surface and can be detected remotely. Table 6-1 lists the types of large-scale activity that are detectable on solid bodies; these are evidenced by observed motion, change over time (either by constant monitoring or by repeated observations), or morphologies known to be associated with specific activity such as lobate lava flow fronts.

The observability of these events depends on a number of factors, including instrument or optical properties such as resolution, imaging speed, or wavelength coverage or sensitivity; observing conditions such as viewing geometry and duration or periodicity of imaging; and system architecture properties such as memory capacity or downlink bandwidth. Detection of certain events on Earth and Mars can be confirmed by

Table 6-1. Detectable Activity in the Solar System

Body	**Detectable Activity***							
Earth	Eruptive Plumes	Volcanic Flows; including Landslides, Lahars, etc.	Cloud Motion	Dust Storms; Precipitation	Vortexes	Surface Color Change, including Vegetation	Ice Sheet or Iceberg Shifting	Thermal Changes
Mars			Cloud Motion	Dust Storms	Dust Devils	Dust Devil Tracks, Slope Streaks		
Io	Eruptive Plumes	Volcanic Flows (by color change)				Surface Color Change		Hotspots
Enceladus	Eruptive Plumes							Thermal Anomalies
Triton	Eruptive Plumes							
Comets or other small bodies	Outgassing							Thermal Anomalies†
Europa†	*Eruptive Plumes*	*Cryovolcanic Flows*				*Surface Color Change*	*Shifting Chaos Plates, Crack Propagation*	*Hotspots*

***by observed motion, change over time, or known associated morphology; not including otherwise inferred non-current activity, thus e.g., volcanic flows on Mars are not included**
† predicted possible

ground truth, a method for which there is no substitute when observing outer solar system bodies – causing an increased reliance on system performance. Also, for those examples of activity noted for Earth and Mars, the majority are quickly changing events which can be observed in real time, even remotely, to reveal motion. Motion is often inferred for activity seen on the other bodies as restrictions on observing sequences and data volume severely limit the concentration of study on any one feature; the lone exception to this is the sequence of five images taken over eight minutes of the Tvashtar plume on Io by New Horizons in 2007 (Spencer et al., 2007); this rapid imaging sequence allowed the visualization of particle motion within the plume (movie available at http://photojournal.jpl.nasa.gov/catalog/PIA09665; Figure 6-1). Definitive observation of these types of features requires long duration observation sequences at the expense of other science or data volume, close proximity at the expense of hazardous conditions, or investigations under uncertain conditions, as is the case for unexplored bodies.

6.2.1 Long Duration Investigations

Volcanic plumes and lava flows on Io (Lopes-Gautier et al., 1999) typify the interior composition of sulfur and silicates, respectively, and lend constraints on the internal pressures and temperatures necessary to produce massive eruptive events. High temperature eruptions affect their observability due to potential saturation of image exposures (i.e., Figure 6-2). These eruptions change the surface over time, making repeated observations over long periods necessary in order to fully understand internal dynamics. Repeated flybys at Io were limited during the Galileo mission due to the hazardous radiation conditions; avoidance precluded degradation of the spacecraft but made long duration monitoring campaigns impossible.

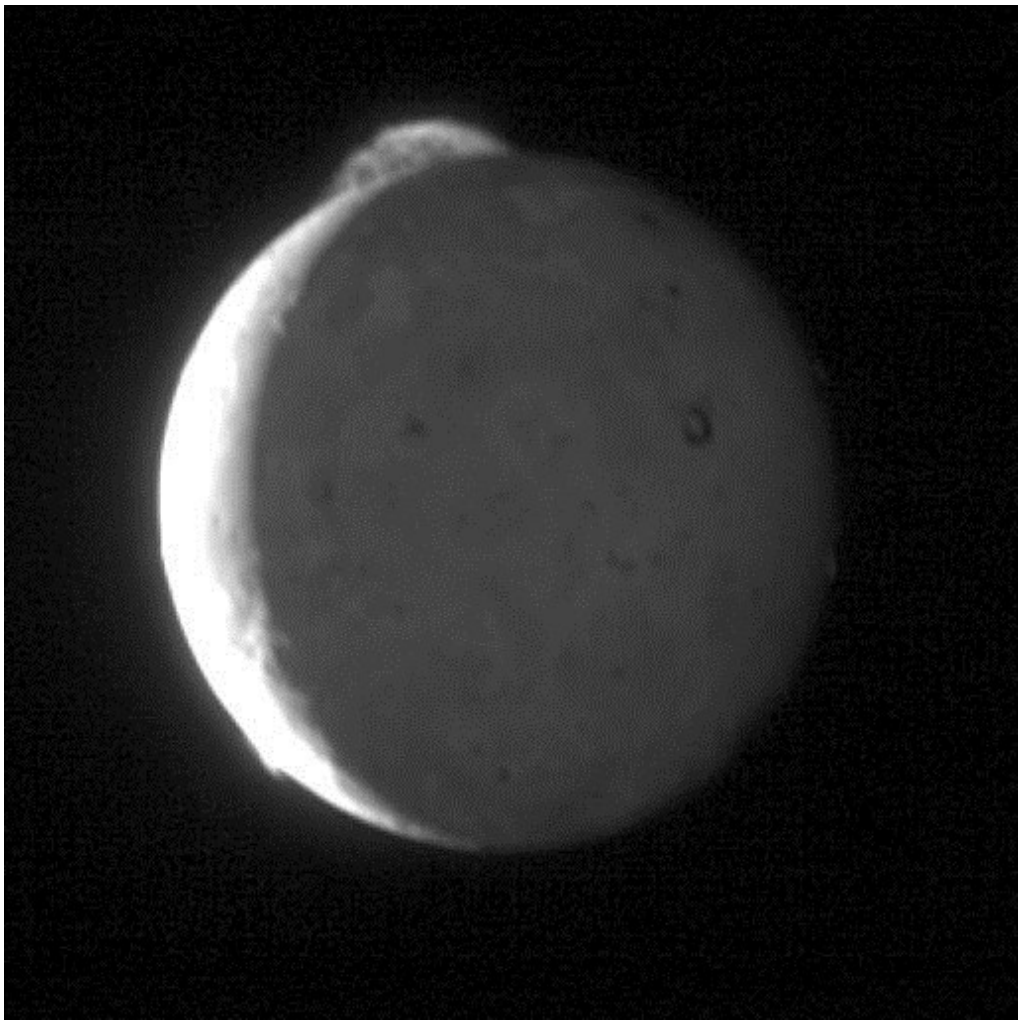

Figure 6-1. New Horizons view of Io's Tvashtar plume (top). Also visible are the Masubi and Zal plumes, at the lower left and upper left just below the Tvashtar plume, respectively. [NASA/Johns Hopkins University Applied Physics Laboratory/Southwest Research Institute]

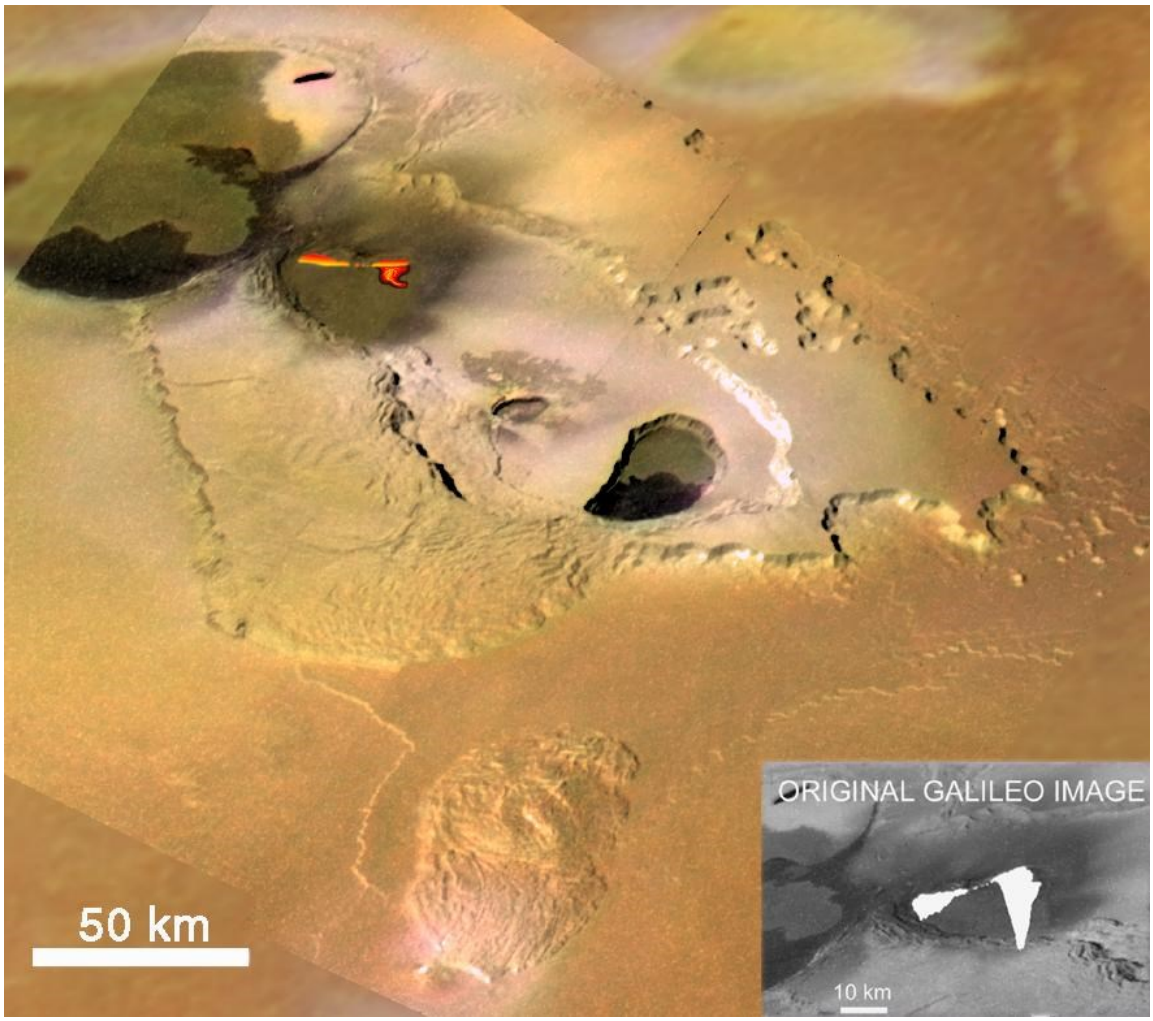

Figure 6-2. Saturation of an image due to extreme brightness. These views show Io's Tvashtar Catena; in the background is a corrected color composite of the image; the original saturated image is in the foreground image. Molten lava from the fire fountain eruption was hot and bright enough to overexpose Galileo's camera, causing electrons to "spill" down the camera's CCD chip leaving the white blur over the image. [NASA/JPL/University of Arizona]

Outgassing of comets or other small bodies (A'Hearn et al., 2011) must be monitored over long periods to estimate the mass flux of the body due to sublimation. Spacecraft views of these bodies are of short duration necessitated by high velocity flybys required to reach great distances from Earth; orbital maneuvers or subsequent flybys are intensely challenging in terms of fuel consumption or orbit dynamics or would be so greatly separated in time, if possible, that accurate mass yields would be ineffectual.

For Europa, the majority of possible activity would only be visible under long-term repeat observations. Any gaseous plumes detectable would require rapid sequence observations to reveal motion as in the case of New Horizons' view of Io's plumes or repeat imaging to observe change. Other types of activity, such as frost deposition or crack propagation could, in theory, be detected with a single pair of observations, though these would need to be conducted under exacting resolution and viewing conditions. Realistically, cost-mitigating optics systems and observing sequence plans would only be able to detect change over long periods after change has occurred incrementally so that the amount of change exceeds the value of error in observation.

6.2.2 Hazardous Conditions and Limited Mission Lifetime

High altitude volcanic plumes entrain material into the exosphere and plasma torus of Io, preventing close mission flybys due to the risk of encounters with hazardous materials. Similar conditions are observed at Enceladus, where the Cassini spacecraft has come into contact with the material being ejected from the south polar jets. The risk imposed by the diffusivity of the jet was a serious concern for mission planners and affected the trajectory plans for the spacecraft. Similar outgassing events have been detected at Triton (Smith et al., 1989, Soderblom et al., 1990) and several comets (e.g.,

A'Hearn et al., 2011), and likely exist at primitive asteroids and other bodies such as Pluto. These outgassing events represent internal changes of each body and range in appearance and size based on the parent body physical parameters and so are unpredictable, making encounter planning challenging. In the case of Pluto, which new Horizons will encounter in 2015, a field of dusty debris remaining from the formation of the system or from outgassing of the bodies, could detrimentally affect the spacecraft (see Figure 6-3); this risk requires that a flyby be conducted at distances greater than any expected debris field range in order to protect the spacecraft and thus limits resolution and quality of imaging. It should be noted that prolonged exposure to cold environments limits the performance of electronics, effectively decreasing the capabilities of missions like New Horizons over time and with distance outward from Earth, limiting performance during the Kuiper Belt observations phase even more than during the Pluto encounter.

Nowhere is a hazardous environment more controlling on spacecraft performance than at Venus. In this case, the extremely high temperature, pressure, and acidity of the atmosphere severely abbreviate the lifetime of a mission once a craft enters the atmosphere (see Figure 6-4). All three conditions negatively affect the performance of electronics such that no previous atmospheric probe or lander has survived longer than ~2 hours. This extremely short opportunity for observation, combined with the light time required to relay observations instructions to Venus from Earth, absolutely requires that observation sequences and other measurements be taken autonomously according to a pre-planned sequence that cannot be altered during the short duration of the mission. In the event of any malfunction, the craft must be able to intelligently react to the problem by resequencing, diverting power from a failing instrument to another for prolonged

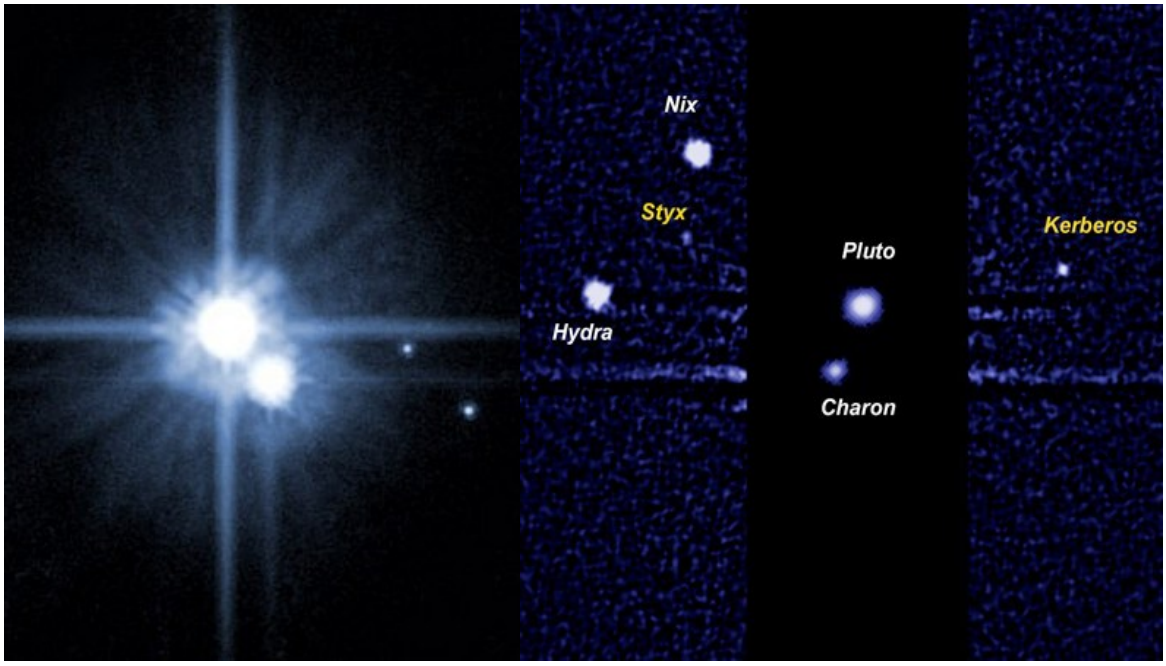

Figure 6-3. The Pluto system likely has a debris field which will impact the trajectory of New Horizons. This is supported by the difficulty in identifying additional satellites; the current total is 5. [NASA/ESA/JHUAPL/SwRI/HST]

Figure 6-4. Concept sketch of Venus In-Situ Explorer. [NASA]

alternative measurements, compensating for a missed observation with another from a different instrument, or saving or relaying data from a failing instrument prior to its demise so as to not lose data. An intricate system of fault reactions must be in place to compensate for increased failures as the mission progresses. Limited human interaction and problem solving time requires intelligent system architecture to work around unexpected problems and to quickly and effectively weigh risks to determine future actions.

6.2.3 Uncertain Environments

The serendipitous discoveries of active and transient geophysical events at Io (Morabito et al., 1979), Enceladus (Hansen et al., 2005, Johnson et al., 2005, Saur et al., 2005, Spencer et al., 2005, 2006), Triton (Smith et al., 1989, Soderblom et al., 1990), and comet nuclei (A'Hearn et al., 2011) have demonstrated the importance of opportunistic observations. Because these types of discovered activity lend important constraints to the interior dynamics of each respective planetary body (Smith et al., 1979; Lopes-Gautier et al., 1999; Porco et al., 2006; A'Hearn et al., 2011), they have become priority observations in order to establish a deeper understanding of planetary evolution. However, the uncertain nature of the activity itself limits potential observational scenarios. As seen in the observations of Io's and Enceladus' plume activity, it is not generally possible to predict when or if a body will exhibit signs of geophysical activity, thus planning observations specific to these events in advance is unlikely to succeed, except where activity has proven to be consistent. The ability to autonomously process observations onboard (Bue et al., 2007, Thompson et al., 2012; Lin et al., 2012) and redirect mission operations based on those results optimizes the science value of returned

data by maximizing opportunistic observations and preserving limited spacecraft memory and bandwidth for priority observations where activity is found or has changed from previous observations.

6.3 Previous Autonomous Successes

Recent successes in the application of onboard processing have enabled the Mars Exploration Rovers (MER) to track dust devil activity (A. Castano et al., 2008) and the Earth Observing One (EO-1) satellite to detect volcanic activity (Davies et al., 2007), to differentiate between surface materials (R. Castano et al., 2008), and to detect cryospheric changes (Doggett et al., 2006). In addition, missions such as the Swift x-ray telescope (XRT) have demonstrated reactive operations. Swift has the ability to prioritize observations; after the detection of an active Gamma Ray Burst (GRB) with the gamma ray telescope, the XRT automatically begins observing the x-ray afterglow of the burst, refines the position of the GRB within 10 seconds of target acquisition, and relays that information to Earth for immediate Earth-based spectroscopic observations (Gehrels et al., 2009).

This work has introduced and validated onboard science data analysis for opportunistic detection of time-varying phenomena such as volcanic plumes (Thompson et al., 2012) and was expanded to establish the capability of statistical techniques (cf. Lowe, 2004) to detect, identify, and classify events and surface features without *a priori* knowledge of the physical characteristics of a target body (Figure 6-5; Lin et al., 2012; Bunte et al., *in prep*). The wide range of observational scenarios and target appearance represented in Figure 1 illustrate the potential for a future mission to successfully make scientific discoveries autonomously.

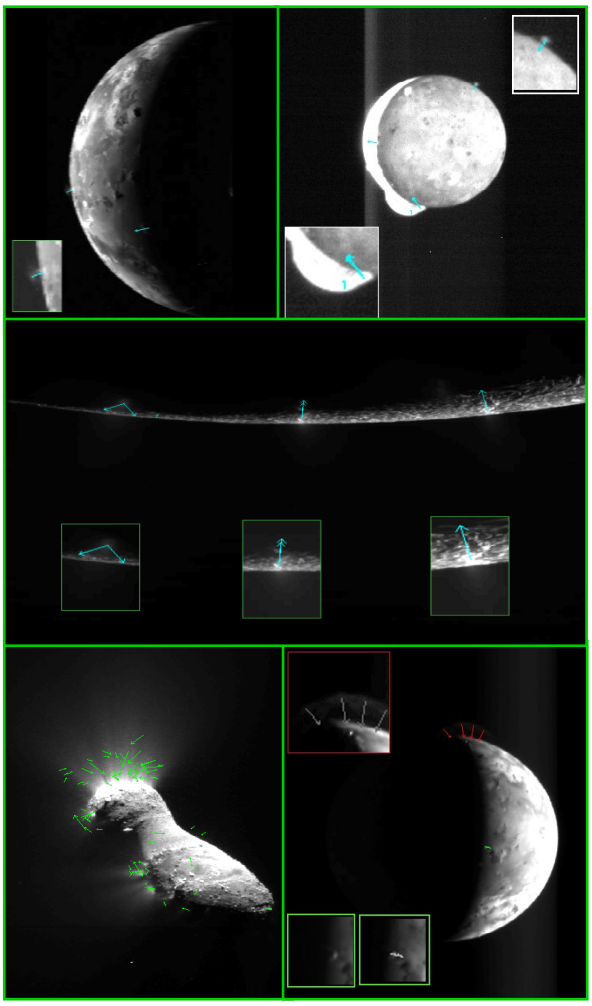

Figure 6-5. Autonomous statistical image analysis is capable of identifying time-varying phenomena and distinguishing between such phenomena and surface features. A-B) Volcanic plumes visible at the limb and terminator of Io are detectable in Galileo and New Horizons images; C) The source regions of Enceladus' jets are identifiable when brighter than surrounding terrain (Cassini image); D) The methods of Lin et al. (2012) and Bunte et al. (*in prep*.) can distinguish separate feature classes (red: plumes, green: mountains; Galileo image); E) Multiple jets are detectable in this EPOXI image of Comet Hartley 2.

6.4 Considerations for Future Technology Advancement or Flexible Systems

Current space missions do not process/analyze science data onboard and use that information to drive further science operations. Notable exceptions to this are EO-1 (Chien et al., 2005) and MER. For most missions, science data is downlinked and is subject to significant ground processing (resulting in delays) prior to science analysis. Typically, the mission plan is developed on the ground weeks or months in advance of execution. Pre-planning results in an inability to perpetuate further operations based on discovery. Current bandwidth limitations dictate the additional caveat that the data available for science is limited by downlink availability. Together, these conditions severely restrict the amount and value of high quality science data that can be acquired.

Onboard processing enables a novel paradigm of science operations, making possible a number of key breakthroughs:

1. **Science Prioritization:** It is possible to acquire and analyze large amounts of data without downlinking; additional data acquired can be searched for key signatures or events and only downlinked when these are found, as demonstrated for volcanic activity and cryospheric changes with EO-1 and dust devils with MER. Other prominent applications include searching for methane rain, geysers, or cryovolcanos on Titan or thermal anomalies or plumes on Europa.
2. **Resource Conservation:** In some cases, summary products that require less memory can be developed. This might mean collecting statistics on event occurrences or event maps rather than downlinking complete data.
3. **Reaction and Resilience:** It is possible to respond to events to capture more data, often with complementary instruments. For example, detecting change on

EO-1 triggers observations on subsequent overflights. For small icy bodies, detecting a thermal anomaly could trigger further observation or downlink of otherwise non-priority visible observations.

All of these capabilities could dramatically increase the science return of the mission with modest or no additional requirements. The novel mission concepts that can be developed in these areas address NASA's long term science goals for application to multiple missions.

6.5 Planned/Proposed Missions that Require Autonomy and Intelligence

Future work can mature systems for autonomous detection and response. Developing onboard analysis techniques for identification, classification, targeting and prioritization of data increases the extent of survey or monitoring campaigns without increasing downlink requirements. Developing models of potential activity and detectability would establish necessary requirements on distance, light gathering capability, limiting magnitudes for optics systems, and algorithm performance. Exploring mission requirements and defining encounter scenarios would enable us to meet or exceed science objectives despite uncertainties. Assessing prospective operations scenarios allows for informing mission design at the critical phase when instrumentation and trajectory decisions are being made and will contribute to paving the way for the next generation of low-cost, low-risk planetary exploration in which autonomy will be a critical enabling factor. In addition, it would help understand the amount of agile science afforded on small satellites meant to perform close-proximity and in situ observations as individual or daughter crafts on larger missions. This work is applicable to many current and proposed

planetary missions outlined in the planetary science decadal survey (Vision & Voyages, 2011) and the detection requirements for those missions, a selection of which follows.

6.5.1 Feature Recognition, Change Detection, and Tracking

The Canny edge-detection method (Canny, 1986) and the Difference of Gaussian method (Lindeberg, 1998; Lowe, 2004) discussed previously are both types of feature recognition software designed to identify certain qualities in an image. Using similar methods to automatically identify geologic structures or geophysical events in future exploration could be advantageous for several reasons. For example, comparisons of previous images with new images could yield change detection over a period of time, even without compensating for image quality, if the algorithm is designed to identify certain trends, i.e., linear features on Europa, and compare those trends to a database of known features at specific coordinates. This might be a computationally inexpensive way to save memory or downlink by relaying only detected changes such as the lengthening or widening of a lineament or a change in flank albedo or morphology; these would indicate changes due to tectonic stresses or the deposition or removal of surface material.

Formal experiments to monitor time-varying activity would enable the Io Volcano Observer (McEwen et al., 2012) to improve models of persistent plume activity or detect surface change (i.e., Figure 4-4) subsequent to previous mission observations in real-time. Real-time change detection would allow for autonomous response to observation content with the goal of retargeting future observations to further characterize the change. An ability to detect change and to autonomously re-task operations enables tracking of time-varying features, not only where targets exhibit prominent persistent activity like Io's active plumes, colored plume deposits, or color-changing flows, but also at asteroids

and comets that are outgassing on timescales much smaller than communications intervals and at other outer moons and small bodies where surface activity may be far less prominent. Those types of situations are likely to be encountered with a Trojan Tour and Rendezvous (Vision & Voyages, 2011) or with the future encounters for the Dawn project (Russell et al., 2006) and New Horizons.

The ability to recognize features also allows selective targeting of unexpected features. As demonstrated for outer solar system plumes, if an algorithm has the ability to recognize a plume or other form of outgassing, the importance of any image containing such a feature is upgraded and the spacecraft can then prioritize and save that data. This action, however, requires *a priori* knowledge of what important features look like in terms of visible imaging. Alternative applications are to identify higher or lower than expected thermal gradients, specific spectral signatures, or other characteristics that indicate the importance of activity.

6.5.2 Intelligent Autonomy, Reactive Operations, and Hazard Avoidance

Establishing detectability of geophysical events enables preparation for future encounters, starting with Rosetta's planned encounter with comet 67P/Churyumov-Gerasimenko in 2014 (Koschny et al., 2007). With the ability to autonomously interpret data, a spacecraft operating with recommended system architecture could react in real time to select ideal observations, optimize instrument operations and even update its trajectory. Rosetta's comet encounter will provide an exemplary suite of spectral and morphological data, which in turn will serve to identify surface locations of specific chemical content for the most time- and energy-efficient sample return collection (Vision & Voyages, 2011). Improved resilience would more effectively utilize the limited

operational lifetime of Venus In-Situ Explorer (Exploration Roadmap, 2006; Hoofs et al., 2009). This work would help evaluate the amount of intelligence that can be ascribed to in situ platforms and instruments (cf. autonomy of MER) to enhance the science return of missions that are time constrained. Detectability models would enable the New Horizons mission to plot trajectories for maximum observation quality at Pluto (Guo and Farquhar, 2005) and extended mission encounters.

6.5.3 Efficient Technology and Flexible Systems

As demonstrated in Chapters 4 and 5 (Thompson et al., 2012; Lin et al., 2012; Bunte et al., *in prep*.), understanding the capabilities of spacecraft instrumentation and algorithm operation is essential in efficiently gathering large volumes of data when downlink bandwidth is limited while ensuring a high science value return. Estimates of expected brightnesses impose limits on viewing conditions and estimates of detectable extent impose limits on instrument resolution and spacecraft range. Additionally, understanding the efficiency of expected detection rates and allowance for false positives or negatives allows resilience of the system in terms of balancing the study of known event types with opportunistic science. A level of flexibility in the system is necessary for this balance to occur, especially in situations where the target environment is unknown as is the case for asteroids, Kuiper Belt objects, distant comet nuclei or previously unobserved satellites in planetary systems, particularly the smallest satellites or rings.

6.6 Future Work

Employing autonomous methods of onboard data analysis for spacecraft missions is fairly novel, having only been employed on several crafts for specific purposes and where ground interaction is possible. Developing similar techniques with the goal of applying

them to missions where near-fully autonomous control is required or where specific autonomous actions are required to preserve power, memory, or downlink bandwidth will necessitate exhaustive testing and consideration of novel testbeds. Implementing flexible systems is essential to maximizing the engineering and science goals of any mission as well as reducing risk.

In support of the objectives of NASA's vision for solar system exploration (Exploration Roadmap, 2006), there must be investigation of technologies for autonomous action/reaction within spacecraft software architectures in regard to autonomous detection of time-varying geophysical events. *Model-driven* experiments designed to utilize onboard data analysis to measure time-varying planetary phenomena will allow for improving the knowledge of the state of the spacecraft and its environment, thus reducing operational risk and increasing the robustness of operations for the ensured success of future planetary missions. This will enable novel time-domain measurements, opening a window on dynamic processes at outer planet moons and primitive bodies. Further work will model a wide range of physical conditions that may be encountered at proposed targets, determine requirements for onboard systems pertaining to spacecraft and observation resilience, and then design onboard event detection and decision-making algorithms to test detection of these conditions.

Models to limit uncertainty in the occurrence and appearance of geophysical activity, ejected material, and surface morphology, thus enabling effectual spacecraft system architecture design are in development. Based on known and suspected conditions within planetary bodies thought to undergo geophysical activity similar to explosive volcanism on Io (Lopes-Gautier et al., 1999), or outgassing/exosphere activity on Enceladus (Porco

et al., 2006), Triton (Soderblom et al., 1990), or comets (A'Hearn et al., 2011), these models can explore the potential geophysical conditions of primitive planetary bodies such as Kuiper Belt objects, main-belt and Trojan asteroids, and small satellites and to assess how those conditions affect their immediate space environments. Of particular interest are the characteristics of eruptive, venting, or jetting activity, including the energy and volume of eruption, the temperature and albedo of eruptive materials, and the altitude and diffusivity of ejected material. Understanding these conditions enables predictions for the degree of risk during a spacecraft encounter and avoidance of hazards by determining safe approach distances, dictates the optimum viewing conditions, observation sequences and instrument measurements needed, and establishes the requirements of the onboard systems such as instrument array, responsiveness, observation and detection accuracy, and trajectory control. Developing strategies to optimize observations of small body activity is directly relevant to the understanding of the evolution of primitive bodies and can contribute to the development of smart instruments to be flown on future missions to the Kuiper Belt and Trojan clouds.

Visible imagery and spectral data can be utilized to model the range of appearances and chemical and thermal characteristics of known geophysical events. These include, but are not limited to: plumes, disrupted terrain such as chaos or cryovolcanic materials, ridges and faults, shorelines (i.e., Titan), known hotspots or locations of thermal uncertainty. Similarities in surface appearance and potential formation mechanisms lead to estimates for the degree of detectability of each event type. Knowing the extent of eruption products will constrain necessary imaging resolutions. Modeling thermal anomalies for events will constrain the spectral range of spectroscopic instruments that

may be employed in future missions. Estimating the periodicity of events will constrain observation exposure times and the need for repeated flybys or orbits at a particular body. Some advance knowledge of these types of needed observations will enable the development of appropriate spacecraft software to capture dynamic events in real-time.

6.7 Expected Outcome of Future Work

Based on modeling results, it will be possible to explore the detectability of modeled parameters for bodies whose activity is unknown and, by comparison to demonstrated detectability of known conditions at other bodies (Thompson et al., 2012; Lin et al., 2012; Bunte et al., *in prep*.), select techniques for onboard data processing to constrain the parameter space within available power and downlink capabilities; establish criteria and system functions to ensure rigorous detection, identification, and classification procedures; and assess the failure, fault, and autonomous recovery scenarios that would ensure maximum resilience and science return. Criteria include the capability to decide which measurements to take, determine content and usability of data, prioritize data for relay, and choose further observations based on the content of previous observations as well as respond to unknown discoveries or failures. With these advancements, every future mission (Figure 6-6) would be improved in terms of science quality and resource utilization.

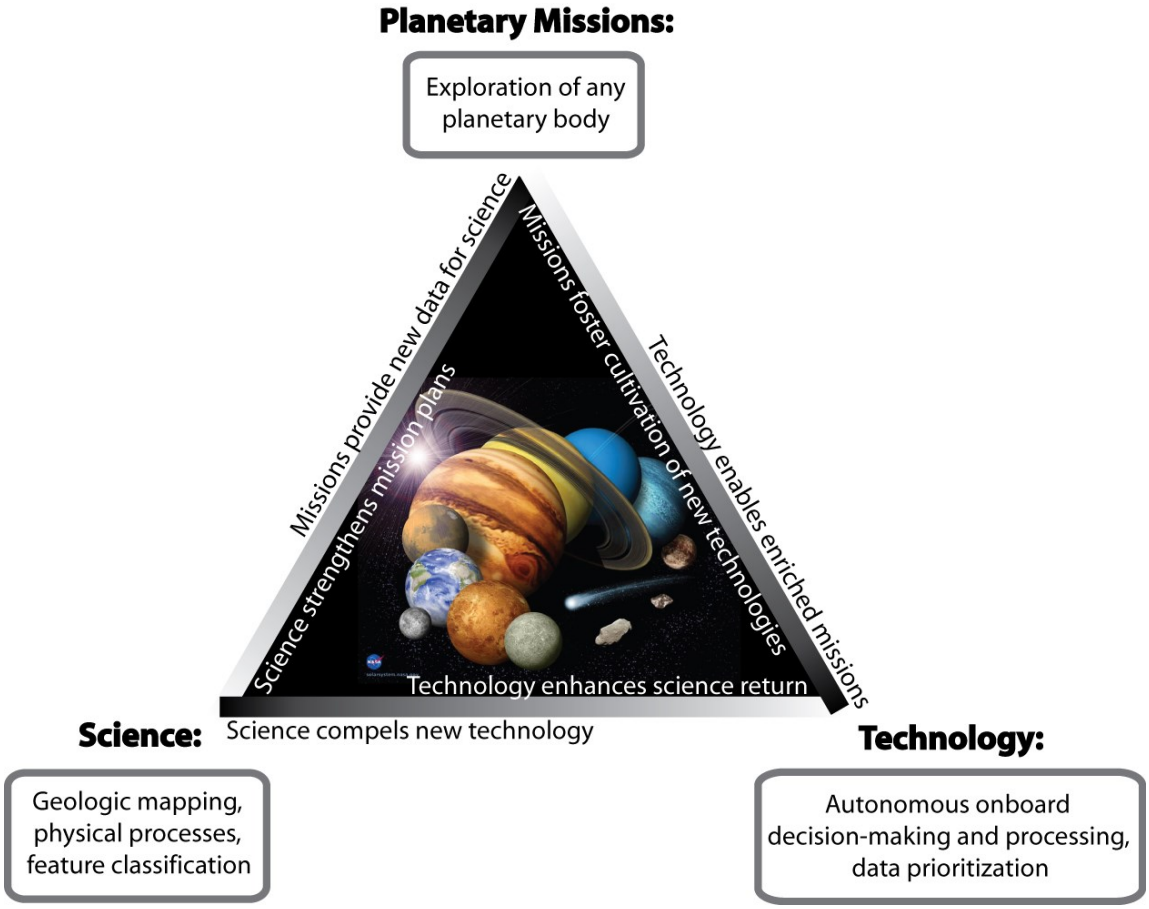

Figure 6-6. Synergy of Science and Technology to enhance the potential of any future exploration. [Background image: NASA/JPL]

REFERENCES

A'Hearn, M.F., Belton, M., Delamere, W., Feaga, L., Hampton, D., Kissel, J., Klaasen, K., McFadden, L., Meech, K., Melosh, H., Schultz, R., Sunshine, J., Thomas, P., Veverka, J., Wllnitz, D., Yeomans, D., Besse, S., Bodewits, D., Bowling, T., Carcich, B., Collines, S., Farnham, T. Groussin, O. Hermalyn, B., Kelley, m., Kelley, M., Li, J., Lindler, D., Lisse, C., McLaughlin, S., Merlin, F., Protopapa, S., Richardson, J., and Williams, J. 2011, EPOXI at Comet Hartley 2, *Science* 332, 1396.

Alexander, C., Carlson, R., Consolmagno, G., Greeley, R., and Morrison, D., 2009, The exploration history of Europa, In: *Europa* (Pappalardo, R.T., McKinnon, W.B., and Khurana, K., Eds.), pp. 3-26, University of Arizona Press, Tucson.

Anderson, J.D., Schubert, G., Jacobson, A., Lau, E.L., Moore, W.B., and Sjogen, W.L., 1998, Europa's differentiated internal structure: Inferences from four Galileo encounters, *Science*, 281, 2019-2022.

Aydin, A., 2006, Failure models of the lineaments on Jupiter's moon, Europa: Implications for the evolution of its icy crust, *Journal of Structural Geology*, 28, 2222-2236.

Barr, A.C., and Showman, A.P., 2009, Heat transfer in Europa's icy shell, In: *Europa* (Pappalardo, R.T., McKinnon, W.B., and Khurana, K., Eds.), pp. 405-430, University of Arizona Press, Tucson.

Batson, R.M., 1987, Digital cartography of the planets - New methods, its status, and its future, *Photogrammetric Engineering and Remote Sensing*, 53, 1211–1218.

Batson, R.M., 1990, Cartography, In: *Planetary Mapping* (Greeley, R., and Batson, R.M., Eds.), New York, Cambridge University Press, p. 60-95.

Becker, T.L., Archinal, B., Colvin, T.R., Davies, M.E., Gitlin, A., Kirk, R.L., and Weller, L., 2001, Final digital global maps of Ganymede, Europa, and Callisto, In: *Lunar and Planetary Science* XXXII, Abstract #2009, Lunar and Planetary Institute, Houston (CD-ROM).

Becker, T.L, Rosanova, T., Cook, D., Davies, M.E., Colvin, T.R., Acton, C., Bachman, N., Kirk, R.L., and Gaddis, L.R., 1999, Progress in improvement of geodetic control and production of final image mosaics for Callisto and Ganymede, In: *Lunar and Planetary Science* XXX, Abstract #1692, Lunar and Planetary Institute, Houston (CD-ROM).

Becker, T.L., Rosanova, T., Gaddis, L.R., McEwen, A.S., Phillips, C.B., Davies, M.E., and Colvin, T.R., 1998, Cartographic processing of the Galileo SSI data—An update

on the production of global mosaics of the Galilean satellites, In: *Lunar and Planetary Science* XXIX, Abstract #1892, Lunar and Planetary Institute, Houston (CD-ROM).

Belton, M.J.S., Klaasen, K.P., Clary, M.C., Anderson, J.L., Anger, C.D., Carr, M.H., Chapman, C.R., Davies, M.E., Greeley, R., Anderson, D., Bolef, L.K., Townsend, T.E., Greenberg, R., Head, J.W., III, Neukum, G., Pilcher, C.B., Veverka, J., Gierasch, P.J., Fanale, F.P., Ingersoll, A.P., Masursky, H., Morrison, D., and Pollack, J.B., 1992, The Galileo Solid-State Imaging Experiment, *Space Science Reviews*, 60, 413-455.

Belton, M.J.S., Head, J.W., III, Ingersoll, A.P., Greeley, R., McEwen, A.S., Klaasen, K.P., Senske, D., Pappalardo, R., Collins, G., Vasavada, A.R., Sullivan, R., Simonelli, D., Geissler, P., Carr, M.H., Davies, M.E., Veverka, J., Gierasch, P.J., Banfield, D., Bell, M., Chapman, C.R., Anger, C., Greenberg, R., Neukum, G., Pilcher, C.B., Beebe, R.F., Burns, J.A., Fanale, F., Ip, W., Johnson, T.V., Morrison, D., Moore, J., Orton, G.S., Thomas, P., and West, R.A., 1996, Galileo's first images of Jupiter and the Galilean satellites, *Science*, 274, 377-385.

Bierhaus, E.B., Chapman, C.R., and Merline, W.J., 2005, Secondary craters on Europa and implications for cratered surfaces, *Nature,* 437, 1125-1127.

Bierhaus, E.B., Chapman, C.R., Merline, W.J., Brooks, S.M., and Asphaug, E., 2001, Pwyll secondaries and other small craters on Europa, *Icarus,* 153, 264-276.

Bierhaus, E.B., Zahnle, K., and Chapman, C.R., 2009, Europa's crater distributions and surface ages, In: *Europa* (Pappalardo, R.T., McKinnon, W.B., and Khurana, K., Eds.), pp. 161-180, University of Arizona Press, Tucson.

Billings, S.E., and Kattenhorn, S.A., 2003, Comparison between terrestrial explosion crater morphology in gloating ice and Europan chaos, In: *Lunar and Planetary Science,* XXXIV, Abstract #1955, Lunar and Planetary Institute, Houston, TX.

Bills, B.G., Nimmo, F., Karatekin, O., van Hoolst, T., Rambaux, N., Levrard, B., and Laskar, J., 2009, Rotational dynamics of Europa, In: *Europa* (Pappalardo, R.T., McKinnon, W.B., and Khurana, K., Eds.), pp. 119-134, University of Arizona Press, Tucson.

Broxton, M.J., Moratto, Z.M., Nefian, A., Bunte, M., and Robinson, M.S., 2009, Preliminary Stereo reconstruction from Apollo 15 Metric Camera imagery, In: *Lunar and Planetary Science Conference* XL, Abstract #2282. Lunar and Planetary Institute, Houston, TX.

Bue, B., Wagstaff, K., Castano, R., and Davies, A., 2007, Automatic onboard detection of planetary volcanism from images, In: *Lunar and Planetary Institute Science Conference Abstracts, XXXVIII,* 1717, Houston, TX.

Bunte, M.K., Y. Lin, S. Saripalli, J. Bell, and R. Greeley *(in preparation) A*utonomous detection and classification of transient phenomena in the outer solar system.

Bunte, M., Thompson, D.R., Castano, R., Chien, S., Greeley, R., 2011, Enabling Europa science through onboard feature detection in hyperspectral images, In: *Lunar and Planetary Institute Science Conference Abstracts, XLII,* 1888, Houston, TX.

Campbell, B., Walker, G.A.H., Yang, S., 1988, A search for substellar companions to solar-type stars, *Astrophysical Journal,* 331, 902-921.

Canny, J., 1986. A computational approach to edge detection. *Institute of Electrical and Electronics Engineers Transactions on Pattern Analysis and Machine Intelligence 6,* 679-698.

Carlson, R.W., Johnson, R.E., and Anderson, M.S., 1999, Sulfuric acid on Europa and the radiolytic sulfur cycle, *Science,* 286, 97-99.

Carr, M.H., Belton, M.J.S., Chapman, C.R., Davies, M.E., Geissler, P., Greenberg, R., McEwen, A.S., Tufts, B.R., Greeley, R., Sullivan, R., Head, J.W., Pappalardo, R.T., Klaasen, K.P., Johnson, T.V., Kaufman, J., Senske, D., Moore, J., Neukum, G., Schubert, G., Burns, J.A., Thomas, P., and Veverka, J., 1998, Evidence for a subsurface ocean on Europa, *Nature,* 391, 363-365.

Cassen, P.M., Reynolds, R.T., and Peale, S.J., 1979, Is there liquid water on Europa? *Geophysical Research Letters, 6,* 731-734.

Cassen, P.M., Peale, S.J., and Reynolds, R.T., 1982, Structure and thermal evolution of the Galilean satellites. In *Satellites of Jupiter* (D. Morrison, ed.), pp. 93-128. University of Arizona Press, Tucson.

Castano, A., Fukunaga, A., Biesiadecki, J., Neakrase, L., Whelley, P., Greeley, R., Lemmon, M., Castano, R., and Chien, S., 2008, Automatic detection of dust devils and clouds on Mars, *Machine Vision and Applications,* 19, 467-482.

Castano, R., Wagstaff, K., Gleeson, D., Pappalardo, R., Chien, S., Tran, D., Scharenbroich, L., Tang, B., Bue, B., and Doggett, T., 2008, Onboard detection of active Canadian sulfur springs, *International Symposium on Artificial Intelligence, Robotics, and Automation in Space,* Universal City, CA.

Chapman, C.R., Merline, W.J., Bierhaus, B., and Brooks, S., 1998, Cratering in the jovian system: Intersatellite comparisons. In: *Lunar and Planetary Science* XXIV, Abstract #1927, Lunar and Planetary Institute, Houston, TX.

Chien, S., Sherwood, R., Tran, D., Cichy B., Rabideau, G., Castano, R., Davies, A., Mandl, D., Frye, S., Trout, B., Shulman, S., and Boyer, D., 2005, Using autonomy flight software to improve science return on Earth Observing One, *Journal of*

Aerospace Computing, Information, and Communication April 2005. JPL Clearance Number CL #05-0079.

Clark, K.B., 2007, Europa Explorer-An exceptional mission using existing technology, *Institute of Electrical and Electronics Engineers Aerospace Conference,* 3-10, 1.

Collins, G.C., Head, J.W., Pappalardo, R.T., and Spaun, N.A., 2000, Evaluation of models for the formation of chaotic terrain on Europa, *Journal of Geophysical Research,* 105, 1709-1716.

Collins, G., and Ninimo, F., 2009, Chaotic terrain on Europa, In: *Europa* (Pappalardo, R.T., McKinnon, W.B., and Khurana, K., Eds.), pp. 259-282, University of Arizona Press, Tucson.

Consolmagno, G.J., 1975, *Thermal History Models of Icy Satellites.* M.S. Thesis, Massachusetts Institute of Technology, Cambridge. 202 pp.

Consolmagno, G.J., and Lewis, J.S., 1976, Structural and thermal models of icy Galilean satellites. In *Jupiter* (T.A. Gehrels, ed.), pp. 103 5-1051. University of Arizona Press, Tucson.

Consolmagno, G.H., and Lewis, J.S., 1977, Preliminary thermal history models of icy satellites, In *Planetary Satellites* (J.A. Burns, ed.), pp. 492-500. University of Arizona Press, Tucson.

Consolmagno, G.J., and Lewis, J.S., 1978, The evolution of icy satellite interiors and surfaces, *Icarus,* 34, 280-293.

Cook, A.F., Shoemaker, E.M., and Smith, B.A., 1979, Dynamics of volcanic plumes on Io, *Nature,* 280, 743-746.

Cover, T.M., Hart, P.E., 1967. Nearest Neighbor pattern classification, *Institute of Electrical and Electronics Engineers Transactions on Information Theory,* 13(1), 21-27.

Cox, R., Ong. L.C.F., and Arakawa, M., 2005, Is chaos on Europa caused by crust penetrating impacts? In: *Lunar and Planetary Science,* XXXVI, Abstract #2101, Lunar and Planetary Institute, Houston, TX.

Crawford, G.D. and Stevenson, D.J., 1988, Gas-driven water volcanism in the resurfacing of Europa. *Icarus,* 73, 66-79.

Dalton, J.B., Mogul, R., Kagawa, H.K., Chan, S.L., and Jamieson, C.S., 2003, Near infrared detection of potential evidence for microscopic organisms on Europa, *Astrobiology,* 3, 505-529.

Dalton, J.B., 2010, Spectroscopy of icy moon surface materials, *Space Science Reviews*, 153, 219-247, doi:10.1007/sl1214-010-9658-7.

Danielson, E. G., Kupferman, P. N., Johnson, T. V., and Soderblom, L. A.., 1981, Radiometric performance of the Voyager cameras, *Journal of Geophysical Research,* 86, 8683-8689.

Davies, A.G., Castano, R., Chien, S., Tran, D., and Mandrake, L., 2007, Rapid response to volcanic eruptions with an autonomous SensorWeb: the Nyamulagira eruption of 2006. *Institute of Electrical and Electronics Engineers Transactions on Automatic Control* #1180, version 7, updated November 18, 2007.

Davies, E., 2011, 'Brinicle'ice finer of death filmed in Antarctic, *BBC Nature*, http://www.bbc.co.uk/nature/15835017, updated November 23, 2011.

Davies, M.E., Abalakin, V.K., Bursa, M., Lieske, J.H., Morando, B., Morrison, D., Seidelmann, P.K., Sinclair, A.T., Yallop, B., and Tjuflin, Y.S., 1996, Report of the IAU/IAG/COSPAR Working Group on cartographic coordinates and rotational elements of the planets and Satellites, *Celestial Mechanics and Dynamical Astronomy,* 63, 127-148.

Davies, M.E., Colvin, T.R., Oberst, J., Zeitler, W., Schuster, P., Neukum, G., McEwen, A.S., Phillips, C.B., Thomas, P.C., Veverka, J., Belton, M.J.S., and Schubert, G., 1998, The control networks of the Galilean satellites and implications for global shape, *Icarus,* 135, 372-376.

Davies, M.E., and Katayama, F.Y., 1981, Coordinates of features on the Galilean Satellites, *Journal of Geophysical Research,* 86, 8635-8657.

Des Marais, D.J., Allamandola, L.J., Benner, S.A., Boss, A.P., Deamer, D., Falkowski, P.G., Farmer, J.D., Hedges, S.B., Jakosky, B.M., Knoll, A.H., Liskowsky, D.R., Meadows, V.S., Meyer, M.A,, 2003, The NASA astrobiology roadmap, *Astrobiology,* 2,219-235.

Doggett, T., Greeley, R., Figueredo, P., and Tanaka, K., 2009, Geologic stratigraphy and evolution of Europa's surface, In: *Europa* (Pappalardo, R.T., McKinnon, W.B., and Khurana, K., Eds.), pp. 137-159, University of Arizona Press, Tucson.

Doggett, T., Greeley, R., Chien, S., Castano, R., Cichy, B., Davies, A.G., Rabideau, G., Sherwood, R., Tran, D., Baker, V., Dohm, J., and Ip, F., 2006, Autonomous detection of cryospheric change with Hyperion onboard Earth Observing-1, *Remote Sensing of Environment* 101 (4), 447-462.

Eliason, E.M., 1997, Production of digital image models using the ISIS system, In: *Lunar and Planetary Science* XXVIII, Lunar and Planetary Institute, Houston, p. 331.

ESA, 2005, Cosmic vision: Space science for Europe 2015-2025. ESA brochure BR-247, ESA Publications Division, ESTEC, Noordwijk, The Netherlands.

Europa Study Team, 2012, Europa Multiple Flyby Mission Study Report, Task Order NM0711062 Outer Planets Flagship Mission, NASA.

Fagents, S.A., Kadel, S.D., Greeley, R., Kirk, R.L., and the Galileo SSI Team, 1998, Styles of cryovolcanism on Europa: Summary of evidence from the Galileo nominal mission, In: *Lunar and Planetary Science,* XXIX, Abstract #1721, Lunar and Planetary Institute, Houston, TX.

Fagents, S.A., Greeley, R., Sullivan, R.J., Pappalardo, R.T., Prockter, L.M., and the Galileo SSI Team, 2000, Cryomagmatic mechanisms for the formation of Rhadamanthys Linea, triple band margins, and other low-albedo features on Europa, *Icarus,* 144, 54-88.

Fagents, S.A., 2003, Considerations for effusive cryovolcanism on Europa: The post-Galileo *perspective, Journal of Geophysical Research,* 108, 10.1029/2003 JE002128.

Figueredo, P.H., Hare, T., and Greeley, R., 2006, Global sequencing of Europan lineaments: A stratigraphic framework, *unpublished manuscript.*

Figueredo, P.H., Hare, T., Ricq, E., Strom, K., Greeley, R., Tanaka, K., and Senke, D., 2004, Europa's northern trailing hemisphere: Lineament stratigraphic framework, *Lunar and Planetary Science Conference* XXXV, #1118, Houston, TX.

Figueredo, P.H., and Greeley, R., 2000, Geologic mapping of the northern leading hemisphere of Europa from Galileo solid-state imaging data, *Journal of Geophysical Research,* 105, 22,629-22,646.

Figueredo, P.H., Chuang, F.C., Rathbun, J., Kirk, R.L., and Greeley, R., 2002, Geology and origin of Europa's "Mitten" feature (Murias Chaos), *Journal of Geophysical Research,* 107, 10.1029/2001JEOO1591.

Figueredo, P.H., and Greeley, R., 2004, Resurfacing history of Europa from pole-to-pole geological mapping, *Icarus,* 167, 287-312.

Fimmel, R.O., Swindell, W., and Burgess, E., 1977, *Pioneer Odyssey: Encounter with a giant,* NASA SP-349, NASA Scientific and Technical Information Office, Washington, D.C.

Fimmel, R.O., Van Allen, J.A., and Burgess, E., 1980, *Pioneer: First to Jupiter, Saturn and Beyond.* NASA SP-446, NASA Scientific and Technical Information Office, Washington, D.C.

Fischler, M.A., Bolles, R.C., 1981. Random sample consensus. *Communications of the ACM,* 24, 381-395.

Gaddis, L.R., Anderson, J., Becker, K., Becker, T.L., Cook, D., Edwards, K., Eliason, E.M., Hare, T., Kieffer, H.H., Lee, E.M., Mathews, J., Soderblom, L.A., Sucharski, T., Torson, J., McEwen, A.S., Robinson, M., 1997, An overview of the Integrated Software for Imaging Spectrometers (ISIS), In: *Lunar and Planetary Science* XXVIII, Lunar and Planetary Institute, Houston, p. 387.

Gaidos, E.J., and F. Nimmo, 2000, Tectonics and water on Europa, *Nature,* 405, 637.

Galilei, G., 1610, *Siderius Nuncius,* Translated by E.S. Carlos (1929) in *A Source Book in Astronomy* (H. Shapley and Howarth, Eds.), McGraw-Hill, New York.

Gehrels, N., Ramirez-Ruiz, E., and Fox, D.B., 2009, Gamma-ray bursts in the Swift era, *Annual Review of Astronomy and Astrophysics,* 47, 567-617.

Geissler, P.E., and Goldstein, D.B., 2007, Plumes and their deposits, In: *Io After Galileo: A New View of Jupiter's Volcanic Moon,* (Lopes, R.M.C., Spencer, J.R., Eds.) Springer Praxis, 162-192.

Geissler, P.E., Greenberg, R., Hoppa, G., Helfenstein, P., McEwen, A., Pappalardo, R.T., Tufts, R., Ockert-Bell, M., Sullivan, R., Greeley, R., Belton, M.J.S., Denk, T., Clark, B., Burns, J., Veverka, J, and the Galileo Imaging Team, 1998a, Evidence for nonsynchronous rotation of Europa, *Nature,* 391, 368-370.

Geissler, P., Greenberg, R., Hoppa, G., McEwen, A., Tufts, R., Phillips, C., Clark, B., Ockert-Bell, M., Helfenstein, P., Burns, J., Veverka, J., Sullivan, R., Greeley, R., Pappalardo, R.T., Head, J.W., Belton, M.J.S., Denk, T., and the Galileo Imaging Team, 1998b, Evolution of lineaments on Europa: Clues from Galileo multispectral imaging observations, *Icarus,* 135, 107-126.

Greeley, R., Pappalardo, R.T., Prockter, L.M., Hendrix, A., and Lock, R.E., 2009, Future exploration of Europa, In: *Europa* (Pappalardo, R.T., McKinnon, W.B., and Khurana, K., Eds.), pp. 655-695, University of Arizona Press, Tucson.

Greeley, R., Sullivan, R., Coon, M.D., Geissler, P.E., Tufts, B.R., Head, J.W., Pappalardo, R.T., and Moore, J.M., 1998a, Terrestrial sea ice morphology: Considerations for Europa. *Icarus,* 135, 25-40.

Greeley, R., Sullivan, R., Klemaszewski, J., Homan, K., Head, J.W., III, Pappalardo, R.T., Veverka, J., Clark, B.E., Johnson, T.V., Klaasen, K.P., Belton, M., Moore, J., Asphaug, E., Carr, M.H., Neukum, G., Drek, T., Chapman, C.R., Pilcher, C.B., Geissler, P.E., Greenberg, R., and Tufts, R., 1998b, Europa: initial Galileo geologic observations, *Icarus,* 135, 4-24.

Greeley, R., Figueredo, P.H., Williams, D.A., Chuang, F.C., Klemaszewski, I.E., Kadel, S.D., Prockter, L.M., Pappalardo, R.T., Head, J.W., III, Collins, G.C., Spaun, N.A., Sullivan, R.J., Moore, J.M., Senske, D.A., Tufts, B.R., Johnson, T.V., Belton, M.J.S.,

and Tanaka, K.L., 2000, Geologic mapping of Europa, *Journal of Geophysical Research,* 105, 22559-22578.

Greeley, R., Chyba, C.F., Head, J.W., III, McCord, T.B., McKinnon, W.B., Pappalardo, R.T., and Figueredo, P.H., 2004, Geology of Europa, In *Jupiter - The Planet, Satellites and Magnetosphere,* (Bagnel, F., Dowling, T.E., and McKinnon, W.B., Eds.), Cambridge University Press, Cambridge, pp. 329-362.

Greeley, R., Fink, J.H., Gault, D.E. and Guest, I.E., 1982, Experimental simulation of impact cratering on icy satellites, In: *Satellites of Jupiter,* (Morrison, D., Ed.), 340-378.

Greenberg, R., 1982, Orbital evolution of the Galilean satellites, In *Satellites of Jupiter* (Morrison, D., Ed.), pp.65-92. University of Arizona Press, Tucson.

Greenberg, R., 1987, Galilean satellites: Evolutionary paths in deep resonance, *Icarus,* 70, 334-347.

Greenberg, R. and Weidenschilling, S.J., 1984, How fast do Galilean satellites spin?, *Icarus,* 58, 186-196.

Greenberg, R., Geissler, P., Hoppa, G., Tufts, B.R., Durda, D.D., Pappalardo, R., Head, J.W., Greeley, R., Sullivan, R., and Carr, M.H., 1998, Tectonic processes on Europa: Tidal stresses, mechanical response, and visible features, *Icarus,* 135, 64-78.

Greenberg, R., Hoppa, B.R., Tufts, B.R., Geissler, P., Riley, J. and Kadel, S., 1999, Chaos on Europa, *Icarus,* 141, 263-286.

Greenberg, R., 2004, The evil twin of Agenor: Tectonic convergence on Europa. *Icarus,* 58, 186-196.

Greenberg, R., Geissler, P., Hoppa, G., and Tufts, B.R., 2002, Tidal-tectonic processes and their implications for the character of Europa's icy crust, *Reviews of Geophysics,* 40, 1.1-1.33.

Greenberg, R., Leake, M.A., Hoppa, G.V., and Tufts, B.R., 2003, Pits and uplifts on Europa, *Icarus,* 161, 102-126.

Guo, Y. and Farquhar, R.W., 2005, New Horizons Pluto-Kuiper Belt Mission: Design and simulation of the Pluto-Charon encounter, *Acta Astronautica* 56, 421-429.

Hand, K.P., Chyba, C.F., Priscu, J.C., Carlson, R.W., and Nealson, K.H., 2009, Astrobiology and the potential for life on Europa, In: *Europa* (Pappalardo, R.T., McKinnon, W.B., and Khurana, K., Eds.), pp. 589—629, University of Arizona Press, Tucson.

Hand, K.P., and Chyba, C.P., 2007, Empirical constraints on the salinity of the Europan ocean and implications for a thin ice shell, *Icarus,* 189, 434-438.

Hansen, C.J., Hendrix, A., Esposito, L., Colwell, J., Shemansky, D., Pryor, W., Stewart, I., and West, R., 2005, Cassini UltraViolet Imaging Spectrograph (UVIS) observations of Enceladus' plume. *American Geophysical Union Fall Meeting 2005,* Abstract P21F-04.

Hansen, C.J., Esposito, L., Stewart, A.I.F., Colwell, J., Hendrix, A., Pryor, W., Shemansky, D., and West, R., 2006, Enceladus' water plume, *Science,* 311, 1422-1425.

Hauck, S.A., Phillips, R.J., and Price, M.H., 1998, Venus: Crater distribution and plains resurfacing models. *Journal of Geophysical Research,* 103, 13635-13642.

Head, J.W., Adams, J.B., McCord, T.B., Pieters, C., and Zinsk, S., 1978, Regional stratigraphy and geologic history of Mare Crisium, In: *Mare Crisium: The view from Luna 24* (Merrill, R.B., and Papike, J.J., Eds.), Peragamon Press, New York, p. 43-74.

Head, J.W., Pappalardo, R.T., Greeley, R., Sullivan, R., Pilcher, C., Schuber. G., Moore, W., Carr, M., Moore, J., Belton, M.J.S., 1997, Evidence for recent solid-state convection on Europa: the nature of pits, domes, spots, and ridges, *Bulletin of the American Astronomical Society,* 29, 983.

Head, J.W., Sherman, N.D., Pappalardo, R.T., Greeley, R., Sullivan, R., Senske, D.A., McEwen, A., and the Galileo Imaging Team, 1998, Geologic history of the E4 region of Europa: Implications for ridge formation, cryovolcanism, and chaos formation, In: *Lunar and Planetary Science* XXIX, Abstract #1412, Lunar and Planetary Institute, Houston, TX.

Head, J.W., Pappalardo, R.T., Prockter, L.M., Spaun, N.A., Collins, G.C., Greeley, R., Klemaszewski, J., Sullivan, R., Chapman, C., and the Galileo SSI Team, 1999a, Europa: recent geologic history from Galileo observations, In: *Lunar and Planetary Science* XXX, Abstract #1404, Lunar and Planetary Institute, Houston, TX.

Head, J.W., Pappalardo, R.T., and Sullivan, R., 1999b, Europa: morphological characteristics of ridges and triple bands from Galileo data (E4 and E6) and assessment of a linear diapirism model, *Journal of Geophysical Research,* 104, 24233-24235.

Head, J.W., and Pappalardo, R.T., 1999, Brine mobilization during lithospheric heating on Europa: implication for formation of chaos terrain, *Journal of Geophysical Research,* 104, 27143-27156.

Hedman, M.M., Gosmeyer, C.M., Nicholson, P.D., Sotin, C., Brown, R.H., Clark, R.N., Baines, K.H., Buratti, B.J., and Showalter, M.R., 2013, An observed correlation between plume activity and tidal stresses on Enceladus, *Nature,* 500, 182-184.

Helfenstein, P. and Parmentier, E.M., 1980, Fractures on Europa - Possible response of an ice crust to tidal deformation, In: *Proceedings of the Lunar and Planetary Science Conference 11th,* 1987-1998, Houston, TX.

Helfenstein, P. and Parmentier, E.M., 1983, Patterns of fracture and tidal stresses on Europa, *Icarus,* 53,415-430.

Helfenstein, P. and Parmentier, E.M., 1985, Patterns of fracture and tidal stresses due to nonsynchronous rotation - Implications for fracturing on Europa, *Icarus,* 61, 175-184.

Hoofs, R.M.T., Titov, D., Svedhem, H., Koschny, D., Witasse, O., and Tanco, I., 2009, Venus Express - Science observations experience at Venus, *Acta Astronautica* 65, 987-1000.

Hoppa, G.V., Tufts, R.B., Greenberg, R. and Geissler, P.E., 1999a, Formation of cycloidal features on Europa, *Science,* 285, 1899-1902.

Hoppa, G.V., Greenberg, R. Geissler, P., Tufts, B.R., Plassmann, J., and Durda, D.D., 1999b, Rotation of Europa: Constraints from terminator and limb positions, *Icarus,* 137, 341-347.

Hoppa, G.V., Tufts, B.R., Greenberg, R., and Geissler, P.E., 1999c, Strike-slip faults on Europa: Global shear patterns driven by tidal stress, *Icarus,* 141, 287-298.

Hurford, T.A., Sarid, A.R., and Greenberg, G., 2007, Cycloidal cracks on Europa: Improved modeling and nonsynchronous rotation implications, *Icarus,* 186, 218-233.

Hurford, T.A., Bills, B.G., Sarid, A.R., and Greenberg, R., 2006, Unraveling Europa's tectonic history: Evidence for a finite obliquity? In: *Lunar and Planetary Institute Science Conference Abstracts, XXXVII,* #1303, Houston, TX.

Hussman, H, Spohn, T., and Wieczerkowski, K., 2002, Thermal equilibrium states of Europa's ice shell: Implications for internal ocean thickness and surface heat flow, *Icarus,* 156, 143-151.

Jeffreys, H., 1923, The constitution of the four outer planets, *Monthly Notices of the Royal Astronomical Society,* 83, 350-354.

Johnson, T.V., Matson, D.L., Blaney, D.L., Veeder, G.J., and Davies, A., 1995, Stealth plumes on Io, *Geophysical Research Letters,* 22, 3293-3296.

Johnson, T., 2005, Imaging Enceladus' exotic south polar regions: Imaging science team results. *American Geophysical Union Fall Meeting 2005.* Abstract P21F-03.

The JUICE Science Study Team, 2012. JUICE Assessment Study Report (Yellow Book). ESA/SRE (2011) 18. European Space Agency.

The JUICE Science Study Team, 2012. JUICE Science Requirement Matrix. European Space Agency.

Kadel, S.D., Fagents, S.A., and Greeley, R., 1998, Trough-bounding ridge pairs on Europa - considerations for an endogenic model of formation, In: *Lunar and Planetary Science* XXIX, Abstract #1078, Lunar and Planetary Institute, Houston, TX.

Kadel, S.D., Chuang, F.C., Greeley, R., Moore, J.C., and the Galileo SSI team, 2000, Geologic history of the Tyre region of Europa: a regional perspective on Europan surface features and ice thickness, *Journal of Geophysical Research,* 105, 22657-22669.

Kargel, J.S., 1991, Brine volcanism and the interior structures of asteroids and icy satellites, *Icarus,* 94, 368-390.

Kargel, J.S., Furfaro, R., Prieto-Ballesteros, O., Rodriguez, J.A.P., Montgomery, D.R., Gillespie, A.R., Marion, G.M., and Wood, S.E., 2007, Martian hydrogeology sustained by thermally insulating gas and salt hydrates. *Geology,* 35, 975-978.

Kargel, J.S., Kaye, J.Z., Head, J.W.I., Marion, G.M., Sassen, R., Ballesteros, O.P., Grant, S.A., and Hogenboom, D.L., 2000, Europa's crust and ocean: Origin, composition, and the prospects for life, *Icarus,* 148, 226-265.

Kattenhorn, S.A., and Hurford, T., 2009, Tectonics of Europa, In: *Europa* (Pappalardo, R.T., McKinnon, W.B., and Khurana, K., Eds.), pp. 199-236, University of Arizona Press, Tucson.

Kattenhorn, S.A., 2002, Nonsynchronous rotation evidence and fracture history in the bright plains region, Europa, *Icarus,* 157, 490-506.

Kattenhorn, S.A., 2004, Strike-slip fault evolution on Europa: Evidence from tail-crack geometries, *Icarus,* 172, 582-602.

Kelley, D.S., Karson, J.A., Blackman, D.K., Fruh-Green, G.L., Butterfield, D.A., Lilley, M.D., Olson, E.J., Schrenk, M.O., Roe, K.K., Lebon, G.T., Rivizzigno, P., and the AT3-60 Shipboard Party, 2001, An off-axis hydrothermal vent field near the Mid-Atlantic Ridge at 30° North, *Nature,* 412, 145-149.

Keszthelyi, L., McEwen, A.S., Phillips, C.B., Milazzo, M., Geissler, P., Turtle, E.P., Radebaugh, J., Williams, D.A., Simonelli, D.P., Breneman, H.H., et al., 2001, Imaging of volcanic activity on Jupiter's moon Io by Galileo during the Galileo Europa Mission and the Galileo Millennium Mission, *Journal of Geophysical Research,* 106, 33025-33052.

Khurana, K.K., Kivelson, M.G., Stevension, D.J., Schubert, G., Russell, C.T., Walker, R.J., and Polanskey, C., 1998, Induced magnetic fields as evidence for subsurface oceans on Europa and Callisto, *Nature,* 395, 777-780.

Kieffer, S.W., 1982, Dynamics and thermodynamics of volcanic eruptions: Implications for the plumes of Io. In: *Satellites of Jupiter* (Morrison, D., Ed.), University of Arizona Press, Tucson, AZ, pp. 647-723.

Kieffer, S.W., Lopes-Gautier, R., McEwen, A., Smythe, W., Keszthelyi, L., and Carlson, R., 2000, Prometheus: Io's wandering plume, *Science,* 288, 1204-1208.

Kirk, R.L., Thompson, K.T., Becker, T.L., and Lee, E.M., 2000, Photometric modeling for planetary cartography, In: *Lunar and Planetary Science* XXXI, Abstract #2025, Lunar and Planetary Institute, Houston.

Kirk, R.L., Soderblom, L.A., Brown, R.H., Kieffer, S.W., Kargel, J.S., 1995. Triton's Plumes: Discovery, characteristics and models. In: *Neptune and Triton* (Cruikshank, D.P., Matthews, M.S., and Schumann, A.M., Eds.), pp. 949-989, University of Arizona Press, Tucson.

Kivelson, M.G., Khurana, K.K., Stevenson, D.J., Bennett, L., Joy, S., Russell, C.T., Walker, R.J., Zimmer, C., and Polanskey, C., 1999, Europa and Callisto: Induced or intrinsic magnetic fields in a periodically varying plasma environment, *Journal of Geophysical Research,* 104, 4609-4626.

Kivelson, M.G., Khurana, K.K., Russell, C.T., Volwerk, M, Walker, R.J., and Zimmer, C., 2000, Galileo magnetometer measurements: A stronger case for a subsurface ocean at Europa, *Science,* 289, p. 1340-1343.

Klemaszewski, J.E., Greeley, R., Prockter, L.M., Geissler, P.E., and the Galileo SSI team, 1999, Geologic mapping of eastern Agenor Linea, Europa, In: *Lunar and Planetary Science* XXX, Abstract #1680, Lunar and Planetary Institute, Houston, TX.

Koschny, D., Dhiri, V., Wirth, K., Zender, J., Solaz, R., Hoofs, R., Laureijs, R., Ho, T.-M., Davidsson, B., and Schwehm, G., 2007, Scientific planning and commanding of the Rosetta payload, *Space Science Reviews,* 128, 167-188.

Laplace, P.S., 1805, *Traite de Mechanique Celeste, Vol. 4.* De Crapelet, Paris. 548 pp. A treatise in celestial mechanics, v. 4, Bowditch, N. (trans.), 1966, Chelsea Publishing Company, New York.

Leith, A.C., and McKinnon, W.B., 1996, Is there evidence for polar wander on Europa? *Icarus,* 120, 387-398.

Lin, Y., Bunte, M.K., Saripalli, S., and Greeley, R., 2012, Autonomous detection of volcanic plumes on outer planetary bodies, *Institute of Electrical and Electronics Engineers International Conference on Robotics and Automation,* 3431-3436.

Lin, Y., Bunte, M.K., Saripalli, S., and Greeley, R., accepted with revisions 2013, planetary feature identification and tracking using autonomous methods onboard spacecraft, *Acta Astronautica.*

Lindeberg, T., 1998, Feature detection with automatic scale selection, *International Journal of Computer Vision,* 30, 79-116.

Lindeberg, T., 2008, Scale-space. In: *Encyclopedia of Computer Science and Engineering,* Wah, B. (Ed.), John Wiley and Sons IV, 2495-2504.

Lintott, C., Schwamb, M.E., Sharzer, C., Fischer, D.A., Barclay, T., Parrish, M., Batalha, N., Bryson, S., Jenkins, J., Ragozzine, D., Rowe, J. F., Schawinski, K., Gagliano, R., Gilardi, J., Jek, K.J., Paakkonen, J.-P., Smits, T., 2013, Planet hunters: New Kepler planet candidates from analysis of Quarter 2, *The Astronomical Journal,* 145, 151-159.

Lopes, R.M.C., and Spencer, J.R., 2007, *Io After Galileo: A new view of Jupiter's volcanic moon,* Springer-Praxis.

Lopes-Gautier, R., McEwen, A., Smythe, W., Geissler, P., Kamp, L., Davies, A., Spencer, J., Keszthelyi, L., Carlson, R., Leader, F., et al., 1999, Active volcanism on Io: Global distribution and variations in activity, *Icarus* 140, 243-264.

Lorenz, R.D., Stiles, B.W., Kirk, R.L., Allision, M.D., del Marmo, P.P., less, L., Lunine, J.I., Ostro, S.J., and Hensley, S., 2008, Titans rotation reveals an internal ocean and changing zonal winds, *Science,* 319, 1649-1651.

Lowe, D.G., 2004, Distinctive image features from scale-invariant keypoints. *International Journal of Computer Vision,* 60, (2), 91-110.

Lowe, D.G., 1999, Object recognition from local scale-invariant features, *International Conference on Computer Vision,* 1150-1157, Corfu, Greece.

Lucchitta, B.K., Soderblom, L.A., and Ferguson, H.M., 1981, Structures on Europa, In: *Lunar and Planetary Science* XII, 1555-1567, Lunar and Planetary Institute, Houston.

Lucchitta, B.K., and Soderblom, L.A., 1982, The geology of Europa, In: *The Satellites of Jupiter* (Morrison, D., Ed.), pp. 521-555. University of Arizona Press, Tucson.

Malin, M.C., and Fieri, D.C., 1986, Europa, In: *Satellites* (Burns, J.A., and Matthews, M.S., Eds.), pp.689-717. University of Arizona Press, Tucson.

Manga, M., and Sinton, A., 2004, Formation of bands and ridges on Europa by cyclic deformation: Insights from analogue wax experiments, *Journal of Geophysical Research,* 109, E09001, DOI: 10.1029/2004JE002249.

Manga, M., and Wang, C.-Y., 2007, Pressurized oceans and the eruption of liquid water on Europa and Enceladus, *Geophysical Research Letters,* 34, DOI: 10.1029/2007GL029297.

Manga, M., 1997, Interactions between mantle diapirs, *Geophysical Research Letters,* 24, 1871-1874.

Marcy, G.W., Bulter, R.P., Vogt, S.S., Fischer, D.A., Henry, G.W., Laughlin, G., Wright, J.T., and Johnson, J.A., 2005, Five new extrasolar planets, *Astrophysical Journal*, 619, 570-584.

McCord, T.B., Hansen, G. B., Fanale, F. P., Carlson, R. W., Matson, D. L., Johnson, T. V., Smythe, W. D., Crowley, J. K., Martin, P. D., Ocampo, A., Hibbits, C. A., Granahan, J.C., and the NIMS Team, 1998, Salts on Europa's surface detected by Galileo's Near Infrared Mapping Spectrometer, *Science,* 280, 1242-1245.

McCord, T.B., Hansen, G.B., Matson, D.L., Johnson, T.V., Crowley, J.K., Fanale, P.P., Carlson, R.W., Smythe, W.D., Martin, P.D., Hibbitts, C.A., Granahan, J.C., and Ocampo, A., 1999, Hydrated salt minerals on Europa's surface from the Galileo Near Infrared Mapping Spectrometer (NIMS) investigation, *Journal of Geophysical Research,* 104, 11827-11852.

McCord, T.B., Hansen, G.B., Combe, J.-P, and Hayne, P.O , 2010, Hydrated minerals on Europa's surface: An improved look from the Galileo NIMS investigation, *Icarus, 209* 639-650.

McEwen, A., Turtle, E., Hibbard, K., Reynolds, E., and Adams, E., 2012, Io Volcano Observer (IVO): Budget travel to the outer solar system, *Act Astronautica* 10.10167 2012.05.028.

McEwen, A.S., and Soderblom, L.A., 1983, Two classes of volcanic plumes on lo. *Icarus,* 55, 191-217.

McEwen, A.S., Keszthelyi, L., Geissler, P., Simonelli, D. Carr, M. Johnson, T., Klaasen, K., Breneman, H., Jones, T., Kaufman, J., Magee, K., Senske, D., Belton, M., and Schubert, G., 1998, Active volcanism on Io as seen by Galileo SSI. *Icarus,* 135, 181-219.

McEwen, A.S., 1986b, Tidal reorientation and the fracturing of Jupiter's moon Europa, *Nature,* 321, 49-51.

McEwen, A.S., 1991, Photometric functions for photoclinometry and other applications, *Icarus,* 92, 298-311.

McKinnon, W.B., 1996, Evolution of the interior of Europa, and the plausibility of active, present-day hydrothermal systems. In: *Europa Ocean Conference Abstracts,* pp. 50-51. San Juan Institute, San Juan Capistrano, California.

Melosh, H.J., Ekholm, A.G., Showman, A.P., and Lorenz, R.D., 2004, The temperature of Europa’s subsurface water ocean, *Icarus*, 168, 498-502.

Millazzo, M.P., Keszthelyi, L.P., and McEwen, A.S., 2001, Observations and initial models of lava-SO_2 interactions at Prometheus, Io, *Journal of Geophysical Research,* 106, 33121-33128.

Moore, J.M., Black, G., Buratti, B., Phillips, C.B., Spencer, J., and Sullivan, R., 2009, Surface properties, regolith, and landscape degradation, In: *Europa* (Pappalardo, R.T., McKinnon, W.B., and Khurana, K., Eds.), pp. 329-352, University of Arizona Press, Tucson.

Moore, J.M., Asphaug, E., Sullivan, R.J., Klemaszewski, J.E., Bender, K.C., Greeley, R., Geissler, P.E., McEwen, A.S., Turtle, E.P., Phillips, C.B., Tufts, B.R., Head, J.W., Pappalardo, R.T., Lones, K.B., Chapman, C.R., Belton, M.J.S., Kirk, R.L., and Morrison, D., 1998, Large impact features on Europa: Results of the Galileo nominal mission, *Icarus,* 135, 127-145.

Moore, J.M., Asphaug, E.,B., Michael, J.S., Bierhaus, B., Breneman, H.H., Brooks, S.M., Chapman, C.R., Chuang, F.C., Collins, G.C., Giese, B., Greeley, R., Head, J.W., Kadel, S., Klaasen, K.P., Klemaszewski, I.E., Magee, K.P., Moreau, J., Morrison, D., Neukum, G., Pappalardo, R.T., Phillips, C.B., Schenk, P.M., Senske, D.A., Sullivan, R.J., Turtle, E.P., and Williams, K.K., 2001, Impact features on Europa: Results of the Galileo Europa Mission (GEM), *Icarus,* 151, 93-111.

Morabito, L.A., Synnott, S.P., Kupferman, P.N., and Collins, S.A, 1979, Discovery of currently active extraterrestrial volcanism, *Science,* 204, 972.

NASA, 2006, Solar system exploration roadmap. NASA Science Mission Directorate, Washington, D.C. http://solarsystem.nasa.gov/multimedia/downloads/SSE_RoadMap_2006 Report FC-A med.pdf.

NASA, 2007, Science plan for NASA's Science Mission Directorate 2007-2016. http://science.nasa.gov/media/medialibrary/2010/03/31/Science_Plan_07.pdf.

Neukum, G., Wagner, R., Wolf, U., and the Galileo SSI Team, 1999, Cratering record of Europa and implications for timescale and crustal development: In: *Lunar and Planetary Science Conference* XXX, 1992,Lunar and Planetary Institute, Houston, TX.

Nimmo, F., and Gaidos, E., 2002, Thermal consequences of strike-slip motion on Europa. *Journal of Geophysical Research,* 107, 5021.

Nimmo, F., and Manga, M., 2009, Geodynamics of Europa's icy shell, In: *Europa* (Pappalardo, R.T., McKinnon, W.B., and Khurana, K., Eds.), pp. 381-404, University of Arizona Press, Tucson.

North American Commission on Stratigraphic Nomenclature, 1983, North American stratigraphic code, *American Association of Petroleum Geologists Bulletin*, 67, 841-875.

O'Brien, D.P., Geissler, P., and Greenberg, R., 2002, A melt-through model for chaos formation on Europa, *Icarus,* 156,152-161.

Ojakangas, G.W., and Stevenson, D.J., 1989, Polar wander of an ice shell on Europa, *Icarus,* 81,242-270.

Ong, L.C.F., 2004, What lies beneath the surface? Europa's icy enigma. B.A. Thesis, Williams College, Williamstown, Massachusetts. 91pp.

Oro, J., Squyers, S.W., Reynolds, R.T., and Mills, T.M., 1992, Europa: Prospects for an ocean and exobiological implications. In: *Exobiology in Solar System Exploration* (G. Carle et al., Eds.), pp. 103-126 (see NTRS document N93- 18545 06- 51).

Pappalardo, R.T., and Barr, A., 2004, Origin of domes on Europa: The role of thermally induced compositional buoyancy, *Geophysical Research Letters,* 31, LO1701, DOI: 10.1029/2003GL019202.

Pappalardo, R.T., Head, J.W., Greeley, R., Sullivan, R.W., Pilcher, C., Schubert, G., Moore, W.B., Carr, M.H., Moore, J.M., Belton, M.J.S., and Goldsby, D.L., 1998a, Geological evidence for solid-state convection in Europa's icy shell, *Nature,* 391, 365-368.

Pappalardo, R.T., Head, J., Sherman, N., Greeley, R., Sullivan, R., and the Galileo Imaging Team, 1998b, Classification of europan ridges and troughs and a possible genetic sequence. In: *Lunar and Planetary Institute Science Conference Abstracts, XXIX,* 1859, Houston, TX.

Pappalardo, R.T., Belton, M.J.S., Breneman, H.H., Carr, M.H., Chapman, C.R., Collins, G.C., Denk, T., Fagents, S., Geissler, P.E., Giese, B., Greeley, R., Greenberg, R., Head, J.W., Helfenstein, P., Hoppa, G., Kadel, S.D., Klaasen, K.P., Klemaszewski, I.E., Magee, K., McEwen, A.S., Moore, J.M., Moore, W.B., Neukum, G., Phillips, C.B., Prockter, L.M., Schubert, G., Senske, D.A., Sullivan, R.J., Tufts, B.R., Turtle, E.P., Wagner, R., and Williams, K.K., 1999, Does Europa have a subsurface ocean? Evaluation of the geological evidence, *Journal of Geophysical Research,* 104, 24015-24056.

Pappalardo, R.T., and Sullivan, R.J., 1996, Evidence for separation across a gray band on Europa, *Icarus,* 123, 557-567.

Pappalardo, R.T., and Coon, M.D., 1996, A sea ice analog for the surface of Europa. In: *Lunar and Planetary Institute Science Conference Abstracts*.XXVII, 997-998, Houston, TX.

Passey, Q.R., and Shoemaker, E.M., 1982, Craters and basins on Ganymede and Callisto: Morphological indicators of crustal evolution. In: *Satellites of Jupiter* (D. Morrison, Ed.), pp. 379-434. University of Arizona Press, Tucson.

Patel, J.G., Pappalardo, R.T., Prockter, G.C., Collins, G.C., Head, J.W., III, and the Galileo SSI Team, 1999, Morphology of ridge and trough terrain on Europa: Fourier analysis and comparison to Ganymede, *Eos Transactions of the American Geophysical Union,* 80, Spring Meeting Supplement, S210.

Patterson, G.W., Head, J.W., and Pappalardo, R.T., 2006, Plate motion on Europa and non-rigid behavior of the icy lithosphere: The Castalia Macula region, *Journal of Structural Geology,* 28, 2237-2258.

Patterson, G.W., Collins, G.C., Head, J.W., Pappalardo, R.T., Prockter, L.M., Lucchitta, B.K., and Kay, J.P., 2010, Global geological mapping of Ganymede, *Icarus,* 207, 845-867.

Peale, S.J., Cassen, P., and Reynolds, R.T., 1979, Melting of Io by tidal dissipation, *Science,* 203, 892-894.

Phillips, C.B., Raubertas, R.F., Arvidson, R.E., Sarkar, I.C., Herrick, R.R., Izenberg, N., and Grimm, R.E., 1992, Impact craters and Venus resurfacing history, *Journal of Geophysical Research,* 97, 15923-15948.

Phillips, C.B., McEwen, A.S., Hoppa, G.V., Fagents, S.A., Greeley, R., Klemaszewski, I.E., Pappalardo, R.T., Klaasen, K.P., and Breneman, H.H., 2000, The search for current geologic activity on Europa, *Journal of Geophysical Research,* 105, 22579-22597.

Pickering, B.C., 1908, Brighter satellites of Jupiter and Saturn. Part I, Chapter VI, *Annals of Harvard College Observatory,* 61, 72-85.

Pieri, B.C., 1981, Lineament and polygon patterns on Europa, *Nature,* 289, 17-21.

Porco, C., Helfenstein, P., Thomas, P., Ingersoll, A., Wisdom, J., West, R., Neukum, G., Denk, T., Wagner, R., Roatsch, T., et al., 2006, Cassini observes the active south pole of Enceladus, *Science,* 311, 1393-1401.

Prockter, L., 2005, Planetary science: Shades of Titan, *Nature,* 435, 749-750.

Prockter, L.M, and Patterson, G.W., 2009, Europa's ridges and bands, In: *Europa* (Pappalardo, R.T., McKinnon, W.B., and Khurana, K., Eds.), pp. 237-258, University of Arizona Press, Tucson.

Prockter, L.M., and Schenk, P.M., 2002, Mapping of Europa's youthful "dark spot" – a potential landing site, In: *Lunar and Planetary Science* XXXIII, 1732, Lunar and Planetary Institute, Houston (CD-ROM).

Prockter, L.M., Antman, A., Pappalardo, R.T., Head, J.W., and Collins, G.C., 1999a, Europa: stratigraphy and geologic history of an anti-Jovian region from Galileo El4 solid-state imaging data, *Journal of Geophysical Research,* 104, 16531-16540.

Prockter, L.M., Head, J.W., Pappalardo, R.T., Collins, G.C., Klemaszewski, I.E., Geissler, P.E., and the Galileo SSI team, 1999b, Geological mapping of central Agenor Linea, Europa (212°-226°), In: *Lunar Planetary Science* XXX, 1299, Lunar and Planetary Institute, Houston (CD-ROM).

Quick, L.C., Barnouin, O.S., Prockter, L.M., and Patterson, G.W., 2013, Constraints on the detection of cryovolcanic plumes on Europa, *Planetary and Space Science,* http://dx.doi.0rg/10.1016/j.pss.2013.06.028.

Rabideau, G.,and Chien, S., 2009. Runtime goal selection with oversubscribed resources, *Proceedings of International Workshop on Planning and Scheduling for Space.*

Rathbun, J.A., Musser, G.S., and Squyers, S.W., 1998, Ice diapirs on Europa: Implications for liquid water, *Geophysical Research Letters,* 25, 4157-4160.

Reynolds, R.T., and Cassen, P., 1979, On the internal structure of the major satellites of the outer planets. *Geophysical Research Letters, 6,* 121-124.

Reynolds, R.T., Squyres, S.W., Colburn, D.S., and McKay, C.P., 1983, On the habitability of Europa, *Icarus,* 56, 246-254.

Riley, J., Hoppa, G.V., Greenberg, R., Tufts, B.R., and Geissler, P., 2000, Distribution of chaotic terrain on Europa, *Journal of Geophysical Research,* 105, 22599-22615.

Russell, C.T., Raymond, C.A., Fraschetti, T.C., Rayman, M.D., Polanskey, C.A., Schimmels, K.A., and Joy, S.P., 2006, Dawn mission and operations, *Asteroids, Comets, Meteors, Proceedings of International Astronomical Union Symposium No. 229,2005,97-119.*

Salvatore, A. (Ed.), 1994, *International stratigraphic guide: a guide to stratigraphic classification, terminology and procedure*, second edition, International Union of Geological Sciences, Trondheim, pp. 214.

Sarid, A.R., Greenberg, R., Hoppa, G.V., Geissler, P., and Preblich, B., 2004, Crack azimuths on Europa: Time sequence in the southern leading face, *Icarus,* 168, 144-157, 2004.

Sarid, A.R., Greenberg, R., Hoppa, G.V., Brown, D. and Geissler, P., 2005, Crack azimuths on Europa: the Gl lineament sequence revisited, *Icarus,* 173,469-479.

Saur, J., Neubauer, P.M., Dougherty, M.K., Khurana, K.K., and Russell, C.T., 2005, Time varying south polar atmosphere on Enceladus from magnetic field measurements analyzed by use of 3D two-fluid plasma simulations, *American Geophysical Union Fall Meeting 2005,* Abstract SH41C-04.

Schenk, P.M., 1995, The geology of Callisto, *Journal of Geophysical Research,* 100, 19023-19040.

Schenk, P.M., 2002, Thickness constraints on the icy shells of the Galilean satellites from a comparison of crater shapes, *Nature,* 417, 419-421.

Schenk, P., 2004, Sinking to new lows and rising to new heights: The topography of Europa, In: *Workshop on Europa's Icy Shell: Past, Present and Future,* LPI contribution No. 1195, 82-83.

Schenk, P.M., and Turtle, E., 2009, Europa's impact craters: Probes of the interior, In: *Europa* (Pappalardo, R.T., McKinnon, W.B., and Khurana, K., Eds.), pp. 181-198, University of Arizona Press, Tucson.

Schenk, P.M., and Pappalardo, R.T., 2004, Topographic variations in chaos on Europa: Implications for diapiric formation, *Geophysical Research Letters,* 31, LI6703, DOI:10.129/2004GL019978.

Schenk, P.M., Chapman, C.R., Zahnle, K., and Moore, J.M., 2004, Ages and interiors: the cratering record of the Galilean satellites, In: *Jupiter: the Planet, Satellites and Magnetosphere* (Bagnel, F., Dowling, T.E., and McKinnon, W.B. Eds.), Cambridge University Press, Cambridge, p. 427-456.

Schenk, P., Matsuyama, I., and Nimmo, F., 2008, Evidence for true polar wander on Europa from global scale small circle depressions, *Nature,* 453, 368-371.

Schenk, P., and McKinnon, W., 1989, Fault offsets and lateral crustal movement on Europa - Evidence for a mobile ice shell, *Icarus,* 79, 75-100.

Schenk, P., 2006, Europa's Topographic Story, In: *Europa Focus Group Workshop 5* (Greeley, R., Ed.), Abstract Volume, p. 119.

Schmidt, B.E., Blakenship, D.D., Patterson, G.W., Schenk, P.M., 2011, Active formation of chaos terrain over shallow subsurface water on Europa. *Nature* 479, 502-505.

Schmidt, B.E., Blankenship, D.D., Patterson, G.W., and Schenk, P.M., 2012, Insights into Europa's shallow water mobility from Thrace and Thera Macula, In: *Lunar and Planetary Science* XLIII, 1743, Lunar and Planetary Institute, Houston, TX.

Schubert, G., Anderson J.D., Spohn, T., and McKinnon, W.B., 2004, Interiror compositions, structure and dynamics of the Galilean staellites, In: *Jupiter – The Planets, Satellites, and Magnetosphere* (Bagenal, F. et al., Eds.), pp. 329-362. Cambridge University Press, Cambridge.

Schubert, G., Sohl, F., and Hussman, H., 2009, Interior of Europa, In: *Europa* (Pappalardo, R.T., McKinnon, W.B., and Khurana, K., Eds.), pp. 353-368, University of Arizona Press, Tucson.

Seidelmann, P.K., Archinal, B.A., A'Hearn, M.E., Conrad, A., Consolmagno, G.J., Hestroffer, D., Hilton, J.L., Krasinsky, G.A., Neumann, G., Oberst, J., Stoke, P.,

Tedesco, E.E., Tholen, D.J. Thomas, P.C., and Williams, I.P., 2007, Report of the IAU/IAG Working Group on Cartographic Coordinates and Rotational Elements: 2006, *Celestial Mechanics and Dynamic Astronomy,* 98, 155-180.

Senske, D.A., Greeley, R., Head, J., Pappalardo, R., Sullivan, R., Carr, M., Geissler, P., Moore, J., and the Galileo SSI team, 1998, Geologic mapping of Europa: Unit identification and stratigraphy at global and local scales, In: *Lunar and Planetary Science* IXXX, 1743, Lunar and Planetary Institute, Houston, TX.

Shoemaker, E.M. and Hackman, R.J., 1962, Stratigraphic basis for a lunar time scale, In: *The Moon* (Kopal, Z. and Mikhailov, Z..K., Eds.), p. 289- 300, Academic Press, London.

Skinner, J.A., and K.L. Tanaka, 2003, How should planetary map units be defined?, In: *Lunar and Planetary Science Conference* XXXIV, 2100, Lunar and Planetary Institute, Houston, TX.

Smith, B.A., Soderblom, L.A., and 63 co-authors, 1989. Voyager 2 at Neptune: Imaging science results, *Science,* 246, 1422-1449.

Smith, B.A., Soderblom, L.A., Beebe, R., Boyce, J., Briggs, G., Carr, M., Collins, S.A., Cook, A.F., II, Danielson, G.E., Davies, M.E., Hunt, G.E., Ingersoll, A., Johnson, T.V., Masursky, H., McCauley, J., Morrison, D., Owen, T., Sagan, C., Shoemaker, E.M., Strom, R., Suomi, V.E., and Veverka, J., 1979a, The Galilean satellites and Jupiter- Voyager 2 imaging science results, *Science,* 206, 927-950.

Smith, B.A., Soderblom, L.A., Johnson, T.V., Ingersoll, A.P., Collins, S.A., Shoemaker, E.M., Hunt, G.E., Masursky, H., Carr, M.H., Davies, M.E., Cook, A.F., II, Boyce, J., Danielson, G.E., Owen. T., Sagan, C., Beebe, R.F., Veverka, J., Strom, R.G., McCauley, J.F., Morrison, D., Briggs, G.A., and Suomi, V.E., 1979b, The Jupiter system through the eyes of Voyager 1, *Science,* 204, 951-972.

Soderblom, L., Becker, T., Kieffer, S., Brown, R., Hansen, C., and Johnson, T., 1990, Triton's geyser-like plumes - Discovery and basic characterization, *Science,* 250, 410-415.

Sotin, C., Head, J.W., and Tobie, G., 2002, Europa: Tidal heating of upwelling thermal plumes and the origin of lenticulae and chaos melting, *Geophysical Research Letters,* 29, DOI: 10.1029/2001GLO13 844.

Spaun, N.A., Pappalardo, R.T., and Head, J.W., 2003, Evidence for shear failure in forming near-equatorial linea on Europa, *Journal of Geophysical Research,* 108, 5060, DOI: 10.1029/2001JEOO1499, E6.

Spaun, N.A., Head, J.W., Pappalardo, R.T., and the Galileo Imaging Team, 1999a, Chaos and lenticulae on Europa: Structure, morphology and comparative analysis, in *Lunar*

and Planetary Science Conference XXX, #1276, Lunar and Planetary Institute, Houston, TX.

Spaun, N.A., Prockter, L.M., Pappalardo, R.T., Head, J.W., Collins, G.C., Antman, A., Greeley, R., and the Galileo Imaging Team, 1999b, Spatial distribution of lenticulae and chaos on Europa, in *Lunar and Planetary Science Conference* XXX, #1847, Lunar and Planetary Institute, Houston, TX.

Spaun, N.A., Head, J.W., Collins, G.C., Prockter, L.M., and Pappalardo, R.T., 1998a, Conomara chaos region, Europa: reconstruction of mobile polygonal ice blocks, *Geophysical Research Letters, 25,* 4277-4280.

Spaun, N.A., Head, J.W., Pappalardo, R.T., and the Galileo Imaging Team, 1998b, Geologic history, surface morphology and deformation sequence in an area near Conamara Chaos, Europa, in *Lunar and Planetary Science Conference* XXIX, #1899, Lunar and Planetary Institute, Houston, TX.

Spencer, J., Stern, S.A., Cheng, A.F, Weaver, H.A., Reuter, D.C., Retherford, K., Lunsford, A., Moore, J.M., Abramov, O., Lopes, R.M.C., Perry, I.E., Kamp, L., Showalter, M., Jessup, K.L., Marchis, F., Schenk, P.M., Dumas, C., 2007, Io volcanism seen by New Horizons: A major eruption of the Tvashtar volcano, *Science,* 318, 240-243.

Spencer, J., Pearl, J., Segura, M., Flaser, F., Mamoutkine, A., Romani, P., Buratti, B., Hendrix, A., Spilker, L., and Lopes, R., 2006, Cassini encounters Enceladus: Background and discovery of a south polar hot spot, *Science,* 311, 1401-1405.

Spencer, J.R., Pearl, J.C., Segura, M., and Cassini CIRS Team, 2005, Discovery of probable endogenic hot spots on Enceladus by the Cassini Composite Infrared Spectrometer. *American Geophysical Union Fall Meeting 2005,* Abstract P32A-04.

Squyres, S.W., Reynolds, R.T., Cassen, P.M., and Peale, S.J., 1983, Liquid water and active resurfacing of Europa, *Nature,* 301, 225-226.

SSB, 2003, New Frontiers in the solar system: An integrated exploration strategy, Space Studies Board, National Research Council, National Academies, Washington, D.C., pp.231.

Stempel, M.M., Barr, A.C., and Pappalardo, R.T., 2005, Model constraints on the opening rates of bands on Europa, *Icarus, 111,* 297-304.

Stempel, M.M., and Pappalardo, R.T., 2002, Lineament orientations through time near Europa's leading point: Implications for stress mechanisms and rotation of the icy shell, In: *Lunar and Planetary Science Conference* XXXIII*,* 1661, Lunar and Planetary Institute, Houston, TX.

Stern, S.A., and McKinnon, W.B., 2000, Triton's surface age and impactor population revisited in light of Kuiper belt fluxes: evidence for small Kuiper belt objects and recent geological activity. *The Astronomical Journal,* 119, 945-952.

Strom, R.G., Schneider, N.M., Terrile, R.J., Cook, A.F., and Hansen, C., 1981, Volcanic eruptions on lo, *Journal of Geophysical Research,* 86, 8593-8620.

Strom, R.G., and Schneider, N.M., 1982, Volcanic eruption plumes on Io. In: *Satellites of Jupiter* (Morrison, D., Ed.), pp. 598-633, University of Arizona Press, Tucson.

Sullivan, R., Greeley, R., Homan, K., Klemaszewski, J., Belton, M.J.S., Carr, M.H., Chapman, C.R., Tufts, J.R., Head, J.W., Pappalardo, R.T., Moore, J., and Thomas, P., 1998, Episodic plate separation and fracture infill on the surface of Europa, *Nature,* 391,371-373.

Sullivan, R., Greeley, R., Klemaszewski, J., Moreau, J., Head, J.W., Pappalardo, R., Moore, J., and Tufts, J.R., 1999b, High resolution Galileo geologic mapping of ridges plains on Europa, In: *Lunar and Planetary Science* XXX, Abstract #1925, Lunar and Planetary Institute, Houston (CD-ROM).

Sullivan, R., Moore, J., and Pappalardo, R., 1999a, Mass-wasting and slope evolution on Europa. In: *Lunar and Planetary Institute Science Conference Abstracts*, XXX, 1747, Houston, TX.

Tanaka, K.L., Skinner, J.A., Jr., and Hare, T.M., 2005, Geological Map of the Northern Plains of Mars, U.S. Geological Survey Scientific Investigations Map SIM-2888, scale 1:15,000,000.

Tanaka, K.L., Moore, H.J., Schaber, G.G., Chapman, M.G., Stofan, E.R., Campbell, D.B., Davis, P.A., Guest, J.E., McGill, G.E., Rogers, P.G., Saunders, R.S., and Zimbelman, J.R., 1994, *The Venus Geologic Mappers Handbook,* U.S. Geological Survey Open File Report, 94-438, pp. 66.

Thompson, D.R., Tran, D., Chien, S., Bunte, M., and Greeley, R., 2012b, Plume detection at irregular bodies using morphological analysis, *International Symposium on Artificial Intelligence, Robotics, and Automation in Space*, Turin, Italy.

Thompson, D.R., Bunte, M., Castano, R., Chien, S., and Greeley, R., 2012a, Image processing onboard spacecraft for autonomous plume detection, *Planetary and Space Sciences,* 62 (1), 153-159.

Thompson, D.R., Mandrake, L., Gilmore, M., and Castano, R., 2010, Superpixel endmember detection, *Transactions on Geoscience and Remote Sensing*, 48 (11), 4023-4033.

Thomson, R.E., and Delaney, J.R., 2001, Evidence for a weakly stratified Europan ocean sustained by seafloor heat flux, *Journal of Geophysical Research*, 106, 12355-12365.

Tobie, G., Mocquet, A., and Sotin, C., 2005, Tidal dissipation within large icy satellites: Applications to Europa and Titan. *Icarus*, 177, 534-549.

Tobie, G., Choblet, G., and Sotin, C., 2003, Tidally heated convection: Constraints on Europa's ice shell thickness, *Journal of Geophysical Research*, 108, DOI: 10.1029/2003JE002099.

Torson, J.M., and Becker, K.J., 1997, ISIS - a software architecture for processing planetary images, in *Lunar and Planetary Science* XXVIII, Lunar and Planetary Institute, Houston, p. 1443.

Tufts, B.R., Greenberg, R., Hoppa, G., and Geissler, P., 1999, Astypalaea Linea, a large-scale strike-slip fault on Europa, *Icarus*, 141, 53-64.

Tufts , B.R., Greenberg, R., Hoppa, G., and Geissler, P., 2000, Lithospheric dilation on Europa, *Icarus*, 146, 75-97.

Turcotte, D.L., 1993, An episodic hypothesis for Venusian tectonics, *Journal of Geophysical Research*, 98, 17061-17068.

Turtle, E.P., Melosh, H.J., and Phillips, C.B., 1998, Tectonic modeling of the formation of europan ridges, *EOS Transactions of the American Geophysical Union*, 79, Fall Meeting Supplement, F541.

Turtle, E.P., Jaeger, W.L., Shenk, P.M., 2007. Ionian mountains and tectonics: Insights into what lies beneath Io's lofty peaks, In: *Io After Galileo: A New View of Jupiter's Volcanic Moon,* Lopes, R.M.C., Spencer, J.R. (Eds.) Springer Praxis, 109-127.

U.S. Geological Survey, 2002, Controlled Photomosaic Map of Europa, U.S. Geological Survey Geological Investigations Series I-2757, scale 1:15,000,000.

U.S. Geologic Survey, Astrogeology Science Center, Europa Voyager/Galileo Image Mosaic Globe, http://astrogeology.usgs.gov/maps/planetary-maps-and-globes, updated September 3, 2013.

Vance, S., and Goodman,, J., 2009, Oceanography of an ice-covered moon, In: *Europa* (Pappalardo, R.T., McKinnon, W.B., and Khurana, K., Eds.), pp. 459-484, University of Arizona Press, Tucson.

vanDover, C.L., 2000, *The ecology of deep-sea hydrothermal vents*, Princeton University Press, pp.352.

Vision and Voyages for Planetary Science in the Decade 2013-2022, 2011, *National Academies Press*, Washington, D.C.

Waite, J H., Jr., Combi, M.R., Ip, W.-H., Cravens, T.E., McNutt, R., L., Kasprzak, W., Yelle, R., Luhmann, J., Niemann, H., Gell, D., Magee, B., Fletcher, G., Lunine, J., and Tseng, W.-L., 2006, Cassini ion and neutral mass spectrometer: Enceladus plume composition and structure, *Science*, 311, 1419–1422.

Whipple, F.L., 1963, *Earth, Moon, and Planets*, Harvard University Press, Cambridge, MA.

Wilhelms, D.E., 1990, Geologic mapping, In: *Planetary Mapping* (Greeley, R., and Batson, R.M. Eds.), Cambridge University Press, Cambridge, 208–260.

Wilhelms, D.E., 1972, Geologic mapping of the second planet, U.S. Geological Survey Interagency Report, *Astrogeology*, 55.

Williams, D.A., Klemaszewski, J.E., Greeley, R., Moore, J.M., Pappalardo, R.T., Prockter, L.M., Head, J.W., Geissler, P.E., Hoppa, G.V., Phillips, C.B., Tufts, B.R., Greenberg, R., Sullivan, R.J., Belton, M.J.S., and the Galileo Imaging Team,1999, Terrain variation on Europa: Overview of Galileo orbit E17 imaging results, In: *Lunar and Planetary Science* XXX, Abstract #1396. Lunar and Planetary Institute, Houston, TX.

Williams, K.K., and Greeley, R., 1998, Estimates of ice thickness in the Conamara Chaos region of Europa, *Geophysical Research Letters*, 25, 4273-4276.

Witkin, A.P., 1983. Scale-space filtering. *International Joint Conference on Artificial Intelligence*, Karlsruhe, Germany, 1019-1022.

Yoder, C.F., 1979, How tidal heating in Io drives the Galilean orbital resonance locks, *Nature*, 79, 7667-770.

Yoder, C.F., and Peale, S.J., 1981, The tides of Io, *Icarus*, 47, 1-35.

Zahnle, K., Schenk, P., Levinson, H., and Dones, L., 2003, Cratering rates in the outer solar system, *Icarus*, 163, 263-289.

Zimmer, C., Khurana, K.K., and Kivelson, M.G., 2000, Subsurface oceans on Europa and Callisto: Constraints from Galileo magnetometer observations, *Icarus*, 147, 329-347.

Zolotov, M., and Kargel, J., 2009, On the chemical composition of Europa's icy shell, ocean, and underlying rocks, In: *Europa* (Pappalardo, R.T., McKinnon, W.B., and Khurana, K., Eds.), pp. 431-458, University of Arizona Press, Tucson.

APPENDIX A

DESCRIPTION OF MAP UNITS AND STRUCTURES

Description of material units (DOMU) for the global geologic map of Europa.

Map Unit/ Symbol	Description	Interpretation
Crater Materials		
Secondary Crater Material	The bright rays emanating from the Pwyll structure are mapped as a separate unit as this is the only rayed ejecta material. Many small circular depressions are evident within the high albedo material that mantles nearby chaos.	Most small craters appear to be secondary impact craters, particularly from the Pwyll impact, as indicated by size-frequency distribution (Bierhaus et al., 2001, 2009; Moore et al., 2001; Schenk et al., 2004). Rayed ejecta from the Pwyll impact is the only preserved rayed material.
Crater Ejecta	Ejecta deposits formed by impact events include hummocky material distributed radially away from crater rims and low albedo material adjacent to impact structures. Some materials are raised as in a pedestal or rampart structure.	Dark ejecta is thought to include non-ice materials excavated from the subsurface and/or brought by the impactor. The pedestal is due to a convex upward scarp, possibly formed by outward creep of warm, plastically deforming ice (Moore et al., 1998).
Crater Material	Crater materials consist of the floor and crater rim as well as the materials associated with multi-ring impact structures. Impact structures range from small simple bow-shaped craters to complex craters with central peak materials and terraces to relaxed multi-ring structures.	The minimum diameter for the transition from simple to complex morphology is 5-6 km, as compared to 10-20 km on terrestrial bodies. Transient crater depths lead to an assessment that craters 10-18 km in diameter and 3-6 km deep did not penetrate to a liquid layer; thus ice must have been several kilometers thick at the time of crater formation (Moore et al., 2001). Structures with multiple concentric rings are interpreted to be relic impacts that penetrated into liquid water or warm ice (Moore et al., 1998; Schenk, 2002). The paucity of primary impact craters suggests a relatively young global surface age of ~40-90 My. (Bierhaus et al., 2009) though the basin-forming impacts have been attributed to the period of Late Heavy Bombardment, resulting in an older inferred age of 1-3 G.y. (Neukum, 1997).

(*Continued on next page)*

Appendix A (continued)

Map Unit/ Symbol	Description	Interpretation
Linea Materials		
Band Material	Linear zones distinguished by contrast in albedo and/or surface texture to surrounding terrain. Margins are sharp; some exhibit bounding ridges. May be high or low albedo. Internal structure may include ridges and troughs which trend sub-parallel to each other and the boundaries of the band. Some exhibit a central narrow trough surrounded by a hummocky zone bounded by the sub-parallel ridges and troughs with triangular cross-section. At low resolution, these bands appear to have a smooth texture.	Dark bands appear to be dilational and margins can be reconstructed to close the band (Schenk and McKinnon, 1989). Bright bands disrupt pre-existing terrain but cannot be reconstructed. Dark bands have been interpreted to form from the following mechanisms: (1) fracturing of a brittle surface layer overlying a ductile subsurface with subsequent rifting and infilling (Pappalardo and Sullivan, 1996 and others), (2) tidal pumping due to cyclically varying tidal stresses (Tufts et al., 2000 and others), and (3) mid-ocean ridge spreading with buoyancy (Sullivan et al., 1998 and others). Bright bands are interpreted to result from (1) dike intrusion (Lucchitta et al., 1981), (2) contraction (Schenk and McKinnon, 1989 and others), or (3) dextral shear with extension (Prockter et al., 2002 and others). Bands may represent a transitional mechanism which exploits pre-existing fractures or develops in a progression along with ridged bands, ridge complexes, and ridges.
Ridges	Material associated with individual ridges is too small to plot on the map print at map scale; general ridge material is plotted as a structural symbol. Only 150 of the most prominent or stratigraphically significant ridges are plotted on the structural map. Ridge material most commonly occurs in the form of double ridges, or ridge pairs separated by a medial trough. Ridges range in length from a few kilometers to >1000 km. Double ridges are typically 0.2-4 km wide, have flank slopes near the angle of repose for loose, blocky material, and exhibit a continuous central trough. Double ridges may be trapezoidal in cross-section. Mass wasting is common along ridge flanks where debris superposes pre-existing terrain.	Double ridges may form by (1) cryovolcanism (Kadel et al., 1998), (2) incremental buildup or wedging (Turtle et al., 1998), (3) upwarping through linear diapirism (Head et al., 1999), or (4) compression along fractures (Sullivan et al., 1998). More likely scenarios include (1) tidal pumping (Pappalardo and Coon, 1996 and others) or (2) shear heating (Gaidos and Nimmo, 2000; Nimmo and Gaidos, 2002; and others).

(*Continued on next page)*

Appendix A (continued)

Map Unit/ Symbol	Description	Interpretation
Linea Materials, continued		
Ridged Bands	Ridged bands or ridge complexes consisting of a collection of sub-parallel anastomosing single or double ridges. Trends are linear or curvilinear with no obvious bilateral symmetry. Margins are sinuous or undulating. Individual ridges may deviate from the overall trend and become incorporated in other through-going complexes.	Ridge complexes or ridged bands likely undergo a similar mechanism to double ridges. May form by successive buildup of individual double ridges within a confined region (Geissler et al., 1998 and others). Active ridges may transition into ridge complexes.
Flexūs	Cycloidal ridges consisting of connected arcuate segments of similar length that show planforms that are convex in the same direction, forming congruent curved segments joined at sharp cusps. Several examples, particularly those in the northern leading hemisphere, exhibit internal morphologies similar to smooth band material.	The cycloidal shape is suggested to be controlled by a changing direction of crack propagation under the control of Europa's diurnally rotating stress field. Propagation speeds are interpreted to be slower than Europa's orbit around Jupiter.
Un-differentiated Lineae	Ridge types without differentiable characteristics at the scale of the map are plotted as undifferentiated linea. These include cracks, raised-flank troughs, or more complex ridge structures with albedo too low to distinguish topography.	These linea are most likely examples of small fractures, ridges, or subdued/brightened ridge complexes that are unclassifiable due to resolution and viewing geometry constraints.
Chaos Materials		
Microchaos	Patches of low albedo material where multiple lenticulae structures appear to be merged such that each individual structure is not differentiated. Occur within the ridged plains units. Commonly occur adjacent to young lineaments.	Transition of lenticulated plains material towards more disrupted chaotic terrain.
Fractured Chaos	Low albedo regions where ridges and fractures are also prominent. Visible linear features are consistent with ridged plains. Viewing geometries tend to make east-went trending lineaments most visible. Lineaments are high albedo. Low albedo material surrounding and embaying the lineaments is consistent with lenticulae, though no individual structures are evident. No elevated material or block structures are evident.	Low albedo material is upwelling to flood the areas between lineaments, perhaps in a partial melting mode.

(*Continued on next page)*

Appendix A (continued)

Map Unit/ Symbol	Description	Interpretation
Chaos Materials, continued		
Chaos	Low resolution images exhibit a low-albedo mottled appearance. As in the type example of Conamara Chaos, high resolution images reveal isolated blocks, plates, and massifs where ridged material is preserved. Blocks, plates, and ridged massifs are juxtaposed with each other such that each material cannot be separated into individual units at the scale of the map. Plates with preserved ridge structures are often elevated relative to the surrounding blocky material or plains (Williams and Greeley, 1998; Schenk and Pappalardo, 2002).	Chaos regions are interpreted as areas of focused heat flow and perhaps local melting (Collins et al., 2000, Collins and Nimmo, 2009). In a melting model, blocks are analogous to buoyant icebergs (e.g., Greenberg et al., 1999). Solid-state ice rising diapirically to the surface is possible in situations of partial melting (Collins et al., 2000). These thermal gradients disrupt the cold, rigid lithosphere, causing fragmented slabs of colder material to rotate and translate within the framework of the original ridged plains matrix material (Pappalardo et al., 1998; Spaun et al., 1998). Other interpretations for chaos formation include: Brine mobilization (Head and Pappalardo, 1999; Collins et al., 2000; Pappalardo and Barr, 2004; Kargel et al., 2007), Sill-injection (Crawford and Stevenson, 1998, Collins et al., 2000; Manga and Wang, 2007), and Impact Modification (Billings and Kattenhorn, 2003; Cox et al., 2005). One or more of these processes may be in action to form the general chaotic texture.
Blocky Chaos	Areas of mottled appearance, often with low albedo. At high resolution, these areas exhibit multiple titled blocks which has been termed "knobby", "blocky", or "hummocky". Occurs in small areal extent. Boundaries are often embaying the surrounding terrain with low albedo material. In some cases, ridged plains textures extend partially into the blocky terrain and then are embayed by the dark albedo material. Thera Macula and Murias Chaos (Figueredo et al., 2002) are typical examples of blocky chaos. In some cases, blocky material is elevated and bounded by scarps.	Blocky chaos regions have been disrupted to the point that no evidence of the ridged matrix remains, except at boundaries where noted.

(*Continued on next page)*

Appendix A (continued)

Map Unit/ Symbol	Description	Interpretation
Chaos Materials, continued		
Subdued Chaos	Regions that exhibit some blocky texture but are dominated by smoother surfaces. Ridges are not present. Blocks are less tilted and elevated than in Blocky Chaos.	Areas of Blocky of other types of chaos that have been relaxed or embayed by medium-to-low albedo materials such that blocks, plates, or ridges are no longer evident.
Un-differentiated Chaos	Consistent with previous definitions of mottled terrain. These areas share characteristics of lenticulated plains or microchaos in low-resolution images such that they appear "speckled". At resolution boundaries, it is possible to trace albedo features into lower resolution coverage areas; these appear disrupted with no ridged matrix visible at high resolution. The density of low albedo "speckles" distinguishes undifferentiated chaos from lenticulated plains and microchaos. Superposing ridges are visible, though these are less prominent in undifferentiated chaos materials than in lenticulated plain units; the ridges are more subdued in undifferentiated units. In some case, image resolution does not permit the distinction of blocks, plates, or elevated massifs. Though these may be present, resolution constraints demand a definition of undifferentiated.	Large regions of chaotic materials that cannot be distinguished due to low resolution and viewing geometries. These areas show some evidence of disruption as in other chaos materials.
Plains Materials		
Banded Plains	Unit characterized by multiple short but wide dark smooth bands. These bands, often termed "wedges", are arcuate. Ridged plains are evident as a background surface. Unit is confined to Argadnel Regio, southwest of the anti-jovian point. High resolution images of Argadnel Regio reveal that the bands are most common in the northern portion of the region while the southern portion of the region is dominated by an increasingly disrupted set of fractures, all of which are short and narrow compared to the ridged plains. The banded portion of the region to the east is also populated by lenticulae, particularly dark spots, and small microchaos. Central and southern areas disrupted by chaos. Overprinted by ridges and flexūs.	Pull-apart bands are inferred to be brittle ice spreading zones that open along fractures and separate the crust into plates. The zones are infilled with darker material derived from the interior and may translate over the lower-viscosity subsurface (Schenk and McKinnon, 1989; Belton et al., 1996; Sullivan et al., 1998; Greeley et al., 1998b; Prockter et al., 1999; Tufts et al., 2000; Doggett et al., 2009). With time, dark materials brighten (Pappalardo and Sulllivan, 1996; Greeley et al., 1998a,b; Geissler et al., 1998). See interpretation for bands.

(*Continued on next page)*

Appendix A (continued)

Map Unit/ Symbol	Description	Interpretation
Plains Materials, continued		
Lenticulated Plains	Ridged plains that exhibit dense populations of structurally independent lenticulae. Ridged plains material is easily discernible but is disrupted, superposed, and embayed by pits, domes, or low albedo material. In some cases, individual ridges or narrow bands appear to superpose the lenticulae. Lenticulated plains are most commonly found at the contact boundaries of chaos material and appear to represent a gradation from chaos to ridged plains materials. Elongated lenticulated areas are common bounding young lineaments or bands. The density of lenticulae gives the surface a darker than average albedo as compared to ridged plains. In low-resolution coverage areas, the dark albedo of the "spots" is the most evident indicator of lenticulation; pits and domes that do not differ in albedo from the background plains are indistinguishable.	The morphological similarities between lenticulae and larger chaos areas suggest related formational processes. Proposed models for lenticulae formation include diapirism, possibly in conjunction with partial melting of a salt-rich icy lithosphere (Pappalardo et al., 1998; Rathbun et al., 1998), ice-shell melt-through (Carr et al., 1998; Greenberg et al., 1999; O'Brien et al., 2002; Greenberg et al., 2003), and ice volcanism (Fagents et al., 1998). Morphological evolution from ridged plains to chaos. See interpretation for Lenticulae.
Ridged Plains	Expansive areas of interwoven and cross-cutting ridges and troughs at multiple scales. Highest albedo of all materials except ejecta from Pwyll Crater. Appears smooth at regional or global resolution but increasingly textured at higher resolutions. Ridged texture exhibits a range of dimensions and various geometries including arcuate, sinuous, and anastomosing. Randomly oriented short ridge segments. Sets of parallel and sub-parallel ridges. Varying degrees of texture, albedo, deformation, lenticulae density, topographic relief, embayment, and linea cross-cutting. Topography is relatively flat with only slight variations in elevation from one ridge structure to the next. Local areas exhibit brighter than average terrain and more limited topography. Cross-cut by wide bands and ridge complexes. Sparsely cratered. Ridge texture is embayed and completely masked by chaos material. Individual young ridges superpose the background ridged texture. Some areas disrupted by pits and domes or appear to be smoothed or subdued with embaying darker albedo material. Small (<5km) areas are smoothed with no apparent ridge texture.	Multiple (Geissler et al., 1998; Patel et al., 1999; Sullivan et al., 1999; Figueredo and Greeley, 2004) or continuous (Greenberg et al., 1998) episodes of ridge building with repeated overprinting. Gradation among multiple types of ridge terrains suggests multiple formation processes or morphological evolution with a temporal resurfacing transition to less overprinting. See interpretation for Ridges.

APPENDIX B

COPYWRITE CONSIDERATIONS

All images used in this dissertation not created by the author are either 1) in the public domain, e.g., those provided by government agencies, 2) un-copyrighted and provided by the original photographer or processor, or 3) are individually copyrighted or excerpted from a copyrighted journal. Those subject to copyright protection are identified here along with usage permission.

Figure 3-1

Description Arctic pack ice.

Date July 2012

Source Own work

Author James Stringer

Copyright Creative Commons Attribution 2.0 Generic License available at http://creativecommons.org/licenses/by-nc/2.0/legalcode

Figure 3-5

Description Methane bubbles at Lake Abraham, Kootenay Plains, Alberta, Canada.

Date 2013

Source Own work

Author Darwin Wiggett

Permission On Thu, Nov 28, 2013 at 8:22 AM, Darwin Wiggett <darwin@oopoomoo.com> wrote:
Sure go ahead but the location is not Ontario, it is Abraham Lake, Kootenay Plains, Alberta, Canada

On Wed, Nov 27, 2013 at 7:18 PM, Melissa Bunte <Melissa.Bunte@asu.edu> wrote:
I am writing a dissertation about the appearance and formation of the icy surface of Jupiter's moon, Europa. I attempt to illustrate what the surface would look like at high resolution using analog images from ice formations

on Earth. Your image of the methane bubbles at Abraham Lake, Ontario is a prime example of sill emplacement of liquid or gaseous material into freezing ice. May I have your permission to use this image in my dissertation? It will be published electronically (PDF) through the Arizona State University library system and will not be used for commercial purposes.

Figure 3-9

Description A photograph of the snow surface at Dome C Station, Antarctica, it is representative of the majority of the continent's surface. The photo was taken from the top of a tower, 32 m above the surface.

Date January 2004

Source Own work

Author Stephen Hudson

Copyright Creative Commons Attribution 2.5 Generic License available at http://creativecommons.org/licenses/by/2.5/legalcode

Figure 4-19 (partial)

Description Europan ridges; NIMS overlain on SSI. Partial figure not showing results.

Date 2003

Source Astrobiology

Author J. Brad Dalton, Rakesh Mogul, Hiromi K. Kagawa, Suzanne L. Chan, Corey S. Jamieson

Permission On Fri, Mar 4, 2011 at 12:06 PM, Dalton, James B (Brad) (3227) <James.B.Dalton@jpl.nasa.gov> wrote:
I think your project looks very interesting. I like your approach to identifying the 2.05-micron feature, which may turn out to be a powerful biomarker. I give you permission to use my image from 11ENCYCLOD01, from Dalton et al., 2003. Just be sure to reference the source correctly.

On 3/3/11 2:48 PM, "Melissa Bunte" <Melissa.Bunte@asu.edu> wrote:
May I have permission to use a figure from one of your journal articles in my dissertation content? The figure is figure 7 from <J. Brad Dalton,

Rakesh Mogul, Hiromi K. Kagawa, Suzanne L. Chan, Corey S. Jamieson. Astrobiology. November 2003, 3(3): 505-529. doi:10.1089/153110703322610618> where you have overlain a Galileo SSI image with the corresponding NIMS image and highlighted the pixels you extracted for spectral averages. Using your figure would serve the dual purpose of showing the location from which we've extracted spectra (our best example) and showing the similarity between your methods and our algorithm's automatic extraction. Our intent is to support both methods.

Figure 5-1

Description Figure of fractures on Europa compared to fissures on a Hawai'ian volcano that both exhibit dark material near the vent.

Date March 2000

Source Cryomagmatic Mechanisms for the Formation of Rhadamanthys Linea, Triple Band Margins, and Other Low-Albedo Features on Europa

Author Sarah A. Fagents,Ronald Greeley,Robert J. Sullivan,Robert T. Pappalardo,Louise M. Prockter, The Galileo SSI Team

Copyright Elsevier, Icarus
Full text of the license agreement is available upon request.

License number	3277241173169
License date	Nov 27, 2013
Licensed content publisher	Elsevier
Licensed content publication	Icarus
Licensed content title	Cryomagmatic Mechanisms for the Formation of Rhadamanthys Linea, Triple Band Margins, and Other Low-Albedo Features on Europa
Licensed content author	Sarah A. Fagents,Ronald Greeley,Robert J. Sullivan,Robert T. Pappalardo,Louise M. Prockter, The Galileo SSI Team
Licensed content date	March 2000
Licensed content volume number	144
Licensed content issue number	1
Number of pages	35
Start Page	54
End Page	88
Type of Use	reuse in a thesis/dissertation
Portion	figures/tables/illustrations
Number of figures/tables/illustrations	1
Format	both print and electronic
Are you the author of this Elsevier article?	No
Will you be translating?	No
Title of your thesis/dissertation	Utilizing Science and Technology to Enhance a Future Planetary Mission: Applications to Europa
Expected completion date	Dec 2013
Estimated size (number of pages)	275
Elsevier VAT number	GB 494 6272 12
Permissions price	0.00 USD
VAT/Local Sales Tax	0.00 USD / 0.00 GBP
Total	0.00 USD

APPENDIX C

CONSTRIBUTION DECLARATIONS AND RELATED PUBLICATIONS

The following is a description of the contributions to each project by each contributor and of the usage of material within each publication. I hereby certify that all co-authors have given permission for the work to be used herein.

Global Geologic Map of Europa

Work on the Global Geologic Map of Europa was begun in 2000 by Patricio Figueredo, a postdoctoral fellow at Arizona State University, under a grant from the Planetary Geology and Geophysics Program and the U.S. Geological Survey. Mr. Figueredo contributed to the creation of the image mosaic that is used as a base for the map, completed regional-to-hemispheric scale mapping (Figueredo and Greeley, 2000, 2004), and contributed the global map and correlation of lineaments. His lineament work was published as a conference abstract (Figueredo et al., 2004) but his complete manuscript was never published. By personal agreement and under the terms of the original grant, his work is included in this final map. Mr. Figueredo defined a system of classification to identify 100 lineaments that most clearly define stratigraphic relationships; those 100 lineaments are included as structures on the map presented here along with approximately 50 additional lineaments of importance. The complete map of lineaments includes more than 1500 individual features and will be included on the final USGS published map.

Sequel to the lineament mapping, Arizona State University graduate student Thomas Doggett contributed additional high resolution images to the base photomosaic and published a preliminary near-global map of geologic units (Doggett et al., 2009). Mr. Doggett's work built upon previous local- to regional-scale mapping efforts as well as low-resolution global or hemispherical unit identification, resulting in identification of

material units that are largely confined to geographic regions. Mr. Doggett attempted to portray unit distribution at a common scale and to correlate the stratigraphic relationships between all units and structures across all hemispheres. The map was, however, incomplete at the time of publication due to factors related to the inability to follow unit contacts across image resolution boundaries. Mr. Doggett's published map does not include unit distribution for the low-resolution image swaths.

During this same period of time, contributions were made by other collaborators as well. David Senske provided detailed high-resolution mapping of chaos areas. These were too detailed to include in the final map. Kate Sever provided a distribution of lenticulae. Lenticulae will only be included in the final USGS published map. Jenny Blue provided assistance with defining feature nomenclature. Nomenclature is not included in this version of the map to allow the reader to view contact lines clearly but will be included in the USGS published map. Additional advisory, editing, and software support was provided by Ken Tanaka, Trent Hare, Ronald Greeley, Sabine Weiser, Kevin Mullins, Eric Kolb, Charles Bradbury, and Dan Ball.

My contributions to the mapping effort include: an assessment of image scaling factors and viewing geometry differences to resolve resolution boundary issues and define unit distribution across the low-resolution swaths; definition of additional material units, separation of lineaments into classes; refinement, separation, or deletion of the units established by Mr. Doggett to better illustrate morphological and textural differences between units, refinement of unit definitions to acknowledge globally occurring general geologic processes over geographic associations; refinement of contact types to better illustrate morphology differences at unit boundaries; and a new assessment of the overall

geologic history which resulted in named periods of formation. These tasks required a new perspective on mapping techniques but built on the previous works. The result is this first complete post-Galileo perspective on global mapping that adheres to the USGS standards of planetary mapping.

In addition to the construction and interpretation of the map itself, my work includes an assessment of all previously published models for potential formation mechanisms that could control the appearance of material units and structures. These models were contributed by many authors but had never been directly compared in the context of processes that could occur in a similar manner on a global scale. My interpretations of the conditions necessary to produce the visible morphologies of features is supplemented by terrestrial analogs of similar, if not comparably scaled, morphology. These are included to indicate the variety of mechanisms that may be operating simultaneously or in succession on Europa. Previous analyses have all attempted to establish only a single mechanism for forming each feature type; my interpretation allows for conjecture on the nature of the ice shell and liquid layer from a global perspective. Thus, I have considered all feature morphologies, the range of formation mechanisms that are likely, and the distribution of those features and formulated a theory of how the ice and liquid layers may vary and how interactions between those layers and the surface may occur.

Autonomy

Several projects were developed an included in my chapters on autonomous processes. These include, chronologically, methods of creating stereo images of the lunar surface, methods to identify regions of homogeneous spectral signature, methods to detect plumes extending beyond the limb of a planetary body by edge detection and planet disk

subtraction, and methods to analyze images for brightness variations and subsequently classify those variations by comparison to a database of features.

The work creating stereo image pairs was led by Michael Broxton of NASA Ames Research Center. He developed the NASA Ames Stereo Pipeline to analyze Apollo images of the surface and indirectly extract topographic information. My involvement in the project included testing of the pipeline in the final stages by comparing Pipeline-created images and topography with manual measurement of dimensions by manual and remote means; primarily, this involved constructing digital elevation models of the Apollo landing sites. The initial results were published in a conference abstract (Broxton et al., 2009). My derivative works are not included here as they do not pertain to the dissertation topic.

Spectral analysis work was led by David Thompson of NASA Jet Propulsion Laboratory. The JPL Machine Learning group developed a superpixel endmember detection algorithm (Thompson et al., 2011) to filter the spectral signatures within an image and identify connected pixels with homogenous signatures. All processing was completed by Dr. Thompson. My contribution was to aid in applying this method to planetary images by identifying a representative database of images that should exhibit detailed spectral signature changes throughout the image, specifically those images of Europa. Additionally, my efforts include assessing the correlation between endmember spectral signatures and surface morphology by comparing the signatures of dark linear features (i.e., fractures, ridges, or flexūs) to those of surrounding icy plains or chaos. This work demonstrated one example of autonomous identification of individual geologic

features and was published as a conference abstract (Bunte et al., 2011). Only the results and my interpretation of the analyses are included here.

Edge detection methods were also developed by David Thompson as a study in the potential to autonomously identify transient features in spacecraft images. My contribution was to develop a database of images which illustrate a variety of transient events at multiple planetary bodies and to assess processed images for positive detections. This work established an efficient process by which plumes could be autonomously detected. A description of the method and highest quality results were published as a journal article (Thompson et al., 2012, where I am second author). Only the results and my interpretation of the analyses are included here. In this dissertation, I expound upon the advantages and disadvantages of this type of processing and use this method as support for developing additional methods.

The majority of autonomous processing work described here includes processing images with SIFT and classifying the results with *k*NN. These are standard methods of statistical analysis and were chosen as a potential method of detecting transient features by Srikanth Saripalli. I worked with his graduate student, Yucong Lin, to develop the work herein. Mr. Lin performed all model modifications and processing. His primary contribution was to explore the capabilities of the SIFT feature recognition method and to establish the most efficient classification technique to use for the purposes of this study. He explored six classification techniques and outlined the specifications of each technique in regard to threshold array sizes and classification thresholds, ultimately determining that *k*NN was the most efficient method of classification. The results of his study were published as a peer-reviewed conference abstract (Lin et al., 2012, where I am

second author). My contributions included: developing the database of all planetary images containing evidence of plumes or other features important for potential identification or classification, manually selecting test image sets for use in testing conditional results, assessing processed images for detections, and evaluating the efficiency with which these methods can detect and identify transient events based on identifiers that I provided. To ensure that my derivative work made appropriate use of these techniques, I also provided detailed documentation of the programming code that we utilized, reprocessed all data to ensure the ability to duplicate the method, and processed additional image sets to explore the limitations of detection.

My application of this work addressed: the need for autonomous processing in solar system exploration and the variety of ways that autonomy could be used to increase mission data return; the range of geophysical events that could occur, their characteristics, and the limits on their detectability; specific analysis of projected activity, and its detectability, at Europa; and specific examples of solar system missions that could benefit from intelligent autonomous processes or resilience.

APPENDIX D

RELATED PUBLICATIONS

As described in Appendix C, sections of the text are based on published works of which I am primary or secondary author. In addition, sections of the text are soon to be published as scientific journal articles.

For the Thompson et al. paper on edge detection methods (2012), I provided the scientific description of the appearance of plumes, identification of positive results or artifacts, and a general perspective on the evaluation of results. Descriptions of the method and discussion on the capabilities of use onboard a spacecraft are attributed to Dr. Thompson. Only figures representing the method and a general description of the results are used in this dissertation, thus it is not necessary or appropriate to include the entire publication as a chapter here. My intent was to use this work as a comparison to illustrate the success rate and efficiency of other methods.

The Lin et al. paper on classification methods (2012) details each of the classification techniques that were explored by Mr. Lin. I provided the geologic context of features and purpose of using this type of processing, a description of the autonomous methods previously used in space exploration, and the geologic perspective on the statistical analysis. Descriptions of the techniques are attributed to Mr. Lin. Only the relevant figures representing *k*NN results are applied to this dissertation and all relevant geologic background is independently included in the chapters related to autonomous processes and applications, thus it is neither necessary nor appropriate to include the entire publication as a chapter here. Likewise, the second paper (Lin et al., in press) primarily concerns the work of Mr. Lin; it describes efforts to improve detection rate. It includes my description of geologic features, the reasoning for autonomous processing, my analysis of the results with respect to efficient detection, and an assessment of future

applications. Neither paper describes the SIFT method in detail, as it is considered a standard practice in statistical analysis. I include a description of the method as it relates to this specific use in Chapter 4.

The Global Geologic Map of Europa will be published as a USGS investigative series map accompanied by a descriptive pamphlet and will include content from Chapters 2 and 3. The map presented herein is under review by the USGS and is subject to change per the results of that review.

Bunte, M.K., R. Greeley, T. Doggett, P. Figueredo, K. Tanaka, and D. Senske (*in preparation; to be submitted Spring 2014)* Global Geologic Map of Europa, *USGS Map Series*.

The map will be supplemented by a more detailed description of the geologic features and my interpretation of formation processes, with specific attention to the benefit of this work to future exploration. This will include content from Chapters 2, 3, and 5.

Bunte, M.K., R. Greeley, T. Doggett, P. Figueredo, K. Tanaka, and D. Senske (*in preparation; to be submitted Spring 2014)* Global Geologic Mapping of Europa: Exploring the Undetermined Nature of Europa's Geophysical Activity, *Journal of Geophysical Research: Planets*.

The work on autonomous image processing and applications to future missions will be included in a third publication which will include content from Chapters 4 and 6.

Bunte, M.K., Y. Lin, S. Saripalli, J. Bell, and R. Greeley (*in preparation; to be submitted Fall 2014*) Intelligent Detection of Large Scale Volcanism During a Spacecraft Flyby and Applications of Spacecraft Resilience to Future Planetary Missions, *Planetary and Space Science*.

TRIBUTE TO AN OUTSTANDING ADVISOR

I owe a great debt of gratitude to Dr. Ronald Greeley, a pioneer in the field of planetary sciences and my advisor through both M.S. and Ph.D. projects until his untimely passing in October 2011. It was both an honor and a pleasure to work with him on a range of projects. Without his guidance and clear sight, this work would not have been possible. I thank him for agreeing to help me develop the projects herein, for advocating on my behalf on funding issues and on career development and for seeing the benefits of these projects to the planetary community. Many who have worked with Ron noted his dedication to the field and the great role he played in promoting his students' work; I count myself fortunate to have been included in the benefits of his tutelage. In regards to the Global Geologic Map of Europa, I believe it to be his last unfinished project; I take great pleasure in finally saying "Here, Ron, is your paper!" though I will certainly remember with fondness his penchant for leaving sticky notes with "See me, ASAP!" on all drafts. Phil Christensen, another former student of Ron's, once discussed with me the purpose of completing a Ph.D. It was his belief that a doctoral student's goal should be to become the world's expert in a very narrow field. However, he commented that the broad nature of this work reveals itself to be "very much a Ron project- where the goal is not to be so focused as to not see the context but rather to change the way that people think about the context". May Ron's vision for the future of planetary exploration carry forth and continue changing our perspectives and perceptions.